N° ordre :

UNIVERSITÉ DE LILLE

ÉCOLE DOCTORALE SCIENCES POUR L'INGENIEUR

THÈSE EN COTUTELLE INTERNATIONALLE

présentée par

Geovana PEREIRA DRUMOND

pour l'obtention du titre de

DOCTEUR EN MÉCANIQUE, ENERGÉTIQUE ET MATERIAUX
DE L'UNIVERSITÉ DE LILLE
ET
DOCTEUR EN GÉNIE OCÉANIQUE DE L'UNIVERSITÉ
FEDERALE DE RIO DE JANEIRO

intitulée

VERS UN CRITÈRE DE DOMMAGE EN FATIGUE D'ACIER POUR PIPELINES BASÉ SUR DES CHANGEMENTS MICROSTRUCTURAUX

Soutenue **le 03 décembre 2019** devant le jury composé de :

Directeurs :	**Francine ROUDET**, Maître de Conférences-HDR, Université de Lille **Ilson PARANHOS PASQUALINO**, Professeur, Université Federale de Rio de Janeiro (UFRJ)
Rapporteurs :	**Marie-José PAC**, Professeure, Université Haute-Alsace **Jean-Louis ROBERT**, Professeur, Université Clermont Auvergne
Examinateurs :	**Didier CHICOT**, Professeur, Université de Lille **Bianca DE CARVALHO PINHEIRO**, Professeure, Université Federale de Rio de Janeiro (UFRJ) **José Luis FREIRE**, Professeur, Université Pontificale Catholique de Rio de Janeiro (PUC-Rio) **Marcelo Igor LOURENÇO DE SOUZA**, Professeur, Université Federale de Rio de Janeiro (UFRJ)

UNIVERSIDADE FEDERAL DO RIO DE JANEIRO

Université de Lille

ACKNOWLEDGMENTS :

Firstly, I would like to express my sincere gratitude to my advisors **Prof. Ilson Paranhos Pasqualino**, **Prof. Francine Roudet** and **Prof. Bianca de Carvalho Pinheiro** for the continuous support during my Ph.D studies, for their patience, motivation, inspiration, and valuable expertise. I am extremely thankful to **Prof. Didier Chicot** for the guidance during the different phases of the work, from the understanding of the subject to the interpretation of results.

I would like to thank **Prof. Marcelo Igor Lourenço de Souza**, from the Federal University of Rio de Janeiro, **Prof. Jean-Loius Robert**, from the *Université Clermont Auvergne*, **Prof. José Luiz de França Freire**, from the Pontifical Catholic University of Rio de Janeiro, and **Prof. Marie-José Pac**, from the *Université de Haute-Alsace*, members of the jury, for their valuable contribution with insightful comments. I would like to thank their time and dedication spent reading and examining the thesis.

I am really grateful to the whole administration and technical staff of the **Subsea Technology Laboratory (LTS)** of COPPE/Federal University of Rio de Janeiro, and of the **IUT A – GMP** of the University of Lille for all support spent in different moments during the accomplishment of this work. I would also like to express my gratitude to my friends from the IUT A – GMP, **Dr. Xavier Decoopman**, **Dr. Cosmin Gruescu**, **Dr. Stephania Kossman**, **Dr. Philémon Nogning**, **Dr. Alberto Mejias**, **Dr. Mohammed Bouchelarm** for sharing his friendship, helping me in several tasks, and sharing valuable insights and motivating conversations. My sincere thanks also go to **Laurence Lagaisse**, secretary of the IUT A – GMP, for always helping me with administrative questions.

I would like to show my gratitude to everyone who helped me in different ways to offer me a wonderful and unforgettable time in France.

I am extremely thankful to the financial support from **Capes-Cofecub** program number 800-14, essential for the accomplishment of this work.

Finally, I would like to thank all my friends and family, and in special my parents, **Sérgio Luis Drumond** and **Maria das Graças Soares Pereira Drumond**, my grandmother **Coracira Soares Pereira**, and in memory, my grandfather **Manoel Rocha Pereira**, for supporting me throughout my life.

TITRE EN FRANÇAIS :

VERS UN CRITERE DE DOMMAGE EN FATIGUE D'ACIER POUR PIPELINES BASE SUR DES CHANGEMENTS MICROSTRUCTURAUX

RESUMÉ :

L'étude des modifications de la microdureté de la surface des matériaux au cours des différentes étapes de la fatigue peut permettre d'évaluer l'évolution de la résistance des matériaux aux déformations microplastiques et ainsi fournir des informations pertinentes sur les dommages cumulés causés par la fatigue à la surface. L'objectif de ce travail est de proposer une nouvelle méthode basée sur les changements microstructuraux pour prédire la durée de vie en fatigue des structures en acier soumises à des charges cycliques, avant la fissuration macroscopique. Des essais d'indentation instrumentée et des analyses par diffraction des rayons X ont été effectués sur des échantillons soumis à grand nombre de cycles (de l'anglais, *High Cycle Fatigue* -HCF), jusqu'à différentes fractions de sa durée de vie en fatigue. Il a été observé que les changements majeurs dans les valeurs de microdureté se produisaient à la surface du matériau, jusqu'à 2 µm de profondeur d'indentation, et à environ 20% de la durée de vie en fatigue des échantillons, ce qui était attendu, car les étapes de nucléation et de microfissuration des fissures sont des phénomènes de surface. Ici, la valeur de 20% de la durée de vie en fatigue a été déterminée comme la période critique pour les changements microstructuraux, et cette valeur a été utilisée dans un ajustement analytique d'une expression polynomiale afin de prédire le nombre de cycles em fatigue jusqu'à rupture (*Nf*) d'une structure en acier.

MOTS-CLÉS :

Amorçage de l'endommagement par Fatigue; Microdéformations; Essais de Microindentation Instrumentés; Diffraction des rayons X; Acier API 5L X65; Pipelines

TÍTULO EM POTUGUÊS :

PROPOSTA DE CRITÉRIO DE AVALIAÇÃO DE DANOS EM FADIGA DE OLEODUTOS DE AÇO COM BASE EM MUDANÇAS MICROESTRUTURAIS

RESUMO :

O estudo das variações dos valores de microdureza na superfície durante a vida em fadiga do material pode ser usado para estimar a evolução da resistência do material às deformações microplásticas e, consequentemente, fornecer informações relevantes sobre os danos acumulados na superfície. O objetivo deste trabalho é propor uma nova metodologia baseada em mudanças microestruturais para prever a vida em fadiga de estruturas de aço submetidas à carga cíclicas antes da propagação macroscópica de trincas. Testes de microindentação instrumentada e análises de difração de raios-X foram realizados nas amostras, previamente submetidas a ensaios de fadiga de alto ciclo, em diferentes frações da vida em fadiga do material. Observou-se que as grandes mudanças nos valores de microdureza ocorreram na superfície e subsuperfície do material, até 2μm de profundidade de penetração, e a cerca de 20% da vida de fadiga das amostras, o que era esperado, uma vez que a nucleação e propagação de microtrincas são fenômenos que ocorrem preferencialmente na superfície do material. No presente trabalho, o valor de 20% da vida em fadiga foi determinado como o período crítico para mudanças microestruturais, e esse valor foi usado em um ajuste analítico através de uma expressão polinomial para prever o número de ciclos até a falha (N_f) de uma estrutura de aço.

PALAVRAS-CHAVE :

Dano por fadiga; Microdeformações; Testes de microindentação instrumentada; Difração de Raios-X; Aço API 5L X65; Dutos de transporte de petróleo (*pipelines*)

TITLE IN ENGLISH :

TOWARDS A PROPOSAL OF FATIGUE DAMAGE ASSESSMENT OF STEEL PIPELINES BASED ON MICROSTRUCTURAL CHANGES

ABSTRACT :

The study of changes in material surface microhardness during the different stages of the fatigue mechanisms can be used to estimate the evolution of the material resistance to microplastic deformations and, consequently, provide relevant information about the cumulated fatigue damage on the surface. The aim of this work is to propose a new methodology based on microstructural changes to predict fatigue life of steel structures submitted to cyclic loading, before macroscopic cracking. Instrumented indentation tests and X-Ray diffraction analysis were carried out in the samples previously submitted to high cycle fatigue (HCF) loads, up to different fatigue life fractions. It was observed that the major changes in the microhardness values occurred at the surface and subsurface of the material, up to 2 µm of indentation depth below the surface, and around 20% of the fatigue life of the steel samples, which was expected, since crack nucleation and microcracking stages result of surface phenomena. Here, the value of 20% of the fatigue life was determined as the critical period for microstructural changes, and this value was used in an analytical fit of a polynomial expression to predict the number of cycles to failure (N_f) of a steel structure.

KEYWORDS :

Fatigue damage; Microstructural changes; Instrumented microindentation tests; XRay Diffraction; API 5L X65 steel; Pipelines

TABLE OF CONTENTS

LIST OF FIGURES

LIST OF TABLES

INTRODUCTION

INTRODUCTION

The world energy matrix is still dependent of the hydrocarbons fuels provided by the oil and gas industry. These inputs are of difficult substitution in the world energy matrix and are the basis of the production and consumption mode and even the culture of modern society [1]. A way to demonstrate the economic strength of the oil industry is to understand the economic importance of the oil companies in a world context. Among the 25 largest companies in the world, 6 (Shell, Exxon Mobil, Chevron, PetroChina, BP and Total) are from the oil and gas sector; among the top 100, 11 are in the oil industry (the six above, plus GazProm, Petrobras, Equinor, Eni and Luk Oil) [2].

Oil and gas exploration and production in deepwater is associated with the use of highly sophisticated equipment and increasing innovative technology. However, the failure of this equipment can cause serious consequences, including material loss and environmental pollution. Critical accidents can even cause the loss of human lives [3]. Pipelines are the safest method to export liquid and gaseous petroleum products or chemicals. However, like any engineering structure, pipelines do occasionally fail. According to Drumond et al. [3], the main failure modes experienced by pipelines during production are identified as mechanical damage (impact or accidental damage), external and/or internal corrosion, construction defect, material or mechanical failure, natural hazards and fatigue.

The phenomenon of metal fatigue presents a complex nature, involving several stages. These stages can be successively identified as microcrack initiation and propagation (Stage I), macrocrack propagation (Stage II) and final fracture (Stage III). Fatigue crack growth rates in Stages I and II have been extensively studied for decades in materials of different microstructures, evidencing some common features of the crack propagation behavior [4]. Stage I crack growth occurs along crystallographic slip bands and is dominated by shear. Stage II crack growth is associated with crack propagation on a plane normal to the direction of the maximum principal tensile stress applied, involving simultaneous or alternating plastic flow along two slip systems forming striations on the fracture surface [4-8].

Several numerical simulation models were developed to predict the fatigue crack growth in materials based on the relation of the crack growth rate and fatigue loading parameters, such as the linear elastic fracture mechanics (LEFM) approach based on the

Paris law [9]. However, this approach is more suitably applied for modeling the fatigue crack propagation in Stage II, when the crack growth is regular and stable. However, in Stage I, modeling of the fatigue crack growth behavior needs a deeper understanding of the microstructural mechanisms [4].

Some assumptions were made trying to better understand the microstructural mechanisms involved in the Stage I fatigue crack growth, in which the microstructural features, such as grain boundaries, grain size and grain orientation, as well as the sample geometry, influence the fatigue microcrack growth [4]. Bjerkén and Melin [10,11] show that the growth of the fatigue microcracks is driven by shear and is dominated by local plasticity, and these micromechanisms are accompanied by the formation of a local plastic zone ahead of the crack tip, while Andersson and Persson [12] and Jono et al. [13] show that the crack growth occurs along preferred slip planes. According to Ye and Wang [14], a great deal of experimental evidence has proved that fatigue damage in the first stage is primarily related to the occurrence and development of localized plastic strain concentration at or near the surface of materials during cycling.

The investigation of the fatigue properties of the material in microstructural scale increases the reliability of fatigue crack growth predictions and allows prevention of the fatigue failures of structural components [4]. Oil and gas pipelines are made of high strength API 5L steels of different grades, as X60, X65, X70 and X80, for instance [15]. And to assure their structural integrity and forewarn a fatigue failure it is important to detect and follow the fatigue damage in microstructural scale, prior to macrocrack propagation. The aim of the present work is to study the microstructural behavior of an API 5L X65 grade steel pipeline during the Stage I of fatigue damage by means of microhardness and X-ray diffraction tests.

The microhardness of a material shows its ability to resist microplastic deformation caused by indentation or penetration and is closely related to the plastic slip capacity of the material. Therefore, the study of the change of microhardness on the material surface could be a relevant and promising approach to evaluate the fatigue damage evolution process, based on the material resistance to microplastic deformations and, consequently, on the resistance to fatigue damage observed on the surface. Here, instrumented indentation tests (IIT) in a depth of 2µm from the surface were done in 35 API 5L X65 grade steel samples, previously submitted to fatigue cycling. Thus, microstructural changes in terms of variations

in the microhardness at the surface are evaluated during the fatigue life of the material.

In the search of a new way to predict the fatigue life of metal structures under cyclic loads, another method of studying the microstructural behavior of an API 5L X65 grade steel pipeline was used aiming to confront and to ratify the indentation results. According to Pinheiro [15], the use of nondestructive evaluation (NDE) techniques to investigate microstructural changes associated with fatigue has greatly increased. Among these techniques, thermography, ultrasonic testing, magnetic inspection, and X-ray diffraction have indicated notable perspectives. As in the work of Pinheiro [15], here, the X-ray diffraction technique is used to evaluate microdeformations, characterized by the full width at half maximum (FWHM) of the XRD peak in real time during high cycle fatigue (HCF) tests. Among available NDE techniques, X-ray diffraction (XRD) was chosen because besides giving important information about microdeformation changes of a fatigued material, this technique allows the use of portable systems to directly evaluate the surface of test pieces in field.

In addition, fatigue tests on annealed samples are also carried out and the results are compared with the as-machined samples. After the annealing treatment, the network of initial dislocations is rearranged, and the state of residual stresses generated during pipe manufacturing is relaxed. The experimental results obtained by instrumented indentation tests and X-ray diffraction are analyzed and compared in view of the determination of a tendency in the behavior of fatigue damaged API 5L X65 grade steel samples. The approach of using a NDE technique that can be used in field, as the X-ray diffraction, with reliable results (confirmed by the instrumented indentation technique) could be of high relevance toward a new way to predict the fatigue life of metal structures under cyclic loads.

STRUCTURE OF THE DISSERTATION

In Chapter I a literature review about fatigue of metals is presented. This chapter is divided in two parts. The first part comprises a brief review of the stress-life method of fatigue life evaluation. The second part deals with fatigue damage mechanisms (initiation of microcracks, microcracking and macrocrack propagation), focusing in the two first stages, up to the transition between the micro and macro domain of the crack propagation.

Chapter II presents a literature review concerning indentation methodology. This chapter is divided in two parts. The first part comprises a literature review of the evolution of indentation hardness tests, focusing in instrumented cyclic microindentation tests, which

are one of the methods used in this work to characterize microstructural changes in the material. The second part deals with microindentation testing applied to fatigue damage assessment.

Chapter III is divided in three parts. The first part presents a brief theoretical review concerning the X-ray diffraction technique. The second part comprises the methods of peak broadening analysis, related to distortion of the grains, dislocation density and calculation of micro residual stresses (microdeformations). Finally, the third part presents a literature review on X-ray diffraction technique applied to fatigue damage analysis of materials focusing in the halfwidth method, or full width at half maximum (FWHM), which here is the chosen method to study the changes in microstructure of metals during fatigue damage accumulation.

Chapter IV presents the characterization of API 5L X65 grade steel carried out by means of chemical composition analyses, metallography analysis and uniaxial tension tests.

In Chapter V the experimental work is presented, comprising the preparation of fatigue test samples, the experimental setup for the fatigue tests, the instrumented indentation tests and X-ray diffraction study of the changes in the microstructural of fatigue damaged API 5L X65 grade steel samples.

Chapter VI presents and discusses the obtained results. For all applied stress amplitudes, for both conditions (as-machined and annealed), and for both analyzing methods (instrumented indentation tests and X-Ray diffraction) was possible to observe that the major microstructural changes occurred at the begging, prior to a quarter of the fatigue life of the material. Depending on the material condition, as-machined or annealed, critical periods for microstructural changes are estimated and used to anticipate the number of cycles to failure (N_f) of an API 5L X65 pipeline.

Finally, the conclusions of the developed work are discussed and future perspectives for coming works are raised.

CHAPTER I

FATIGUE OF METALS

CHAPTER I. FATIGUE OF METALS

This chapter is divided in two parts. The first part comprises a brief review of the stress-life method of fatigue life evaluation. The second part deals with fatigue damage mechanisms (initiation of microcracks, microcracking and macrocrack propagation), focusing in the two first stages, prior to the transition between the micro and macro domain of the crack propagation.

The phenomenon of fatigue is defined as a cycle-by-cycle accumulation of damage in a material undergoing alternating stresses and strains [16]. A significant feature of fatigue is that the load is not large enough to cause immediate failure. Instead, failure occurs after a certain number of load fluctuations have been experienced, i.e., after the accumulated damage has reached a critical level [17]. Fatigue damage is particularly dangerous due to its progressive and localized character; it usually develops without any obvious warning. Variables such as stress concentration, surface finish, corrosion, temperature, load frequency, metallurgical structure and residual stresses can affect the material fatigue behavior [15].

Long before the linear elastic fracture mechanics (LEFM) to characterize fatigue failure were developed, the importance of cyclic loading in causing failures (e.g. railroad axles) was recognized. Starting with the work of Wöhler [18], who performed rotating bend tests on various alloys, and empirical methods have been developed. Nowadays, the three major fatigue life methods used in design and analysis are the stress-life method, the strain-life method, and the LEFM method. These methods attempt to predict the life in number of cycles to failure, *N*, for a specific level of loading [15].

- **Strain-life (ε-N) method:** The local strain-life (ε-N) method, first formulated in the 1960s, is a detailed analysis of plastic deformation at localized regions; however, several idealizations are compounded, leading to uncertainties in results [19]. This method relates the fatigue life to the amount of plastic strain suffered by the part during the repeated loading cycles. When the stress in the material exceed the yield strength and the material is plastically deformed, the material will be strain hardened and the yield strength will increase if the part is reloaded again. However,

if the stress direction is reversed (from tension to compression), the yield strength in the reversed direction will be smaller than initial value which means that the material has been softened in the reverse loading direction (this is referred to as Bauschinger Effect). Each time the stress is reversed, the yield strength in the other direction is decreased and the material gets softer and undergoes more plastic deformation until fracture occurs [20].

- **Linear Elastic Fracture Mechanisms (LEFM) method:** The Linear Elastic Fracture Mechanisms (LEFM) approach, also formulated in 1960s, predicts crack growth with respect to stress intensity [19]. The LEFM method assumes that a small crack already exists in the material, and it calculates the number of loading cycles required for the crack to grow to be large enough to cause the remaining material to fracture completely [20].
- **Stress-life (S-N) method:** The stress-life (S-N) model, first formulated between the 1850s and 1870s, is the least accurate method, particularly for low cycle applications; but it is the most traditional and easiest to implement [19]. This method relates the fatigue life to the alternating stress level, but it does not give any explanation to why fatigue failure happens [20]. Only the stress-life method will be considered in this work, and it is detailed as follows.

I.1 STRESS-LIFE METHOD

A typical stress history during cyclic loading is depicted in Figure I-1 where $\Delta\sigma$ is the stress range, σ_a the stress amplitude, σ_m the mean stress and R the load ratio. These parameters are defined in Equation I-1 to Equation I-4.

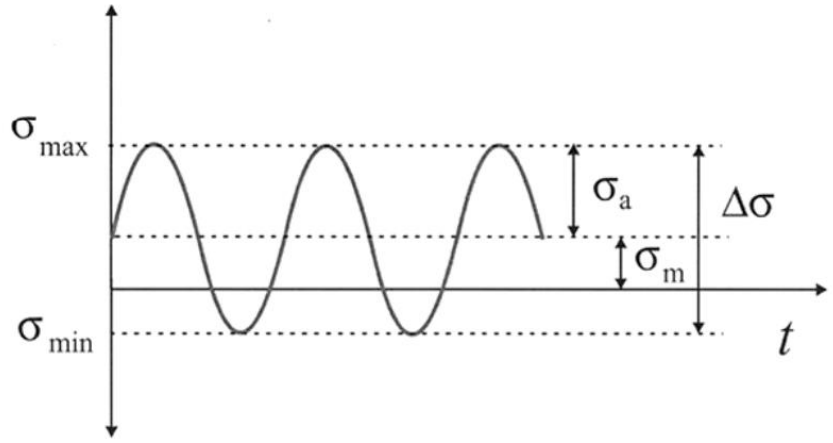

Figure I-1:Typical stress history during cyclic loading [21].

Stress Range	$\Delta\sigma = \sigma_{\max} - \sigma_{min}$	**Equation I-1**
Stress Amplitude	$\sigma_a = \frac{1}{2}(\sigma_{\max} - \sigma_{min})$	**Equation I-2**
Mean Stress	$\sigma_m = \frac{1}{2}(\sigma_{\max} + \sigma_{min})$	**Equation I-3**
Load Ratio	$R = \frac{\sigma_{\min}}{\sigma_{max}}$	**Equation I-4**

If $|\sigma_{max}| = |\sigma_{min}|$, the mean stress is zero ($\sigma_m = 0$), and completely or fully reversed loading is attached (*R=-1*). To handle with cases where $\sigma_m \neq 0$, some expressions can be used to correct the S-N curve. Figure I-2(a) illustrates the effect of mean stress on fatigue strength. For a given number of cycles N, fatigue strength decreases with increasing mean stress. Figure I-2(b) presents the three methods most used to account for the mean stress effects, and the expressions describing these methods are shown in Equation I-5 to Equation I-7.

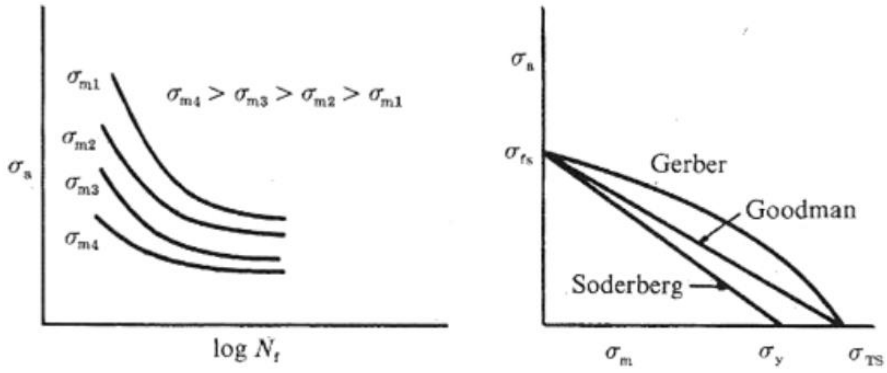

Figure I-2: (a) S-N curves for $\sigma_m \neq 0$; (b) Gerber, Goodman and Soderberg curves [23].

Soderberg	$\sigma_a = \sigma_a\|_{\sigma_m = 0}\left(1 - \frac{\sigma_m}{\sigma_y}\right)$	**Equation I-5**
Goodman	$\sigma_a = \sigma_a\|_{\sigma_m = 0}\left(1 - \frac{\sigma_m}{\sigma_{TS}}\right)$	**Equation I-6**
Gerber	$\sigma_a = \sigma_a\|_{\sigma_m = 0}\left(1 - \left(\frac{\sigma_m}{\sigma_{TS}}\right)^2\right)$	**Equation I-7**

In the previous expressions, σ_a is the stress amplitude denoting the fatigue strength for

a nonzero mean stress, $\sigma_a|_{\sigma_m=0}$ is the stress amplitude (for a fixed life) for fully reversed loading (σ_m = 0 and R = -1), and σ_y and σ_{TS} are the yield strength and the tensile strength, respectively.

The stress-life relation is obtained experimentally, where test specimens are subjected to repeated alternating stresses while counting cycles to failure. Many fatigue tests are performed at different values of stress amplitudes. Each test will produce a different number of cycles to failure. The data obtained is used to generate the fatigue strength *vs.* fatigue life diagram, which is known as the S-N curve, or Wöhler curve (Figure I-3). The number of cycles should be plotted in logarithmic scale (abscise axis) and fatigue strength should be indicated in logarithmic or Cartesian scale (ordinate axis). The fatigue strength S_n is usually expressed in terms of alternating stress amplitude σ_a or maximum stress σ_{max} [15]. Figure I-3 shows S-N curves in log-log and semi-log scales for superalloy S/SAV. S-N curve is a straight line in log-log plot. However, in semi-log plot, a smooth curve is fitted.

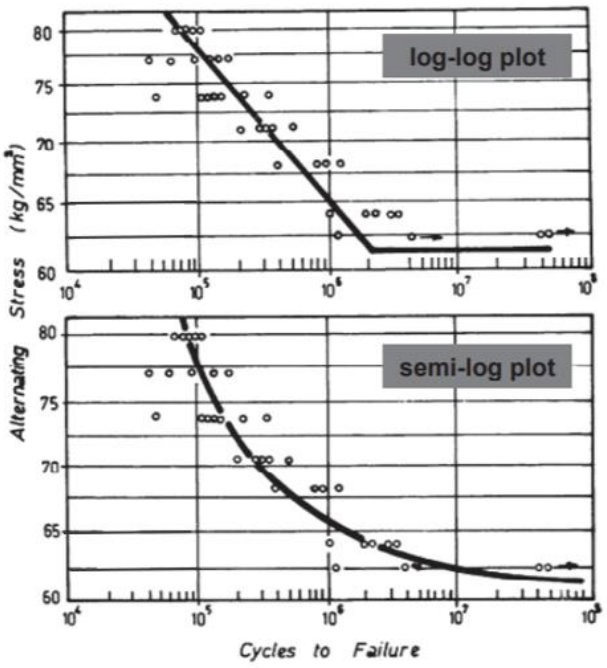

Figure I-3: S-N curves in log-log and semi-log scales for superalloy S/SAV [22].

Figure I-4 shows schematic S-N curves for ferrous alloys and titanium (Curve A) and nonferrous alloys (except titanium) and nonmetallic materials (Curve B). For ferrous alloys and titanium, the curve becomes asymptotic to horizontal line (the specimen will not fail for an infinite number of cycles). The stress level at such point is called endurance limit, denoted by *Se*. It is not observed for nonferrous alloys and nonmetallic materials, their

fatigue strength is determined for a specified number of cycles. When a specimen does not fail even if the specified cycle is reached, test is stopped, and the corresponding stress value is marked on the curve as "runout" (given by an arrow as in Curve B). The fatigue limit in such case is assumed as $5x10^7$ cycles for design purposes.

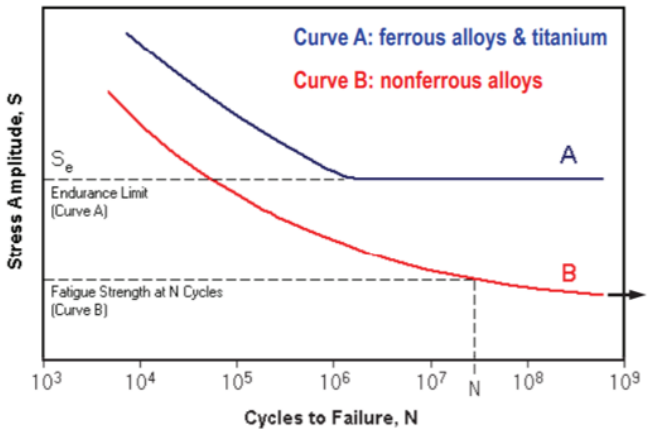

Figure I-4: Ferrous and nonferrous S-N curves [22].

Two domains of fatigue life can be distinguished in an S-N curve (log-log scale) for steel (Figure I-5): finite life ($N < 10^{6\sim7}$), where the material can be under low cycle ($10^0 < N < 10^3$) or high cycle fatigue ($N \geq 10^3$), and infinite life ($N > 10^{6\sim7}$).

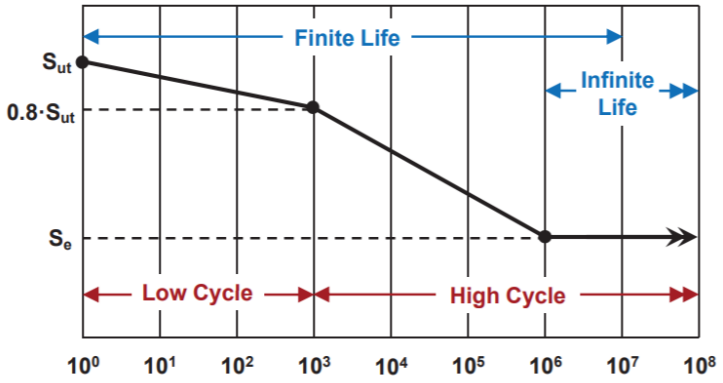

Figure I-5: S-N curve (log-log) scale for steel [22].

Low cycle fatigue (LCF) has two fundamental characteristics: plastic deformation in each cycle, and low cycle phenomenon. Fatigue tests are conducted under strain control, and the strain-life method is used for life prediction. High cycle fatigue (HCF) concerns failures corresponding to stress cycles greater than 10^3 cycles. In high cycle fatigue, even if stresses are elastic at the macroscopic scale, highly localized deformations are observed in the material. In this case, stresses remain globally elastic and fatigue tests can be conducted

either under stress control or strain control. From design viewpoint, the main interest in engineering is for the high cycle region of S-N curve. However, low cycle fatigue data can be advantageous when only a short service life is required. In this work, the samples were tested under high cycle fatigue domain.

The endurance limit

For materials submitted to high-cycle fatigue, it is important to make sure that the stress level in the material is below the endurance limit, but finding this limit experimentally is time consuming because it requires testing many samples and the time for each test is relatively long. Therefore, it is usual to relate the endurance limit to other mechanical properties that are easier to determinate (such as the ultimate tensile strength, UTS) [23]. Figure I-6 shows a correlation between the ultimate strength and endurance limit, and as can be observed, for ultimate strengths up to 1400 MPa, the endurance limit seems to have a constant value. The relationship between the endurance limit and ultimate strength for steels is given in Equation I-8.

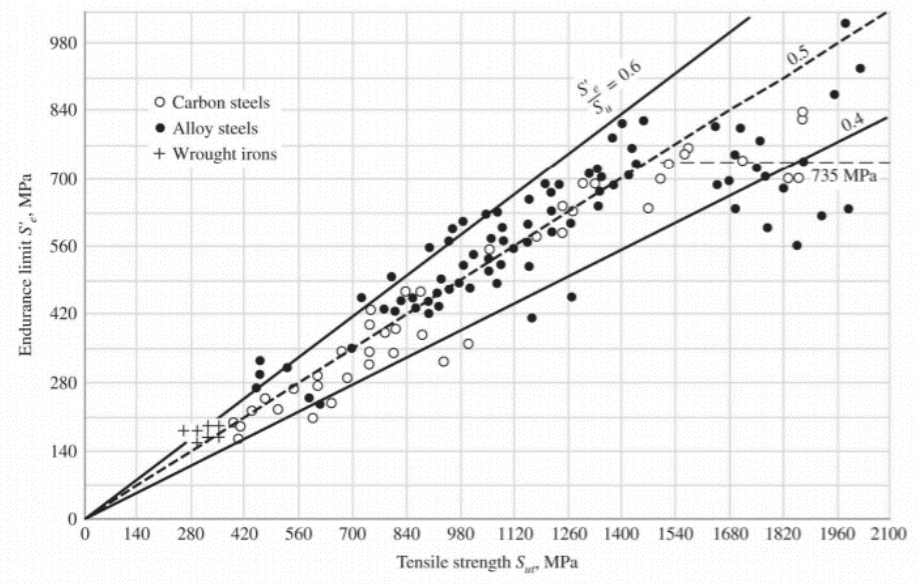

Figure I-6: Correlation between the ultimate strength and endurance limit [23].

$$S'_e = \begin{cases} 0.5\ \text{UTS} & for\ \text{UTS} \leq 1400\ MPa \\ 700\ MPa & for\ \text{UTS} > 1400\ MPa \end{cases}$$

Equation I-8

The prime (') (Equation I-8) is used to denote that this value was obtained for that sample, experimentally. It is unrealistic to expect the endurance limit of a mechanical or structural equipment to match the values obtained in the laboratory [23]. Thus, some

modifications factors are used to correlate the endurance limit for a given material to the value obtained from experimental tests (Equation I-9).

$$S_e = k_a k_b k_c k_d k_e k_f S'_e$$

Equation I-9

where

k_a = surface condition modification factor

k_b = size modification factor

k_c = load modification factor

k_d = temperature modification factor

k_e = reliability factor

k_f = miscellaneous-effects modification factor

S'_e = experimental test specimen endurance limit

S_e = endurance limit at the critical location of a machine part in the geometry and condition of use.

Deeper explanation about each one of these k's factors (k_a to k_f) can be found in [23].

The fatigue strength

Besides the endurance limit, another point of the S–N curve is required to completely define the stress-life fatigue behavior [24].The S-N curve in the high cycle fatigue ($10^3 \leq N \leq 10^6$) is usually described by the Basquin equation $S_n = CN^b$, in where S_n is the fatigue strength, and the constants *C* (y intercept) and *b* (slope) are determined from the end points $(S_n)_{10^3}$ and $(S_n)_{10^6}$as illustrated in Figure I-7 and as defined in Equation I-10 and Equation I-11.

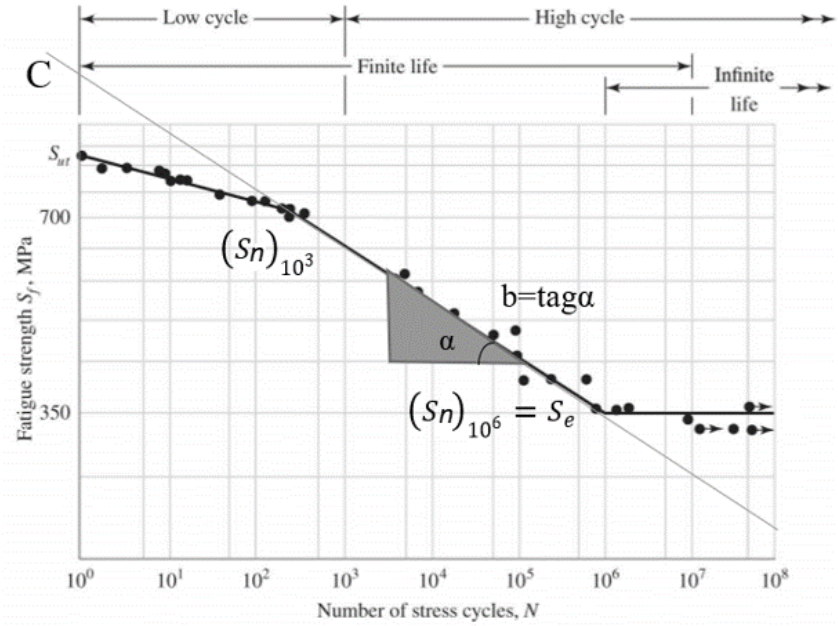

Figure I-7: S-N curve plotted from results of completely reversed axial fatigue tests. Material: normalized UNS G41300 steel. Adapted from [15].

$$C = \frac{(S_n)^2{}_{10^3}}{S_e}$$

Equation I-10

$$b = -\frac{1}{3}\, log\left(\frac{(S_n)_{10^3}}{S_e}\right)$$

Equation I-11

where $S_e$is the modified endurance limit.

$(S_n)10^3$ can be related to UTS as Equation I-12.

$$(S_n)_{10^3} = f\ x\ UTS$$

Equation I-12

where *f* is found as Equation I-13.

$$f = \frac{\sigma_f'}{UTS}(2\ x\ 10^3)^b$$

Equation I-13

where σ_f' is the true stress at fracture and, for steels with Brinell hardness low than 500 ($H_B \leq 500$), σ_f' is given by Equation I-14.

$$\sigma_f' = UTS + 345\ MPa$$

Equation I-14

Using the equations above, the value of *f* is found as a function of UTS (using $N=10^6$) and it is presented graphically in Figure I-8. For ultimate tensile strength (UTS) values less than 490 MPa, *f* can be estimated as 0.9 to be conservative.

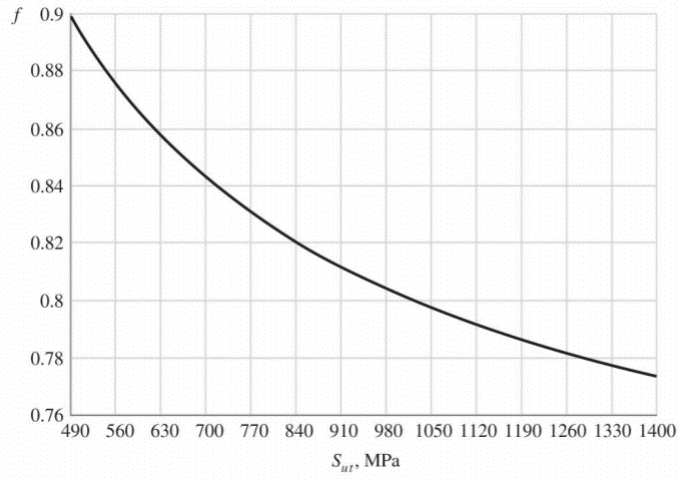

Figure I-8: Value of *f* as a function of S_{ut} [20].

If the value of *f* is known, the constant *b* can be directly found as Equation I-15.

$$b = -\frac{1}{3}\ log\left(\frac{f\ x\ UTS}{S_e}\right)$$

Equation I-15

And *C* can be rewritten as Equation I-16.

$$C = \frac{(f\ x\ UTS)^2}{S_e}$$

Equation I-16

I.2 FATIGUE DAMAGE IN HIGH CYCLE FATIGUE

Cumulative fatigue damage (CFD) analysis still plays a key role in predicting the life of components and structures subjected to field-load histories. Fatigue damage is fundamentally a result of material structural changes at the microscopic level, such as dislocations of the atomic structures [25].

In general, three stages of damage mechanisms can be distinguished during the

process of high cycle fatigue of a sample initially without cracks. These three stages can be successively identified as microcrack initiation and microcracking (Stage I), macrocrack propagation (Stage II) and final fracture (Stage III) [26]. Stage I crack growth (microcracking) occurs along crystallographic slip bands and is dominated by shear. Stage II crack growth (macrocrack propagation) is associated with crack propagation on a plane normal to the direction of the maximum tensile principal stress attained. Stage II takes place up to a critical length of the crack is attained and the stress intensity reaches a critical value, when the crack becomes unstable with acceleration of crack propagation, and rupture occurs after few cycles in Stage III [26-30].

Figure I-9 schematically represents stages I and II of fatigue crack growth, and final fracture at 45° to the surface.

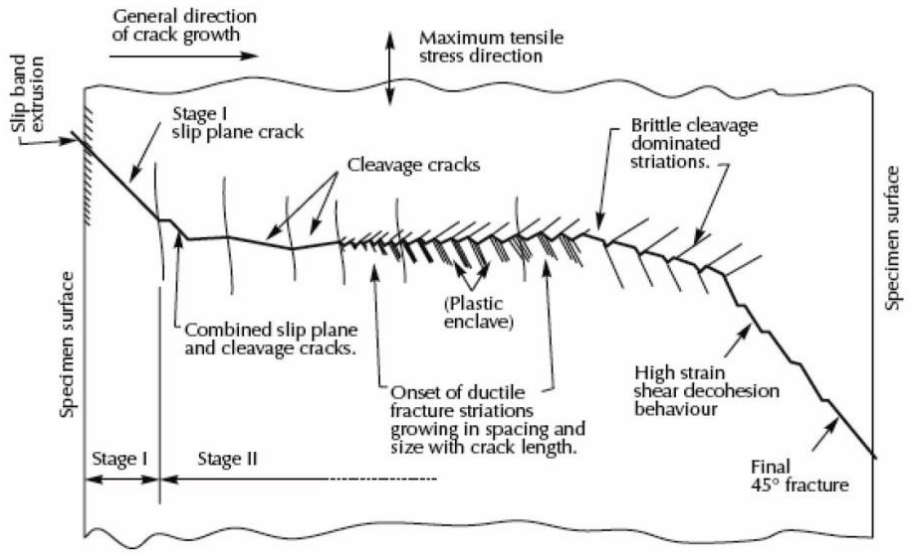

Figure I-9:Schema of stages I and II of fatigue crack growth in an AlZnMg alloy [15].

The macrocrack phase of the fatigue phenomenon (Stages II and III) have been extensively studied for decades in different materials, evidencing some common features in the behaviour of the crack propagation [26]. Numerous analytical empiric and semi-empiric models were developed to predict the fatigue crack increase in materials based on the relation of the crack growth rate and fatigue loading parameters, such as the Paris law based totally at the linear elastic fracture mechanics (LEFM) approach [31]. However, this approach is more suitably applied for modeling the fatigue crack propagation in Stage II, when the crack growth is regular and stable. However, in Stage I, the modeling of the fatigue crack growth behavior wishes a deeper knowledge of the microstructural

mechanisms [26]. As the objective of the present work is to predict fatigue life of steel structures submitted to high cyclic loads before macroscopic cracking, it is of fundamental importance to better understand the mechanisms involved in the Stage I (nucleation and microcrack propagation), which is better detailed as follows.

I.2.1 MICROCRACK NUCLEATION

In this phase, intense deformation is observed at grains favorably oriented to shear slip and relatively less confined due to proximity to the surface, grains close to a local geometrical discontinuity (stress concentration), or grains affected by stress-corrosion effects. Figure I-10 schematically illustrates atomic rearrangements that accompany the motion of an edge dislocation as it moves in response to an applied shear stress. Dislocations are then arranged along dense crystalline planes giving rise to bands with high localized strain, called persistent slip bands (PSBs) [32], as schematically represented in Figure I-11. PSBs multiply and interact with cycling. Sequential slip of adjacent PSBs results in the development of intrusions and extrusions [33], which act as initiation sites for microcracks.

A model for the mechanism of development of slip band extrusions and intrusions was proposed by Wood [34], considering that slip bands are the result of a systematic buildup of free slip movements (of the order of 1 nm). This model is schematically illustrated in Figure I-12, where the fine structure of a slip band is represented at magnifications obtainable with electron microscope. The back-and-forth fine slip movements build up notches (Figure I-12(b)) or ridges (Figure I-12(c)) at the surface, which act as stress raisers and initiation sites for microcracks. The basic premise of this model is that repeated cycling of the material leads to different amounts of net slip on different slip planes. The irreversibility of shear displacements along slip bands then results in roughening of the material surface and gradual development of a notch-ridge surface morphology. The "micro-notches" act as stress raisers and promotes additional slip [15].

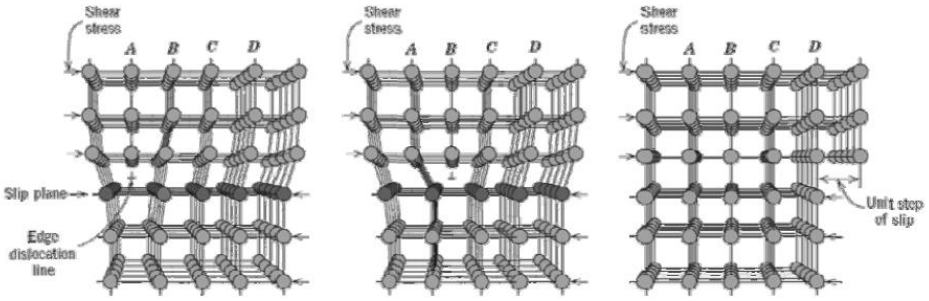

Figure I-10: Atomic rearrangements that accompany the motion of an edge dislocation as it moves in response to an applied shear stress. Adapted from [15].

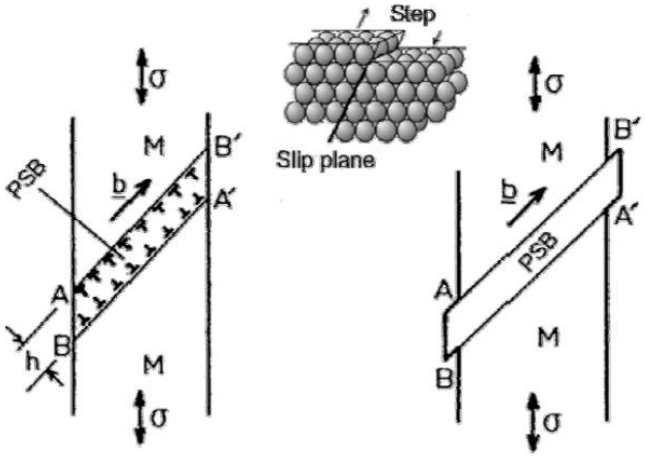

Figure I-11: Damage mechanism of development of a persistent slip band (PSB) and an irreversible step at the surface. Adapted from [15].

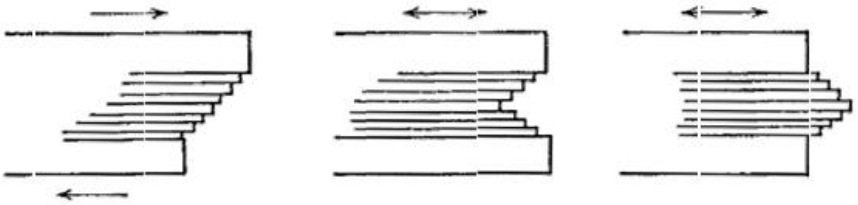

(a) (b) (c)

Figure I-12: Model for the mechanism of formation of slip band extrusions and intrusions proposed by Wood [78]. (a) Static deformation. (b) Cyclic deformation leading t surface notch (intrusion) and (c) surface ridge (extrusion). Adapted from [15].

I.2.2 MICROCRACK PROPAGATION

After initiation, microcracks propagate gradually into the grains along persistent slip bands. In a polycrystalline metal, the crack may extend for only a few grain diameters before crack propagation changes to the next phase (macrocrak propagation). The rate of microcrack propagation is generally very low, on the order of nm/cycle, compared to crack

propagation rates (on the order of μm/cycle). Microcrack propagation is limited to the near-surface zone of the material. Microcracks are frequently interrupted at grain boundaries that they cannot easily overcome, when adjacent grains are not favorably oriented. Microcracks are very difficult to be detected by nondestructive evaluation (NDE) techniques [15].

CHAPTER II

INDENTATION HARDNESS

CHAPTER II. INDENTATION HARDNESS

This chapter is divided in two parts. The first part comprises a review of indentation hardness tests, focusing in instrumented cyclic microindentation tests, which are one of the methods used in this work to characterize microstructural changes in the material. The second part deals with microindentation testing applied to fatigue damage assessment, showing a literature review in the theme.

The hardness of a solid material can be defined as a measure of its resistance to a permanent shape change when a constant compressive force is applied. The deformation can be produced by different mechanisms, like indentation, scratching, cutting, mechanical wear, or bending. In metals, ceramics, and most of polymers, the hardness is related to the plastic deformation of the surface. Hardness has also a close relation to other mechanical properties like strength, ductility, and fatigue resistance, and therefore, hardness testing can be used in the industry as a simple, fast, and relatively cheap material quality control method [35]. Nowadays it is known that material hardness is a multifunctional physical property depending on a large number of internal and external factors.

II.1 MICROINDENTATION HARDNESS TESTING

The first indentation hardness test was done by Johann Brinell in 1900 [36]. In this test, for a typical situation, a steel ball of diameter 0.39in is used to indent the material through the application of a load of 29.4kN. For soft or really hard materials, the load value is changed. Years later, in 1919, the Rockwell [37] test was introduced, and it has become the most common hardness test in use in the US. This test could be conducted rapidly because the depth of the indentation was detected by the instrument rather than the operator measuring the indentation. For the Vickers test, developed in 1925, a square-based diamond indenter was chosen with an angle of 136° between opposite faces in order to obtain hardness numbers similar in magnitude to Brinell numbers. Development of the light load Vickers test in 1932 and the Knoop test by the National Bureau of Standards in 1939 has made microindentation testing a routine procedure. Both of these tests use precisely shaped diamond indenters and various loads to determine the hardness of a wide variety of materials. The term microhardness is commonly used in place of microindentation hardness;

however, it can be misleading because the term micro is intended to describe the indentation size and not the magnitude of hardness. Microindentation hardness testing provides information on the hardness characteristics that cannot be revealed with other tests such as Brinell [36] or Rockwell [37].

Microindentation tests are characterized by indentations loads L in the range of $L < 2\ N$ and penetrations $h > 0.2$ µm [35]. There are two main tests used at this scale: Vickers and Knoop. These indentation hardness tests determine the material resistance to the penetration of a diamond indenter with a shape of a pyramid. Like in the case of macroindentation tests, the hardness is correlated with the depth that such indenter will sink into the material, under a given load, within a specific period of time.

The Vickers diamond hardness number, HV, is calculated using the indenter load L and the actual contact surface area of the impression Ac (Equation II-1) [35]. The time for the initial application of the force is 2–8s, and the test force is maintained during 10–15s.

$$HV = \frac{L}{A_c} = \frac{2L}{d^2}\sin\frac{136^o}{2} = 1.8544\frac{L}{d^2}$$

Equation II-1

where L is measured in kgf and d (mm) is equal to the length of the diagonal measured from corner to corner on the residual impression in the specimen surface. If the load is measured in N, Equation II-1 should be divided by 9.8065.

What characterizes a Vickers microindentation test is the use of a lower applied load range when compared to the microhardness tests. The use of forces below 1 kgf (≈9.8 N) with the Vickers test was first evaluated in 1932 at the National Physical Laboratory in the UK [35]. Four years later, Lips and Sack [38] constructed the first microhardness Vickers tester designed for applied forces ≤ 1 kgf (≈9.8 N). The test is normalized by ASTM E384 [39] and ISO 6507 [40].

The microindentation Koop test was developed in 1939 at the USA National Bureau of Standards (nowadays NIST) by Frederick Knoop, the indenter is a rhombic-based pyramidal diamond that produces an elongated diamond shaped indent: the angles from the opposite faces of the indenter are 130 and 172.5 [35]. The Knoop indenter produces a rhombic-shaped indentation having approximate ratio between long and short diagonals of 7 to 1 (Figure II-1). The Knoop hardness number (KHN) is defined as the ratio of the applied load

L divided by the projected contact area *Ap* of the indent (Equation II-2). Knoop tests are mainly done at test forces from 10 to 1000g (≈ 98 mN to 9.8 N), so a high-magnification microscope is necessary to measure the indent size [35].

$$KHN = \frac{L}{A_p} = \frac{2L}{d^2\left(\cot\frac{172.5^O}{2}\tan\frac{130^O}{2}\right)} = 14.24\frac{L}{d^2}$$

Equation II-2

where *d* is the length of the longest diagonal (in mm). *L* was originally measured in kgf; if *L* is measured in N, Equation II-2 should be divided by 9.8065.

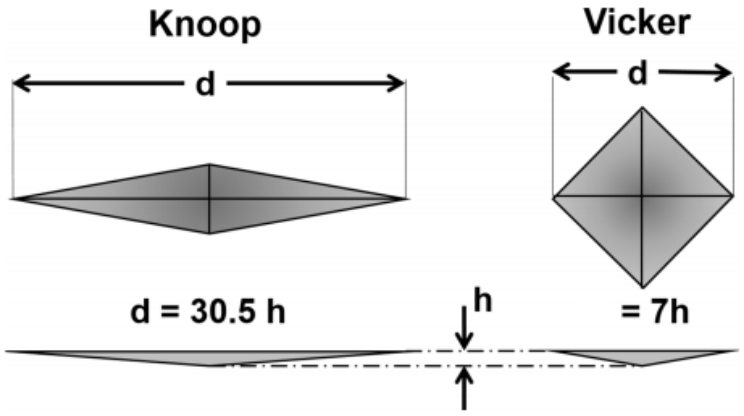

Figure II-1: Comparison of Knoop and Vickers microindentations [35].

INSTRUMENTED CYCLIC MICROINDENTATION TESTS

Instrumented cyclic indentation testing refers to applying and releasing indentation load on the surface of a test material using an indenter. Conventional cyclic indentation uses specified loading cycles in which the load is increased step by step up to a maximum. The indenter is pushed into the surface of the sample producing both elastic and plastic deformation of the material (Figure II-2). The displacement *h* and the load *P* are continuously monitored with high precision, as schematically shown in Figure II-3.

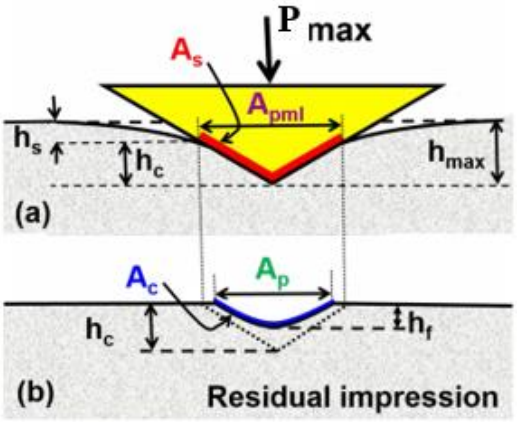

Figure II-2: (a) Elasto-plastic deformation at the maximum applied load P_{max}; (b) plastic deformation after releasing the load [35].

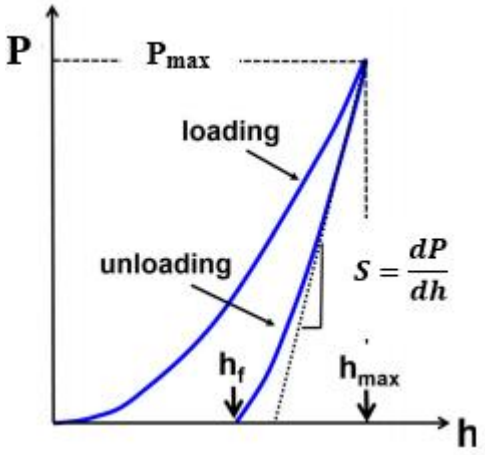

Figure II-3: Schematic load-indenter displacement curve obtained from instrumented indentation test [35].

During the process, the indenter will penetrate the sample until a predetermined maximum load P_{max} is reached, where the corresponding penetration depth is h_{max}. When the indenter is withdrawn from the sample, the unloading displacement is also continuously monitored until the zero load is reached and a final or residual penetration depth *hf* is measured. The slope of the upper portion of the unloading curve, denoted as $S = dP/dh$, is called the elastic contact stiffness.

In this work, a Berkovich indenter shape was used due to the availability of just this type of indenter in the laboratory during the realization of the experimental tests. The Berkovich indenter is a three-sided pyramid with a face angle of 65.3° with respect to the indentation vertical axis, and its area-to-depth function is the same as that of a Vickers indenter. Berkovich and Vickers projected contact areas are compared in Figure II-4.

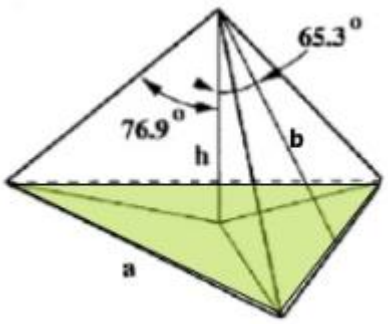

Berkovich projected area

$$\tan 60^o = \frac{l}{a/2}$$

$$l = \frac{\sqrt{3}}{2}a$$

$$A_{proj} = \frac{al}{2} = \frac{\sqrt{3}}{4}a^2$$

$$cos65.27^o = \frac{h}{b}$$

$$h = \frac{acos65.3^o}{2\sqrt{3}sin65.3^o} = \frac{a}{2\sqrt{3}tan65.3^o}$$

$$a = 2\sqrt{3}htan65.3^o$$

$$\boldsymbol{A_{pc} = 3\sqrt{3}h^2tan^2 65.3^o = 24.56h^2}$$

(a)

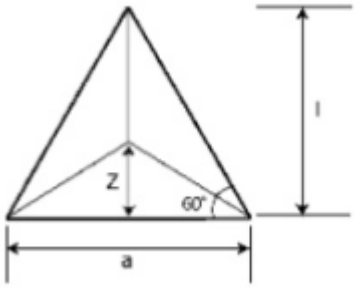

Vicker projected area

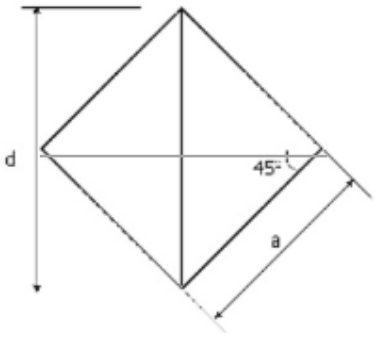

$$\boldsymbol{A_{pc} = 4h^2tan^2 68^o = 24.504h^2}$$

(b)

Figure II-4: (a) Berkovich and (b) Vickers projected areas.

From cyclic instrumented indentation measurements leading to a load (P) – indenter displacement (h) curve (Figure II-3), instrumented hardness, H_{IT}, is defined as the ratio between the maximum load (P_{max}) and the projected contact area (A_{pc}) (Equation II-3).

$$H_{IT} = \frac{P_{max}}{A_{pc}}$$

Equation II-3

The projected contact area (A_{pc}) is a parameter of fundamental importance to the computation of the material hardness, and its calculation is not trivial. By analyzing the unloading part of a load–depth curve obtained by instrumented indentation, Oliver and Pharr

[41] proposed the correlation of the contact area, with the reduced modulus, E_R, by means of the total compliance of the system, C, and the frame compliance of the instrument, C_f, as follows:

$$\sqrt{A_{pc}} = \frac{\sqrt{\pi}}{2\beta}\frac{1}{(C - C_f)}\frac{1}{E_R}$$

Equation II-4

where β is a correction factor, whose value differs according to the authors [42]. For example, according to King's finite element calculations [43], for the Berkovich indenter, β= 1.034. On the other hand, $C=dh/dP$ and represents the total compliance of the system, i.e. the inverse of the slope of the load (P) versus penetration depth (h) curve at the beginning of the unloading. C_f is supposed to have a constant value.

E_R is expressed as a function of E_m, E_i, ν_m and ν_i, which represent the elastic modulus and Poisson's ratio of the material and of the indenter, respectively. For a diamond indenter, E_i = 1140 GPa and ν_i = 0.07:

$$\frac{1}{E_R} = \frac{1 - \nu_m^2}{E_m} + \frac{1 - \nu_i^2}{E_i}$$

Equation II-5

For fused silica, the reduced modulus is then equal to 69.6 GPa.

For a perfect Berkovich indenter, the projected contact area, A_{pc}, included in Equation II-3 is a function of the contact depth [44], h_c, and it is expressed as follows:

$$A_{pc} = \pi \tan^2 \psi h_c^2 = 24.56 h_c^2$$

Equation II-6

where ψ= 70.32° and represents the effective semi-angle of the conical indenter equivalent to the Berkovich one.

To calculate h_c, it should be considered that during indentation tests, the material can flow under the indenter by two different modes of deformation: sinking-in or piling-up, which are explained by the authors as follows:

- Sinking-in: when the material is pulled down toward the tip of the indent and
- Pilling-up: when the material is pushed away from the center of the indent.

Consequently, corrections proposed by Oliver and Pharr [41] for sinking-in and

Loubet et al. [45] for piling-up should be done, in addition to other corrections associated with the indenter tip defect as well as the compliance of the instrument. A schematic representation of the two modes of deformation is presented in Figure II-5 for a Vickers indenter.

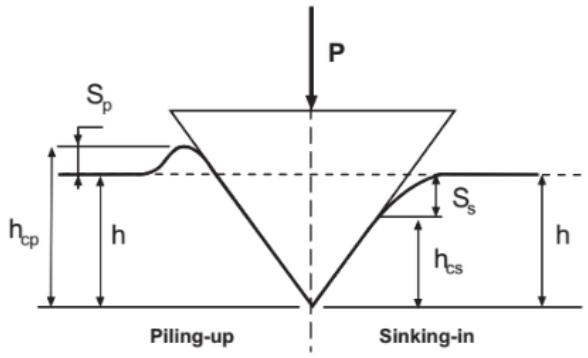

Figure II-5: Representation of piling-up and sinking-in during an instrumented indentation test [46].

It is clear that both modes of deformation render difficult a precise determination of the penetration depth and consequently of the contact area. Methods have been proposed by various authors. For the two different modes of deformation (sinking-in and piling-up), Oliver and Phar [41] and Loubet et al. [45] expressed the contact depth h_C by Equation II-7 and Equation II-8, respectively.

- For sinking-in (Oliver and Phar [41]):

$$h_{cs} = h_{max} - \varepsilon \frac{P_{max}}{S}$$

Equation II-7

where h_{max} is the maximum indentation depth, P_{max}, the maximum load, and S the elastic unloading stiffness. The coefficient ε is a constant whose value depends on the geometry of the indenter. For a conical punch, ε=0.72, for a paraboloid of revolution which approximates to a sphere ε=0.75 and fora flat punch ε = 1.00 [46].

- For piling-up (Loubet et al [45]):

$$h_{cp} = \alpha(h_{max} - \frac{P_{max}}{S})$$

Equation II-8

where α is a constant equal to 1.2.

Unfortunately, a perfect Berkovich indenter is a utopia. Even if they are carefully manufactured, the indenter tips are usually blunted and/or can have other defects, or they become imperfect after few indentations, and when the indenter has not a perfect shape, the

contact depth is modified. In the work of N'jock et al. [46], the authors showed a relation (Equation II-9) that take into account the tip defect, considering an indenter displacement higher than a value around 200 nm, which is often the case in microindentation.

$$A_{pc} = 24.56(h_c + h_b)^2$$

Equation II-9

where h_b is the truncation length of the tip defect defined as the distance between the ideal indenter tip and the blunted one.

Introducing the different contact depths, Equation II-7 and Equation II-8, in Equation II-9, the following expressions are obtained:

- For sinking-in (Oliver and Phar):

$$A_{pc_{,OP}} = 24.56(h_{max} - \varepsilon\frac{P_{max}}{S} + h_b)^2$$

Equation II-10

- For piling-up (Loubet et al):

$$A_{pc_{,LA}} = 24.56\alpha^2(h_{max} - \frac{P_{max}}{S} + h_b)^2$$

Equation II-11

Some investigations on the indenter used in this work have been made for the determination of h_b using SEM direct observations. Values of 50 nm for Berkovich indenter and 150 nm for Vickers indenter were determined.

N'jock et al. [46] presented a criterion to determine the predominant mode of deformation. According to them, for materials for which the ratio between the residual indentation depth and the maximum indentation depth, reached at the maximum load, is higher than 0.83, piling-up prevails, while it is sinking-in when it is lower than 0.83. When the ratio equals 0.83, the two modes of deformation should coexist since the calculations made using either correction of Oliver and Pharr [41] and Loubet et al. [45] give the same results. In this work it is shown the results for a specimen that the ratio between the residual indentation depth and the maximum indentation depth is higher than 0.83, and because of that, Loubet et al. equation for the contact area were used (Equation II-11).

II.2 MICROHARDNESS TESTING APPLIED TO FATIGUE DAMAGE ASSESSMENT

Use microhardness testing as a mean of predicting fatigue damage of metal specimens is not a new approach. In 1996, Ye [48] measured the Vickers microhardness of ferrite and pearlite on the surface of an annealed 0.46% carbon steel sample during different cycle numbers under high cycle fatigue. The authors observed that the curves of microhardness versus cycles to ferrite and pearlite show three periods, i.e., microhardness increasing, stabilizing and decreasing (Figure II-6).

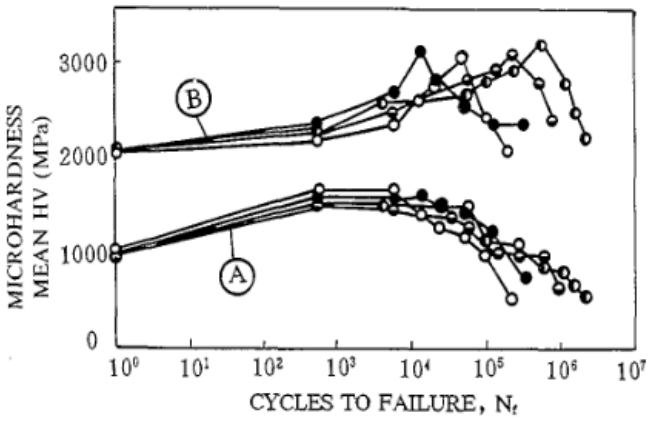

Figure II-6: The change of microhardness mean of ferrite and pearlite during cycles: (A) ferrite; (B) pearlite. , ◐ 200 MPa , ◒220 MPa; ● 240 MPa; ○ 260 MPa [48].

Ye [48] explained the results obtained as follows: at the beginning of fatigue, due to the fact that the surface of the specimen is subjected to alternating stress, slip occurs preferably in some grains which are oriented such that the planes of easy slip and makes grains produce a cyclic hardening effect. Because of cyclic hardening, the resistance to plastic deformation in the material increases and the microhardness value of the grains increases. When cyclic hardening reaches saturation, fine slip band, instead of homogeneous plastic deformation, occurs at the surface of some grains. The local softening, due to the fact that the plastic deformation concentrates intensively in the slip band, decreases the resistance to plastic deformation, i.e., the microhardness value. Therefore, after that the mean curve of microhardness begins decreasing. With increasing cycle number, the slip bands tend to broaden and thicken and induce neighbor grains to produce new slip bands, so that the mean curve of microhardness decreases continuously.

Surface effects are of particular importance for the fatigue phenomenon, since in most

cases the surface is the preferred site of the nucleation of microcracks because of the easier slip and the higher strain amplitude at the surface. According to Ye and Wang [49], a great deal of experimental evidence has proved that the fatigue damage in the stages prior to nucleation of microcracks is primarily related to the occurrence and development of localized plastic-strain concentration at or near the surface of materials during cycling. So, the resistance of microplastic deformation on the surface is the target that reflects the fatigue damage resistance of metal components. The microhardness of a material shows the ability of that material to resist microplastic deformation caused by indentation or penetration and is closely related to the plastic slip capacity of the material. Therefore, it is significant to study, from the change of microhardness on the surface, the resistance to microplastic deformations and consequently, the resistance of fatigue damage caused on the surface.

Ye [50] did a deeper investigation in fatigue hardening/softening behavior through Vickers microhardness measurement during high cycle fatigue from the changes of micromechanical properties. The author showed that it is possible to detect fatigue hardening/softening of a metal by measurement of the post-cycled tensile curves. Figure II-7 shows the curves for several specimens with the same initial conditions but different numbers of applied cycles (denoted by *Ni* to *Nj*).

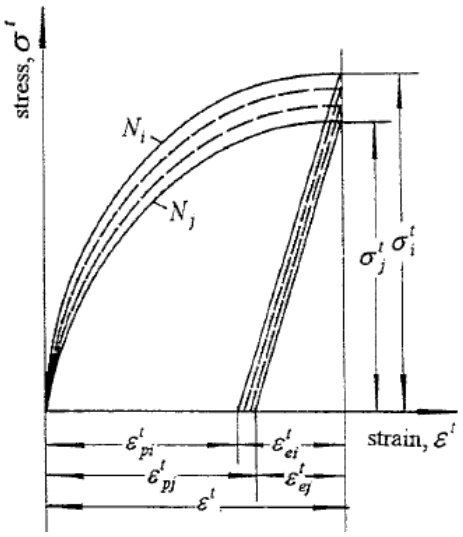

Figure II-7: Cycle-dependent changes in tensile curve [50].

In Figure II-7, it can be noted that tensile curve at *Nj* lies below that at *Ni*, so the material shows cyclic softening. The components of the tensile curve of Figure II-7 have the following relation:

$$\varepsilon_t = \varepsilon_e + \varepsilon_p = \frac{\sigma_t}{E} + \varepsilon_p$$

Equation II-12

where ε_t, ε_e and ε_p are the total, elastic and plastic strains, respectively, and σ is the true stress. The index 't' indicates that both strain and stress are determined in a tensile test [50]. This means that for achieving the same deformation ε_t, a lower stress is required to be applied at *Nj* than at *Ni*, and simultaneously the material keeps a higher degree of residual (plastic) deformation after unloading at *Nj*. Therefore, the fatigue hardening/softening of the material can actually be determined by detecting the changes of σ_t (or ε_p) in tensile curves while the total strain ε is held constant.

For Vickers hardness tests, Ye [50] considered an ideal geometry of a pyramidal indenter (Figure II-8) penetrating into the specimen surface ('pile-up' and 'sink-in' formations were not taken into account).

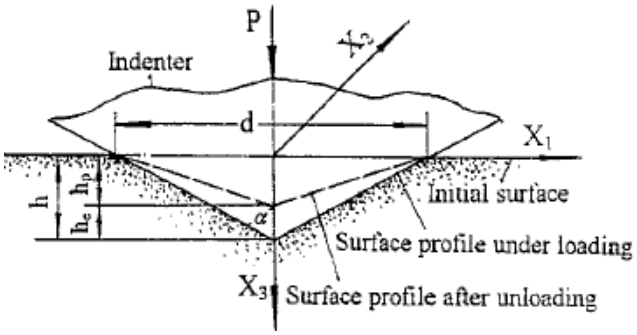

Figure II-8: Geometric scheme of a pyramidal indenter penetrating into a specimen surface (X_1, X_2, X_3, Cartesian coordinates): *P*, load; *d*, imprint diagonal; *h*, indentation depth; *he*, elastic backformation; *hp* plastic deformation [50].

Aiming to write an expression that correlates the total deformation experienced by the samples and the hardness measurements obtained in Vickers hardness tests, Ye [50] did some assumptions and derivations based on the geometric scheme of the indenter and obtained an expression for total deformation as follows:

$$\varepsilon^{\mathrm{H}} = \ln(\sin\alpha) = \varepsilon_{\mathrm{e}}^{\mathrm{H}} + \varepsilon_{\mathrm{p}}^{\mathrm{H}} = \left[-\frac{Hv}{E\sin\alpha}(1 - v + 2v^2)\right] + \varepsilon_{\mathrm{p}}^{\mathrm{H}}$$

Equation II-13

where α is the angle between the surface profile after and before loading, *E* is the Young's modulus and *v* is the Poisson's ratio. The latter two parameters (*E* and *v*) were introduced in the expression by means of Hooke's law. Complete calculus can be obtained in [50].

The diagram of Vickers hardness versus elastic, plastic and total deformation can be obtained from Equation II-3, as shown in Figure II-9, where i.and j denote several different

states of a material.

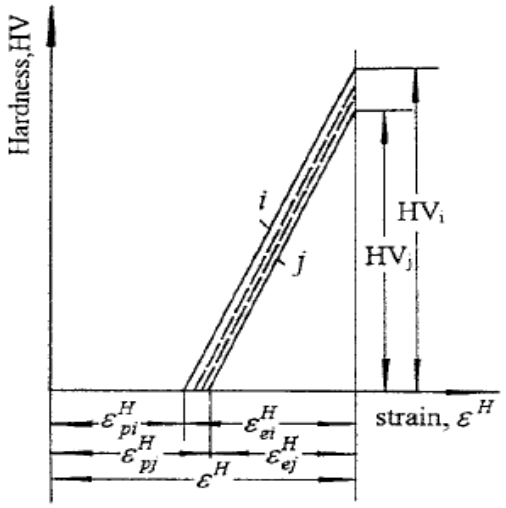

Figure II-9: Diagram of Vickers hardness vs. deformation for several different states of a material [50].

Comparing Figure II-7 and Figure II-9, it can be noted that mechanical response under the Vickers pyramidal indenter in a certain sense is analogous to strain-controlled tensile testing where ε_t is constant. In other words, fatigue hardening/softening of a material can be determined by means of Vickers hardness measurement. With these prerogatives in mind, Ye [50] started the experimental tests. The authors did high-cycle fatigue tests under controlled conditions of fully reversed uniaxial constant stress amplitude. The frequency of stress cycling was kept around 157 cycles per second, and the stress amplitude ranged from 231 to 271 MPa and 315 to 352 MPa for the 16Mn and 45# steel, respectively. Fatigue testing was interrupted after various chosen numbers of cycles and the Vickers microhardness was measured at the surface of the specimen. The results are shown in Figure II-10.

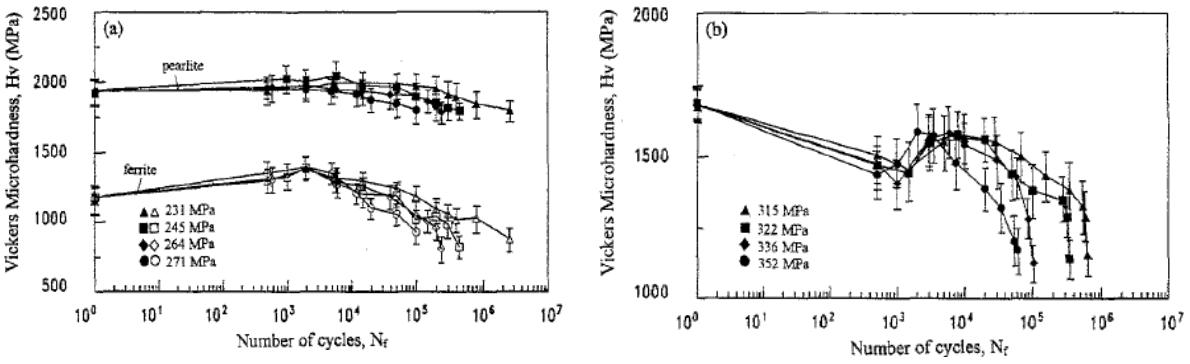

Figure II-10: Variation of Vickers microhardness with the number of cycles in (a) annealed 16Mn steel, (b) normalized 45# steel [50].

It can be observed in Figure II-10(a) that, for 16Mn annealed steel, the mean value of microhardness in both ferrite and pearlite increases at the beginning of cycling, reaches its maximum and then asymptotically decreases. Therefore, the variation of microhardness mainly corresponds to rapid hardening during the initial stages, followed by a continuous softening process until fracture occurs on the surface of the specimen. From Figure II-10(b), normalized 45# steel, it is noted that the mean value of the microhardness of the ferrite-pearlite composite is mainly characterized by a slight decrease at the initial stages of cycling, followed by an increasing process. After attaining the maximum, the mean value of microhardness decreases asymptotically with increasing number of cycles. Therefore, for normalized 45# steel, the local deformation behavior of the surface is characterized by initial softening, hardening after certain number of cycles and softening again at the later stages of cycling [50].

Still in the theme of microhardness measurement during cyclic loading aiming the analysis of fatigue behavior of steel samples, Ye and Wang [49] introduced the concept of continuum damage mechanics (CDM). The authors proposed a damage variable describing pre-nucleation fatigue damage with the objective of studying a new approach for non-destructive inspection of fatigue damage, especially at the early stages of fatigue failure of engineering components under service conditions.

Based on experimental evidences and using concepts of stress-strain already highly regarded in literature, Ye and Wang [49] obtained a mathematical relation of the hardness (HD) with damage variable (D) for a damage material (Equation II-14). Complete calculus can be found in the authors published work [49].

$$H_D = C(1-D)K\,(\varepsilon + \varepsilon_H)^m$$

Equation II-14

where C is a proportionality constant that takes different values depending on the type of indenter used, D is the damage variable representing the deterioration of the material's properties and microstructures under the loading of external forces, K and m are material constants, ε is the plastic natural strain, and ε_H is the strain introduced by the hardness test itself within the indentation plastically deformed zone (ε_H is approximately 0.08 in the case of Vickers indentation).

In terms of the variation of hardness for the isotropic damage case, damage variable

(D) can be evaluated as Equation II-15.

$$D = 1 - \frac{H_D}{H}$$

Equation II-15

where H_D and H are the hardness of a damaged material and a non-damaged material, respectively.

As the hardness at the submicroscopical level is particularly structure sensitive and related closely to the intrinsic structural factors of the specimen tested (crystal structure, grain size and orientation, phase distribution, deformation bands, precipitates, dislocations), the microhardness measured at the different surface regions of a specimen has stochastic distribution characteristics [49]. This implies that the damage variable, *D*, should be further expressed in probabilistic function forms. Therefore, the authors derived from Equation II-15 a probabilistic expression on the basis of the fact that the Vickers microhardness (*HV*) of both ferrite and pearlite is governed by a normal distribution during cycling, and by means of the algebraic rule of the normal distribution function (Equation II-16).

$$D_{\mu} = 1 - \frac{HV_{D\mu}}{HV_{\mu}}\left[1 + \left(\frac{HV_{D\sigma}}{HV_{\mu}}\right)^2\right]$$

Equation II-16

$$D_{\sigma} = \frac{1}{HV_{\mu}^2}\sqrt{\left(HV_{D\mu}\right)^2 HV_{\sigma}^2 + HV_{\mu}^2 (HV_{D\sigma})^2}$$

Equation II-17

where $D\mu$ and $D\sigma$ are the mean and standard deviation of damage variable *D*.

Therefore, the stochastic damage variable *D* can also be represented by the following normal distribution (Equation II-18).

$$f(D) = \frac{1}{\sqrt{2\pi D_{\sigma}}} exp\left[-\frac{\left(D - D_{\mu}\right)^2}{2D_{\sigma}^2}\right]$$

Equation II-18

The mean values and standard deviation of the damage variable D calculated by Equation II-16 and Equation II-17 respectively, coupled with the measured Vickers microhardness are plotted against the cycle fraction, *N/Nf* (where *Nf* is the number of cycles

up to rupture), in Figure II-11, in which error bars represent plus or minus one standard deviation of *D*.

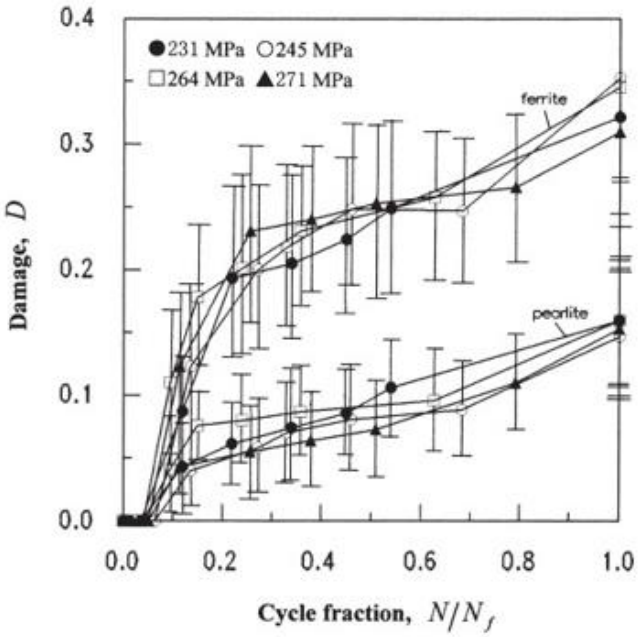

Figure II-11: Evolution of surface damage in different constitutive phases, ferrite and pearlite, during cycling [49].

It can be seen in Figure II-11 that damage values in the surface grains increase initially corresponding to the process of microhardness increasing and reaching saturation. The increase in the rate of damage decreases gradually with the increasing number of cycles while the cycles attain about 20–35% of the total number of cycles to fracture, depending on the stress levels.

Several authors studied the relationship between fatigue behavior of metallic materials and Vickers hardness [51-54]. However, differently from what is been stated until now in the present work, these authors used the plastic deformation caused by indentation as the defect from which the process of initiation and propagation of cracks originate.

According to Casagrande [51] if the fatigue fracture origin is a small defect or a non-metallic inclusion, the fatigue limit is determined by the matrix Vickers hardness and the square root of the projected area of defects onto a plane perpendicular to the maximum principal stress, $\sqrt{area}$, according to Murakami's equation (Equation II-19).

$$\sigma_w = \frac{1.43(HV + 120)}{\left(\sqrt{area}\right)^{1/6}}$$

Equation II-19

Casagrande [51] modified Murakami's equation aiming to determine an empirical fatigue limit in practical engineering problems. In the proposed approach, the √area is calculated by the square root of the projected area identified by the slip band extension around the plastic deformation induced by the indenter's tip. Plastic deformation zones were observed by optical microscope before and after etching. Therefore, suggested modification to Equation II-19 for fatigue limit determination is simply related to √area, calculated here as the mechanically deformed region perpendicular to the stress direction, considered as a semi- elliptic cap (Figure II-12) Calculus for area is shown in Equation II-20.

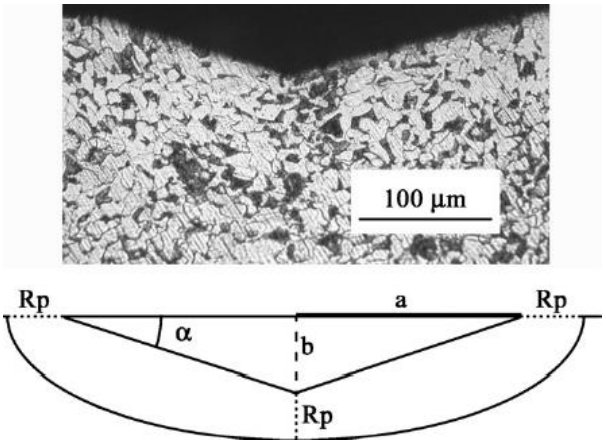

Figure II-12: Cross-sectional geometry and transversal micrograph of the artificial defect: relationship between applied load and plastic deformation at the tip of the indentation [51].

$$area = \frac{\pi}{2}(Rp + a)(Rp + b)$$

Equation II-20

The two axes are respectively the sum of the semi-diagonal, *a*, and the depth of the indentation, *b*, and the plastic radius of the deformed zone *Rp*. The depth of indentation can be calculated as a function of the indentation diagonal.

$$b = a\tan(\alpha)$$

Equation II-21

where α is the Vickers tip angle, 136◦. The plastic radius *Rp* is assumed to be constant in the plane perpendicular and along the stress direction (the depth of indentation).

Casagrande [51] used two different models for the estimation of *Rp*. The first was the experimental measurement by optical microscopy, observing the plastically deformed area around the indentation on the polished surface (Model 1). Thus, the indentation was

considered a simple artificial defect. In the second way (Model 2), *Rp* was calculated by relation for the plane strain (Equation II-22):

$$Rp = \frac{1}{6\pi}\left(\frac{K_I}{\sigma_y}\right)^2$$

Equation II-22

The value of Equation II-22 can be calculated by the use of experimental σ_y values or must be correlated to basic mechanical behaviour performance parameters of metallic alloys such as the strain hardening exponent and strength coefficient with the yield stress–strain behaviour, the Hollomon's equation.

The empirical fatigue data obtained by Model 1 are also comparable with those obtained by Murakami (Equation II-19), which consider the effects of non-metallic inclusions on fatigue strength of hard steels but not those referring to microstructural effects. Model 1 also takes microstructural effects into account and makes it possible to obtain a linear trend in the fatigue limit/hardness relationship, also for high values of hardness. Since, according to Casagrande [51], the location, shape and size of inclusions can influence the fatigue limit, the indentation method improves the fatigue limit estimation because it depends only on the correct measurement of the plastic deformation extension surrounding the impression. Moreover, the indentation used in the proposed method is unaffected by the choice of the critical defect size. Based on the analysis of the results, the real extension of the plastic deformation surrounding the impression can be more easily and reliably measured than calculated.

According to Vuherer [52], not even the hardness and the √area are crucial parameters when applying Murakami's theory (Equation II-19), but the effects of the local residual stress (LRS) that arise due to the indenting. Therefore, Vuherer [52] investigated the influence of the local residual stresses caused by Vickers-pyramid indenting on the initiation and early propagation of small cracks from indentations in coarse-grain martensitic steel. Specimens with and without a local residual stress field were tested on a rotary bending machine. The authors observed that the existing local residual stresses assist in the initiation of cracks at a level lower than the fatigue limit. The early small-crack propagation is gradually obstructed by the residual stress-field configuration until the cracks become non-propagating cracks. At levels higher than the fatigue limit, both cracks succeed in breaking through the compressive stressed domain and link together. From that moment the crack begins to behave as a long

crack, penetrating outside the indentation into the tensile-stressed domains. So, the LRS play an important role during small-crack initiation from the Vickers indentation and its early propagation. They accelerate the crack initiation, but later on they retard crack propagation. Using this correction, the fatigue properties are still only dependent on two parameters, i.e., the hardness and the indentation size, calculated as $\sqrt{area}$.

As previous authors, Wu et al. [54] also emphasized that the fatigue limit of metal that has a defect can be predicted by the Murakami's equation (Equation II-19). When predicting a fatigue limit using Murakami's equation, Vickers hardness is measured and used; however, the following question arises: which of the varying measured values should be used? Because there are many slip systems in the case of body centered cubic (BCC) metal, this scatter is small compared to that of face-centered cubic (FCC) metal; however, because there are few slip systems in the case of FCC metal, the scatter in Vickers hardness becomes greater compared to BCC metal. Furthermore, when an inhomogeneous metal has a scatter in its intrinsic hardness, Vickers hardness indicates that scatter. Therefore, the Vickers hardness value used to predict a fatigue limit has not been clarified. In the work of Wu et al. [54], the intrinsic hardness distribution of the fatigue specimen is obtained from Vickers hardness distribution in several test zones. Then, the influence of intrinsic hardness of the softest zone on fatigue behavior is discussed to find the HV value that can be used to predict the fatigue limit by Murakami's approach for an inhomogeneous FCC metal.

The authors concluded that Vickers hardness and intrinsic hardness are both variable in an inhomogeneous FCC metal, and Vickers hardness is more variable in FCC metal than in BCC metal. The mean HV affect the level of residual stress leads to crack closure, and cracks initiate and propagate easily in the softest zone of an inhomogeneous FCC metal; therefore, the mean HV value of the softest zone can be used to predict the fatigue limit by Murakami's approach for an inhomogeneous FCC metal. The Vickers hardness distribution in the softest zone can be obtained using a normal probability scale and an extreme value probability scale.

Hirano [53] studied the relationship between Vickers hardness (*Hv*) and the elastic-plastic material constants by using Finite Element (FE) analyses. Finite element contact analyses were carried out for various yield stresses (σ_y), strain hardening coefficients (A) and exponents (n). Based on the quantitative relationship between *Hv* and material constants, an equation for predicting the hardness from the material constants was proposed. The accuracy

of the equation will be discussed by comparing the hardness between the prediction, FE analysis and experimental results. A new equation for predicting Vickers hardness as a function of yield stress (σ_y), strain hardening coefficient (A) and exponent (n) is described by Equation II-23 to Equation II-25.

$$Hv = \alpha A + \beta$$

Equation II-23

$$\alpha = 4.499n^2 - 5.886n + (-1.810x10^{-4}A + 2.525)$$

Equation II-24

$$\beta = 2.701\sigma_y + 123$$

Equation II-25

Still in the basis of Murakami's equation (Equation II-19), Hirano et al. [53] studied the relationship between threshold of stress intensity factor (ΔK_{th}), fatigue limit (σ_w) and Vickers hardness. Figure II-13(a), (b) and (c) show the influence of the σ_y, A and n on fatigue limit for steels calculated by Murakami's Equation, respectively. The threshold of stress intensity factor calculated by Equation II-26 is shown in Figure II-14.

$$\Delta K_{th} \cong 2.77x10^{-3}(Hv + 120)\left(\sqrt{(area)i}\right)^{\frac{1}{3}}$$

Equation II-26

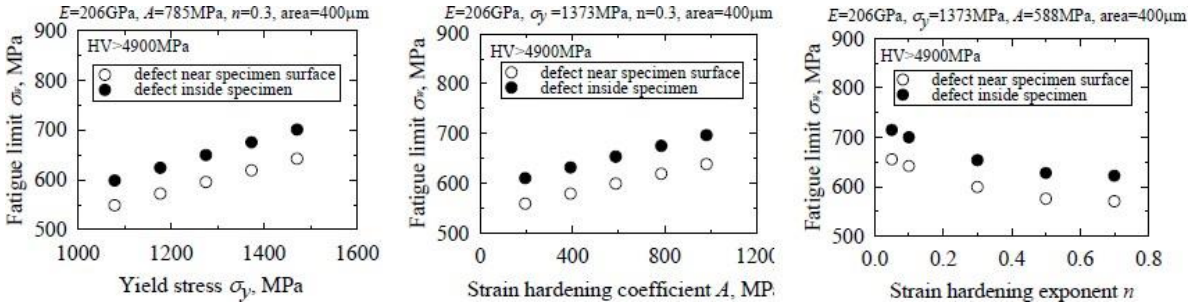

Figure II-13: Influence of the materiaç constants on the fatigue limit for high hardness steels [53].

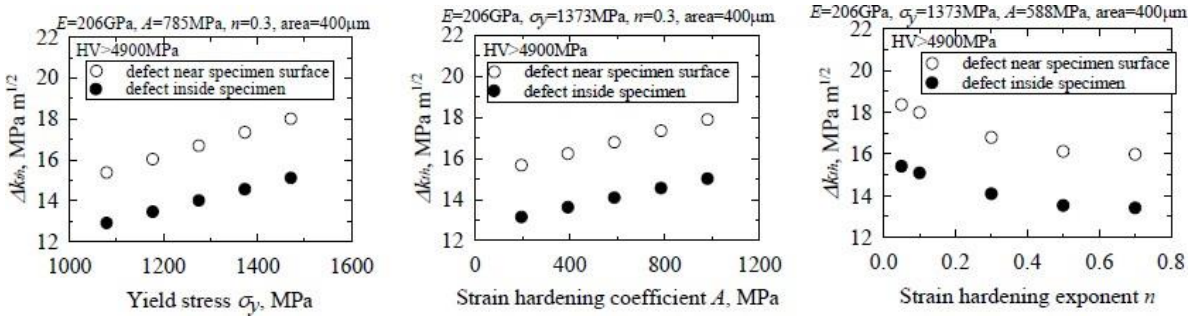

Figure II-14: Influence of material constants on the threshold of stress intensity factor for high hardness steels [53].

Hirano [53] concluded that the fatigue limit of soft materials only increased with the

increase of yield stress but it did not depend on strain hardening coefficient and exponent. The fatigue limit of hard materials increased with the increase of yield stress and strain hardening coefficient, but it slightly decreased with increasing strain hardening exponent. The threshold of stress intensity factor of hard materials increased with increasing yield stress and strain hardening coefficient, but it decreased with increasing strain hardening exponent.

CHAPTER III

X-RAY DIFFRACTION

CHAPTER III. X-RAY DIFFRACTION

This chapter is divided in three parts. The first part presents a brief theoretical review concerning the X-ray diffraction technique. The second part comprises the methods of peak broadening analysis, related to distortion of the grains, dislocation density and calculation of micro residual stresses (microdeformations). Finally, the third part presents a literature review on X-ray diffraction technique applied to fatigue damage analysis of materials focusing in the halfwidth method, or full width at half maximum (FWHM), which here is the chosen method to study the changes in microstructure of metals during fatigue damage accumulation.

III.1 PRINCIPLES OF X-RAY DIFFRACTION

X-ray diffraction (XRD) is a non-destructive technique used to determine thickness, lattice parameters, residual stresses, microstrain, composition and defects in the microstructure of the material [54]. The X-ray microbeam diffraction technique was first developed by Hirsch [55] and was applied to the study of the deformed microstructure of various metals. Taira and his colleagues have widely used this technique for engineering studies on deformation and fracture of metallic materials [56-58].

In this work, X-ray diffraction technique is used to investigate the variations in microstructure of materials during fatigue stressing. Among the variety of experimental tools available for this kind of study, optical and electron microscopy are widely used for this end and a number of papers have been published in this field [58]. However, it should be noted that the X-ray diffraction method is one of the most powerful tools for this purpose, since the non-destructive nature of its experimental procedure enables us to make successive observations of change in the microstructure of metals during the process of fatigue until fracture.

X-ray diffraction involves probing a crystal with x-ray radiation having a wavelength close to the crystal lattice spacing [59]. A crystal may be defined as a solid composed of atoms arranged in a pattern periodic in three dimensions. As such, crystals differ in a fundamental way from gases and liquids because the atomic arrangements in the latter do not possess the essential requirement of periodicity [60]. It is often convenient to ignore the

actual atoms composing the crystal and their periodic arrangement in space and think instead of a set of imaginary points which has a fixed relation in space to the atoms of the crystal (Figure III-1). This set of points can be formed as follows. Imagine space to be divided by three sets of planes (crystallographic planes), the planes in each set being parallel and equally spaced (distance *d*, in Figure III-1). This division of space will produce a set of cells each identical in size, shape, and orientation to its neighbors. Each cell is a parallelogram. The space-dividing planes will intersect each other in a set of lines, and these lines in turn intersect in the set of points referred to above. A set of points so formed as an important property: it constitutes a point lattice, which is defined as an array of points in space so arranged that each point has identical surroundings, as it is schematically shown in Figure III-1.

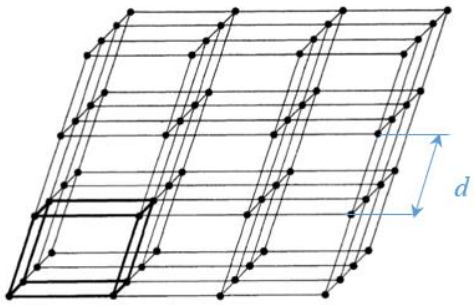

Figure III-1: A lattice point , where d is the lattice spacing [60].

X-rays are generated by bombarding a metal (typically Cu) with electrons in an evacuated tube and monochromatic x-rays are usually selected. These x-rays are scattered by the electron cloud surrounding each atom in the crystal [59]. Constructive interference occurs between the scattered x-rays and they can be diffracted with concentrated energy (diffraction pick) only if they are in agreement with the Bragg's law, expressed in Equation III-1.

$$2d \sin\theta = n\lambda$$

Equation III-1

where *d* is the lattice spacing of diffraction planes, θ is the diffraction angle (Bragg's angle), *n* is the order of the diffraction (integer number), and λ is the wavelength of the incident radiation.

Two geometrical facts are worth remembering [60]:

1) The incident beam, the normal to the reflecting plane, and the diffracted beam are always coplanar.

2) The angle between the diffracted beam and the transmitted beam is always 2θ. This is known as the diffraction angle, and it is this angle, rather than θ, which is usually measured experimentally.

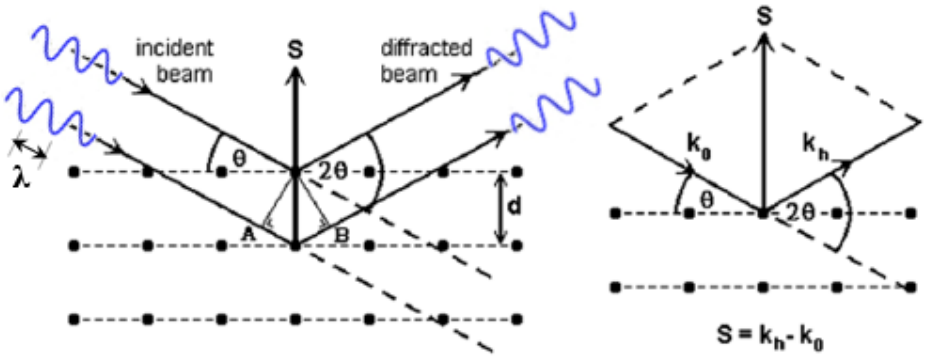

Figure III-2: Schematic of x-ray diffraction; (a) illustration of the conditions required for Bragg diffraction to occur and (b) relationship of the incident (k_0), diffracted (k_h) and scattering (S) vectors with respect to the crystal [59].

Experimentally, the angle 2θ is measured. The crystal acts as a 3D diffraction grating, so as the sample and/or the detector are moved, a 3D array of diffraction maxima can be investigated. Each set of crystal planes will produce a diffraction spot, with the positions and shapes of the diffraction spots being inversely related to the spacings of the crystal planes and size of the crystallites. The crystal planes are associated with real space and the diffraction spots with reciprocal space; the latter form a 3D reciprocal lattice. For a better understanding of XRD theory, introductory textbooks on crystallography [61] and x-ray diffraction [60] are recommended.

In order to obtain a diffraction pattern, the detector (in most designs) rotates to various 2θ angles to measure diffraction from the sample. Figure III-3 shows a schematic diagram for a X-ray diffractometer, showing the rotating detector, and resulting XRD peak. The source shown is an X-ray tube, which is the most common source of X-rays. Filters are used to provide a narrow wavelength range for analysis.

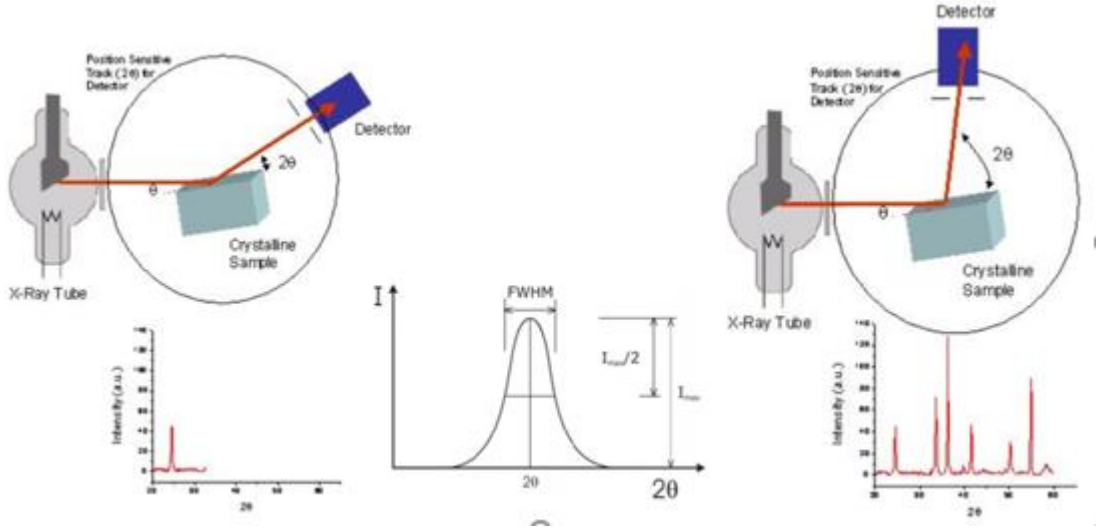

Figure III-3: Schema of XRD measurement and XRD peak, characterized by the angular position 2θ and the full width at half maximum (FWHM).

The lattice deformation in a crystalline material can produce different effects on the XRD peak. The deformation can be uniform, resulting in first order residual stresses, or nonuniform, resulting in second and third order residual stresses (microdeformations) [15]. Uniform deformation is homogeneous over many grains, and the angular position of the XRD peak is shifted according to the Bragg's law, as can be seen in Figure III-4b. Nonuniform deformation is homogeneous over small domains, such as a part of a grain, and broadening of the XRD peak is observed (Figure III-4c) due to changes in the dislocation network [15].

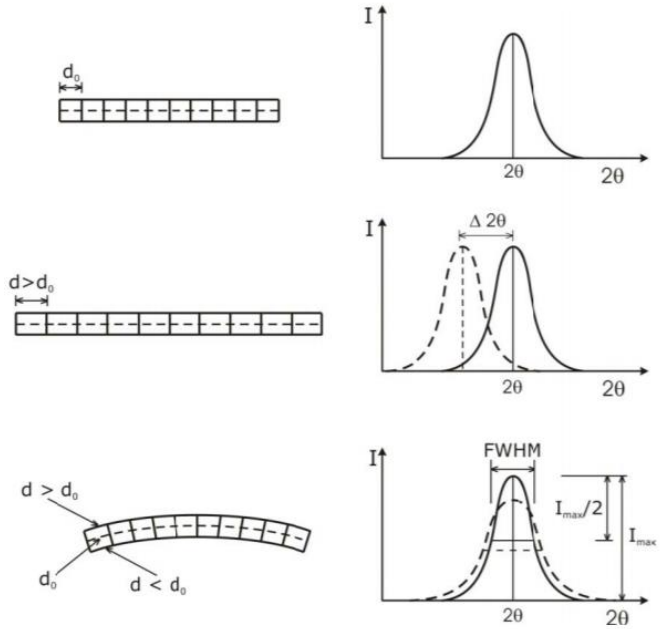

Figure III-4: Effects of lattice deformation on XRD peaks for (a) nondeformed material, (b) uniform deformation (macrostresses), and (c) nouniform deformation (microdeformations) [15].

One of the great advantages of the X-ray diffraction technique is the possibility of calculating independently macroscopic stresses (by evaluation of the shift of the angular position of the XRD peak) and microdeformations (by analysis of peak broadening). The shift of the XRD peak allows the measurement of the elastic deformation of the crystal lattice space, while the peak broadening gives the deformation of the crystallographic planes [15]. For estimation of macro residual stresses, a well-established mathematical method named $\sin^2\psi$ is used. The XRD-$\sin^2\psi$ technique calculates the residual stresses existing in the surface layer of polycrystalline materials by assuming a plane-stress state. The theory of the technique can be found in numerous literatures, e.g. in references [62-70]. For peak broadening evaluation, there are some mathematical theories available, as the Warren-Averbach analysis [71,72], Williamson-Hall plot [73] and variance method [74]. Peak broadening can also be characterized by parameters such as the integral width (peak area/height ratio) or the full width at half maximum (FWHM), which can give qualitative information upon the dislocation network state. As the objective of this work is to study microstructure changes in metals during fatigue damage accumulation in the phases prior to fatigue macrocrack, knowing how to calculate microdeformations in the surface of the material is of extreme importance, therefore the methods of analyzing peak broadening is detailed as follows.

III.2 METHODS OF PEAK BROADENING ANALYSIS

On a very small scale, a plastically deformed metal can be considered as divided into small crystallites called coherently diffracting domains (CDDs); these domains being themselves elastically distorted [15]. Each domain is formed from a group of cell columns, whose length L is perpendicular to the diffracting planes. The mean value of the column length L is the size D of the CDD. The distortion of each column can be expressed by $\varepsilon_L = \Delta L/L$ and, considering the same length L for all columns, the microstrain is defined as $\langle \varepsilon_L^2 \rangle$. Distortions of the regular crystal lattice as well as the size D of the coherently diffracting domain lead to peak broadening. Separation of the distortion (strain) effect from the size effect becomes possible considering that the diffraction order dependence of each effect is different. Different methods for peak broadening analysis have been proposed and the most known are described as follows.

In 1952 Warren and Averbach [71,72] developed the first theory for the broadening of the diffraction peaks, in which it was assumed that the broadening is caused due to size effect and strain effect. This method is one of the most powerful methods for the separation of size and strain broadening contributions in X-ray diffraction profiles, since complete information can be obtained without make any assumptions on the shape of the profiles [78-88]. Warren and Averbach [72] calculated the diffracted intensity of a X-ray beam in Fourier space for the case of small crystallites and strain being present in the sample. The result is that the intensity of the profile is given by the convolution of size and strain broadening [79]. Years later it was pointed out by some scientists that if the strain is only due to dislocation, Warren-Averbach method cannot be applied [75]. Warren and Averbach considered that the distributions of dislocations are completely random, which led to a serious shortcoming of their work: the Fourier coefficients diverge logarithmically when the crystal size tends to infinity. This problem was solved by Wilkens [76,77] by the introduction of the concept of restricted random dislocation distribution, creating the known Modified Warren-Averbach method.

In 1953 Williamson and Hall [73] calculated the integral width of a Bragg's peak from the work of Warren and Averbach [71,72]. In the classical Williamson-Hall method, with the plot of the FWHM or integral width of the peak profile against the magnitude of the diffraction vector, size and distortion broadening effects can be separated if an average particle size accurately describes the coherently diffracting domains (CDD) distribution.

Years later, in 1998, Groma [74] has developed a variance method which is based on the asymptotic behavior of the second and fourth order restricted moments. The mathematical foundation of this theory is based only on the analytical properties of the displacement field of straight dislocations and no assumption is made on the actual form of the dislocation distribution and thus it can be employed for the inhomogeneous dislocation distribution [75].

The full width at half maximum (FWHM), also called just halfwidth, or even the integral width β, is a qualitative or semiquantitative method of analysis of peak broadening [15,90,91]. This method does not directly distinguish the two causes of broadening (size and distortion) [15]. However, if the instrumental errors of peak broadening are negligible, the FWHM can be used to estimate the average size D of the CDD by the Scherrer's equation [90]

$$D = \frac{k\lambda}{FWHM cos\theta}$$

Equation III-2

where k is the Scherrer's constant, λ is the wavelength of X-rays, θ is the diffraction angle and FWHM is expressed in radians. The reader is encouraged to learn more about the Scherrer's equation in [90]. Assuming a Gaussian distribution for the diffraction peak, Warren obtained the value of 0.9 for k [91].

For its simplicity of measurement, the FWHM represents an interesting parameter to study the dislocation network state. The more common application of the method is the characterization of the work hardening state of materials [15]. The FWHM is adopted in this work to estimate changes in microdeformations with fatigue cycling.

III.3 X-RAY DIFFRACTION APPLIED TO MECHANICAL CHARACTERIZATION OF MATERIALS

Using X-ray diffraction to mechanical characterization of materials is not a new approach, reported in a number of previous works [15,56,57,92-110]. This section is dedicated to the literature review about X-ray diffraction technique applied to fatigue damage analysis of materials.

Changes in the microstructural parameters due to fatigue cycling manifest as changes in the characteristics of X-Ray diffraction profiles. The parameters commonly used to characterize diffraction profiles are FWHM (full width at half maximum), also referred to as halfwidth b, integral width β, variance and Fourier coefficients. Although the three parameters integral width, variance and Fourier coefficients are considered more reliable than halfwidth, the latter is more easily derived and interpreted [102]. A large number of fatigue investigations based on the halfwidth values are reported in literature [56,57,97-110]. In the early 60's, Taira *et al.* [56,57] separated the effects due to domain size and average microstrain in a normalized 0.16% carbon steel. The authors reported that microstrains initially increased with cycling and then remained essentially constant for the remainder of the fatigue life.

Years later, in the late 70's, Pangborn *et al.* [101] employed X-ray double crystal diffractometry to examine the defect structure induced by fatigue of A1 2024 specimens. The authors observed that dislocation density in the surface layer increased rapidly early in

the fatigue life and maintained virtually a plateau value from 20 to 90% of the life. After about 5% of the fatigue life a minimum halfwidth value could be detected, located at about 100 µm in depth. In Figure III-5, β_0 represents the average halfwidth value of the grain prior to fatigue cycling, and β_x refers to the average halfwidth value of the grains at a depth distance, x, for the fraction of life indicated.

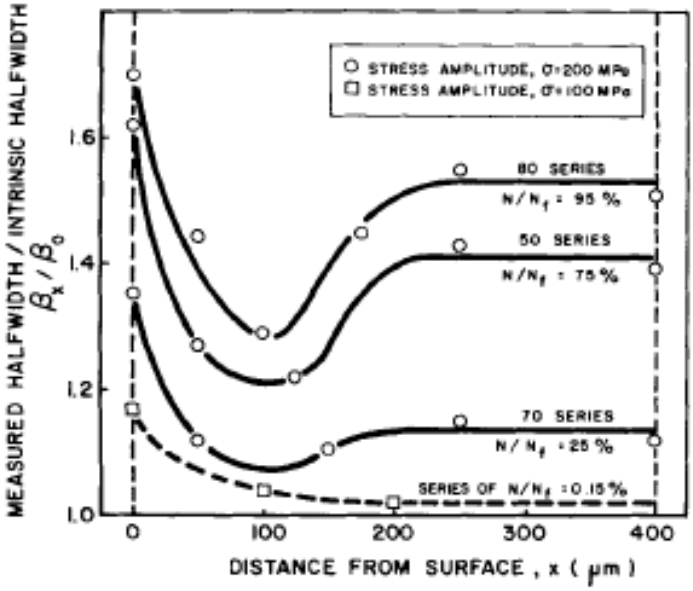

Figure III-5: Depth profiles for various fractions of the total fatigue life of A1 2024 specimens, obtained by incrementally removing surface layers and carrying out X-ray analysis with CuX; radiation at each depth [101].

It can be observed from Figure III-5, the halfwidth ratio in the interior increased with the number of fatigue cycles but never exceeded that at the surface. According to the authors, the bulk is really instable because the rapidly work-hardened surface layer blocks the egression of dislocations from the bulk. If the X-ray radiation does not penetrate beyond this surface layer, the slight increase of β (or X-ray line broadening) falls well within the experimental error band. The blocking aspect of the defect structure developed in the surface layer is clearly demonstrated by inspecting the curves of Figure III-6 for specimens cycled 75 and 95% of N_f.

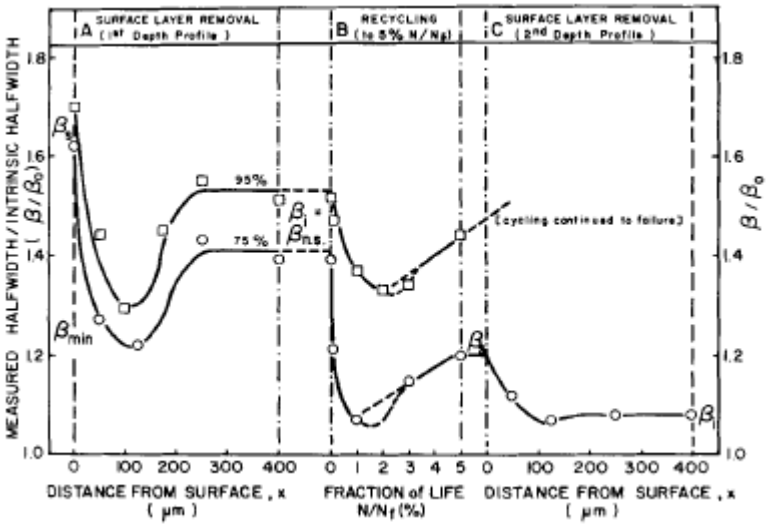

Figure III-6:Diagram for Al 2024 specimens given prior fatigue cycling to 75 and 95% of their fatigue life at ±200 MPa, followed by surface removal and recycling treatment (A and B), and either continued recycling or a second depth profile analysis (C) [101].

Figure III-6(a) shows the dependence of β/β_0 on the depth distance up to 400 µm, with plateau levels extending well into the bulk material. When this layer of 400 µm thickness was removed by electropolishing, and the specimen was recycled, the curves in Figure III-6(b) were obtained and the β/β_0 values declined upon initial recycling, indicating that the dislocation structure and arrangement in the bulk became unstable during cycling in the absence of the hardened surface layer. According to Pangborn *et al.* [101], it may be seen also from Figure III-6(b) that continued cycling caused an increase of the β/β_0 values because a new, work-hardened surface layer was being formed. If the recycling process was interrupted after 5% of the life, and the newly formed surface layer was polished away, very low half-width values were measured for the specimen originally cycled to 75% of its life, as shown in Figure III-6(c).

Kuo and Cohen [103] also investigated how the fatigue cycling effects vary with depth below the surface. Changes in the positions and shapes of X-ray diffraction peaks have been examined after high cycle fatigue of normalized and cold-worked AISI1008 steel. After 78340 cycles, normalized specimens contained small cracks, and the data are given in Figure III-7(a). In this case the breadth also passes through a minimum at about 100µm but is even larger at 400µm than at the surface, probably as a result of the cracks. For cold-worked specimens the results for 90000 cycles appear in Figure III-7(b). Once again, the peak breadth, although exhibiting a minimum 50-100 µm under the surface, is larger in the deep interior than at the surface. The domain size passes through a broad minimum, as does the

microstrain. The domain size and microstrain are similar to those after high cycle fatigue of the normalized state, but the stresses are lower.

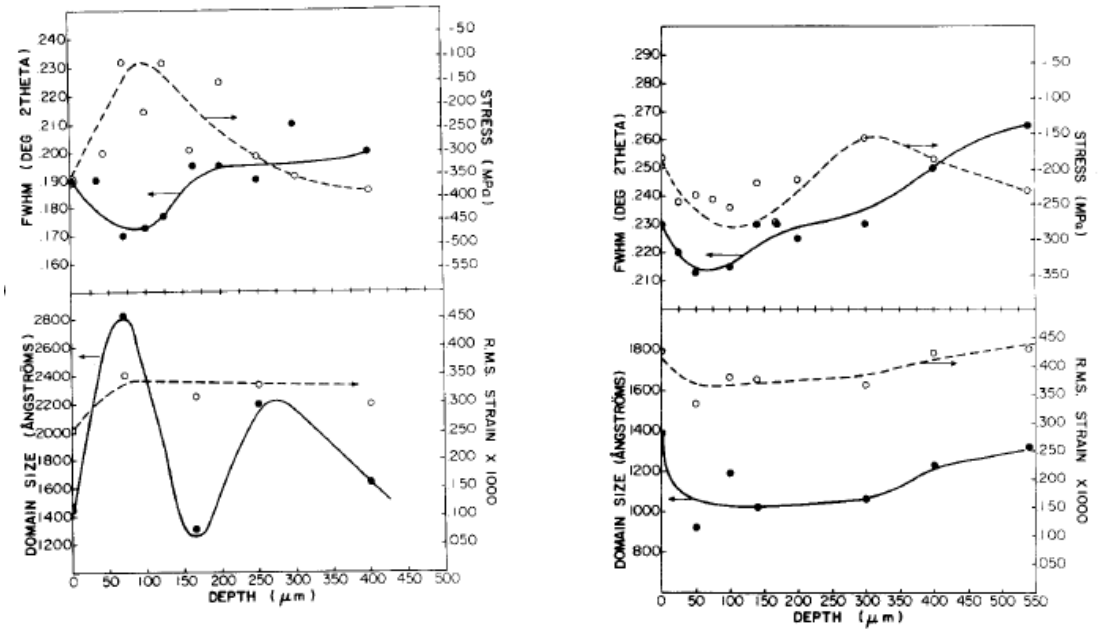

(a) (b)

Figure III-7:The half-breadth of 220 peak (FWHM) and longitudinal residual stress and the microstrain in the[110] direction *vs.* depth for the high cycle fatigue (a) 78340 cycles of normalized AIS11008 steel; and (b) 90000 cycles of cold-worked AISI 1008 steel [103].

Still in the theme of fatigue behaviour obtained primarily from the halfwidth values, Vijayan et al. [102] carried out fatigue cycling experiments at a frequency of 15 Hz and at constant stress amplitudes of 32 and 46 MPa in annealed specimens of ALFAX aluminum. The fatigue cycling was interrupted at chosen intervals, and X-ray diffraction patterns were recorded using CuKα radiation. The halfwidths were measured on the recorded profiles. In these experiments, the choice of the radiation restricted the examination to only the near-surface region of the specimens. The microstrains (E) at various stages of fatigue cycling were calculated using the single line method [102]. The b/b_0 *vs* N curve obtained at fine intervals for the applied stress amplitude of 32 and 46 MPa is presented in Figure III-8(a) and (b), respectively. Here b_0 and b are the respective halfwidths of a Bragg reflection, before and after N fatigue cycles.

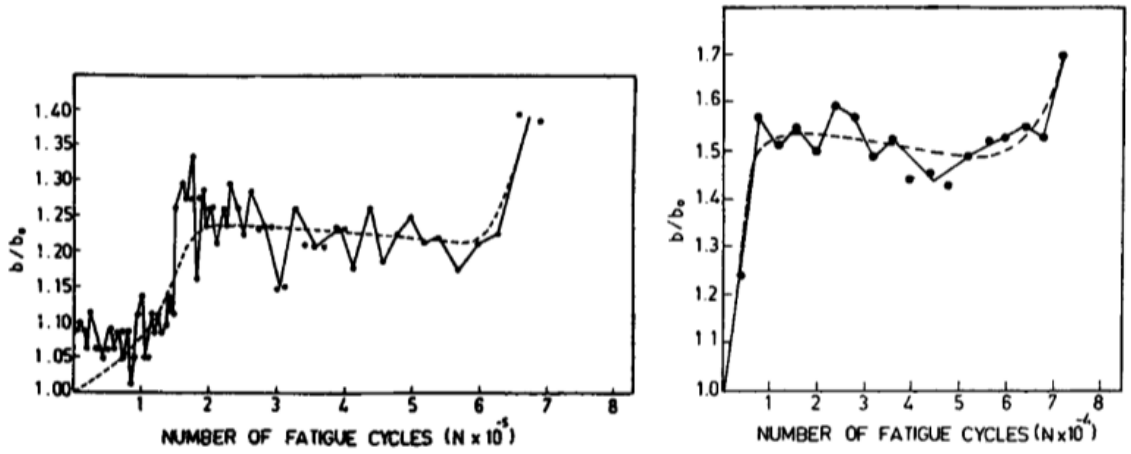

(a) (b)

Figure III-8: *b/b₀ vs N* data at (a) 32 MPa and (b) 46 MPa. Dashed line represents the average curve [102].

The occurrence of oscillations independent of the applied stress amplitude is clearly noted in Figure III-8. In both cases, the oscillations are statistically significant and the mean curve in each case closely resembles the three-stage curve reported early by Pangborn *et al.*[104], which can be seen in Figure III-9. The oscillations start at very early stages of fatigue cycling and persist until fatigue failure occurs. Absence of oscillations in stage I of the curve in Figure III-8(b) is due to the inappropriate choice of the interval of X-Ray diffraction measurements used in this stage.

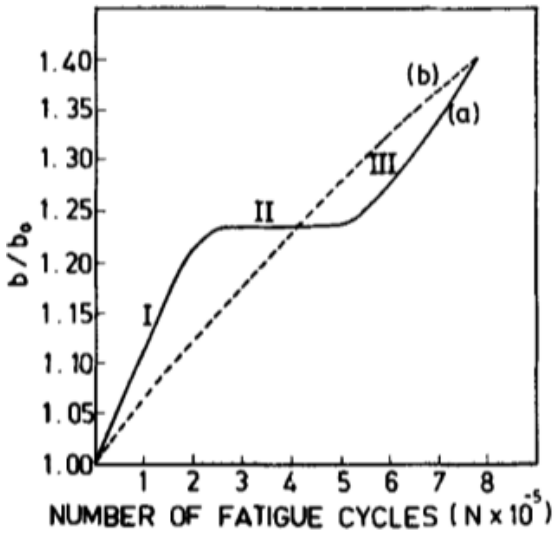

Figure III-9: A typical, three-stage *b/b₀ vs N* curve when the diffraction patterns are recorded from the near-surface region of the specimen. The three stages are marked as I, II and III respectively [104].

Figure III-10 shows the variation of the microstrain values with *N*. The *E vs N* curve is strikingly similar to the corresponding *b/b₀ vs N* curve in Figure III-8(a). The E's exhibit an

oscillatory distribution about a mean line. The mean line is characterized by the presence of three stages marked in Figure III-10. The average E values of $0.15x10^{-3}$, $0.30x10^{-3}$ and $0.40x10^{-3}$ corresponding to stages I, II and III of the E *vs* N curve point out that the microstrain values increase with the progress of fatigue cycling.

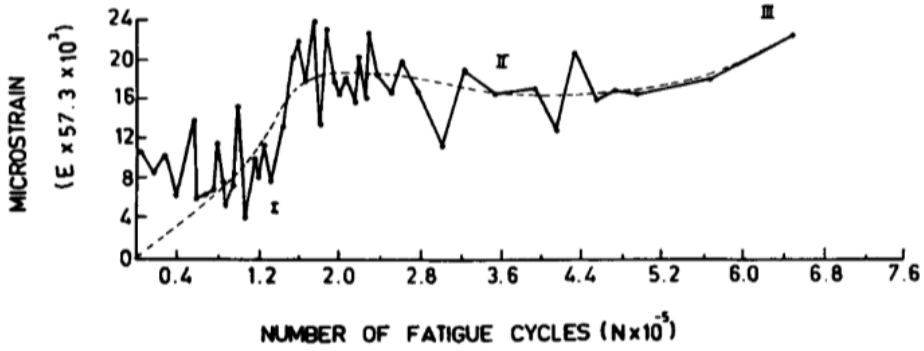

Figure III-10: Variation of microstrain *E* with *N* [102].

Winholtz and Cohen [105] studied the changes in both the macrostresses and microstresses in order to characterize their individual roles in the fatigue of steel. Stress-controlled fatigue tests were carried out at two stress levels, 276 and 345 MPa. Specimens were heat treated to give three different microstructures: pearlite, spheroidite and tempered martensite. Four specimens were tested at 276 MPa; one of each microstructure in the as-heat-treated condition and a fourth with a spheroidite microstructure that had been shot peened to introduce compressive stresses in the surface region. Nine specimens were tested at 345 MPa, three for each microstructure.

Stress measurements were made with chromium radiation using the 211 diffraction peak at approximately 156° 2θ for the ferrite phase and the 250 peak at approximately 148° 2θ for the cementite phase. The diffraction peaks were measured at 31 different φ and ψ tilts and fitted with pseudo-Voigt functions [105] to determine the peak positions. The stresses were then determined by a least-squares procedure [105]. Figure III-11 shows the macrostresses and microstresses along the loading direction with fatigue at 276 MPa in pearlite, spheroidite, tempered martensite, and in a shot-peened spheroidite sample.

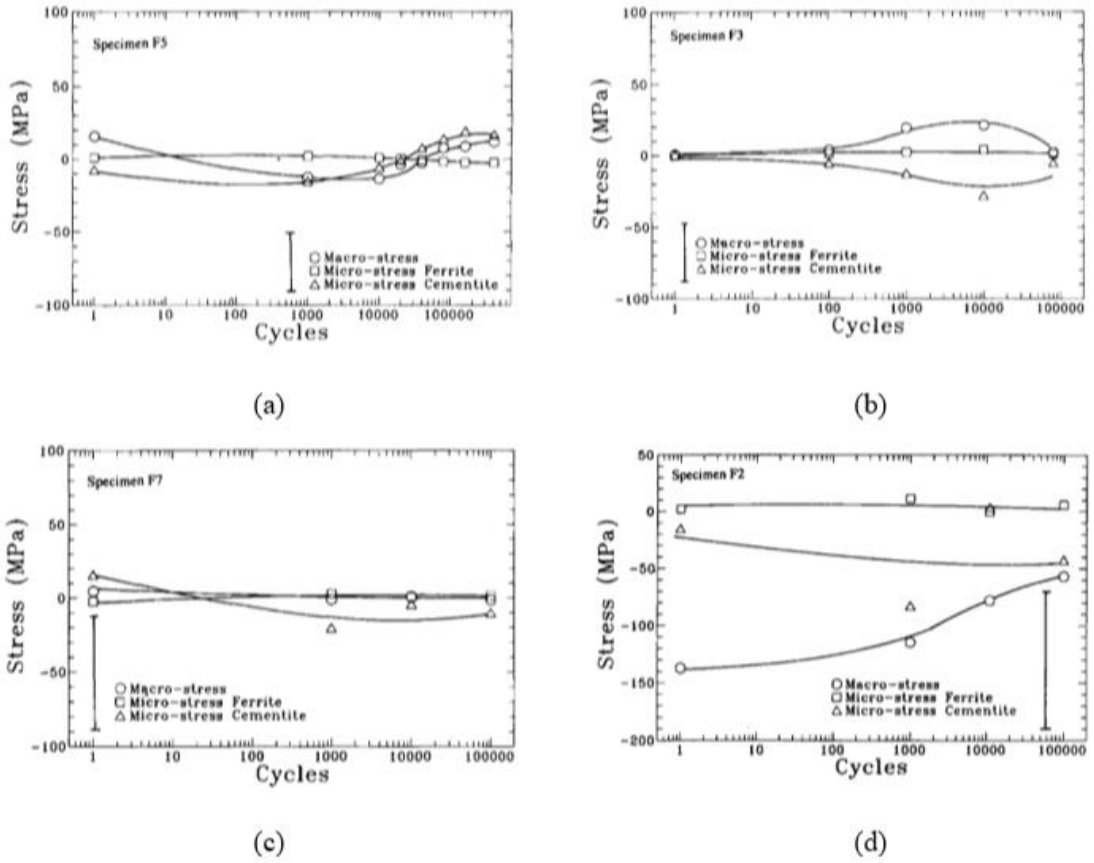

Figure III-11: Macrostresses and microstresses along the loading direction with fatigue at 276 MPa in (a) peartite, (b) spheroidite, (c) tempered martensite, and (d) shot-peened spheroidite sample [105].

The stress tensors measured in the specimens fatigued at 345 MPa can be found in [105]. According to Winholtz and Cohen [105], the specimens with initial tensile deformation show large tensile microstresses in the cementite phase, whereas those with initial compressive deformation show large compressive microstresses in the cementite. The authors concluded that in as-heat-treated specimens of pearlite, spheroidite and tempered martensite with no initial residual stresses, no development of residual stresses was seen for fully reversed uniaxial fatigue loading, and that macrostresses initially present fade with fatigue (as, for example, after shot peening). The reader is encouraged to consult [105] for further information about this study.

Still in the theme of microstrain evaluation during fatigue damage, Fourspring and Pangborn [99] used X-Ray double crystal diffractometry (XRDCD) to assess cyclic microstructural deformation in a face centered cubic (FCC) steel (AISI304) and a body centered cubic (BCC) steel (SA508 class2). Characterization of microstructural deformation was also carried out to identify differences in the accumulation of damage from the surface

to the bulk. In the near surface region (0-10µm), the procedure was to interrupt the cyclic loading of the test bars at various estimated fractions of life and then characterize the near surface of the test bars at each interruption. For the study of the subsurface region (10-300µm), a layer of material was removed from the surface by electropolishing to permit characterization of the newly exposed surface. Therefore, by repeating this procedure several times at varying depths into the material, a profile of the microstructural deformation within the subsurface region emerged. Finally, for the bulk characterization, Fourspring and Pangborn [99] received from industry samples from fatigued test bars in which the bulk material was exposed by cutting the gage section of the test bars perpendicular to the longitudinal axis to produce disk shaped samples.

Fourspring and Pangborn [99] used two methods for their microstructural analysis, the first method is referred to as the variance analysis, and the second method is referred to as the individual peak analysis. Figure III-12 and Figure III-13 show the trends in results from the individual peak analysis of the XRDCD data with accumulated fatigue damage from the near surface through the bulk.

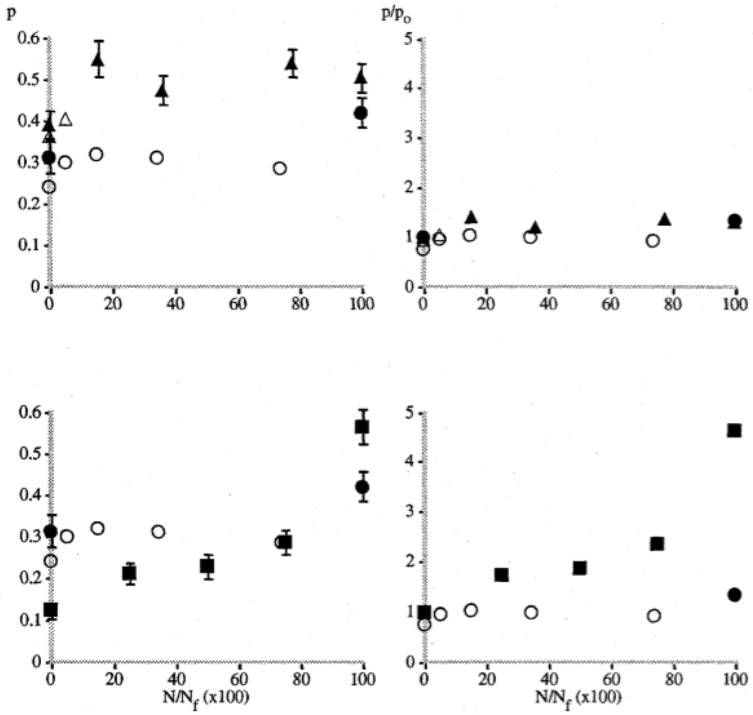

Figure III-12: Individual peak analysis of the XRDCD data for AISI304. Comparison of the combined results from the Δε = 0.60% and Δε = 1.20% regimes (top) and the combined results from near surface and bulk for the A€ = 0.60% regime (bottom). ● (○) Δε = 0.60% near surface, ▲ (△) Δε= 1.20% near surface, ■ (□) Δε= 0.60% bulk. The solid symbols represent results which have a statistically significant difference from the initial state; and, the outlined symbols represent results which have no statistically significant difference from the initial state [99].

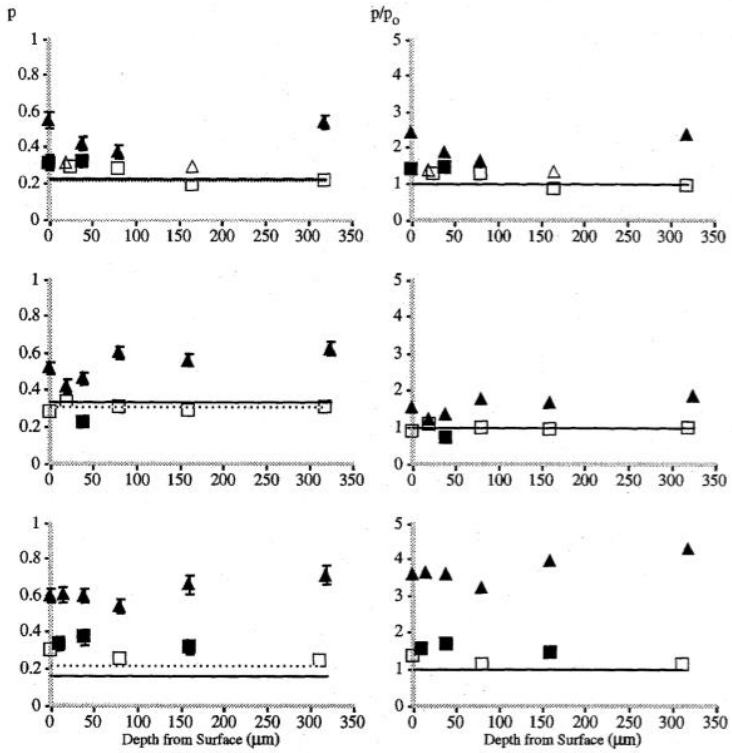

Figure III-13: Individual peak analysis of the XRDCD data for AISI304. Comparison of the combined results from the near surface and subsurface for the both the Δε = 0.60% and Δε = 1.20% regimes at 5% N/N$_f$ (top), 50% N/N$_f$ (middle), and failure (bottom). The solid horizontal bars represent the initial state values from the Δε = 1.20% regime, and the broken horizontal bars represent the initial state values from the Δε = 0.60% regime. ■ (□) Δε = 0.60% regime, ▲ (△) Δε = 1.20% regime. The solid symbols represent results which have a statistically significant difference from the initial state; and, the outlined symbols represent results which have no statistically significant difference from the initial state [99].

Figure III-14 shows the results of the variance analysis for the bcc material.

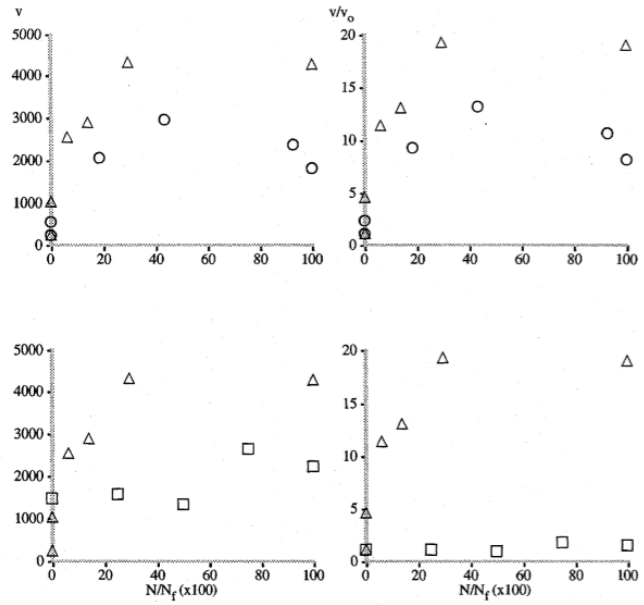

Figure III-14: Variance analysis of the XRDCD data for SAS08. Comparison of the combined results from the Δε = 0.48% and Δε = 0.78% regimes (top) and the combined results from near surface and bulk for the Δε=0.78% regime (bottom). O Δε = 0.48% near surface, △ Δε = 0.78% near surface, □ Δε = 0.78% bulk [99].

The XRDCD data indicate a measurable change from the initial state to subsequent states induced by fatigue of both the fcc material (AISI304) and the bcc material (SAS08). For the fcc material, lattice distortion increased as fatigue damage accumulated in the near surface, subsurface, and bulk regions. Figure III-12 and Figure III-13 show an increase in the integral breadths with fatigue damage. The increase in the integral breadth indicates that the diffraction profiles from the XRDCD data "broadened".

Comparing the results from the near surface and the subsurface, it can be noticed that the level of lattice distortion increased as the strain amplitude increased. The increase in the integral breadths (Figure III-12 and Figure III-13) was greater for the material fatigued with a 1.20% than the material cycled with a 0.60% strain range. The larger strain amplitude increased the rate of dislocation regeneration.

For the fcc material, the level of lattice distortion was greater in the bulk material than the near surface material. Figure III-12 shows a comparison between the near surface and the bulk for the material cycled with a 0.60% strain range. The change in the integral breadths from the bulk material is greater than the change in the integral breadths from the near surface material. Similarly, although less apparent, the lattice distortion and the development of cell dislocation configurations were greater in the subsurface than the near surface (Figure III-13).

For the bcc material, the decrease in the lattice distortion was greater in the near surface material than in the bulk material, in contrast to the results for the fcc material. Figure III-14 shows a comparison between the results from the near surface and the bulk regions for the material cycled with a 0.78% strain range. As a material that cross slips with ease, the bcc material has a greater rate of dislocation regeneration than the fcc material. Therefore, the dislocation density reduction in the near surface of the bcc material due to egress at the free surface was quickly reversed as dislocation regeneration occurred to allow the material to accommodate the imposed strains. And as expected, in the near surface of the bcc material, the magnitude of the lattice distortion increased as the strain amplitude increased. The increase in the variance parameter (Figure III-14) was greater for the material fatigued at a strain range of 0.78% than the material cycled with a strain range equal to 0.48%.

The work of Fourspring and Pangborn [99] is really significant because until them,

assessing fatigue damage with X-Ray diffractometry had not yet be demonstrated on steels.

Olchini *et al.* [100] investigated microstructural behaviour of specimens of AISI 316L stainless steel during interrupted high cycle fatigue tests by means of the integral breadth β, defined as the peak area/peak height ratio of the $K_{\alpha 1}$ component of a suitable XRD line (Figure III-15) [100]. The authors analyzed both pulsed laser surface treated and untreated condition. Laser surface melting is a very successful treatment on the fatigue behavior; obtaining a smooth surface characterized by a refined microstructure.

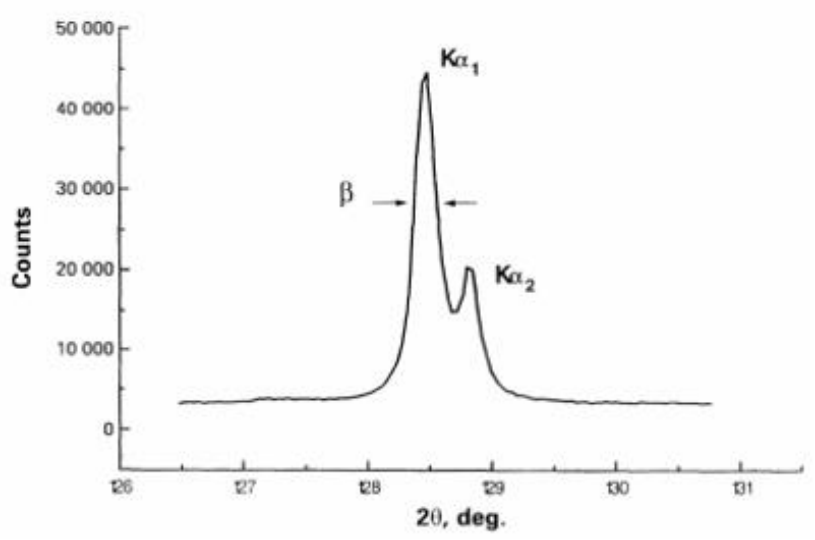

Figure III-15: Characteristic (220) XRD line of AISI 316L stainless steel (Cr Kα radiation): integral breadth β is evaluated on $K_{\alpha 1}$ component of peak [100].

Several points were considered in order to account for all the possible levels of damage. Position '0' was chosen in the middle of the gauge length on the unbroken specimens and close to the fracture on the broken ones. In the latter case the two regions on both sides of the fracture were examined. X-ray measurements were carried out with a conventional diffractometer operating with CrKα X-ray radiation, whose penetration depth is less than 10µm. Some examples of the results of β measurements on the specimens are reported in Figure III-16. It was found that during fatigue β increases appreciably within the gauge length up to a maximum value β_{max}. During fatigue β_{max} increases continuously up to a critical value β* where fracture occurs.

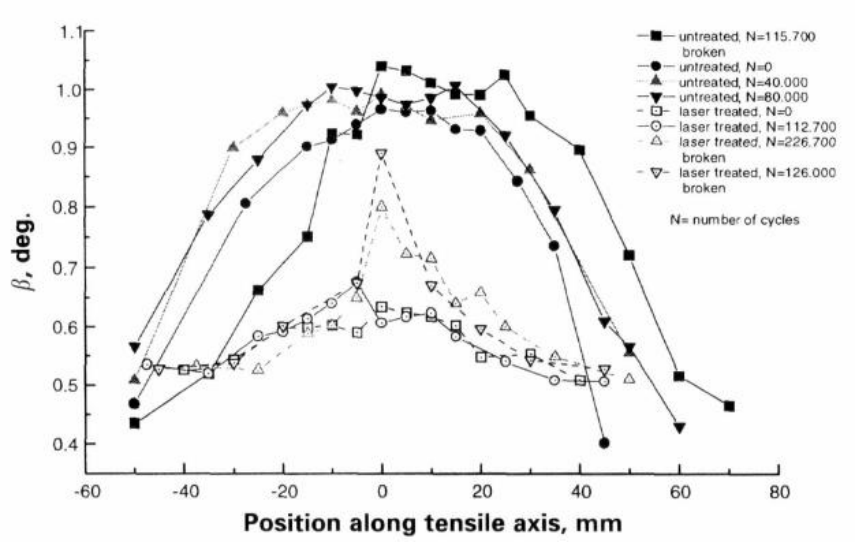

Figure III-16: Results of β measurements on surface of untreated and laser treated AISI 316L specimens fatigued at load of 500 MPa [100].

Assuming β as an estimate of the work hardening induced by fatigue, Olchini *et al.* [100] concluded that, by the surface monitoring of β, the work hardening of the surface increases during fatigue life; at each fatigue life fraction a maximum work hardening level, represented by β_{max}, is reached in some point of the gauge length; and the highest level of work hardening bearable by the material is found in the fracture point and is represented to a good approximation by β^*. All these facts support the idea that fatigue damage is associated with progressive surface work hardening.

Akiniwa et al. [97] used the X-ray diffraction method to measure the loading and residual stresses induced by fatigue in each constituent phase of specimens of an aluminum alloy 2024-T6 reinforced with 20 vol% of silicon carbide particles (SiCp). Change of the loading stress was analyzed on the basis of the residual stress and the relaxation due to initiated and grown-up fatigue cracks. Fatigue tests were conducted under four-point bending, under a constant load with triangular waveform in air at room temperature. The maximum applied load was 245 N. The stress ratio of fatigue tests was 0.1. The X-ray diffractions from Al 222 and SiC 116 by CrKα radiation were used to measure the stress.

Figure III-17 shows the change of the half value breadth, HVB, with the number of stress cycles. The dashed line in the figure indicates the value obtained at $N = 0$. Although the scatter is large, the value of HVB becomes large just before fracture. The line broadening is caused by inhomogeneous strain induced by fatigue cracks and

plastic deformation. The results are significant because it is an indicative that the fatigue damage can be detected by the change of HVB.

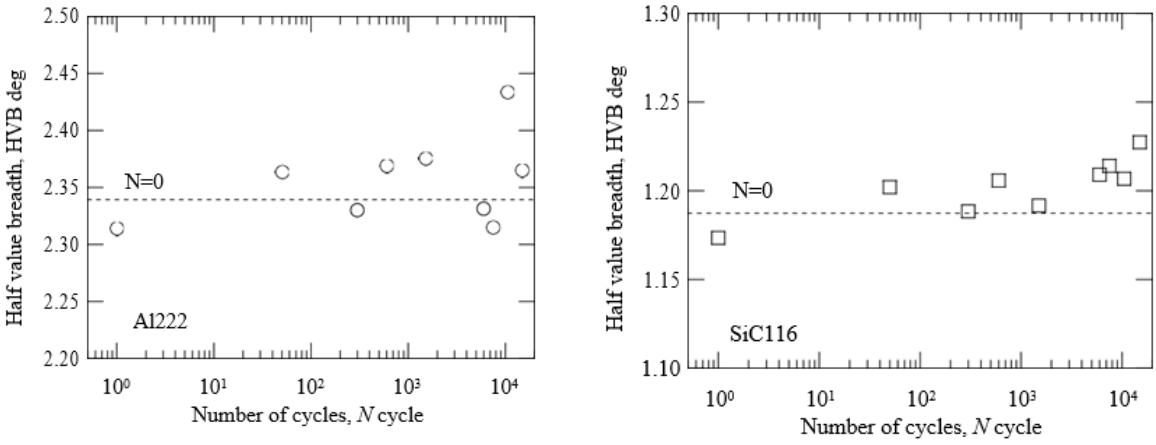

(a) (b)

Figure III-17: Change of half value breadth with number of cycles: (a) Al phase; (b) SiC phase [97].

In a second work, Akiniwa et al. [98] published the results for the same experimental procedure but using the full width at half maximum, FWHM, as an analyzing tool. Figure III-18(a) shows the change of FWHM with number of stress cycles. The specimen fractured at N_f = 7500 cycles. The scatter for the aluminum phase is relatively large. Although the value of FWHM slightly increases with stress cycles, the change is not so remarkable. On the other hand, for the case of the SiC phase, the value increased steeply just before fracture. Similar results were also obtained at the minimum applied stress.

According to Akiniwa et al. [98], the line broadening is caused by the inhomogeneous strain induced by fatigue cracks and plastic deformation. However, the SiC phase is hardly deformed plastically. Then the effect of the plastic deformation on the change of FWHM can be negligible. The steep increasing of FWHM in the SiC phase corresponds to the increase of heterogeneity of the strain due to decohesion and fatigue cracks. In a rigorous manner, the relation between the increase in FWHM and the increasing decohesion and particle fracture due to crack propagation should be verified in this fatigue conditions.

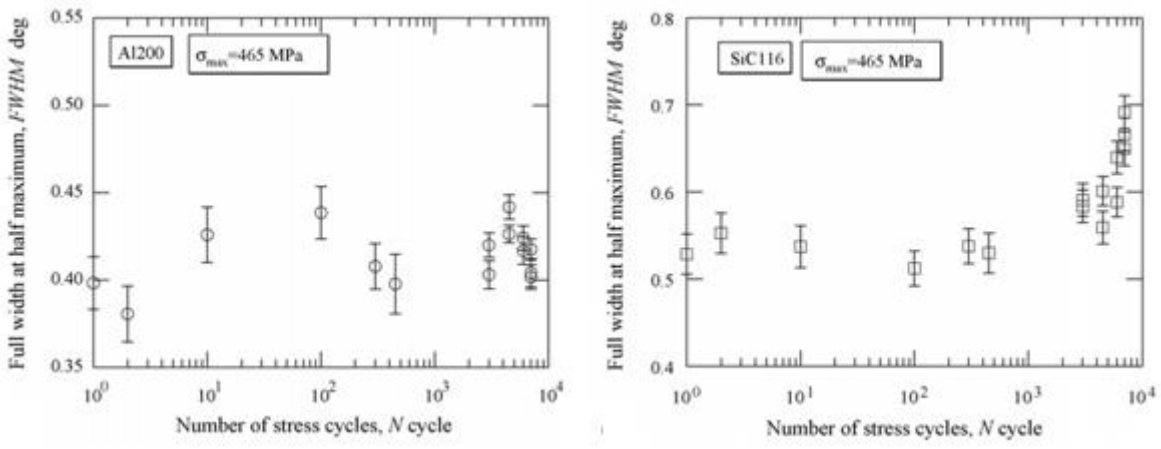

(a) (b)

Figure III-18: Change of full width at half maximum with number of stress cycles: (a) aluminum phase; (b) SiC phase [98].

The authors could conclude that fatigue damage can be successfully evaluated by the value of FWHM. The effects of the stress ratio and the stress amplitude on the diffraction parameters must be clarified for the engineering application [98].

The most recent works found in the literature involving the FWHM of the X-Ray diffraction peak to study microstructural changes in steel behavior during fatigue cycling was published by Pinheiro et al. [15,108-110]. Pinheiro studied microstructural changes related to fatigue damage initiation in the API 5L X60 grade steel. Fatigue tests were regularly interrupted for XRD measurements at periods of 10000 load cycles maximum up to sample failure. Four different alternating bending loadings were applied with stress ratios R around 1 (fully reversed stress). Additionally, fatigue tests were performed with $R = 2.8$ at the highest strain amplitude (0.19%).

In Figure III-19, variations in FWHM of the X-ray diffraction peak measured during fatigue tests at different alternating stress amplitudes are presented. The FWHM change measured at a given number of cycles is defined as the difference between FWHM values at this point and at $N = 0$, i.e., $FWHM - FWHM_0$.

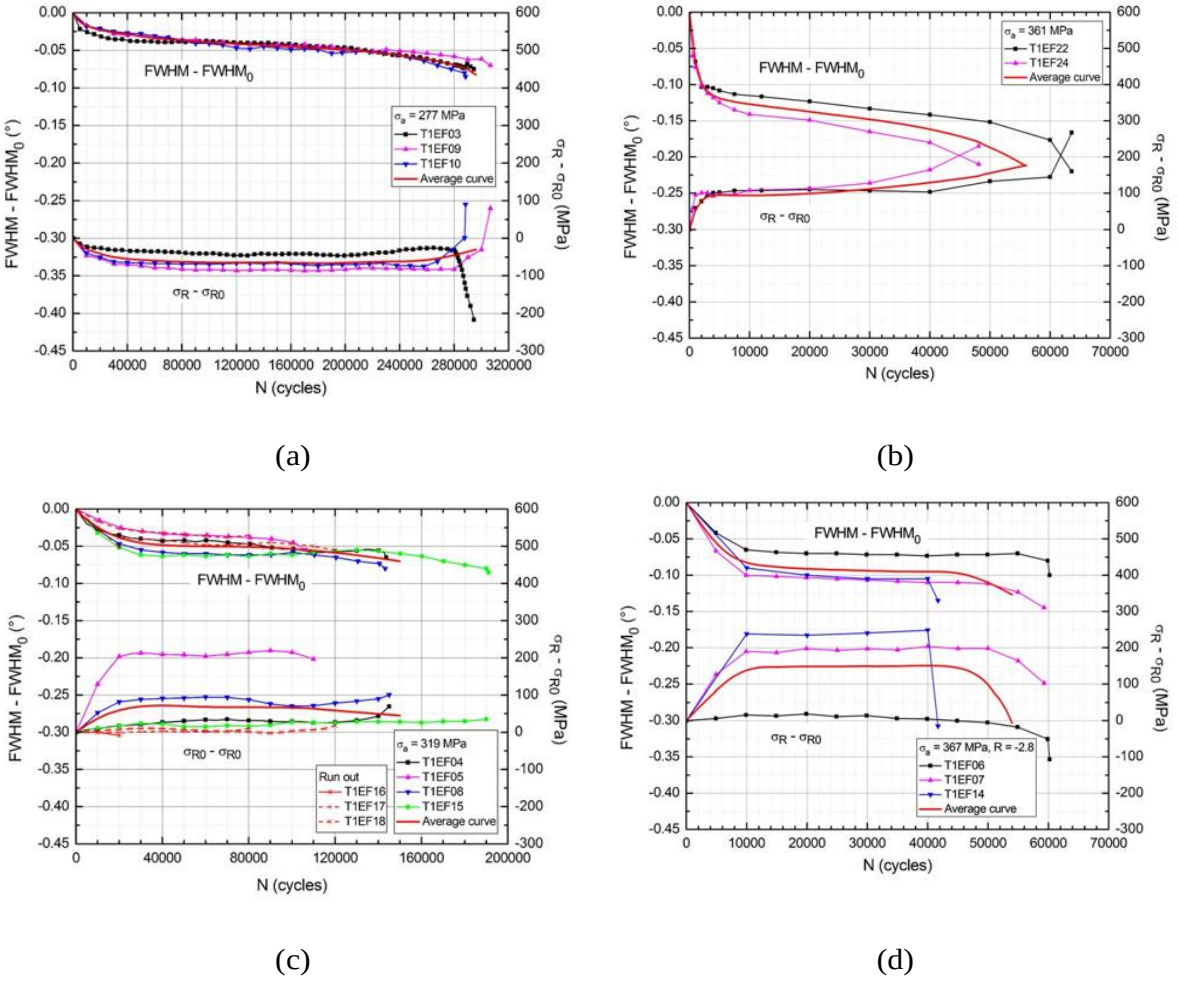

Figure III-19: Evolution of FWHM and residual stresses σ_R with fatigue cycling at (a) σ_a = 277 MPa and *R=-1*; (b) σ_a = 361 MPa and *R=-1*; (c) σ_a = 319 MPa and *R=-1;* (d) σ_a =367 MPa and *R*=−2.8 [109].

For all stress amplitudes, three stages can be identified in FWHM changes during fatigue cycling. The first stage (Stage 1) takes place in the early cycles and is characterized by a fast decrease of FWHM. In the second stage (Stage 2), the rate of FWHM decrease is considerably reduced. This stage comprises the major fraction of fatigue life (about 50%). Finally, the third stage (Stage 3) occurs in the last cycles with a rapid decrease in FWHM until complete fracture [109].

CHAPTER IV

MATERIAL CHARACTERIZATION

CHAPTER IV. MATERIAL CHARACTERIZATION

This chapter presents the characterization of API 5L X65 grade steel carried out by means of chemical composition analyses, metallography analysis and uniaxial tension tests.

Specific tests coupons were machined from a sample of seamless API 5L X65 grade steel pipe, with nominal diameter and thickness of 219.08 mm and 15.06 mm, respectively. The steel pipe was provided by the Subsea Technology Laboratory (LTS) of COPPE/Federal University of Rio de Janeiro. Figure IV-1 shows the machining sketch of test coupons.

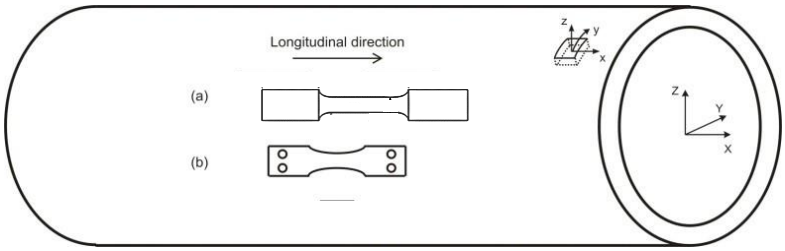

Figure IV-1: Test coupons and samples cut off from an API 5L X65 grade steel pipe for:(a) uniaxial tension tests and (b) fatigue, indentation and X-Ray tests.

IV.1 UNIAXIAL TENSION TESTS

Uniaxial tension tests were carried out to evaluate relevant mechanical properties of the API 5L X65 grade steel. Nine tension test specimens were machined from the longitudinal direction of the pipe sample (Figure IV-1(a)). Tension test coupons were identified with the reference T2ET followed by a sequential number (i.e., T2ET01 to T2ET09), which means "traction samples from tube two", in French, *tube 2 éprouvette traction (T2ET)*. The geometry and dimensions of tension test coupons are presented in Figure IV-2. Tensile tests were carried out in an INSTRON (8802) universal testing machine equipped with a 10kN load cell. Tests were run with a strain rate of 2.64 x 10^{-4} m/ms^{-1}, at room temperature, according to specifications of ASTM E8M-04 standard [111]. The strains were measured using a clip gage. With the objective of studying the behavior of the material in different conditions, three test coupons were annealed for 1h at a temperature of 850 °C. These samples also have an "R" at the end of the name that makes reference to an annealed sample, in French, *recuit (R).*

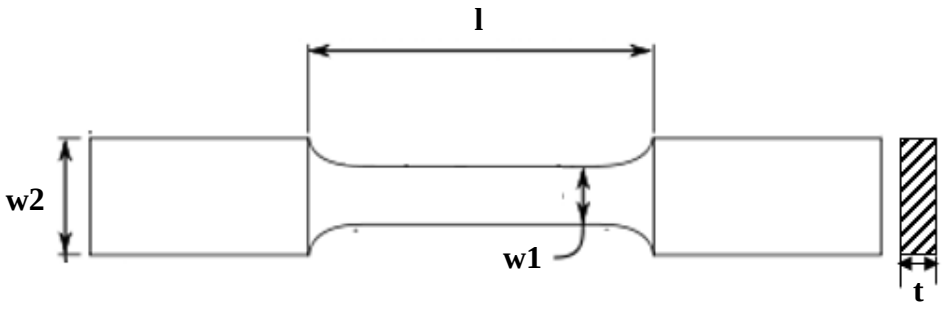

Figure IV-2: Tensile samples, where w1 = 20 mm, w2 = 30 mm, l = 40 mm, and t = 3 mm.

Figure IV-3 and Figure IV-4 show the engineering stress-strain curves for as-machined and annealed samples, respectively. Table IV-1 presents average mechanical properties obtained, which are in agreement, when considered the standard deviation for each parameter, with the requirements of the standard API SPEC 5L – Specification for Line Pipe [113] shown in Table IV-2.

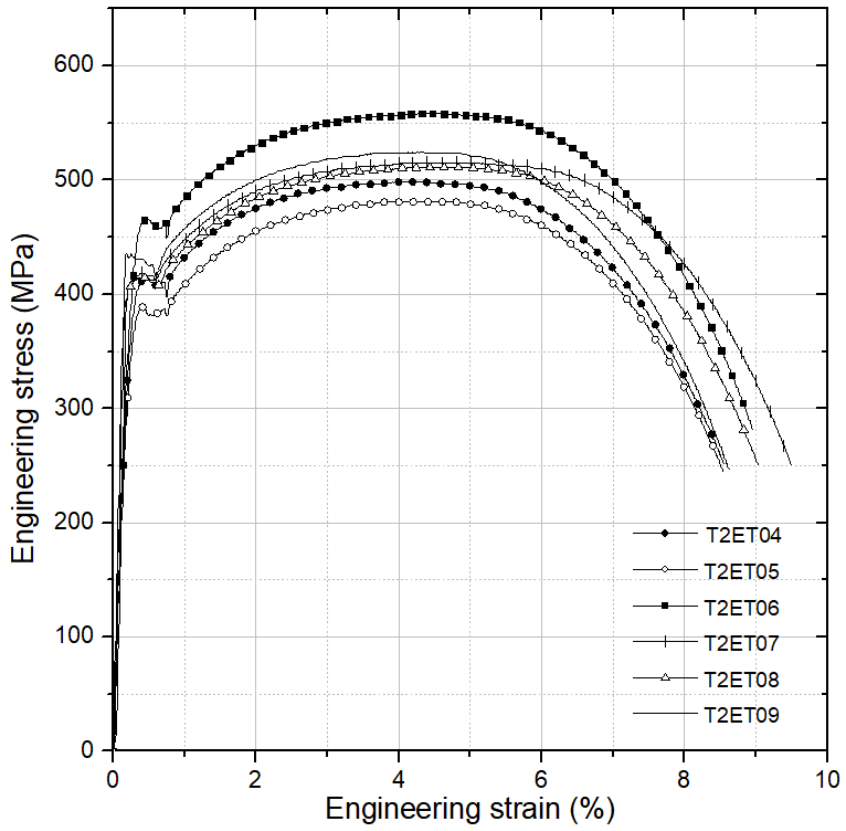

Figure IV-3: Stress-Strain curves for API X65 steel as-machined samples.

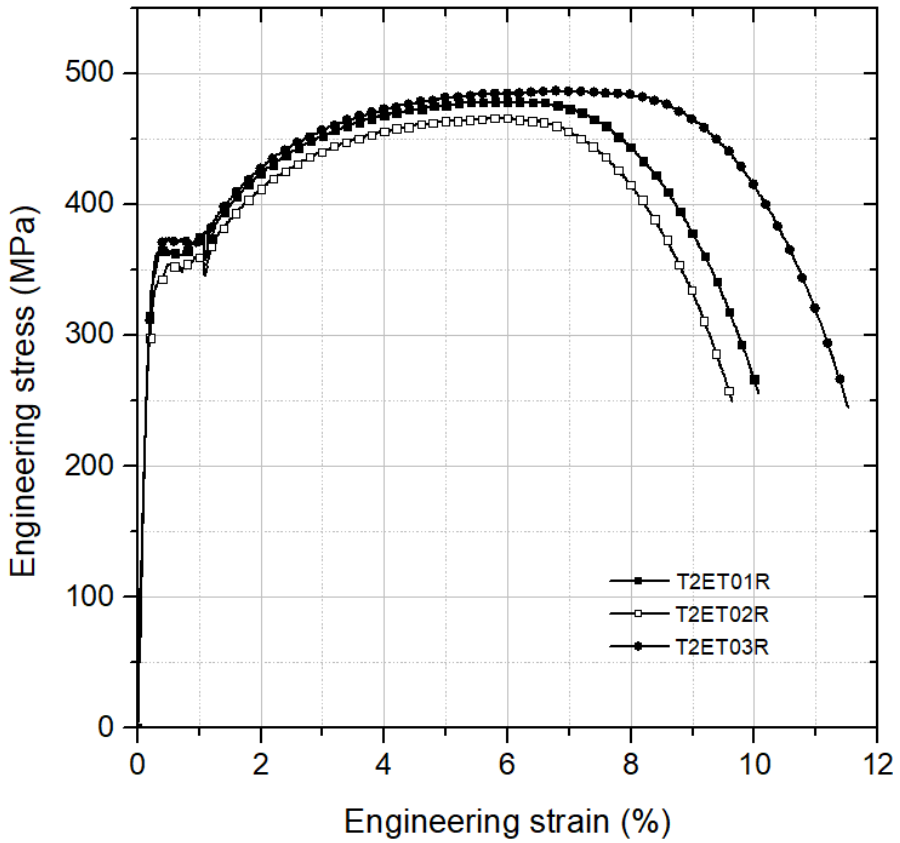

Figure IV-4: Stress-Strain curves for API X65 steel annealed samples.

Table IV-1: Average mechanical properties obtained for API 5L X65 grade steel as-machined and annealed samples.

Condition	E (GPa)	YS (MPa)	UTS (MPa)
As-machined	201 ± 16	442 ± 36	520 ± 27
Annealed	190 ± 17	365 ± 8	477 ± 10

where E = Young Modulus; YS = Yield Strength a 0,2% offset and UTS= Ultimate Tensile Strength

Table IV-2: Minimum and maximum tensile requirements for API 5L X65 grade steel [113]

Condition		YS (MPa)	UTS (MPa)
As-machined	Minimum	448	531
	Maximum	600	758

where YS = Yield Strength a 0,2% offset and UTS= Ultimate Tensile Strength

When a metal is deformed under stress, bending or compression, during the manufacture of pipelines for example, the stress required to continue deformation increases continuously with deformation. This hardening mechanism is called cold work hardening or just hardening and is caused by the continuous increase in the density of dislocations with

plastic deformation [116]. Since elongated grains are anisotropic, after cold work the original grain size can be restored by annealing heat treatment [117]. In annealing, the hardened metal is submitted to a sufficiently high temperature, at which the total energy available to the deformed regions enables the atoms to be ground to their equilibrium positions and, consequently, the reduction of elastic deformation and stored energy can be observed. The density of dislocations decreases, and the grains increase in size, besides a decrease in strength values and hardness near to the original values [118].

For the annealing samples tested in this work, it can be noted a decrease in strength properties when compared to the as-machined samples properties (Table IV-1). As explained before, the samples were taken from the tube illustrated in Figure IV-1, after the process of cold-work during manufacture of the tube, therefore, it can be concluded that the as-machined samples suffered hardening and after annealing there was tension relaxation with consequent strength properties decrease. To study changes in the microstructure of the material and grain size behaviour after annealing, metallographic analyses were done and are shown later in item IV.3.

IV.2 CHEMICAL COMPOSITION ANALYSES

Chemical composition for the API 5L X65 steel was obtained by optical emission spectrometer analysis by *Tecmetal Soluções Tecnológicas em Materiais LTDA*, in room temperature and moisture of 22%, using as reference the standard ASTM E 415 [112]. Average results of chemical composition in percentage of weight (wt. %) are shown in Table IV-3. Table IV-4 presents the chemical composition requirements (maximum values) for API 5L X65 Steel provided by the standard API SPEC 5L – Specification for Line Pipe [113], which provide standards for pipe suitable for use in conveying gas, water, and oil in both the oil and natural gas industries. API SPEC 5L Specification for Line Pipe [113] also states that the sum of columbium (niobium, Nb), vanadium (V), and titanium (Ti) contents shall not exceed 0.15%. Therefore, analyzing Table IV-3 and Table IV-4, it was found that the chemical composition of the material is in agreement with the requirements.

Table IV-3: Average chemical composition in percentage of weight (wt. %) estimated for API 5L X65 grade steel.

Al	As	B	Bi	C	Ca	Ce	Co	Cr
0.059	0.008	0.001	0.007	0.078	0.002	0.007	0.006	0.076
Cu	**Fe**	**La**	**Mn**	**Mo**	**Nb**	**Ni**	**P**	**Pb**
0.016	97.70	<0.001	1.450	0.070	0.041	0.025	0.009	<0.003
S	**Si**	**Sn**	**Ti**	**V**	**W**	**Zn**	**Zr**	
<0.001	0.352	0.005	0.006	0.041	0.044	<0.002	0.006	

Table IV-4: Maximum chemical composition requirements in percentage of weight (wt. %) for API 5L X65 grade steel by the standard API SPEC 5L.

C	Mn	P	S	Ti	Fe
0.26	1.45	0.030	0.030	0.06	Balance

IV.3 METALLOGRAPHIC ANALYSES

The surface of two specimens, one as-machined and one annealed, were prepared for metallographic examination by grinding with a sequence of SiC papers from 80 to 1200 grit numbers under water cooling, followed by wet grinding with diamond micro powders from 6 μm to 1 μm and etching with 5% Nital. The material microstructure was observed using optical microscope with magnification factors of 100, 200, 500 and 1000x. Figure IV-5 and Figure IV-6 show the results for the as-machined and annealed samples, respectively.

A ferrite-pearlite structure is observed in both conditions, as-machined and annealed. It can be observed in Figure IV-5 and Figure IV-6 a matrix of ferrite (white) with distribution of pearlite (black) better located at triple joints. After annealing treatment is observed just a redistribution of the pearlite phase, and grains considerably bigger than for the as-machined material.

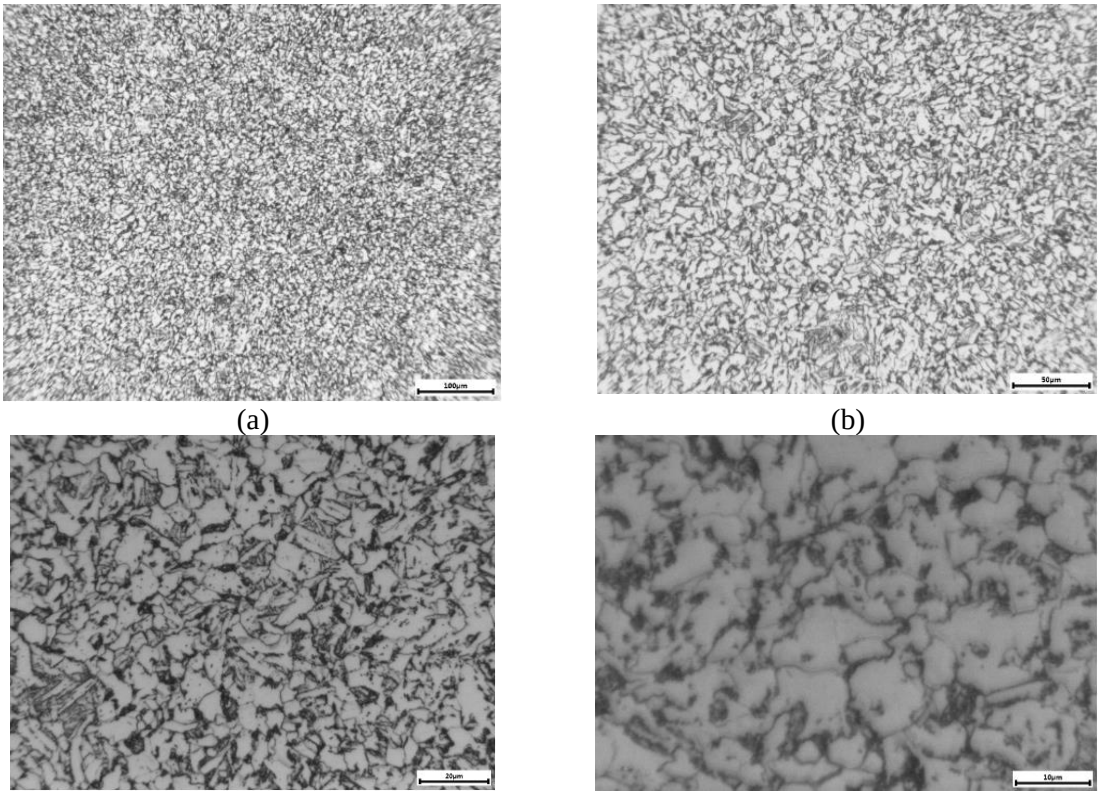

(a) (b)

(c) (d)

Figure IV-5: Microstructure of an as-machined specimen observed through optical microscope, magnification factor of (a) 100x, (b) 200x, (c) 500x and (d) 1000x.

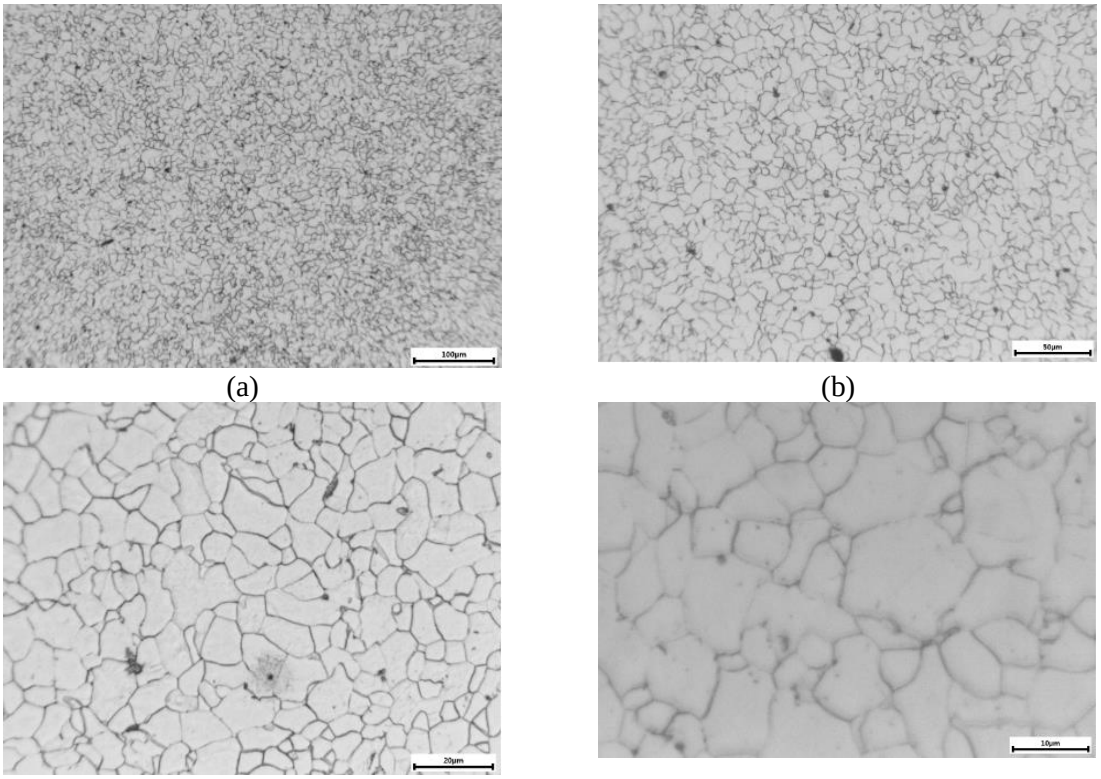

(a) (b)

(c) (d)

Figure IV-6: Microstructure of an annealed specimen observed through optical microscope, magnification factor of (a) 100x, (b) 200x, (c) 500x and (d) 1000x.

A fine grained material is stronger than a coarse grained material, since the first has a larger total grain boundary area which makes it difficult the movement of dislocations [115]. Therefore, is expected that after annealing, with the increasement of grain size, the material presents lower values of strength properties, as observed in Table IV-1, and lower hardness when compared do the as-machined material. The hardness properties of both conditions will be compared in Chapter VI.

Aiming to study the augmentation in grain size during heat treatment, the images of Figure IV-5(b) and Figure IV-6(b), as-machined and annealed samples with magnification factor of 200x, were treated with the aid of the software Image J. The results are shown in Figure IV-7 and Figure IV-8.

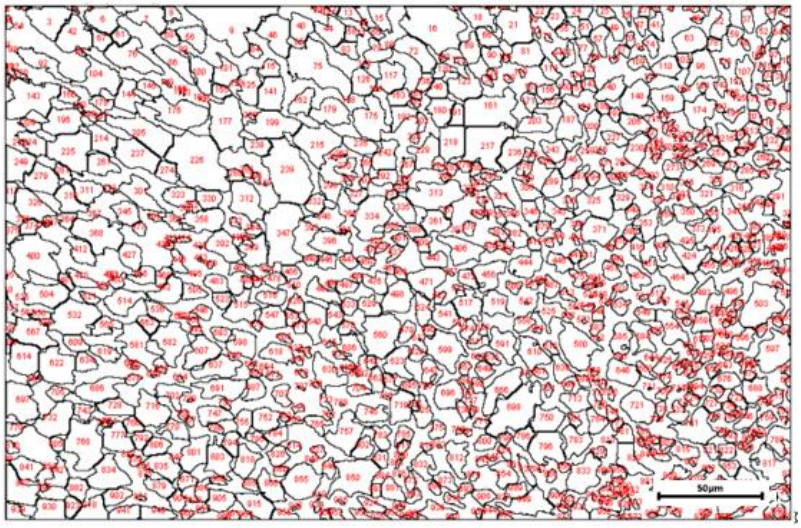

977 grains, 60% of the total area, 14µm in size

Figure IV-7: Image J analyses of grain size for an as-machined sample with 200x of magnification factor.

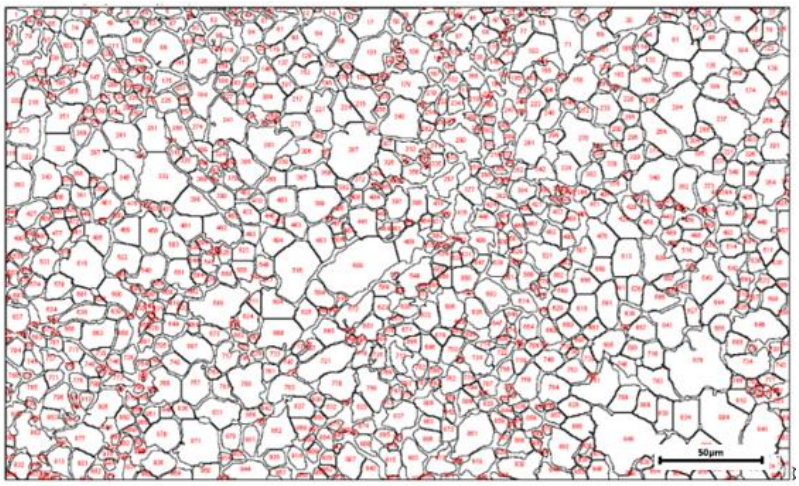

981 grains, 78% of the total area, 31µm in size

Figure IV-8: Image J analyses of grain size for an annealed sample with 200x of magnification factor.

The software identifies the contour of the grains and gives as results the area of each grain, the size (based on the approximate diameter of each grain) and the percentage of total area occupied for the grains. For the as-machined condition (Figure IV-7) the analyzed area have 977 grains, that fills 60% of the total area. The average of grain size is 14µm. For the annealed condition (Figure IV-8), 981 grains were analyzed, which fills 78% of the total area. The average of grain size is 31µm. It can be clearly noted that due to the annealing treatment the grains have grown from 14 to 31µm, and new crystals were formed once the area filled by the grains had increased from 60 to 78% of the total area.

After fatigue failure, metallographic examinations were done at the same specimens showed before, with the same surface preparation. N_f values for the as-machined and annealed specimens were 25200 and 14400 cycles, respectively. The region analyzed was the middle of the gauge section, which due to the geometry of the specimen, is the region with the highest stress concentration and where the fracture will preferably occur. The region analyzed is indicated with a red square in Figure IV-9. Figure IV-10 and Figure IV-11 compare the microstructure of the specimen prior fatigue testing (non-cycled) and after fatigue failure for the as-machined and annealed conditions, respectively, for a magnification factor of 500x.

Figure IV-9: Fatigue cycled specimen with the red square indicating where the metallographic examinations were done.

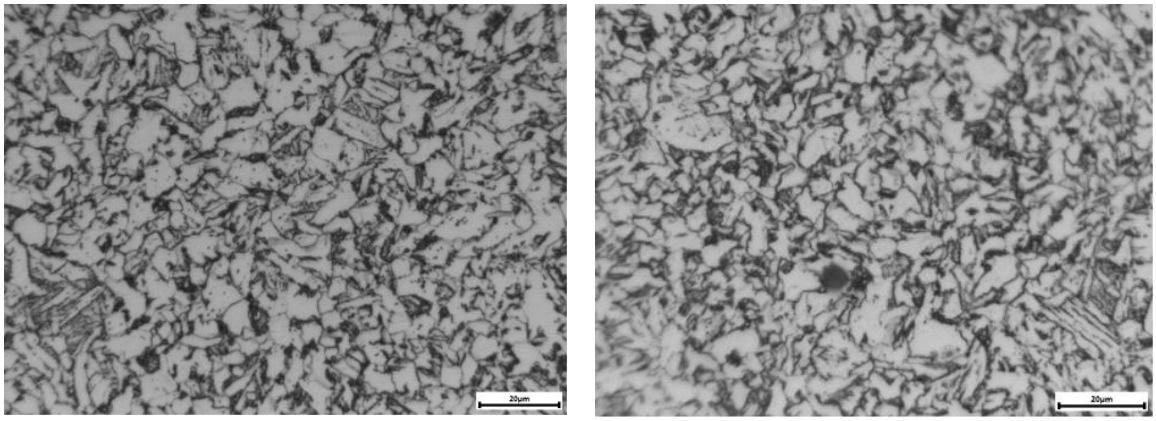

(a) (b)

Figure IV-10: Microstructure of an as-machined specimen observed through optical microscope, magnification factor of 500x, (a) non-cycled and (b) after fatigue failure.

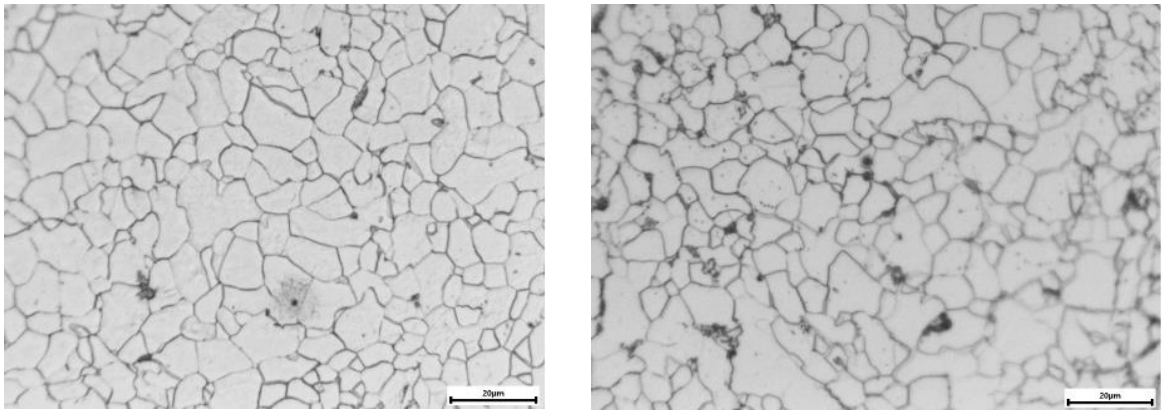

(a) (b)

Figure IV-11: Microstructure of an annealed specimen observed through optical microscope, magnification factor of 500x, (a) non-cycled and (b) after fatigue failure.

Observing Figure IV-10 and Figure IV-11, for both as-machined and annealed conditions, respectively, no major differences can be noted in the microstructure of the samples before and after fatigue cycling. The material was cycled under high cycle fatigue ($N \geq 10^3$) thus plastic deformation is really localized and concentrated, and the microstructure of the sample is not modified during cycling. If the sample were under low cycle fatigue ($10^{0<}N < 10^3$), plastic deformation could be seen in a bigger scale, more generalized and not so localized with early damage nucleation, and the microstructure images could show significantly changes between the non-cycled and cycled samples. But the samples were tested under high cycle fatigue and because of that, a metallographic observation using optical microscope was not the appropriate and effective method of studying fatigue damage evolution during cycling. Therefore, alternative methods, like indentation and X-Ray analyses are indicated and applied in this work.

Once again, the software Image J was used to analyze the size of the grains and to ratify that high cycle fatigue domain does not cause significant changes in the microstructure of the material. Figure IV-12 and Figure IV-13 shows the results.

For the as-machined condition (Figure IV-12) 977 grains was analyzed, that fills 60% of the total area and the average of grain size is 14µm, for the non-cycled sample. For the sample analyzed after fatigue failure, 976 grains were accounted for, that fills 58% of the total area and the average grain size is 11µm. It can be noted that the grains did not present increase in size, and despite the difference in the number of grains analyzed, the percentage of the area filled by then are very close.

For the annealed condition (Figure IV-13) 981 grains were analyzed, which fills 78% of the total area, with average of grain size of 31µm for the non-cycled sample. 996 grains were analyzed for the sample submitted to fatigue failure, which fills 76% of the total area and the average grain size is 28µm. It can be observed that the percentage of the area filled by the grains and the grain size are very close, like for the as-machined samples, showing that the phenomenon of fatigue damage under high cycle fatigue did not changed the microstructure of the material.

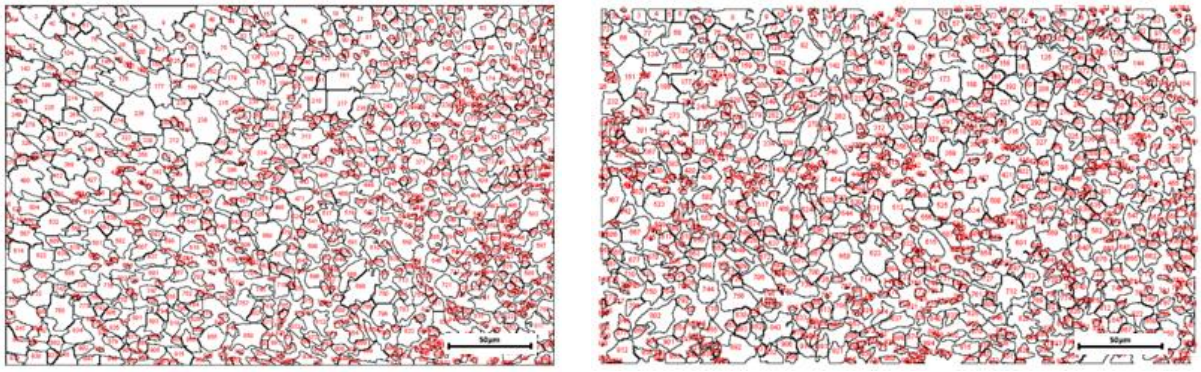

977 grains, 60% of the total area, 14µm in size (a)

979 grains, 58% of the total area, 11µm in size (b)

Figure IV-12: Image J grain size analyses of an as-machined sample, magnification factor of 200x, (a) non-cycled and (b) after fatigue failure.

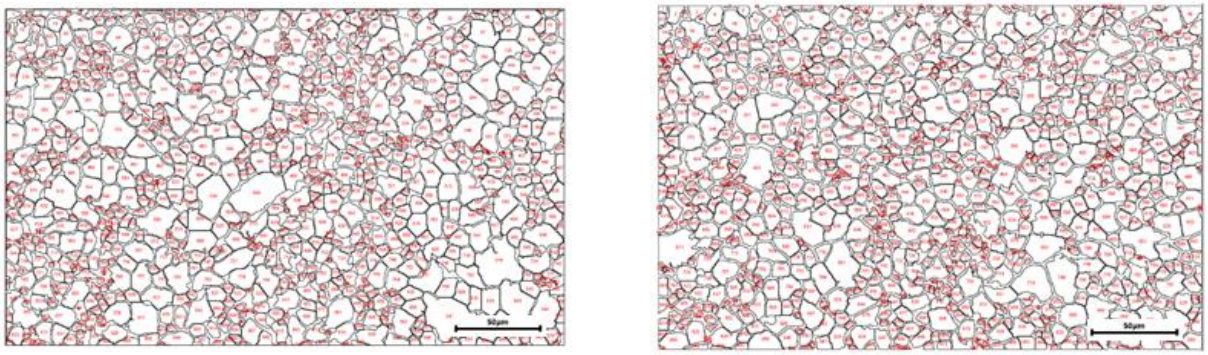

981 grains, 78% of the total area, 31µm in size
(a)

996 grains, 76% of the total area, 28 µm in size
(b)

Figure IV-13: Image J grain size analyses of an annealed sample, magnification factor of 200x, (a) non-cycled and (b) after fatigue failure.

CHAPTER V

EXPERIMENTAL TESTS

CHAPTER V. EXPERIMENTAL TESTS

In this chapter the experimental work is presented, comprising the preparation of fatigue test samples, the experimental setup for the fatigue tests, the instrumented indentation tests and X-ray diffraction study of the changes in the microstructural of fatigue damaged API 5L X65 grade steel samples.

V. 1 FATIGUE TESTS

API 5L X65 steel samples were submitted to high cycle fatigue tests with alternating bending loads under strain control at room temperature. Fatigue tests were regularly interrupted for Instrumented Indentation Tests (IIT) and X-Ray Diffraction (XRD) measurements at periods pre-stated up to sample failure.

V.1.1 EXPERIMENTAL SETUP

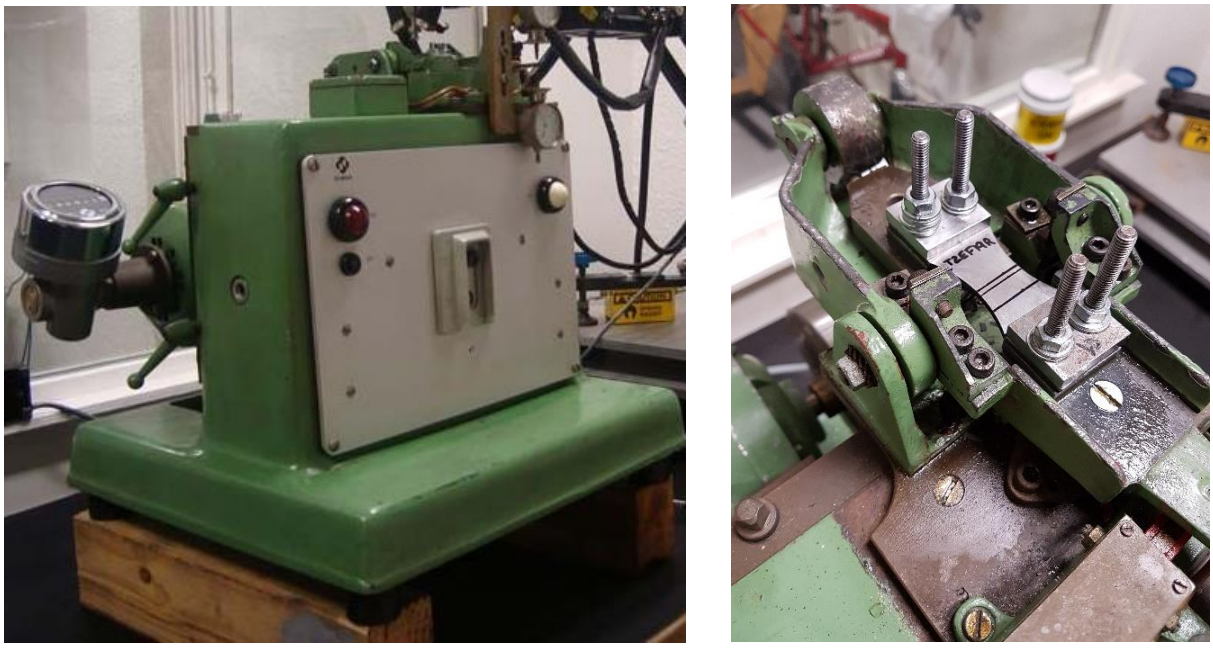

(a) (b)

Figure V-1: (a) Schenck fatigue machine; (b) Positioning of the samples at the machine.

Fatigue tests were performed in a Schenck machine model PWON [119] (Figure V-1), which is intended for fatigue strength evaluation of samples made of steels and non-ferrous metals in accordance with the German standard DIN 50142 [119]. Within tolerable capacity limits of the testing machine, static and dynamic bending moments to different superposition

conditions can be applied. Strain-controlled alternating bending loads were applied by prescribing the oscillation amplitude of the dual eccentric gear in the fatigue testing machine. Alternating bending loads followed a sinusoidal waveform at a frequency of approximately 25 Hz. The testing machine was previously calibrated through loading tests with strain gage instrumentation of one sample to set the range of strain amplitudes for the fatigue tests.

Figure V-2 schematically presents the alternating bending fatigue testing machine, showing (1) dial indicator gauges; (2) rotation measuring lever arm; (3) flexure leaf steel spring support; (4) axis of rotation; (5) test sample; (6) drive arm; (7) connecting rod; (8) dual eccentric; (9) preload adjustment by relocation (static stress), and (10) measuring spring- dynamometer. The fatigue test sample was clamped to the testing machine with the aid of fixing devices so that one extremity was constrained and the other was free to move in the vertical direction, following the dual eccentric oscillation (Figure V-1(b)).

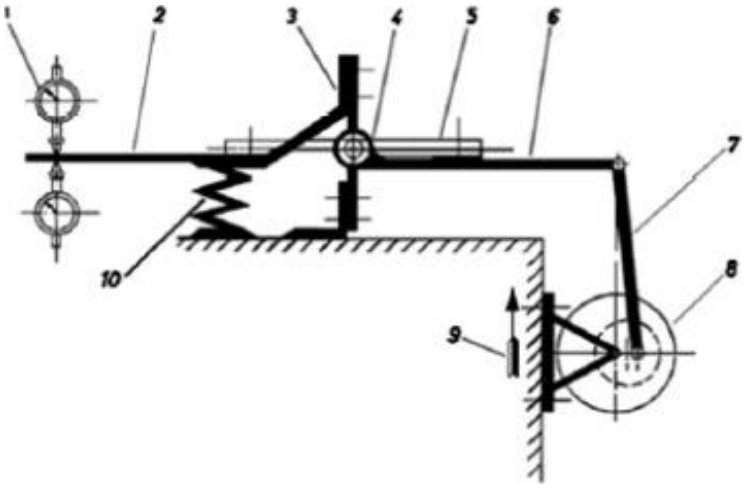

Figure V-2: Schematic representation of the alternating bending fatigue testing machine [119].

V.1.2 CALIBRATION OF THE FATIGUE MACHINE

The fatigue machine was calibrated by loading tests. One fatigue sample was instrumented with a biaxial strain gauge, and signals from it were transmitted to a data acquisition software. Five oscillation amplitudes were prescribed for the dual eccentric, as can be seen in Table V-1. Minimum and maximum strain values for each eccentric amplitude were obtained, and stress values were calculated by multiplying the strain by the modulus of elasticity (E) obtained in the uniaxial tensile test ($\sigma_{min/max} = E\varepsilon_{min/max}$). Stress amplitude ($\sigma_a$) and stress ratio (R) were calculated by Equation I-2 and Equation I-4, respectively. The results are summarized in Table V-1.

Table V-1: Calibration of the fatigue testing machine.

Eccentric	Δε/2 (%)	σ_a (MPa)	ε_{min} (%)	ε_{max} (%)	σ_{min} (MPa)	σ_{max} (MPa)	R
3.5	0.071	150	-0.068	0.074	-143	157	-0.91
6.5	0.129	272	-0.127	0.131	-268	277	-0.99
7.0	0.138	291	-0.132	0.144	-278	304	-0.91
8.0	0.160	337	-0.156	0.164	-328	346	-0.95
8.5	0.171	358	-0.170	0.170	-358	359	-1.00

In order to avoid corrections for medium stress and thus add uncertainties to the results due to the use of Goodman, Gerber, Soderberg or other models, it was chosen to work with stress ratios *R* around -1 (fully reversed stress). Two series of fatigue tests were carried out, the first one with stress amplitude of 272MPa, corresponding to an eccentric amplitude of 6.5, and the second one with stress amplitude of 358MPa and eccentric amplitude of 8.5, as can be seen in Table V-1.

V.1.3 FATIGUE TEST SAMPLES

Fatigue test samples were machined from the same pipe sample used to produce test coupons for material properties characterization (Figure IV-1). Flat samples were machined from the central region of the pipe wall thickness by cutting the internal and external walls. Fatigue test samples were identified with the reference T2EF followed by a sequential number (i.e., T2EF01, T2EF02, T2EF03 and so forth), which means "fatigue samples from tube two", in French, *tube 2 éprouvette fatigue (T2EF)*, making reference to the pipe from which they were cut off (T2) and the type of test they were submitted, in this case, fatigue tests, in French, *essais de fatigue* (EF). Figure V-3 shows the geometry and dimensions of the fatigue test samples, which were defined in order to fit Schenck model PWO requirements [119].

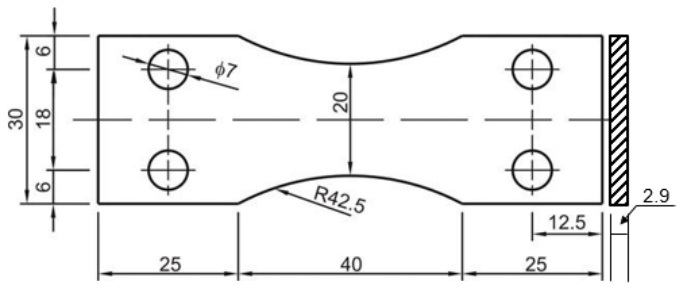

Figure V-3: Geometry and dimensions (in mm) of fatigue test samples.

The test samples were polished in order to reduce the surface roughness that can affect XRD measurements and IIT analyses. Pinheiro [15] analyzed different polishing procedures and the electrolytic polishing technique was selected as the most suitable, since it helps to reduce the surface roughness and the near-surface residual stresses induced by machining. Here, as-machined samples were submitted to electrolytic polishing, and annealed samples were submitted to grinding followed by electrolytic polishing. Due to the heat treatment, a surface crust was formed over the annealed samples, and before the electrolytic polishing it was necessary to grind the surface to remove it. In the grinding procedure, the sample surface was ground with a sequence of SiC papers from 80 to 1200 grit numbers under water cooling.

The electrolytic polishing procedure was performed in the Struers Lectropol 5 device (Figure V-4) at 25 V during 40s and 100s, for the as-machined and annealed samples, respectively, using a perchloric-based acid solution (standard electrolyte Struers A2). The electrolytic polishing was done in two different regions, as indicated schematically by the shaded areas in Figure V-5. Due to the specimen positioning in the fatigue machine, a restrained condition is produced at the region between the holes, i.e. no cyclic loading is applied at this region. Thus, the properties calculation in this region is taken as the reference value for the sample. Polishing was also done within the gage length region of the sample surface, which is the region were the hardness and XRD measurements were concentrated. Polishing of these two areas were done with the aid of two plastic masks in where the geometry of the desired polishing area was cut off to assure that the polishing will be restricted to those areas. The positioning of the samples at the Struers Lectropol 5 device can be seen in Figure V-4(b).

(a) (b)

Figure V-4: (a) Struers Lectropol 5 device, (b) Positioning of the samples at the machine.

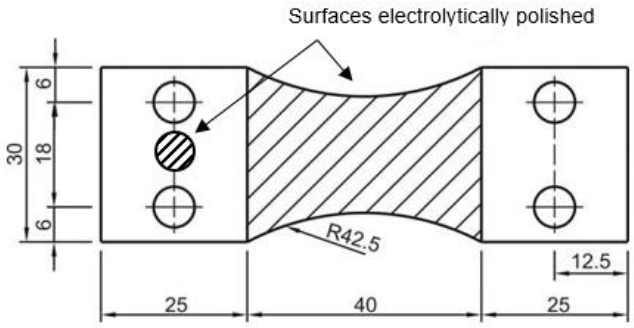

Figure V-5: Geometry and dimensions of the surface electrolytically polished.

V.1.4 S-N CURVE

To estimate the alternating stresses to be applied in fatigue tests, an S-N curve was estimated. As explained in Chapter I, for the high cycle domain, the S-N curve is described by the Basquin equation in the form of $S_n = CN^b$, where S_n is the alternating stress amplitude, C and b depend on the material properties. The Basquin equation was defined assuming two points. The first one, at N=10^6, considered as the endurance limit (S_e), and the second one, at N=10^3. As can be seen in Equation I-12, the value of fatigue strength at N=10^3 can be related to the ultimate tensile stress (UTS); the endurance limit can be calculated by Equation I-8, and constants b and C by Equation I-15 and Equation I-16, respectively.

From the tensile properties obtained for API 5L X65 (Table IV-1) and the surface condition factor (K_a) as 0.91705 for ground surface finish [15], endurance limits of 238MPa and 219MPa were estimated for as-machined and annealed samples, respectively. .

Finally, Basquin equations for as-machined and annealed samples were estimate as Equation V-1 and Equation V-2.

$$S_n = 872.1N^{-0.0953}$$

Equation V-1

$$S_n = 842.6N^{-0.0974}$$

Equation V-2

Figure V-6 shows estimated S-N curves for as-machined and annealed conditions.

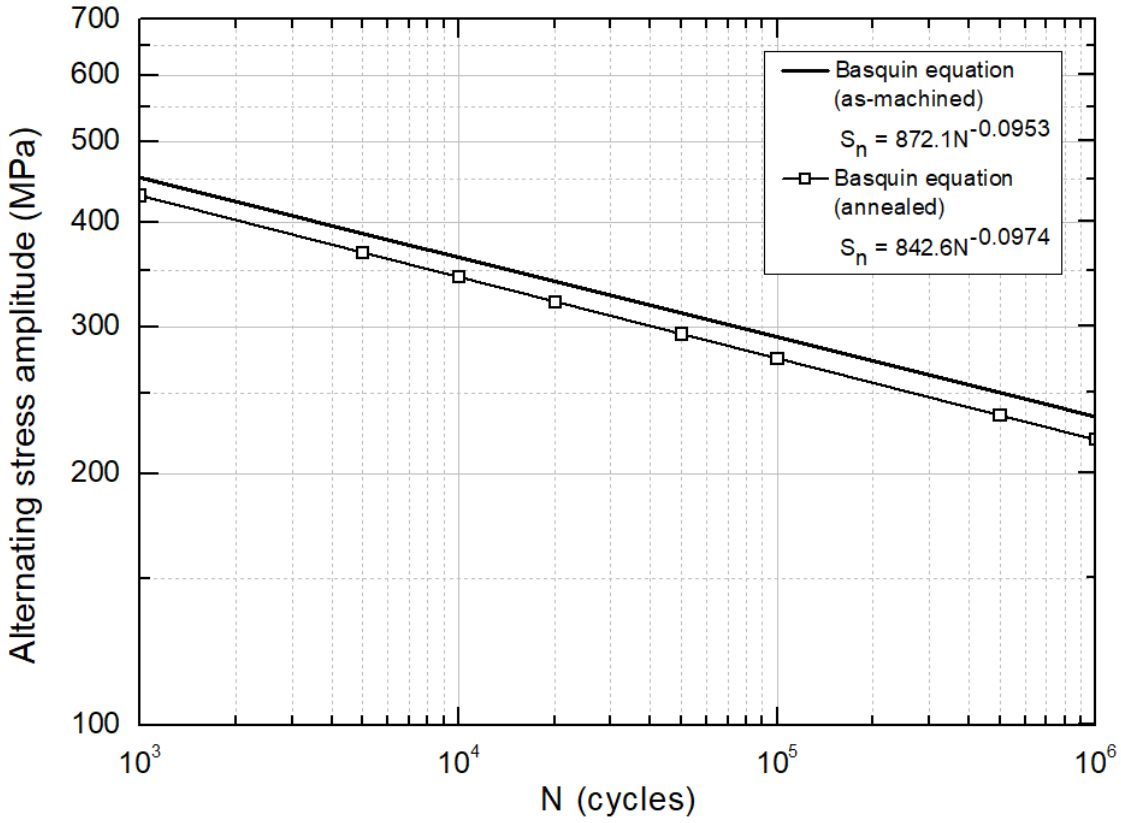

Figure V-6: Estimated S-N curves for as-machined and annealed conditions.

V.2 INDENTATION TESTS

Aiming to study the fatigue damage accumulated in the microstructure of the samples, Berkovich microhardness tests were carried out in the specimens previously submitted to high cycle fatigue (HCF) tests. Instrumented Indentation Tests (IIT) have been performed using a CSM 2-107 microhardness tester. Experimental setup for indentation tests is shown in Figure V-7.

Figure V-7: Experimental setup for microindentation tests.

Berkovich indenter was used for each sample analysis with maximum loads ranging from 0.2 to 2 N. A dwell-time of 15s was imposed at the maximum applied load, and loading and unloading rates have been set up at 100 mN/min. The load resolution is 100 µN and the depth resolution is 0.3 nm (provided by the CSM Instruments Group) [120]. Berkovich indentations were done in 4 different points of the specimen, which are represented by a cross symbol in Figure V-8. For each point, the machine performed 20 cycles of indentation, generating a curve of the type load/unloading that is shown in Figure V-9. Examples of impressions made by the Berkovich indenter at specimen surface are shown in Figure V-10.

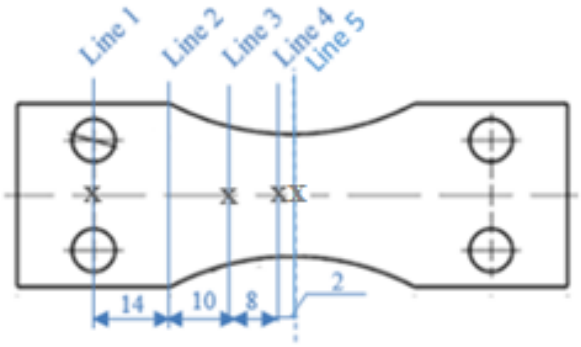

Figure V-8: Microhardness tests samples (dimensions in millimeters).

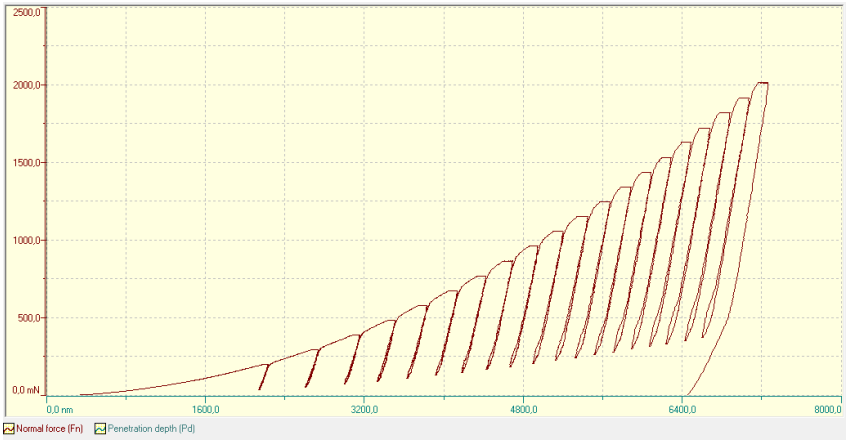

Figure V-9: Curve load vs penetration depth for 20 cycles of indentation.

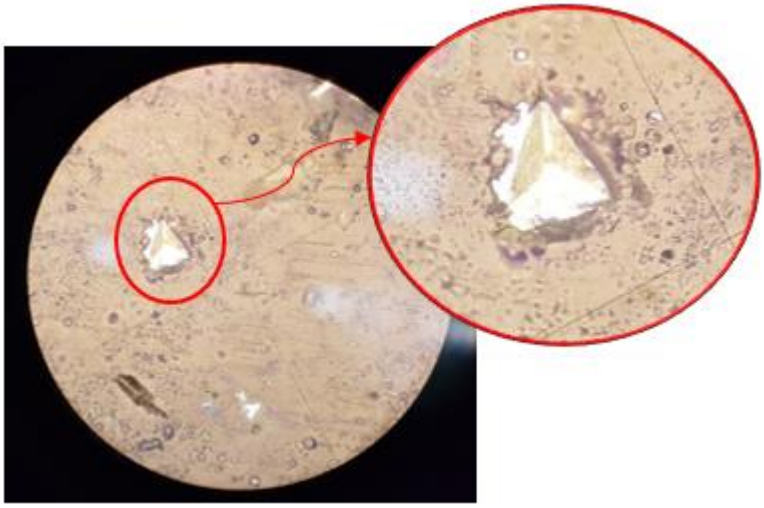

Figure V-10: Impressions made with a Berkovich indenter (three-sided pyramid).

It is known that during indentation tests, the material can flow under the indenter by two different modes of deformation: sinking-in (the material is pulled down toward the tip of the indent) or pilling-up (the material is pushed away from the center of the indent) [46]. See Figure II-5. A criterion to determine the predominant mode of deformation was developed by N'Jock et al. [46]: for materials for which the ratio between the residual indentation depth and the maximum indentation depth reached at the maximum load is higher than 0.83, pilling-up prevails, while sinking-in is observed when this ratio is lower than 0.83. Here, the results for all samples showed a ratio higher than 0.83, therefore all the deformations experienced was in a pilling-up mode. After determination of the mode of deformation, corrections proposed by Oliver and Pharr [41] for sinking-in or Loubet et al. [45] for piling-up should be applied in contact area equations. Loubet's et al. [45] modified

contact area equation used in this work is shown in Equation II-11. Detailed development of the contact area equation can be found in Chapter II item II.1.2

The accuracy of the indentation response is defined by the calibration of three factors: applied load, displacement of the indenter tip, and load frame compliance (C_f) of the indentation machine. Accurate determination of frame compliance is an essential component of instrumented micro- and nanoindentation experiments. In load frames of finite stiffness, the load applied via the indenter induces displacement in both the sample and the load frame. Frame compliance must be identified and subtracted from the total indenter displacement to account properly for sample deformation [122]. In 2004, Van Vliet [122] published that experimental procedures, in which the frame compliance is inferred from the elastic unloading indentation response of a reference sample, based on several assumptions and simplifications that can propagate significant uncertainty with respect to subsequent analyses of mechanical behavior of the sample. Years later, in 2013, Bandyopadhyay *et al.* [123] published that a common approach to determine C_f is instrument calibration using well known calibration samples. But this approach is not error free since the frame compliance of the instrument does not have a constant value. Commercial instruments exhibit C_f in the range of 10^{-5} to 10^{-7} m/N, which means that the instrument displaces as much as 10 μm displacement for an applied load of 10 N during microindentation tests [123]. Therefore, Chicot et al. [42] have proposed that the frame compliance of the material should be separately determined for each series of indentation from the plot of total compliance (C_T) versus the square root of the reciprocal contact area ($1/\sqrt{A_C}$). This method of calculating C_f was used in this work and the relevant equation is shown below.

$$C_T = \frac{1}{S} = \frac{\sqrt{\pi}}{2}\frac{1}{\beta E_r \sqrt{A_C}} + C_f$$

Equation V-3

where C_T is the total compliance, S is the elastic unloading stiffness, E_r is the reduced modulus, Ac is the contact area, C_f is the frame compliance and β is a correction factor, whose value was determined by King's finite element calculations [43], for the Berkovich indenter, as β= 1.034.

The coordinate at the origin for the curve of total compliance C_T versus the square root of the reciprocal contact area ($1/\sqrt{A_C}$) gives C_f value while the slope of the straight line

allows determining E_r. Afterwards, compliance correction was applied to the contact depth using the methodology proposed by Chicot et al. [42]:

$$h' = h_{mes} - C_f P$$

Equation V-4

where *h'* is the corrected contact depth, h_{mes} is the contact depth measured by the equipment, C_f is the frame compliance, and P is the applied load.

Equation V-4 can be now used to rebuild the loading–unloading curve and consequently to recalculate the contact area. Therefore, for the microhardness analysis, the equations to calculate indentation depth, contact area and consequently, hardness, englobed some corrections in relation to the deformation mode of the tip (piling-up or sinking-in), a non-perfect tip (h_b), and the calculation of the compliance of the frame (C_f) at each indentation cycle. These corrections avoid assumptions and simplifications that can propagate uncertainties in the results. A flow chart detailing all the steps of the methodology adopted to calculate hardness values is shown in Figure V-11.

A large number of results was expected since all the calculations showed in Figure V-11 were done for each indentation cycle of each sample. Therefore, an Excel Macro was developed where the programmer enters the indentation software results (load (F_m), maximum indentation depth (h_{max}), residual indentation depth (h_r) and elastic unloading stiffness (S)) and obtains the hardness values. An example of the use of this Excel Macro for one sample is shown in Figure V-12.

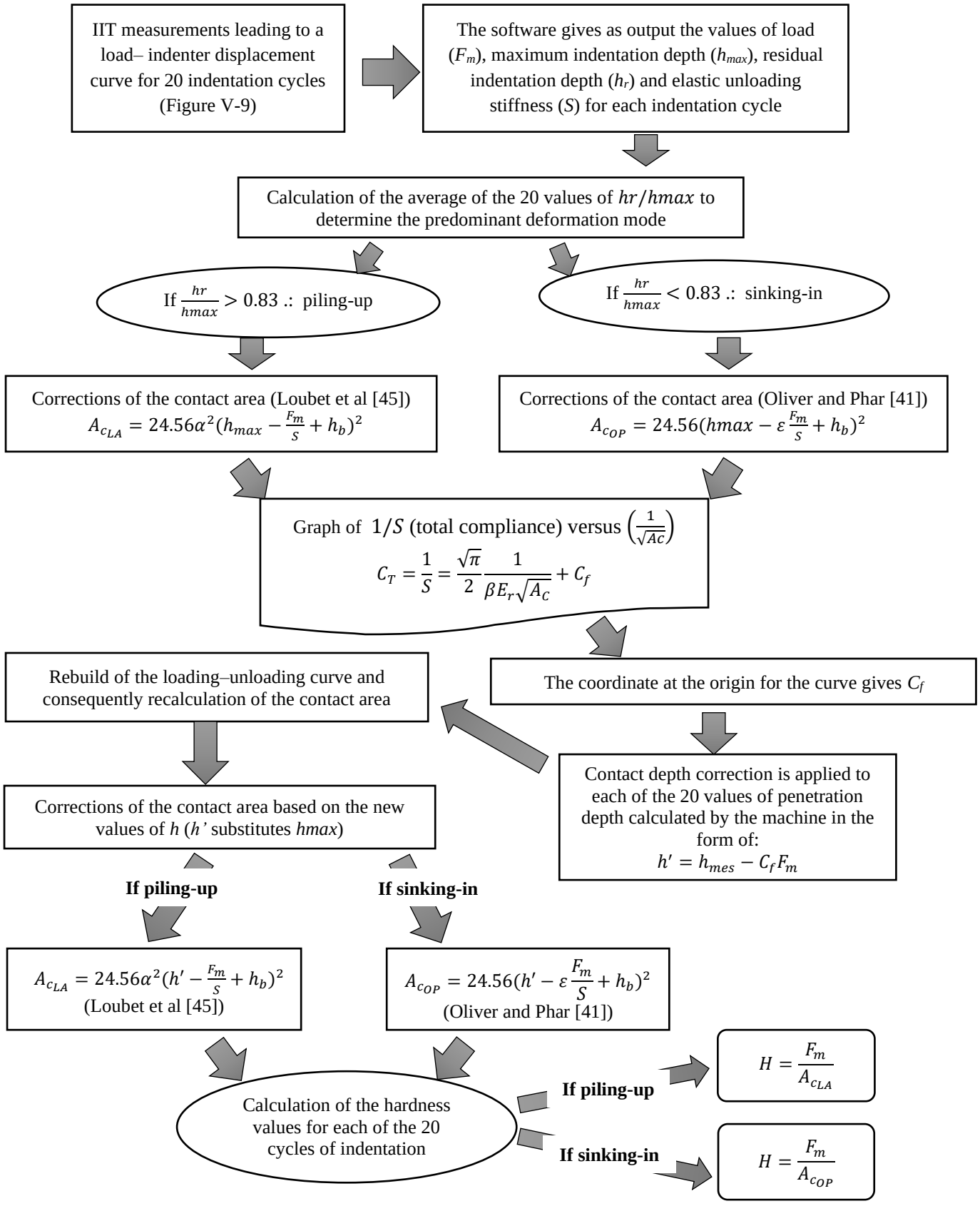

Figure V-11: Flow chart of the indentation analysis methodology.

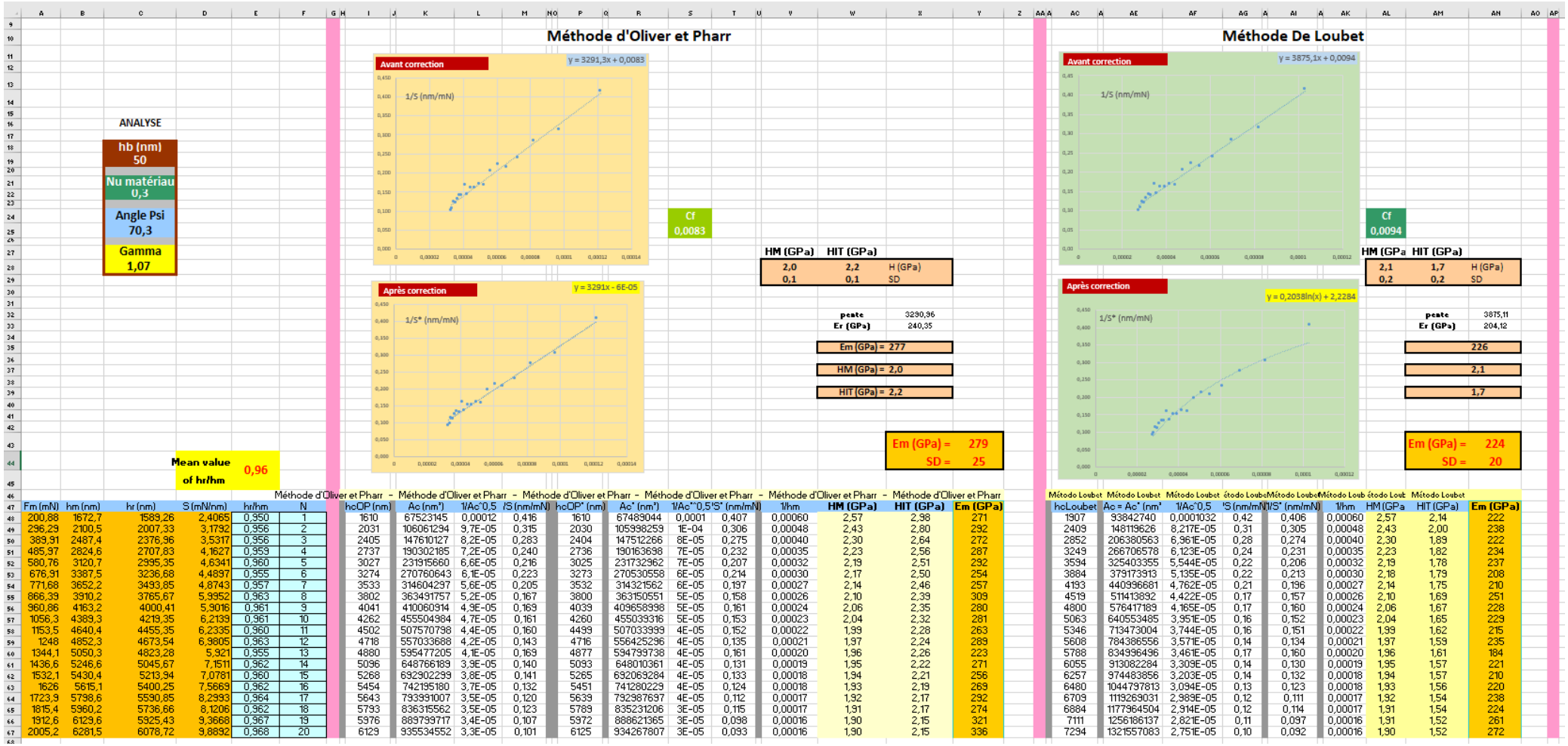

Méthode d'Oliver et Pharr - Méthode d'Oliver et Pharr - Méthode d'Oliver et Pharr - Méthode d'Oliver et Pharr - Méthode d'Oliver et Pharr - Méthode d'Oliver et Pharr

Fm (mN)	hm (nm)	hr (nm)	S (mN/nm)	hr/hm	N	hcOP (nm)	Ac (nm²)	1/Ac^0,5	1/S (nm/mN)	hcOP* (nm)	Ac* (nm²)	1/Ac*^0,5	1/S* (nm/mN)	1/hm	HM (GPa)	HIT (GPa)	Em (GPa)
200,88	1672,7	1589,26	2,4065	0,950	1	1610	67523145	0,00012	0,416	1610	67489044	0,0001	0,407	0,00060	2,57	2,98	271
296,29	2100,5	2007,33	3,1792	0,956	2	2031	106061294	9,7E-05	0,315	2030	105998259	1E-04	0,306	0,00048	2,43	2,80	292
389,91	2487,4	2376,96	3,5317	0,956	3	2405	147610127	8,2E-05	0,283	2404	147512266	8E-05	0,275	0,00040	2,30	2,64	272
485,97	2824,6	2707,83	4,1627	0,959	4	2737	190302185	7,2E-05	0,240	2736	190163698	7E-05	0,232	0,00035	2,23	2,56	287
580,76	3120,7	2995,35	4,6341	0,960	5	3027	231915660	6,6E-05	0,216	3025	231732962	7E-05	0,207	0,00032	2,19	2,51	292
676,91	3387,5	3236,68	4,4897	0,955	6	3274	270760643	6,1E-05	0,223	3273	270530558	6E-05	0,214	0,00030	2,17	2,50	254
771,68	3652,2	3493,85	4,8743	0,957	7	3533	314604297	5,6E-05	0,205	3532	314321562	6E-05	0,197	0,00027	2,14	2,46	257
866,39	3910,2	3765,67	5,9952	0,963	8	3802	363491757	5,2E-05	0,167	3800	363150551	5E-05	0,158	0,00026	2,10	2,39	309
960,86	4163,2	4000,41	5,9016	0,961	9	4041	410060914	4,9E-05	0,169	4039	409658998	5E-05	0,161	0,00024	2,06	2,35	280
1056,3	4389,3	4219,35	6,2139	0,961	10	4262	455504984	4,7E-05	0,161	4260	455039316	5E-05	0,153	0,00023	2,04	2,32	281
1153,5	4640,4	4455,35	6,2335	0,960	11	4502	507570798	4,4E-05	0,160	4499	507033999	4E-05	0,152	0,00022	1,99	2,28	263
1248	4852,3	4673,54	6,9805	0,963	12	4718	557033688	4,2E-05	0,143	4716	556425296	4E-05	0,135	0,00021	1,97	2,24	289
1344,1	5050,3	4823,28	5,921	0,955	13	4880	595477205	4,1E-05	0,169	4877	594739738	4E-05	0,161	0,00020	1,96	2,26	223
1436,6	5246,6	5045,67	7,1511	0,962	14	5096	648766189	3,9E-05	0,140	5093	648010361	4E-05	0,131	0,00019	1,95	2,22	271
1532,1	5430,4	5213,94	7,0781	0,960	15	5268	692902299	3,8E-05	0,141	5265	692063284	4E-05	0,133	0,00018	1,94	2,21	256
1626	5615,1	5400,25	7,5663	0,962	16	5454	742195180	3,7E-05	0,132	5451	741280229	4E-05	0,124	0,00018	1,93	2,19	269
1723,9	5798,6	5580,85	8,2393	0,964	17	5643	793991007	3,5E-05	0,120	5639	792987837	4E-05	0,112	0,00017	1,92	2,17	292
1815,4	5960,2	5736,66	8,1206	0,962	18	5793	836315562	3,5E-05	0,123	5789	835231206	3E-05	0,115	0,00017	1,91	2,17	274
1912,6	6129,6	5925,43	9,3668	0,967	19	5976	889799717	3,4E-05	0,107	5972	888621365	3E-05	0,098	0,00016	1,90	2,15	321
2005,2	6281,5	6078,72	9,8892	0,968	20	6129	935534552	3,3E-05	0,101	6125	934267807	3E-05	0,093	0,00016	1,90	2,15	336

Método Loubet	Método Loubet	Método Loubet	étodo Loubet	Método Loubet	Método Loub	étodo Loub	Método Loubet
hcLoubet	Ac = Ac* (nm²	1/Ac^0,5	'S (nm/mN	1/S* (nm/mN)	1/hm	HM (GPa	HIT (GPa)	Em (GPa)
1907	93842740	0,0001032	0,42	0,406	0,00060	2,57	2,14	222
2409	148119626	8,217E-05	0,31	0,305	0,00048	2,43	2,00	238
2852	206380563	6,961E-05	0,28	0,274	0,00040	2,30	1,89	222
3249	266706578	6,123E-05	0,24	0,231	0,00035	2,23	1,82	234
3594	325403355	5,544E-05	0,22	0,206	0,00032	2,19	1,78	237
3884	379173913	5,135E-05	0,22	0,213	0,00030	2,18	1,79	208
4193	440396681	4,762E-05	0,21	0,196	0,00027	2,14	1,75	210
4519	511413892	4,422E-05	0,17	0,157	0,00026	2,10	1,69	251
4800	576417189	4,165E-05	0,17	0,160	0,00024	2,06	1,67	228
5063	640553485	3,951E-05	0,16	0,152	0,00023	2,04	1,65	229
5346	713473004	3,744E-05	0,16	0,151	0,00022	1,99	1,62	215
5608	784386556	3,571E-05	0,14	0,134	0,00021	1,97	1,59	235
5788	834936496	3,461E-05	0,17	0,160	0,00020	1,96	1,61	184
6055	913082284	3,309E-05	0,14	0,130	0,00019	1,95	1,57	221
6257	974483856	3,203E-05	0,14	0,132	0,00018	1,94	1,57	210
6480	1044797813	3,094E-05	0,13	0,123	0,00018	1,93	1,56	220
6709	1119269031	2,989E-05	0,12	0,111	0,00017	1,92	1,54	238
6884	1177964504	2,914E-05	0,12	0,114	0,00017	1,91	1,54	224
7111	1256186137	2,821E-05	0,11	0,097	0,00016	1,91	1,52	261
7294	1321557083	2,751E-05	0,10	0,092	0,00016	1,90	1,52	272

Figure V-12: Excel Macro developed to execute all the steps of the methodology adopted for the microhardness analysis.

V.3 X-RAY DIFFRACTION TESTS

X-Ray diffraction (XRD) tests were performed using a diffractometer Proto iXRD (portable mode) employing Cr-Kα radiation (wavelength λ of 2.291 Å) generated at 20 kV and 4 mA. The incident beam was collimated by a circular aperture with 2 mm diameter, giving an irradiated area of 3.14 mm^2 at a focal distance of 40 mm. XRD measurements were taken at [211] planes of the ferrite phase (α-Fe), under seven tilt angles β, 0, ±3, ±7 and ±10°,with ± 3° oscillations at each angle. Ten radiation expositions of 2 s each for every tilt angle were conducted. The penetration depth for chromium radiation in ferritic steels is approximately 6μm at β = 0 [121]. Table V-2 summarizes the parameters adopted for XRD measurements.

Table V-2: Parameters of XRD measurements.

Radiation	Voltage/ current	Diffraction plane	Method	Exposition time	Bragg's angle	β
Cr-Kα	20kV/4mA	α-Fe [211]	Multiple expositions (10 expositions)	2s	156.41°	0, ±3, ±7, ±10

Two X-ray detectors intercepted the diffraction cone from the sample and converted X-ray intensities into electronic data. Signals from X-ray detectors were transferred to a data acquisition system controlled by computational software. A Gaussian distribution function was used to fit XRD peaks. Figure V-13 shows the screen display of software results, comprising diffraction peaks, diagrams of lattice spacing d versus sin2β and listing of macro residual stresses and peak widths (integral width and FWHM).

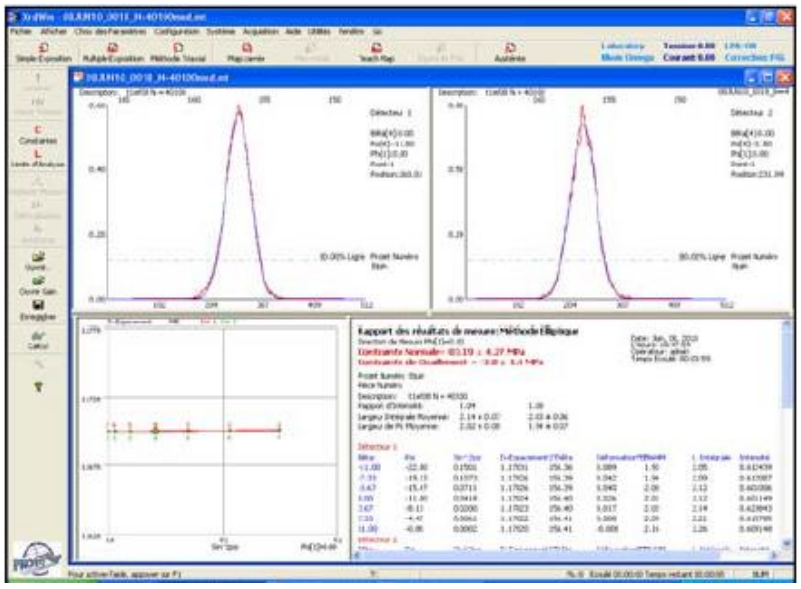

Figure V-13: Screen display of software results.

The experimental setup for the X-ray tests comprises the portable mode of the Proto iXRD diffractometer installed on the same bench as the fatigue machine (the bench is designed to absorb possible vertical movements from the fatigue machine during cycling), to enable real-time testing, i.e., without the need of removing the sample from the fatigue test machine, as can be observed in Figure V-14 and Figure V-15. Fatigue tests were regularly interrupted for XRD measurements up to sample failure. XRD measurements were taken at the center of the sample gage length.

Figure V-14: Experimental setup for X-ray diffraction measurements with the portable mode of the Proto iXRD diffractometer and the fatigue machine.

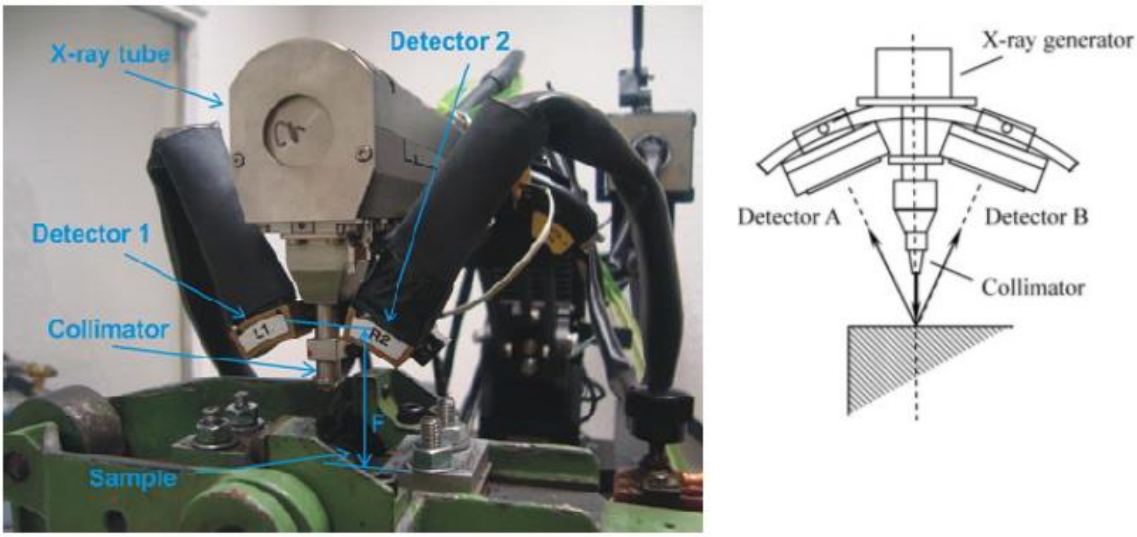

(a) (b)

Figure V-15: (a) Experimental setup for X-Ray diffraction measurements in the sample longitudinal direction (X-Ray detectors L1 and R2), and (b) schematic representation of the X-Ray diffractometer. Adapted from [15].

CHAPTER VI

RESULTS AND DISCUSSION

CHAPTER VI. RESULTS AND DISCUSSION

In this chapter the experimental results are presented and discussed. For all applied stress amplitudes, for both conditions (as-machined and annealed), and for both analyzing methods (instrumented indentation tests and X-Ray diffraction) was possible to observe that the major microstructural changes occurred at the begging, prior to a quarter of the fatigue life of the material. Depending on the material condition, as-machined or annealed, critical periods for microstructural changes are estimated and used to anticipate the number of cycles to failure (N_f) of an API 5L X65 pipeline.

Two series of fatigue bending tests were conducted. For the first one, an alternating stress amplitude (σ_a) of 272 MPa was applied, and for the second one, the value of σ_a was 358 MPa, both applied at the middle of the gauge length of the sample, with stress ratios R around -1 (fully reversed stress). A total of 53 samples were tested, and Basquin equations were updated for the experimental values of number of cycles to failure (N_f) (Equation V-1 and Equation VI-2 for as-machined and annealed conditions, respectively).

$$S_n = 1741N^{-0.1529}$$

Equation VI-1

$$S_n = 12703.3N^{-0.3616}$$

Equation VI-2

The experimental S-N curve is compared with the estimated one in Figure VI-1 and Figure VI-2 for as-machined and annealed conditions, respectively.

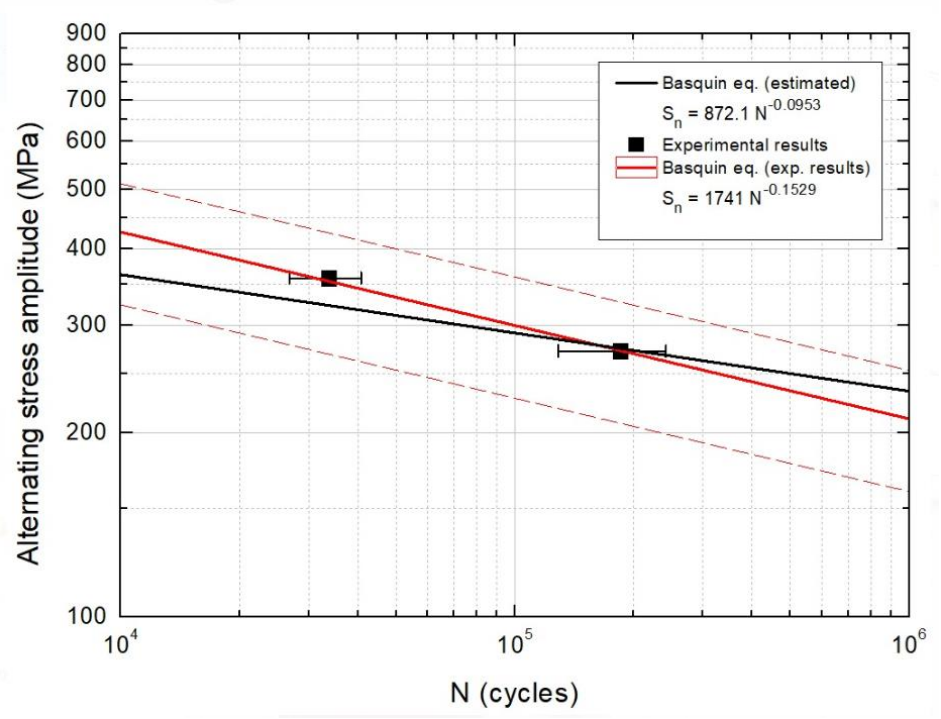

Figure VI-1: Comparison between the estimated (in black) and experimental (in red) Basquin equation for as-machined samples.

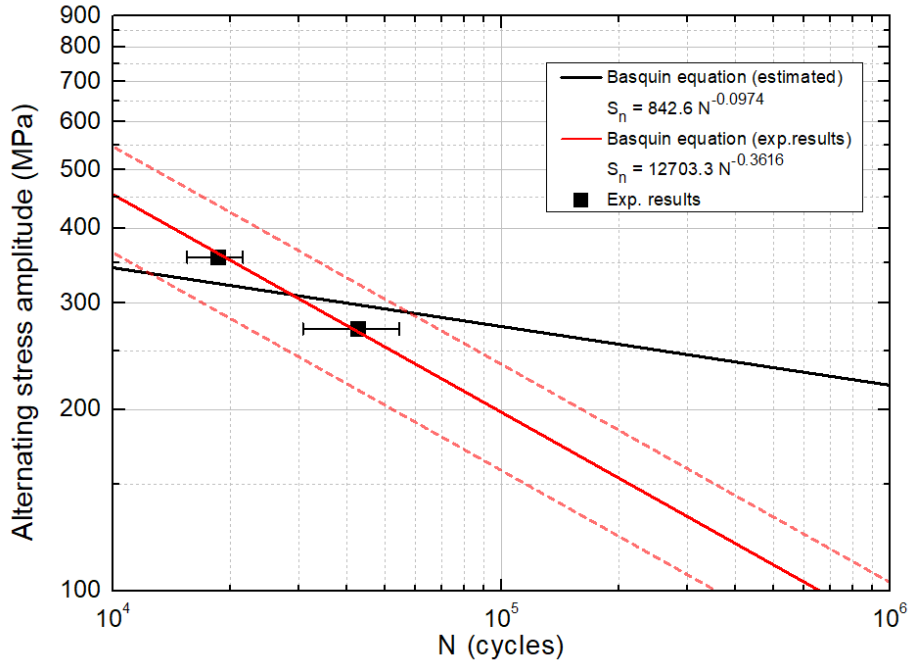

Figure VI-2: Comparison between the estimated (in black) and experimental (in red) Basquin equation for annealed samples.

The microstructural behavior of the X65 API steel samples during fatigue life was analyzed by means of instrumented indentation and X-Ray diffraction tests.

VI.1 INSTRUMENTED INDENTATION RESULTS

For the stress amplitude of 272 MPa, 5 specimens were cycled up to failure, 3 for the as-machined and 2 for the annealed condition, giving mean values of 190350 ± 97227 and 55900 ± 12794 cycles for the fatigue lives, respectively. Other 14 samples were fatigue cycled under the stress amplitude of 272 MPa, in which half were as-machined and half annealed. The as-machined samples T2EF31, T2EF32, T2EF35, T2EF01, T2EF02 and T2EF03 were fatigue cycled up to 5, 10, 15, 25, 50 and 75% of the fatigue life, respectively. Another sample (T2EF36) was fatigue cycled up to 15% to add reliability to the results. The annealed samples T2EF21R, T2EF22R, T2ER33R, T2EF15R, T2EF28R and T2EF16R were fatigue cycled up to 5, 10, 15, 25, 60 and 75% of the fatigue life, respectively. Again, one test was repeated, at 10% of the fatigue life, with the sample T2EF26R.

For the stress amplitude of 358 MPa, 3 as-machined and 2 annealed samples were cycled up to failure, giving fatigue lives of 30900 ± 872 and 19000 ± 848 cycles, respectively. In addition, others 17 samples were tested, in with 10 were as-machined and 7 annealed. The as-machined samples T2EF33, T2EF34, T2EF37, T2EF40, T2EF09, T2EF10 and T2EF11 were fatigue cycled up to 5, 10, 15, 20, 25, 50 and 75% of the fatigue life, respectively. In performing the tests, the authors noticed that the beginning of the fatigue life is the critical period for the variation of the hardness, so the tests for 10, 15 and 25% were repeated using the samples T2EF39, T2EF41 and T2EF38, respectively, to ratify the results. The annealed samples T2EF23R, T2EF24R, T2EF32R, T2EF27R, T2EF20R, and T2EF19R were fatigue cycled up to 5, 10, 15, 20, 25 and 75% of the fatigue life, respectively. The test for 10% of the fatigue life was repeated using the sample T2EF31R.

For the two test series and the two material conditions, a total of 41 specimens were tested. Table VI-1 and Table VI-2 summarize the samples tested for a stress amplitude of 272 and 358 MPa, respectively. After cycling, indentation tests were performed to evaluate hardness changes and fatigue damage accumulation at different stages of fatigue life.

Table VI-1: Samples tested for a stress amplitude of 272 MPa.

Applied stress amplitude = 272 MPa							
As-machined				**Annealed**			
Sample[(a)]	**N_f (%)**	**N (cycles)**	**N_f (mean value)**	**Sample**[(a)]	**N_f (%)**	**N (cycles)**	**N_f (mean value)**
T2EF04	100	121600	190350 ± 97227	T2EF12R	100	51100	55900 ±12794
T2EF05		259100		T2EF13R		70400	
				T2EF14R		46200	
As-machined				**Annealed**			
Sample[(b)]	**N_f (%)**	**Sample**[(b)]	**N_f (%)**	**Sample**[(b)]	**N_f (%)**	**Sample**[(b)]	**N_f (%)**
T2EF01	25	T2EF32	10	T2EF15R	25	T2EF26R	10
T2EF02	50	T2EF35	15	T2EF16R	75	T2EF28R	60
T2EF03	75	T2EF36	15	T2EF21R	5	T2EF33R	15
T2EF31	5			T2EF22R	10		

[(a)]Samples tested up to failure with the aim of calculating N_f value.
[(b)]Samples tested up to specific percentages of the fatigue life.

Table VI-2: Samples tested for a stress amplitude of 358 MPa.

Applied stress amplitude = 358 MPa							
As-machined				**Annealed**			
Sample[(a)]	**Nf (%)**	**N (cycles)**	**N_f (mean value)**	**Sample**[(a)]	**Nf (%)**	**N (cycles)**	**N_f (mean value)**
T2EF06	100	30500	30900 ± 872	T2EF17R	100	19600	19000 ± 848
T2EF07		31900		T2EF18R		18400	
T2EF08		30300					
As-machined				**Annealed**			
Sample[(b)]	**Nf (%)**	**Sample**[(b)]	**Nf (%)**	**Sample**[(b)]	**Nf (%)**	**Sample**[(b)]	**Nf (%)**
T2EF09	25	T2EF37	15	T2EF19R	75	T2EF31R	10
T2EF10	50	T2EF38	25	T2EF20R	25	T2EF32R	15
T2EF11	75	T2EF39	10	T2EF23R	5		
T2EF33	5	T2EF40	20	T2EF24R	10		
T2EF34	10	T2EF41	15	T2EF27R	20		

[(a)]Samples tested up to failure with the aim of calculating N_f value.
[(b)]Samples tested up to specific percentages of the fatigue life.

Finished the indentation test for the percentage of the fatigue life predicted, each sample was cycled to rupture for the calculation of the real value of $N_{f,}$ called *experimental* N_f. The values of 5, 10, 15, 20, 25, 50, and 75% of N_f were calculated based on the reference values of 190350 (as-machined) and 55900 (annealed), for the stress amplitude (σ_a) of 272 MPa, and 30900 (as-machined) and 19000 (annealed) for the stress amplitude (σ_a) of 358

MPa. These percentage values were revised according to the experimental values of N_f obtained for each sample. Table VI-3 compares the predicted percentage of the fatigue life for each sample with the experimental values regarding the applied stress amplitude of 272 and 358 MPa.

Table VI-3: Fatigue cycled samples under 272 and 358 MPa of applied stress amplitudes, values in percentage.

Applied stress amplitude = 272 MPa					
As-machined			**Annealed**		
Sample	**Predicted N_f**	**Experimental N_f**	**Sample**	**Predicted N_f**	**Experimental N_f**
T2EF03	75	94	T2EF16R	75	80
T2EF02	50	40	T2EF28R	60	80
T2EF01	25	37	T2EF15R	25	41
T2EF35	15	22	T2EF33R	15	10
T2EF36	15	15	T2EF22R	10	19
T2EF32	10	7	T2EF26R	10	8
T2EF31	5	4	T2EF21R	5	7

Applied stress amplitude = 358 MPa					
As-machined			**Annealed**		
Sample	**Predicted N_f**	**Experimental N_f**	**Sample**	**Predicted N_f**	**Experimental N_f**
T2EF11	75	64	T2EF19R	75	75
T2EF10	50	46	T2EF20R	25	19
T2EF09	25	24	T2EF27R	20	22
T2EF38	25	32	T2EF32R	15	19
T2EF40	20	23	T2EF24R	10	12
T2EF37	15	20	T2EF31R	10	11
T2EF41	15	11	T2EF23R	5	7
T2EF34	10	11			
T2EF39	10	7			
T2EF33	5	4			

As explained before, two test series of fatigue were conducted, the first one applying 227 MPa, and the second, 358 MPa in middle of the gauge length of the sample. However other regions of the specimen experience different values of alternating stress due to the geometry of the sample. The smaller width in the center of the sample leads to the highest stress amplitude in this region, in which the rupture ends up. Aiming to study the behavior

of the material under different values of alternating stresses, hardness measurements were done in other regions than the middle of the specimen, indicated as lines 4 and 3 in Figure VI-3. Lines positioned away from the sample center undergo lower stress amplitudes, due to width increase, resulting in stress amplitudes of 255 and 171 MPa at lines 4 and 3, respectively, when the applied stress amplitude is 272 MPa. And 335 and 225 MPa at lines 4 and 3, respectively, when the applied stress amplitude is 358 MPa. The calculation of stress amplitudes for each line is described as follows.

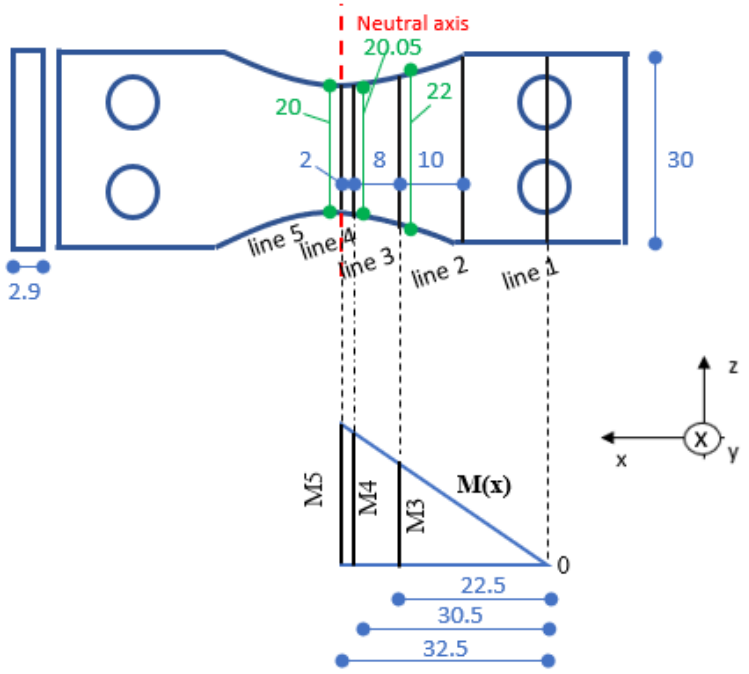

Figure VI-3: Sample geometry.

The stress in line 5 (σ_{a5}) is equal to 358 MPa (or 272 MPa for the second test series), and in line 1 is equal to zero due to a restrained condition produced at the fatigue machine. Indentation results were not interesting in line 2, therefore it was decided not to work in this region. The stress in lines 4 (σ_{a4}) and 3 (σ_{a3}) were calculated by Equation VI-3 to Equation VI-6.

Stress applied in each line is inversely proportional to the moment of inertia (Equation VI-3).

$$\sigma_a = \frac{My}{I}$$

Equation VI-3

where *M* is linear moment and *I* is moment of inertia, which is defined in Equation VI-4.

$$I = \frac{bh^3}{12}$$

Equation VI-4

where *h* is thickness and *b*, width of the sample.

Replacing $y = \frac{h}{2}$ (y_{max}) in Equation VI-3, Equation VI-5 can be obtained:

$$\sigma_a = M\frac{h}{2}\frac{12}{bh^3} = \frac{6M}{bh^2}$$

Equation VI-5

For $\sigma_{a5} = 358\ MPa$, the value of moment in line 5 is calculated using Equation VI-5 as follows.

$$M5 = 358\ x\ 20\ x\ 2.9^2 x\ \frac{1}{6} = 10035.93\ Nmm$$

As the moment is linear, M4 can be calculated through similarity of triangles (Figure VI-3).

$$\frac{M5}{32.5} = \frac{M4}{30.5}$$

Equation VI-6

$$\frac{10035.93}{32.5} = \frac{M4}{30.5} \therefore M4 = 9418.33\ Nmm$$

With the aid of Equation VI-5 and knowing that *b* for line 4 is equal 20.5mm (Figure VI-3), the value of the stress in line 4 can be calculated as:

$$\sigma_{a4} = \frac{6M}{bh^3} = \frac{6\ x\ 9418.33}{20.5\ x\ 2{,}9^2} = 335\ MPa$$

Alternating stress for line 3 is calculated using the same methodology.

Figure VI-4 illustrates the distribution of alternating stress amplitudes calculated for the two test series.

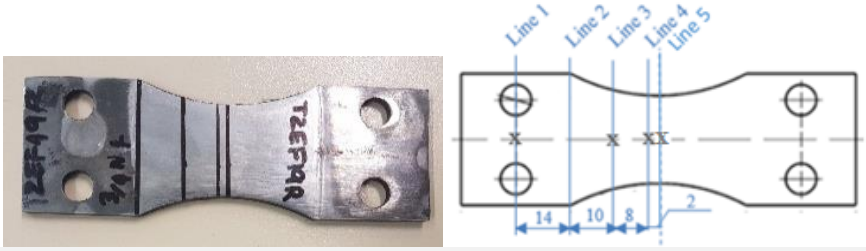

Test series 1	**Test series 2**
σ_{a5} =272 MPa	**σ_{a5} =358 MPa**
(prescribed at Line 5)	**(prescribed at Line 5)**
σ_{a4} = 255 MPa (Line 4)	σ_{a4} = 335 MPa (Line 4)
σ_{a3} = 171 MPa (Line 3)	σ_{a3} = 225 MPa (Line 3)
$\sigma_{a2} = \sigma_{a1}$ = 0 (Lines 1 and 2)	$\sigma_{a2} = \sigma_{a1}$ = 0 (Lines 1 and 2)

Figure VI-4: Distribution of alternating stress amplitudes in the sample.

As explained before, due to the specimen positioning in the fatigue machine, a restrained condition is produced at line 1 (Figure VI-4), i.e. no cyclic loading is applied at this region. Thus, the hardness calculation in line 1 is taken as the reference hardness value (H_0) for the sample. The hardness variations before and after fatigue cycling were evaluated based on the difference between hardness values of lines 3, 4 and 5 (H_3, H_4 and H_5, respectively) with respect to line 1 (H_0). Figure VI-5 and Figure VI-6 show the evolution of the hardness values in relation to the fatigue life of the material for the as-machined and annealed samples, respectively. As it can be noticed, the graphs show the results for the two test series, with values of alternating stresses ranging from 171 to 358 MPa.

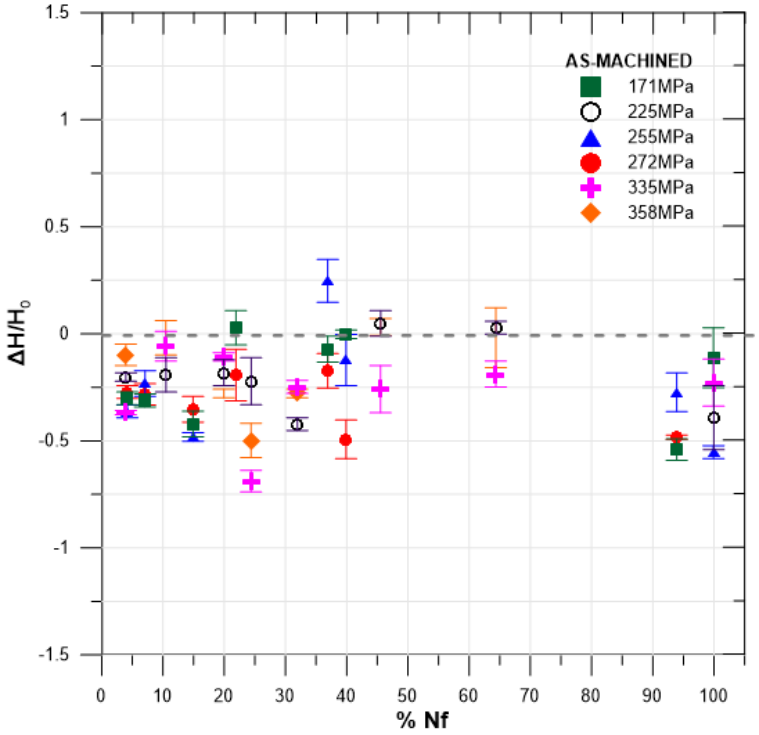

Figure VI-5: Variation of hardness during fatigue life for as-machined X-65 steel samples.

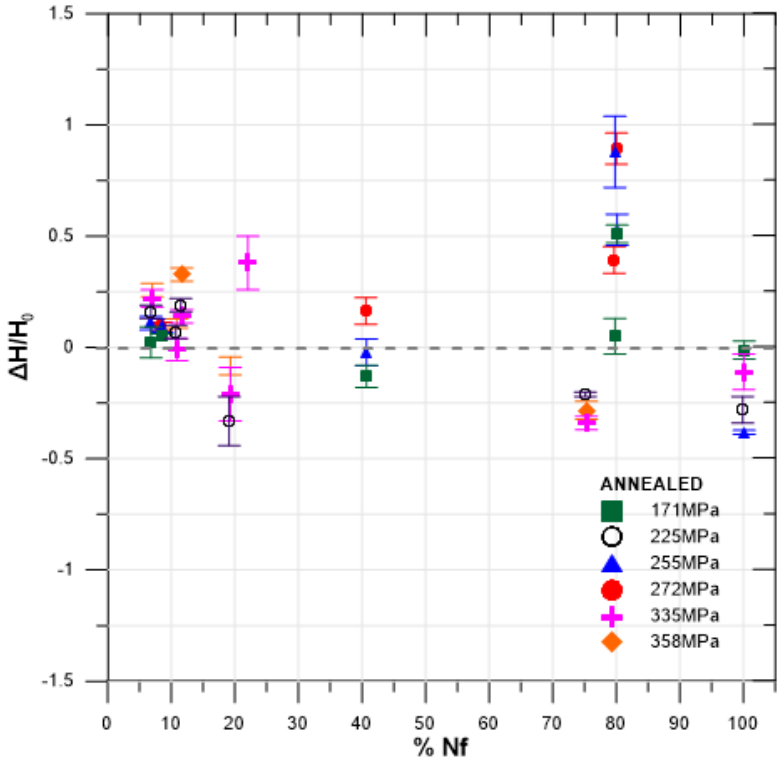

Figure VI-6: Variation of hardness during fatigue life for annealed X-65 steel samples.

It is important to note that, as explained in Chapter IV, item IV-3, is expected that after annealing, with increase of grain size, the material presents lower values of strength properties and hardness. Results for Young Modulus (*E*), Yield Strength (*YS*) and Ultimate Tensile Strength (*UTS*) is shown in Table IV-1 and a decrease in these properties for annealed material is observed when compared with the as-machined material. For hardness, the values of H_0 (hardness calculated in a non-cycled specimen) for both conditions and for all test samples were compared in Table VI-4. H_0 for each sample is an average of the microhardness values obtained in the 20 cycles of indentation done at each point, as explained in Chapter V, item V-2. It can be noted that for annealed condition, the values are considerably lower. However, what is observed in Figure VI-5 and Figure VI-6 is an interesting phenomenon, that even with lower initial values of hardness, this property presents an increase with cycling for annealed condition, while the as-machined material experienced decrease in hardness values with cycling.

Table VI-5 shows the average and standard deviation of H_0 values for as-machined and annealed samples.

Table VI-4: Comparison of initial hardness values for as-machined and annealed samples.

	As-machined		Annealed	
	Sample	**H_0 (GPa)**	**Sample**	**H_0 (GPa)**
272 MPa	T2EF01	1.91	T2EF12R	1.17
	T2EF02	2.05	T2EF13R	1.04
	T2EF03	2.31	T2EF14R	1.05
	T2EF04	2.02	T2EF15R	1.22
	T2EF05	2.86	T2EF16R	0.86
	T2EF31	3.06	T2EF21R	1.10
	T2EF32	2.74	T2EF22R	1.14
	T2EF35	2.68	T2EF26R	1.14
	T2EF36	2.50	T2EF28R	0.95
			T2EF33R	1.37
358 MPa	T2EF06	2.00	T2EF17R	1.02
	T2EF07	3.04	T2EF18R	1.38
	T2EF08	2.05	T2EF19R	1.16
	T2EF09	2.37	T2EF20R	1.22
	T2EF10	1.69	T2EF23R	1.05
	T2EF11	1.93	T2EF24R	1.07
	T2EF33	2.77	T2EF27R	0.96
	T2EF34	2.49	T2EF31R	1.49
	T2EF37	2.85	T2EF32R	1.22
	T2EF38	3.02		
	T2EF39	2.96		
	T2EF40	2.39		
	T2EF41	2.85		

Table VI-5: Mean values and standard deviation of H_0 for as-machined and annealed samples.

	Mean value (GPa)
As-machined	2.48± 0.43
Annealed	1.13± 0.15

For the as-machined samples the decrease in hardness can be associated with the movement and multiplication of dislocations and rearrangement of the initial dislocation network. A part of the initial dislocation network is produced during the pipe manufacturing process by cold working. Another part may come from the sample preparation (machining, grinding and polishing), which is also likely to induce some level of residual stresses. At the early stages of fatigue, it is expected microstructural changes related to the movement and reorganization of dislocations, leading to a reduction of microdeformations and consequently, a softening behavior of the material.

For the annealed samples, the increase in hardness can be associated with the process of microcracks initiation and propagation. It is believed that the multiplication of dislocations and microdeformations leads to material hardening. After the annealing process, the structure of the material is relaxed and free of residual stresses, so the stage of rearrangement of the initial dislocation network is not relevant, and the material does not present the initial stage of softening as observed for as-machined samples.

Surface effects are of particular importance for the fatigue phenomenon, since in most cases the surface is the preferred site for nucleation of microcracks due to easier slip movements and higher strain amplitudes at the surface. According to Ye and Wang [49], a great deal of experimental evidence has proved that fatigue damage in the stages prior to nucleation of microcracks is primarily related to the occurrence and development of localized plastic-strain concentration at or near the surface of materials during cycling. Aiming to study the influence of depth in hardness results, hardness values versus depth of penetration curves were plotted for each sample. Examples for some samples are shown in Figure VI-7 to Figure VI-10.

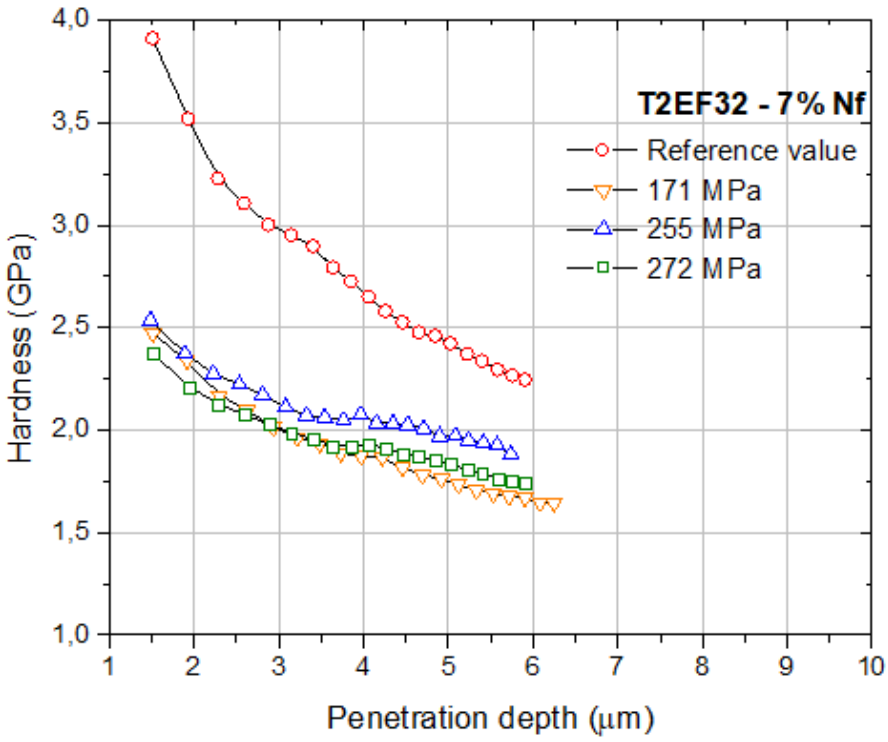

Figure VI-7: Hardness versus depth of penetration curves for the as-machined sample T2EF32, cycled until 7% of the fatigue life.

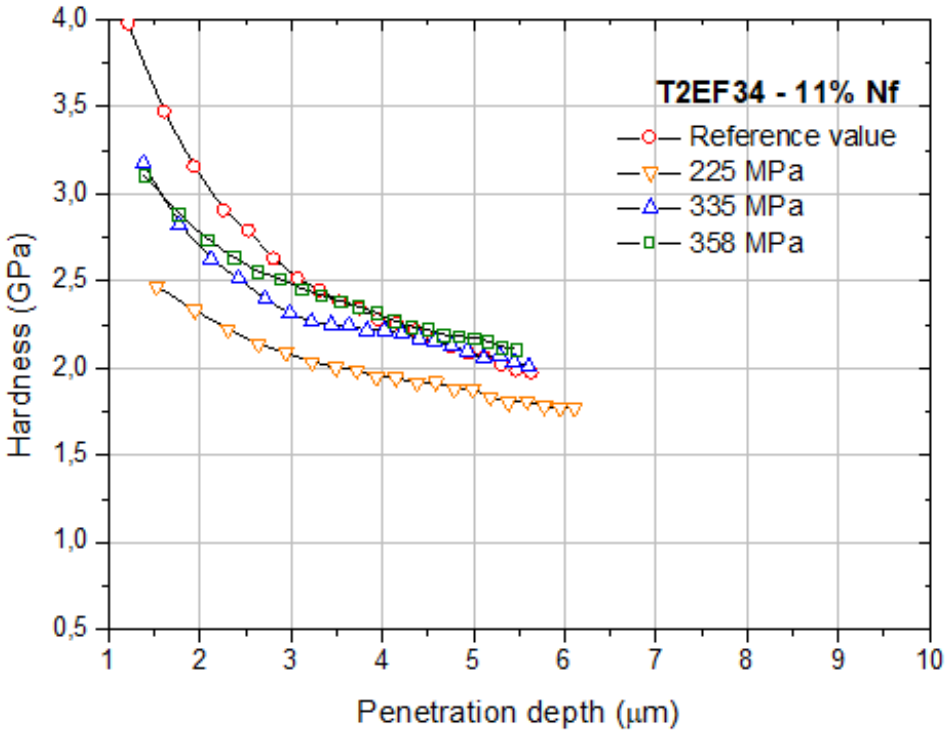

Figure VI-8: Hardness versus depth of penetration curves for the as-machined sample T2EF34, cycled until 11% of the fatigue life.

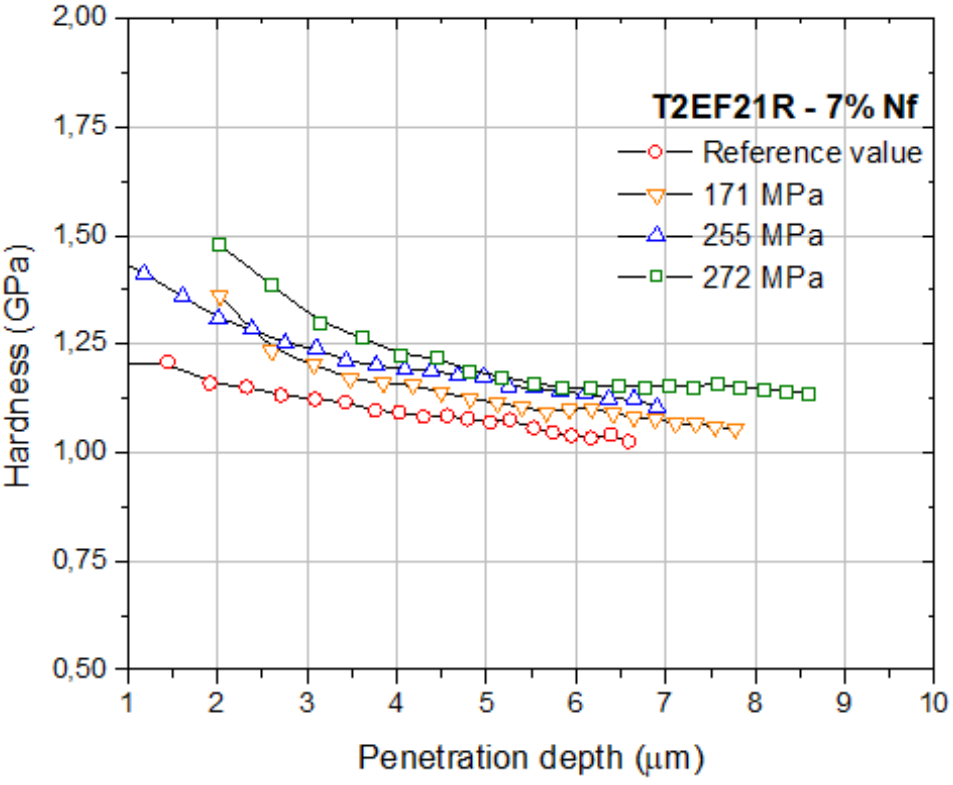

Figure VI-9: Hardness versus depth of penetration curves for the as-machined sample T2EF21R, cycled until 7% of the fatigue life.

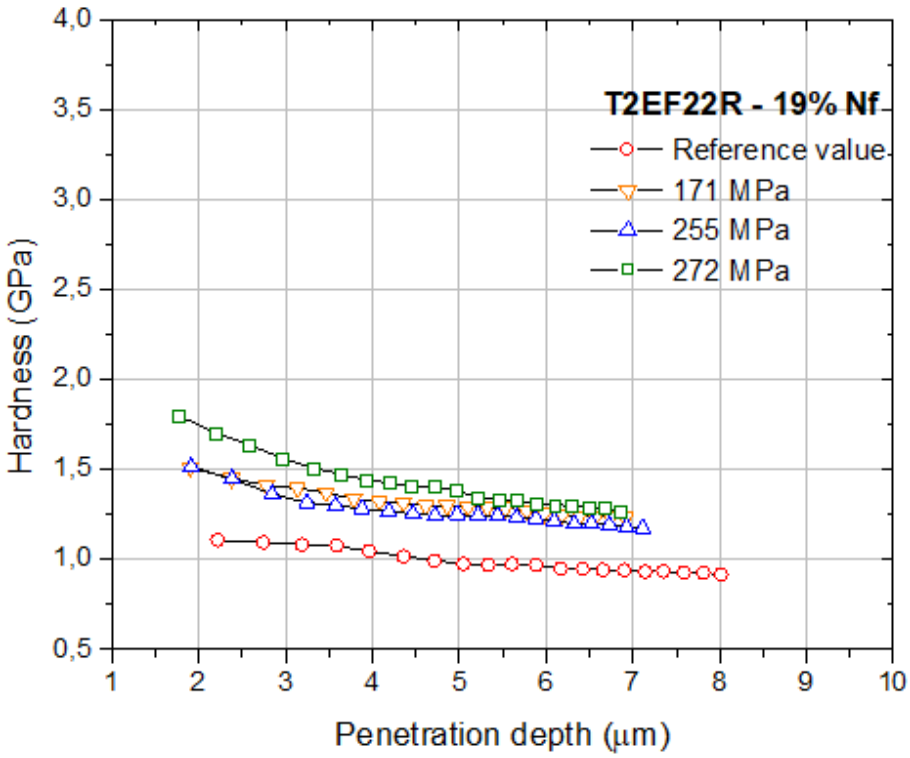

Figure VI-10: Hardness versus depth of penetration curves for the as-machined sample T2EF22R, cycled until 19% of the fatigue life.

It can be noticed that hardness values experienced a noticed variation (decrease) at the surface of the sample (up to 2 or 3 µm) with tendency of stabilization of results as the depth increases. Comparing the curves for as-machined (Figure VI-7(a) and Figure VI-7(b)) and annealed samples (Figure VI-7(c) and Figure VI-7(d)) it can be observed that the variations in hardness values are more representative for as-machined samples, as expected. Nevertheless, even in annealed samples, the variations are more pronounced at the surface of the samples, the amplitude of hardness variation is bigger in 2 or 3µm of penetration depth.

For better comprehension of fatigue as a surface phenomenon, the results of all test coupons were summarized in graphs for different penetration depths (Figure VI-11 to Figure VI-13 for as-machined samples, and in Figure VI-14 to Figure VI-16 for annealed samples). Here, the values of hardness variations in relation to the reference value H_0 during the fatigue life of the material were plotted for all the samples tested, for stress amplitudes from 171 to 358MPa, in graphs for 2, 4 and 6 µm of penetration depth.

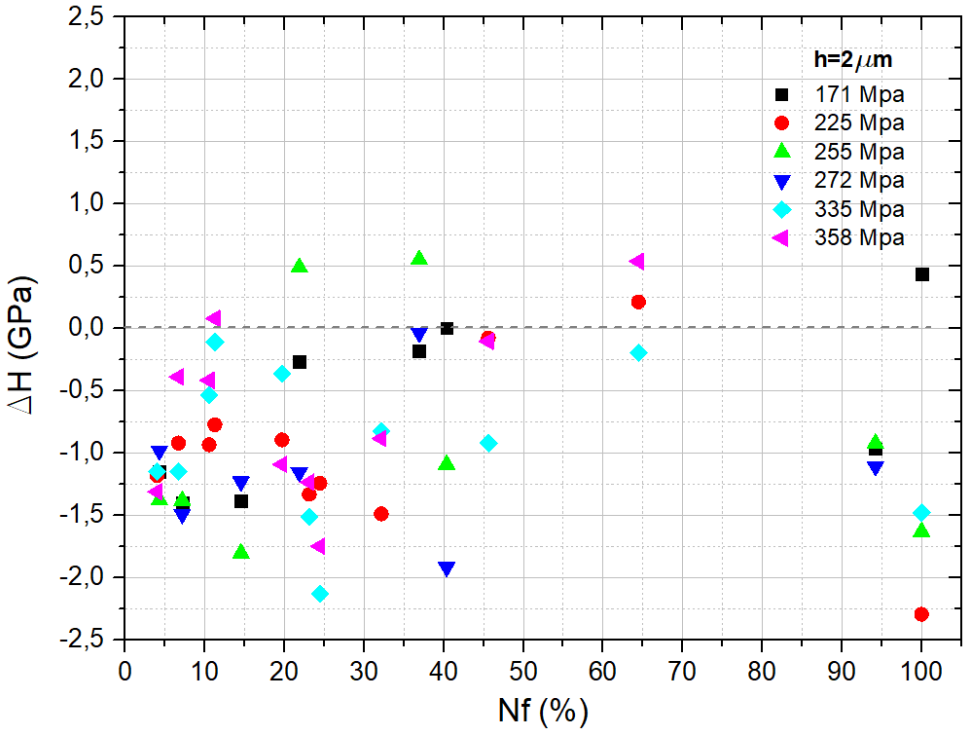

Figure VI-11: Variation of hardness during fatigue life for all stress amplitudes studied at a penetration depth of 2µm from surface for as-machined samples.

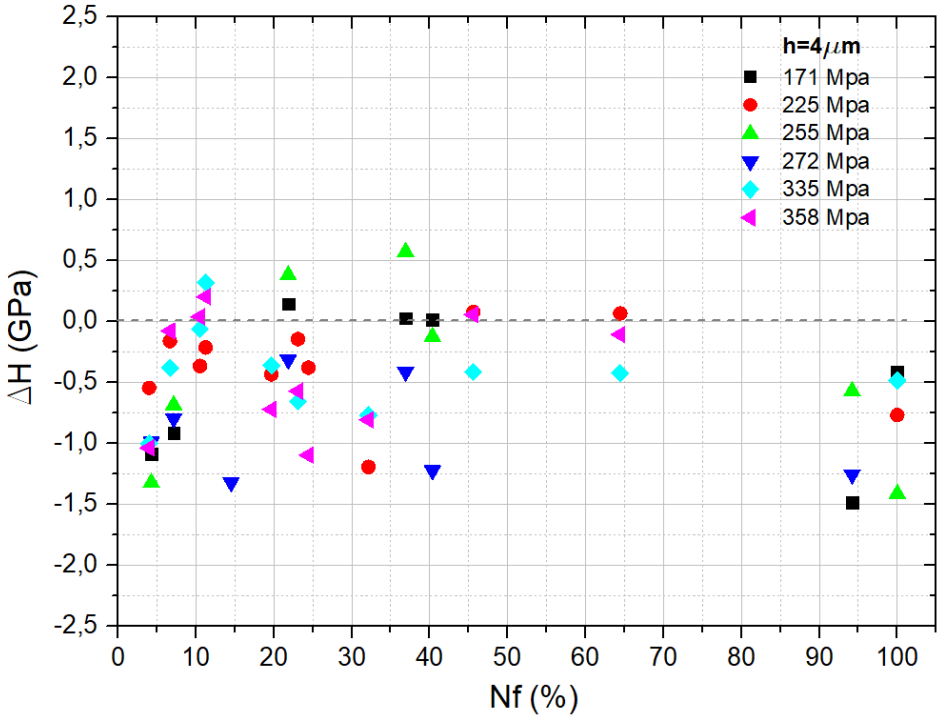

Figure VI-12: Variation of hardness during fatigue life for all stress amplitudes studied at a penetration depth of 4µm from surface for as-machined samples.

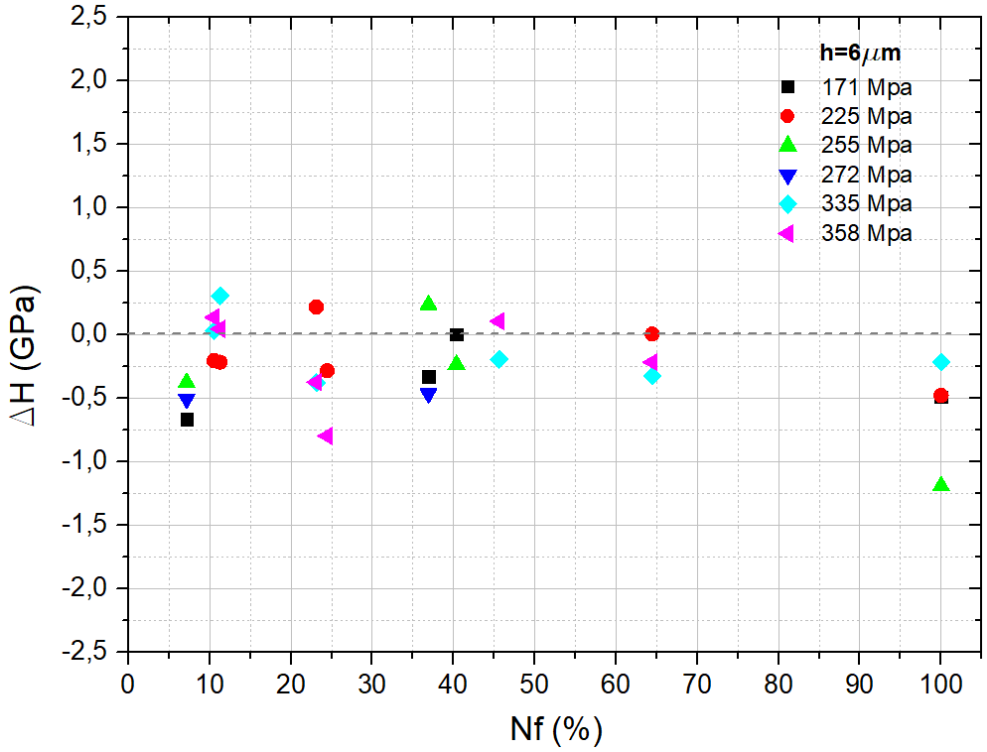

Figure VI-13: Variation of hardness during fatigue life for all stress amplitudes studied at a penetration depth of 6µm from surface for as-machined samples.

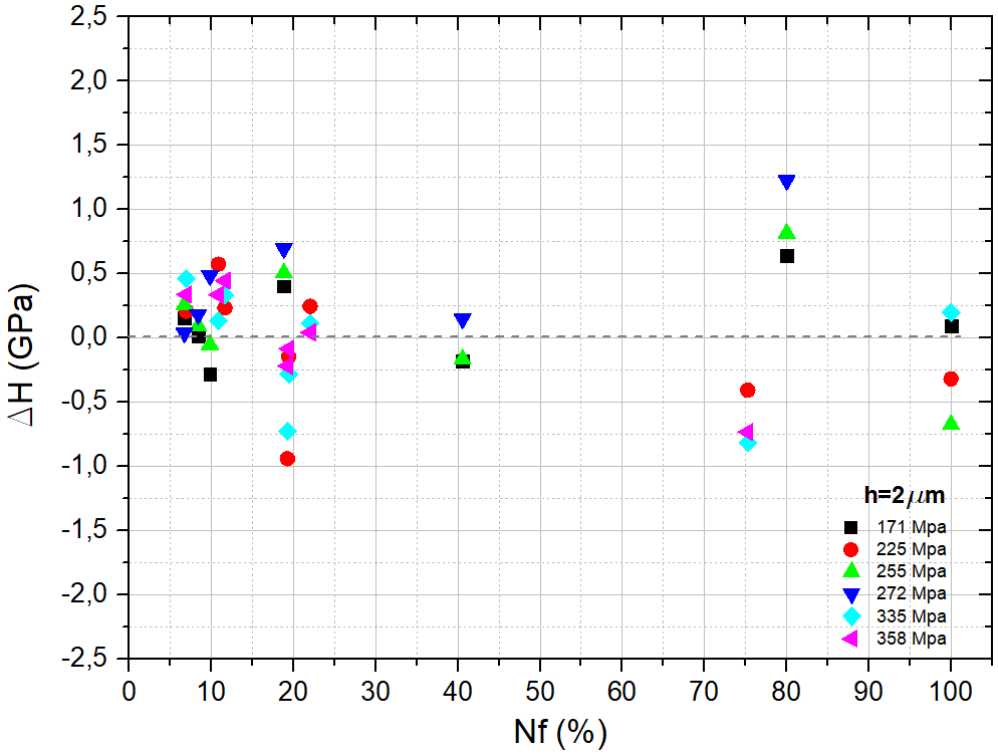

Figure VI-14: Variation of hardness during fatigue life for all stress amplitudes studied at a penetration depth of 2µm from surface for annealed samples.

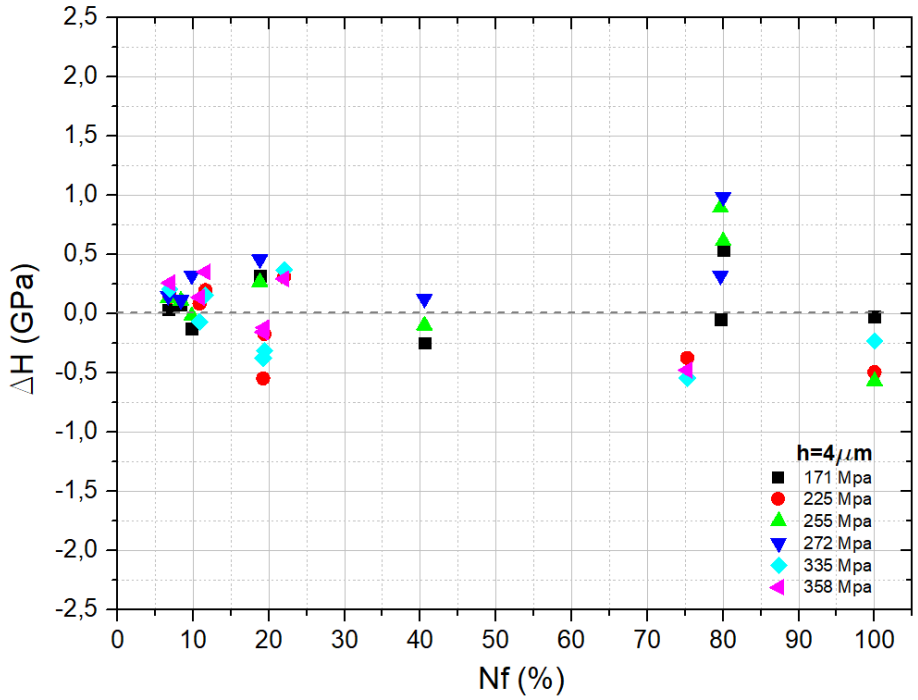

Figure VI-15: Variation of hardness during fatigue life for all stress amplitudes studied at a penetration depth of 4µm from surface for annealed samples.

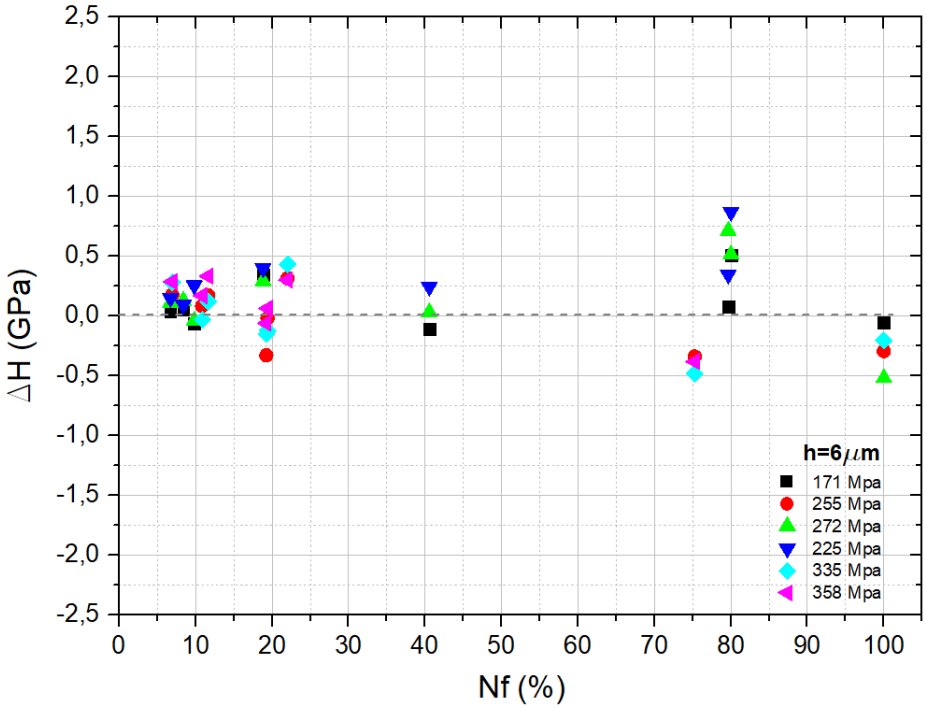

Figure VI-16: Variation of hardness during fatigue life for all stress amplitudes studied at a penetration depth of 6µm from surface for annealed samples.

Three important results are ratified observing Figure VI-11 to Figure VI-16: most important variations in hardness values occur at the beginning of the fatigue life of the material, with a decrease experienced by as-machined samples and increase experienced by annealed ones; variations in hardness values are more representative for as-machined

samples than for annealed; and the variations are more pronounced at the surface of the samples. Either for as-machined and annealed samples, it can be noticed a bigger dispersion in the hardness results for the penetration depth of 2µm (Figure VI-11 and Figure VI-14), followed by a dispersion still perceived for 4µm (Figure VI-12 and Figure VI-15) but not as pronounced as for 2µm, and a not expressive distribution of results for 6µm (Figure VI-13 and Figure VI-16). Therefore, it was decided to work with the hardness values measured at the depth of 2µm. All the graphs and analyses shown hereafter use the data for 2µm of indentation depth.

For each alternating stress level, two second order polynomials in the form of $y=ax^2+bx+c$ were fitted, one for the as-machined and one for the annealed results. Polynomials resulted of this procedure for stress levels from 171 to 358 MPa are shown in Figure VI-17 to Figure VI-22. In order to determine the fatigue life ratio in which the most important changes in the hardness values occur, the inflection point of the curve (minimum or maximum x value) was determined by equalizing the first derivative of the polynomial to zero. Table VI-6 summarizes the inflection points obtained for as-machined samples (minimum) and annealed samples (maximum). Finally, an average value of 22 and 7% of the fatigue life was obtained for the as-machined and annealed samples, respectively (Table VI-7).

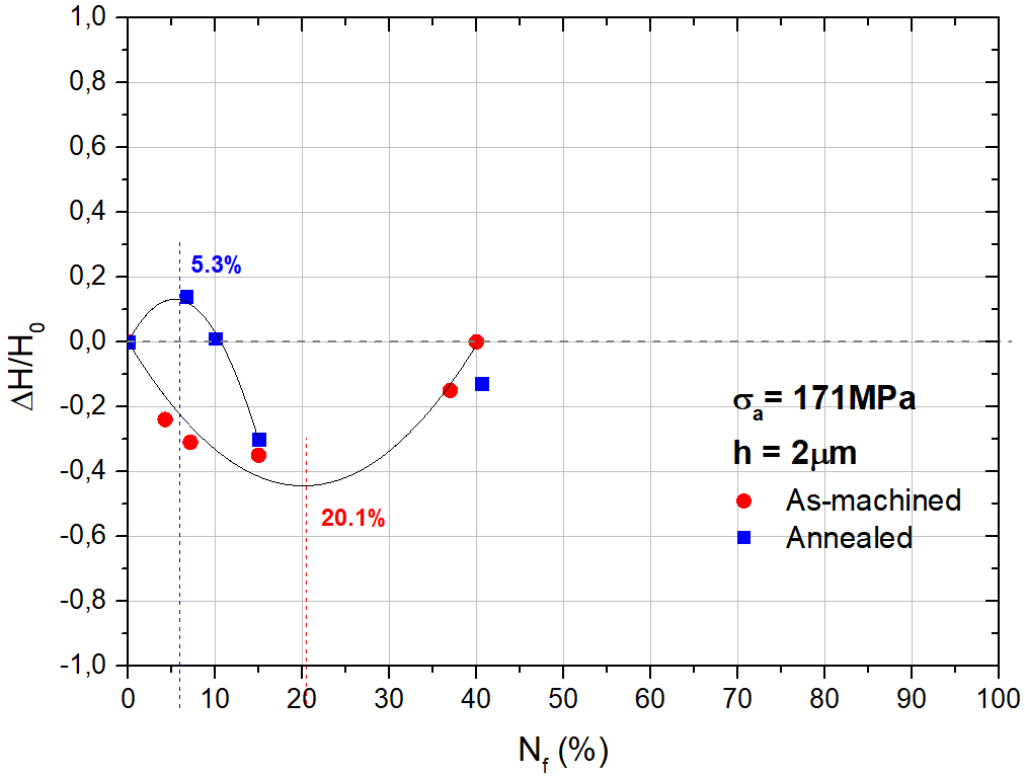

Figure VI-17: Microhardness changes during fatigue life at 2µm for σ = 171 MPa.

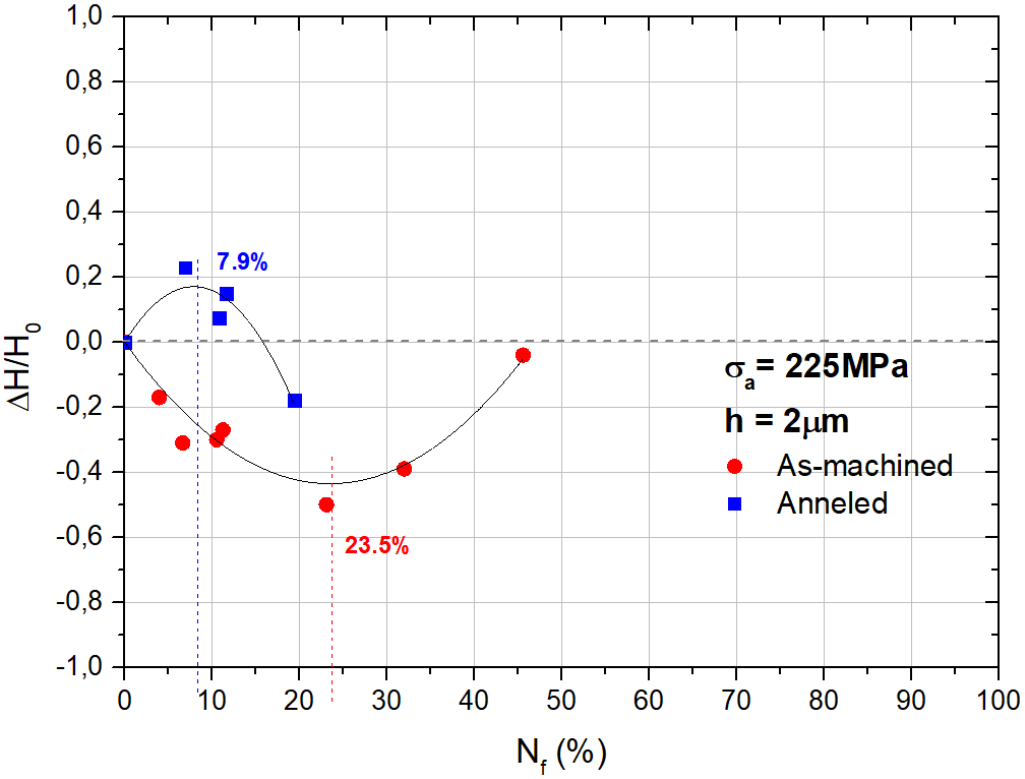

Figure VI-18: Microhardness changes during fatigue life at 2µm for σ = 225 MPa.

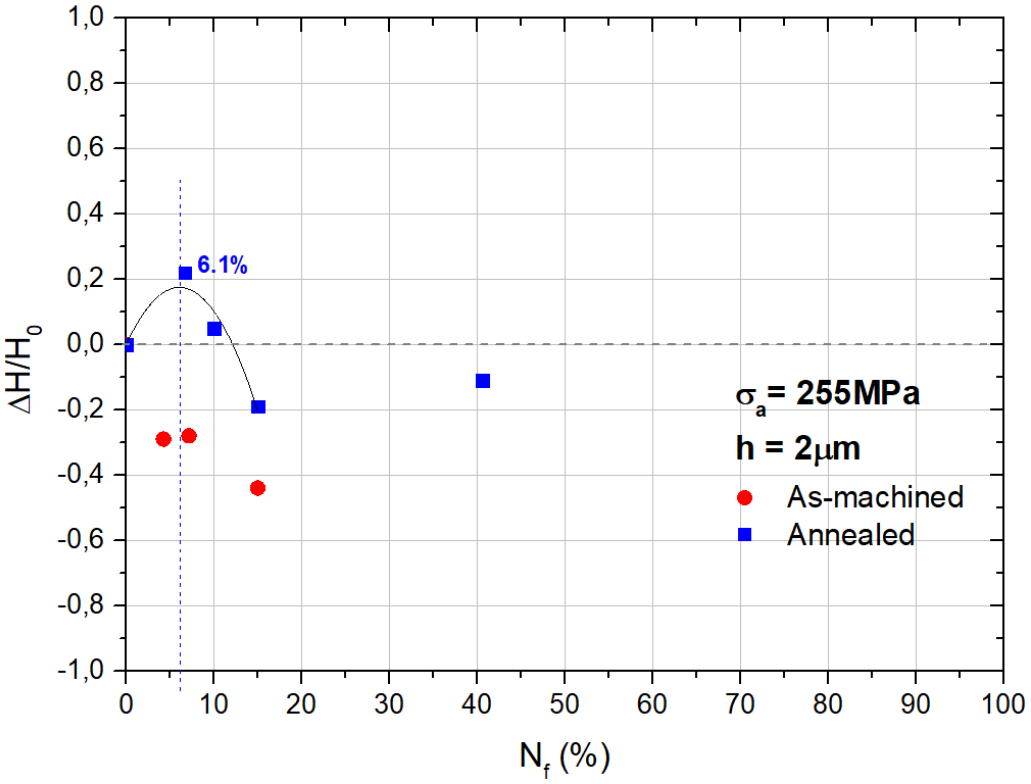

Figure VI-19:Microhardness changes during fatigue life at 2µm for σ = 255 MPa.

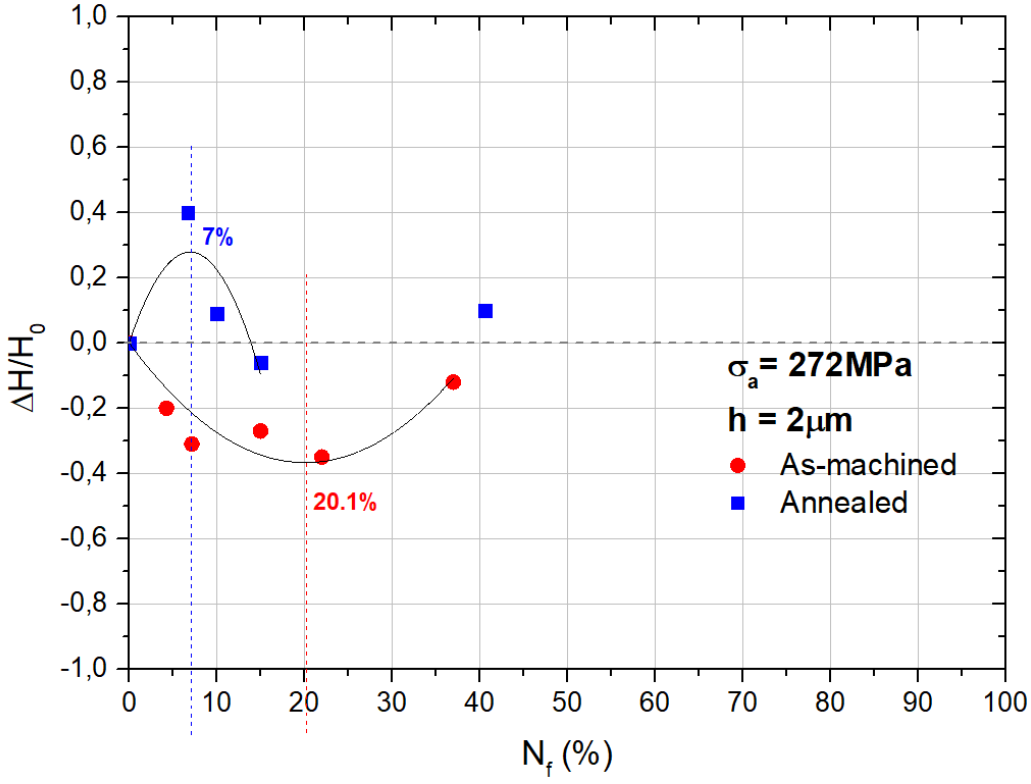

Figure VI-20: Microhardness changes during fatigue life at 2µm for σ = 272 MPa.

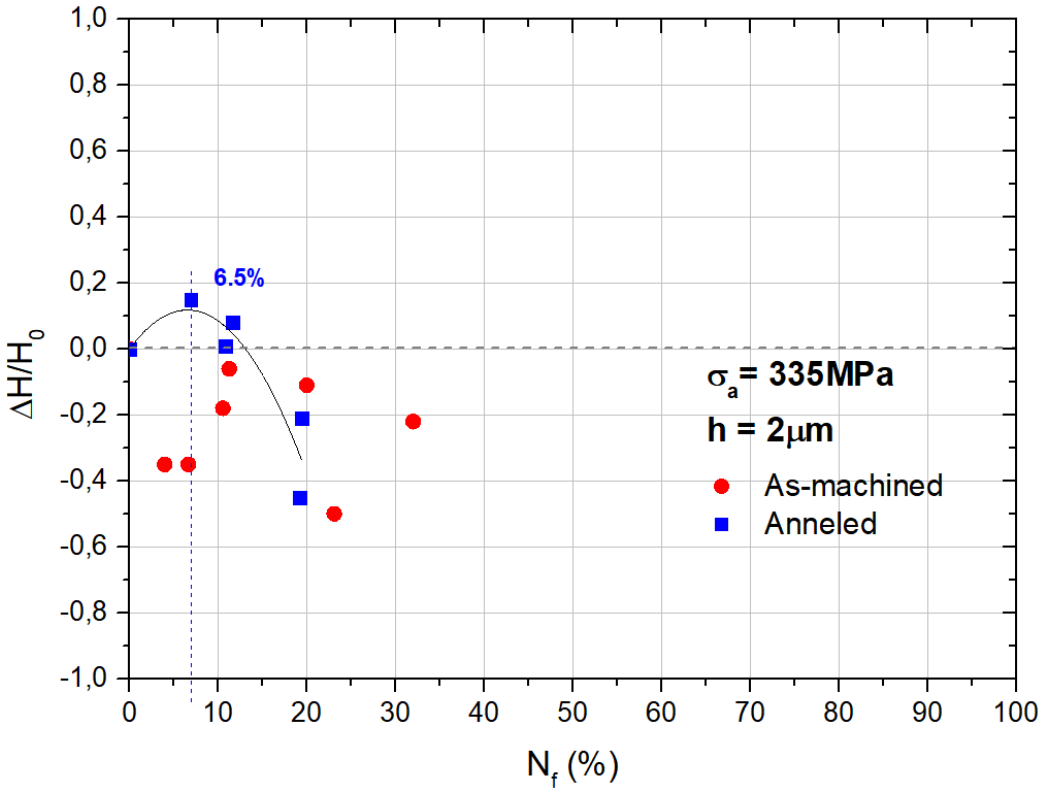

Figure VI-21: Microhardness changes during fatigue life at 2µm for σ = 335 MPa.

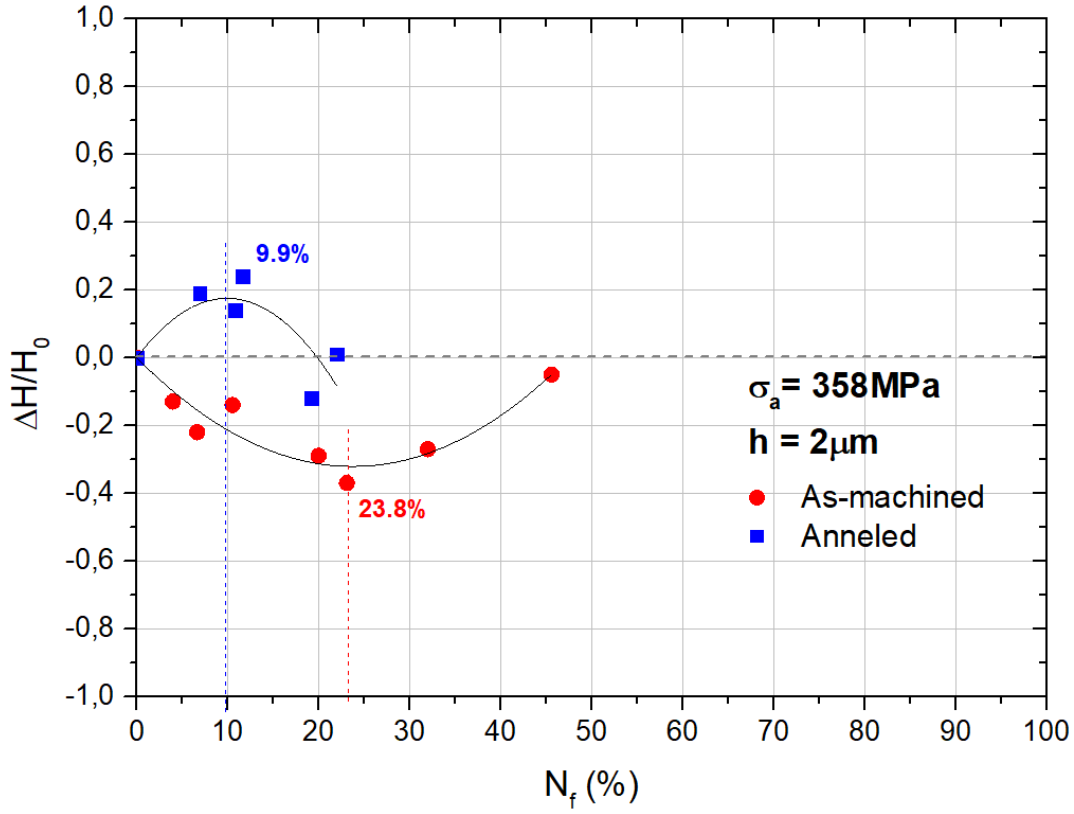

Figure VI-22: Microhardness changes during fatigue life at 2µm for σ = 358 MPa.

Table VI-6: Minimum/maximum x value measured at 2000 nm as a function of the stress amplitude between 171 and 358 MPa.

Stress amplitude (σ in MPa)	As-machined (%)	Annealed (%)
171	20.1	5.3
225	23.5	7.9
255	---*	6.1
272	20.1	7.0
335	---*	6.5
358	23.8	9.9

*There were not sufficient results to adjust a polynomial for this alternating stress value.

Table VI-7: Average and standard deviation calculated for minimum/maximum x values measured at 2000 nm as a function of the stress amplitude between 171 and 358 MPa.

	Mean value (%)
As-machined	21.9± 2.1
Annealed	7.1± 1.6

To determine the number of cycles in which the most important changes in the hardness values occur, the results for variation of microhardness *vs* number of cycles were plotted and two second order polynomials in the form of $y=ax^2+bx+c$ were fitted. Polynomials resulted of this procedure for stress levels from 171 to 358 MPa are shown in Figure VI-23 to Figure VI-28.

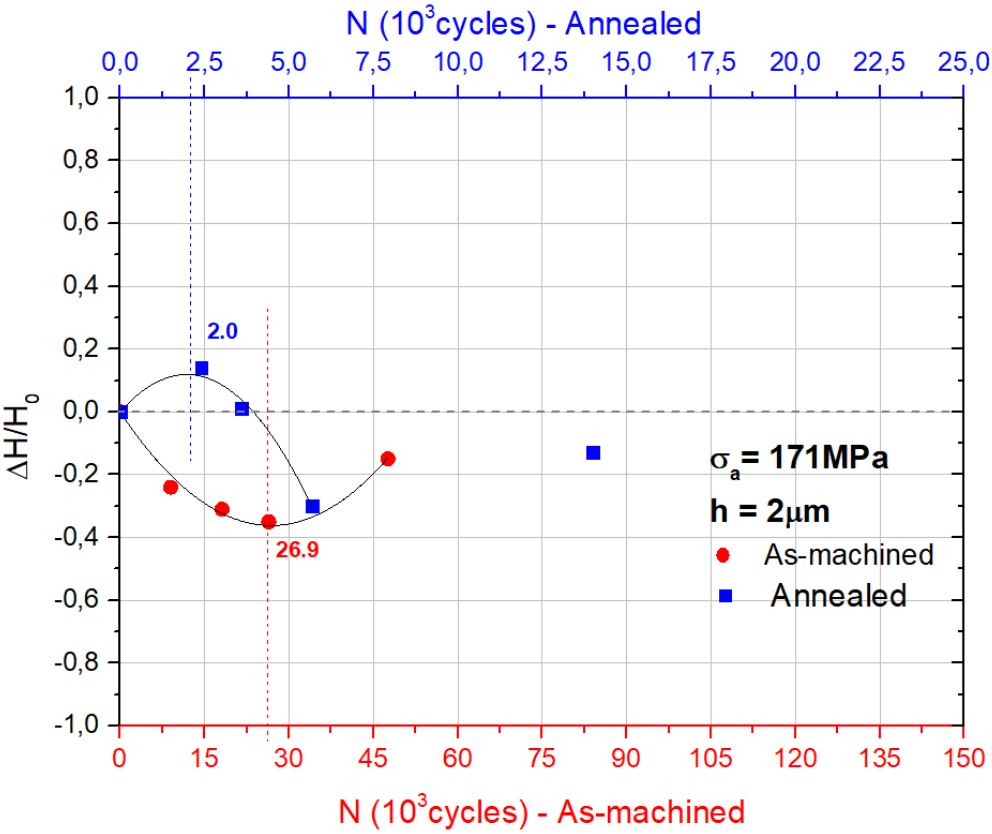

Figure VI-23: Microhardness changes during fatigue life at 2µm for σ = 171 MPa.

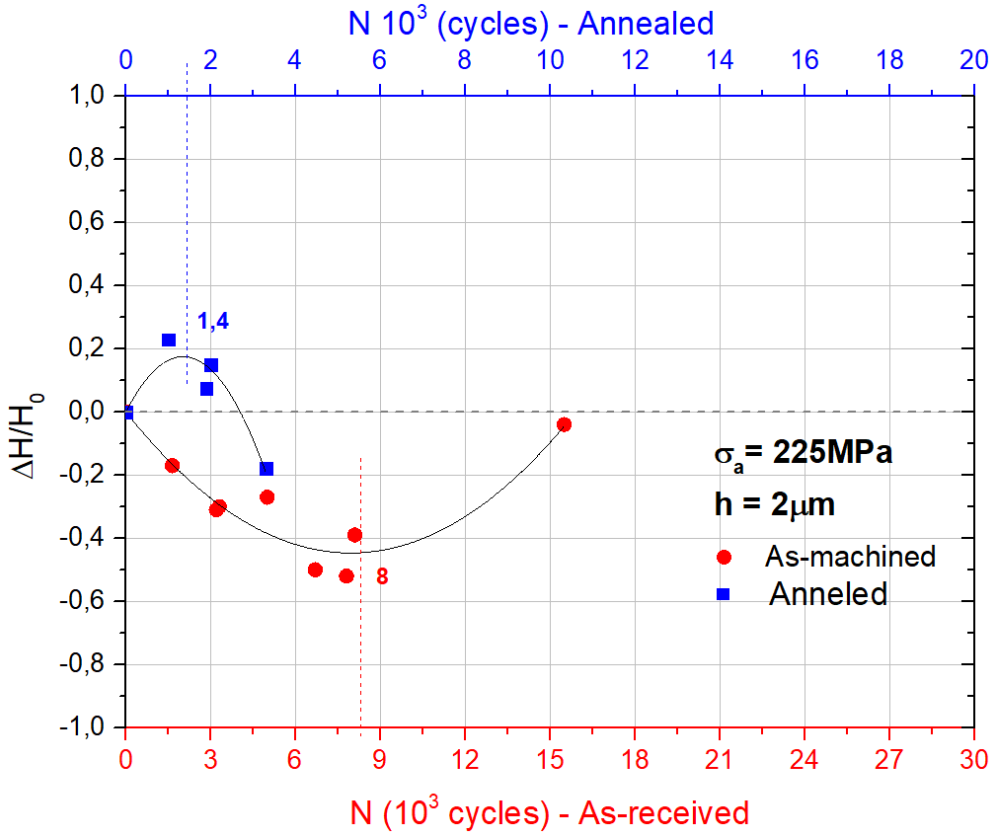

Figure VI-24: Microhardness changes during fatigue life at 2µm for σ = 225 MPa.

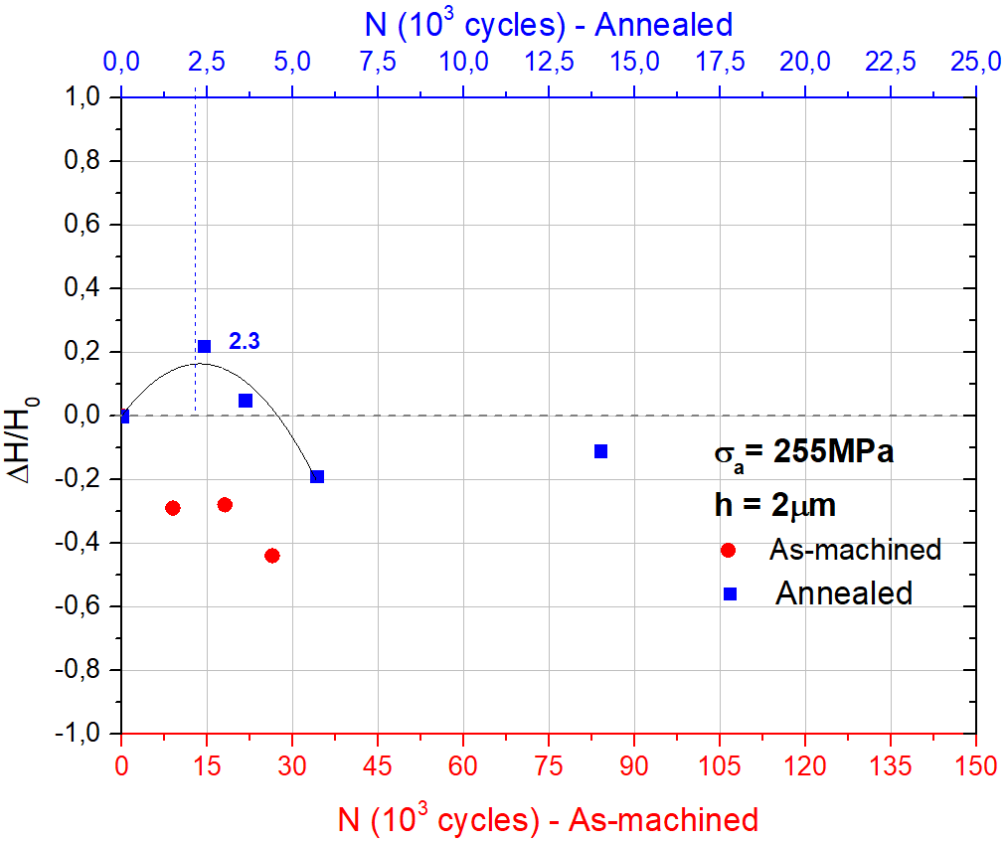

Figure VI-25: Microhardness changes during fatigue life at 2µm for σ = 255 MPa.

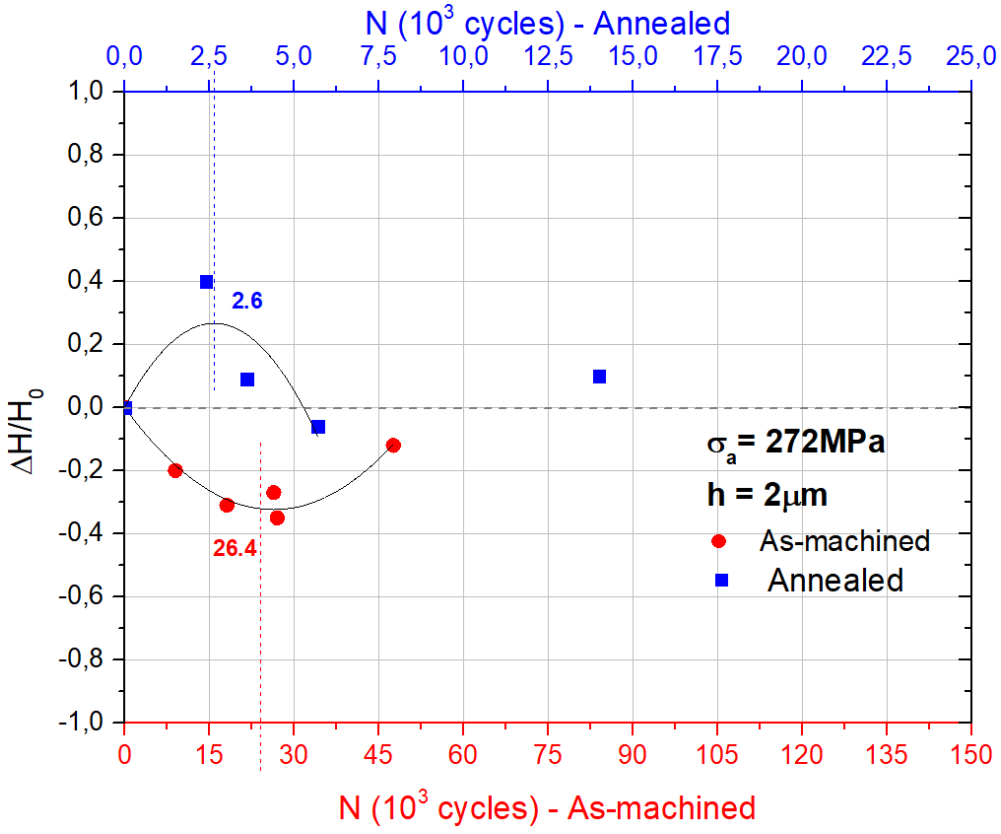

Figure VI-26: Microhardness changes during fatigue life at 2µm for σ = 272 MPa.

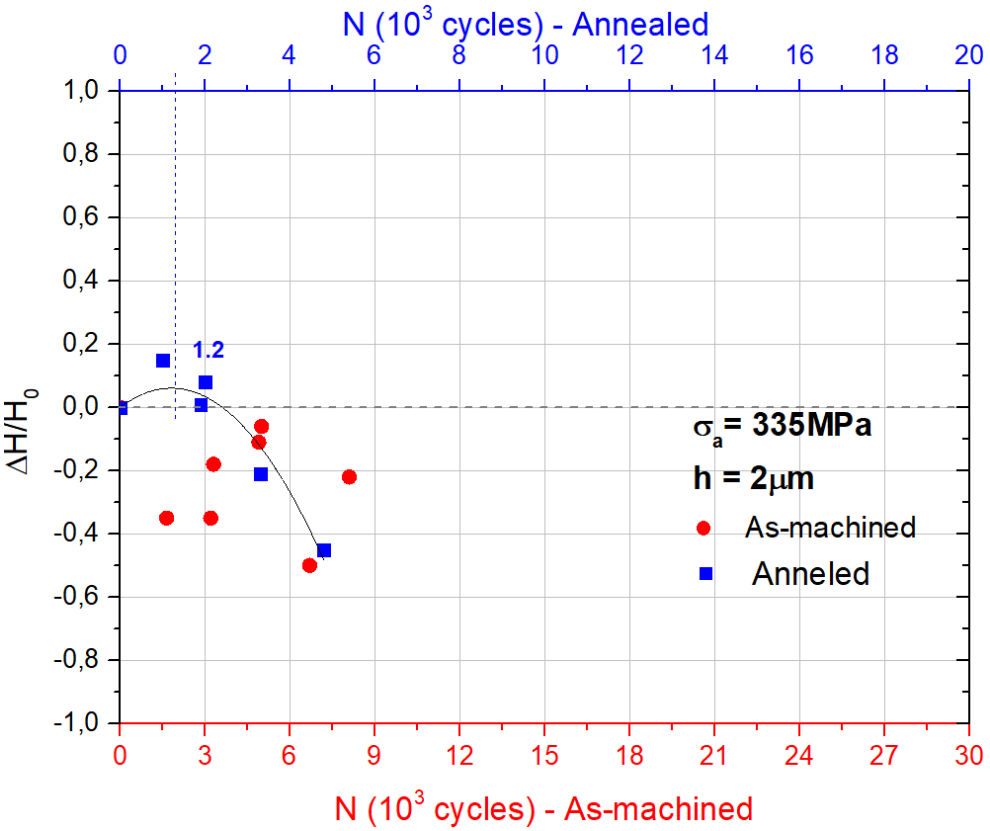

Figure VI-27: Microhardness changes during fatigue life at 2µm for σ = 335 MPa.

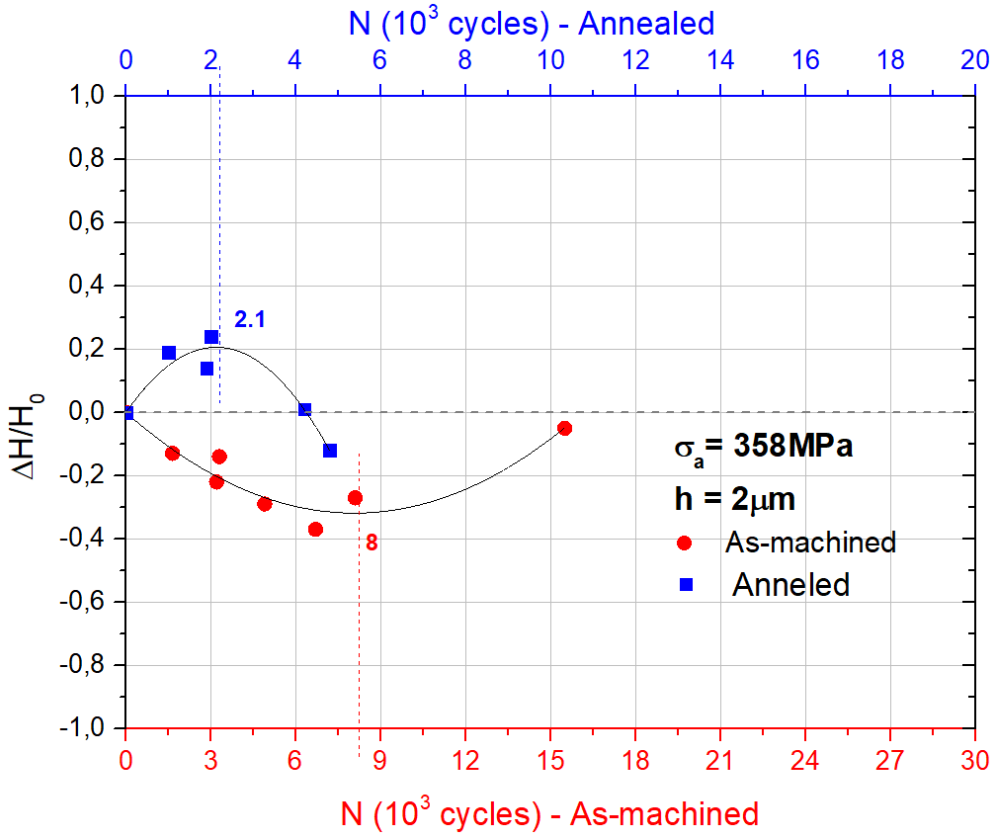

Figure VI-28: Microhardness changes during fatigue life at 2µm for σ = 358 MPa.

As done before for the porcentage of the fatigue life, here, the inflection point of the curve (minimum or maximum x value) was determined by equalizing the first derivative of the polynomial to zero. Table VI-8 summarizes the inflection points obtained for as-machined samples (minimum) and annealed samples (maximum).

Table VI-8: Minimum/maximum x value measured at 2µm as a function of the stress amplitude between 171 and 358 MPa.

Stress amplitude (σ in MPa)	As-machined (Nb of cycles)	Annealed (Nb of cycles)
171	26.9×10^3	2.0×10^3
225	8.0×10^3	1.4×10^3
255	---*	2.3×10^3
272	26.4×10^3	2.6×10^3
335	---*	1.2×10^3
358	8.0×10^3	2.1×10^3

*There were not sufficient results to adjust a polynomial for this alternating stress value.

Each value of number of cycles (N) obtained for the six levels of alternative stress studied (171 to 358 MPa), was equated to the average percentage of the fatigue life ($\%N_f$) showed in Table VI-6, i.e. 21.9% for the as-machined, and 7.1% for the annealed samples, in order to determine the total life in fatigue of the material. For example, for 171 MPa of stress, the value of the inflection point shown in Table VI-8 is 26900, so if 21.9% of fatigue life corresponds to 26900 cycles, this means that the material fails after 122830 cycles (complete fatigue life). According to this procedure, by means of the polynomial fit method, the number of cycles up to fatigue failure (*Nf*) of the samples can be determined for the different levels of stress amplitudes produced and for both material conditions, namely as-machined and annealed.

As previously stated, after the indentation tests, each sample was cycled up to rupture aiming to calculate the value of experimental N_f. The experimental values are compared to the values obtained by the method of adjustment of polynomials in Table VI-9 and Table VI-10, and shown graphically in Figure VI-29 and Figure VI-30, for as-machined and annealed samples, respectively. It can be observed that the values of N_f obtained using adjustment of polynomials approach those of experimental N_f for each stress level (except for the stress level of 358 MPa for annealed samples). Therefore, the values of 21.9% and 7.1%, rounded for 22 and 7% of the fatigue life, for as-machined and annealed samples, respectively, obtained with the polynomial adjustment, can be validated as a critical value of fatigue life fraction, when occur the main microstructural changes, represented by an inflection of microhardness variations.

Table VI-9: Comparison between the values of experimental N_f and the values obtained by the method of adjustment of polynomials for as-machined samples.

Stress (MPa)	N_f Nb. of cycles up to rupture	Samples										
		T2EF01	**T2EF02**	**T2EF03**	**T2EF04**	**T2EF31**	**T2EF32**	**T2EF35**	**T2EF36**			
171	**Experimental**	129000	236100	151800	121600	210800	252800	123500	181800			
	Polynomial Model	122830										
255	**Experimental**	129000	236100	151800	121600	210800	252800	123500	181800			
	Polynomial Model	----*										
272	**Experimental**	129000	236100	151800	121600	210800	252800	123500	181800			
	Polynomial Model	120550										
		T2EF08	**T2EF09**	**T2EF10**	**T2EF11**	**T2EF33**	**T2EF34**	**T2EF37**	**T2EF38**	**T2EF39**	**T2EF40**	**T2EF41**
225	**Experimental**	30100	31900	34000	36000	41150	31300	24900	25200	48000	29000	44400
	Polynomial Model	36530										
335	**Experimental**	30100	31900	34000	36000	41150	31300	24900	25200	48000	29000	44400
	Polynomial Model	----*										
358	**Experimental**	30100	31900	34000	36000	41150	31300	24900	25200	48000	29000	44400
	Polynomial Model	36530										

*There were not sufficient results to adjust a polynomial for this alternating stress value.

Table VI-10: Comparison between the values of experimental N_f and the values obtained by the method of adjustment of polynomials for annealed samples.

Stress (MPa)	N_f Nb. of cycles up to rupture	Samples							
		T2EF15R	**T2EF16R**	**T2EF17R**	**T2EF21R**	**T2EF22R**	**T2EF26R**	**T2EF28R**	**T2EF33R**
171	**Experimental**	34500	52600	55900	35800	25000	42900	36000	58000
	Polynomial Model	28170							
255	**Experimental**	34500	52600	55900	35800	25000	42900	36000	58000
	Polynomial Model	32390							
272	**Experimental**	34500	52600	55900	35800	25000	42900	36000	58000
	Polynomial Model	36620							
		T2EF18R	**T2EF19R**	**T2EF20R**	**T2EF23R**	**T2EF24R**	**T2EF27R**	**T2EF31R**	**T2EF32R**
225	**Experimental**	19000	19000	24950	14400	17200	19100	17500	17000
	Polynomial Model	19720							
335	**Experimental**	19000	19000	24950	14400	17200	19100	17500	17000
	Polynomial Model	16900							
358	**Experimental**	19000	19000	24950	14400	17200	19100	17500	17000
	Polynomial Model	29580							

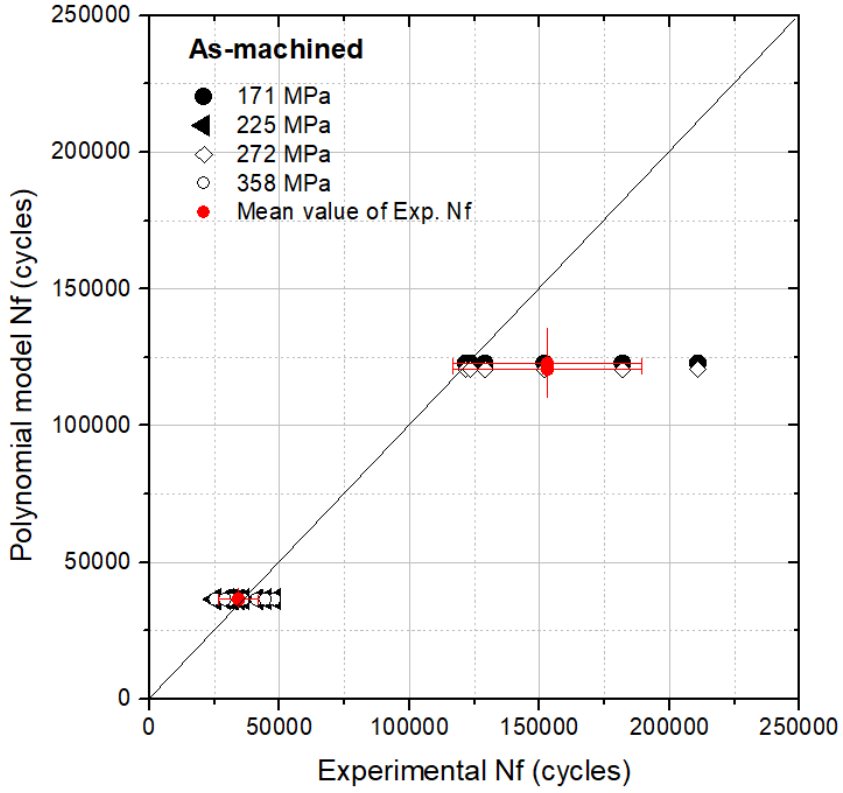

Figure VI-29: Graphic comparison between the values of experimental N_f and the values obtained by adjustment of polynomials for as-machined samples.

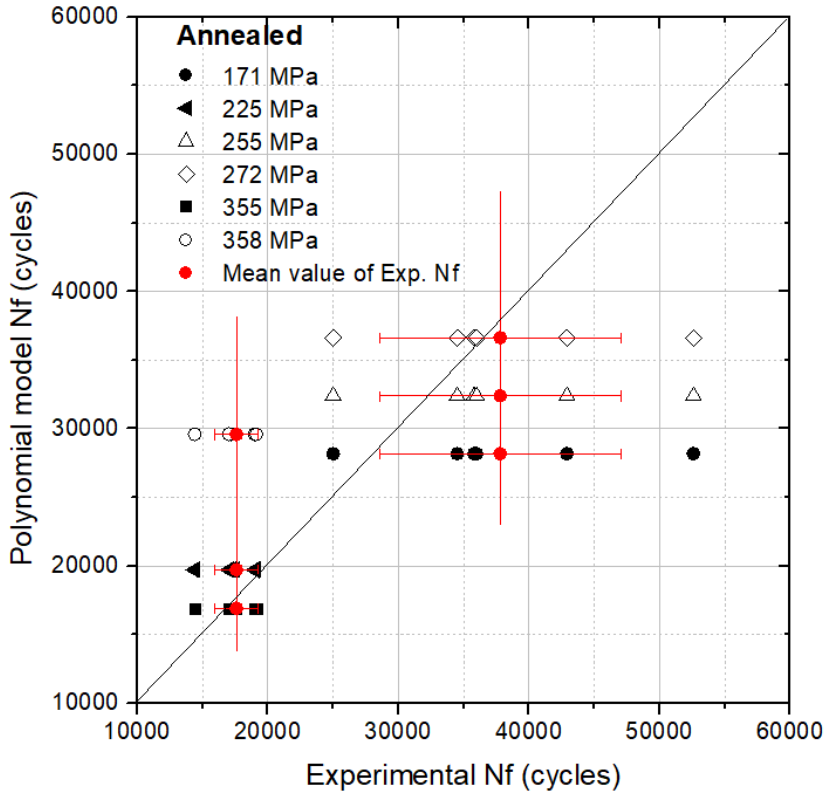

Figure VI-30: Graphic comparison between the values of experimental N_f and the values obtained by adjustment of polynomials for annealed samples.

VI. 2 X-RAY DIFFRACTION RESULTS

Differently from the indentation tests, the experimental setup for the X-Ray diffraction analyses enabled real time measurements during fatigue life, i.e., without the need of removing the sample from the fatigue test machine. Fatigue tests were interrupted in predetermined time intervals for X-Ray diffraction measurements. The setup of the X-Ray test with the portable mode of the diffractometer at the same bench of the fatigue machine is shown in Chapter V, Figure V-14. X-Ray measurements were done at the middle of the gauge length of the sample. Figure VI-31 illustrates the evolution of a crack and the diffractometer operating during cycling of one specimen.

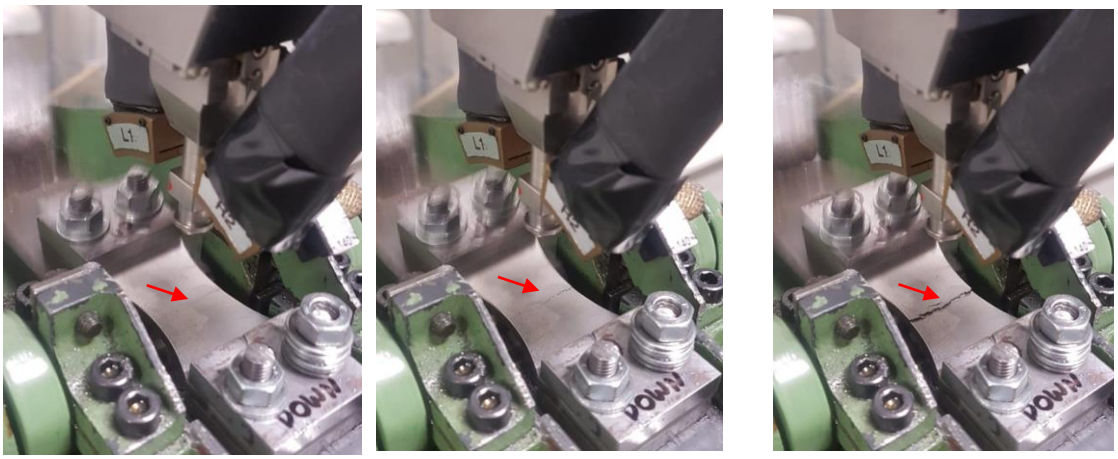

Figure VI-31: Crack propagation during cycling.

It is well known that damage mechanisms observed during high cycle fatigue can be generally described as initiation of microcracks, microcrack propagation and macrocrack propagation. As the general objective here is to predict fatigue life of steel structures submitted to high cyclic loads before macroscopic cracking, it is of fundamental importance to better understand the mechanisms involved at the early stages of fatigue phenomenon. Therefore, the X-Ray measurements were concentrated at the beginning of the fatigue life, with measurements every 0.3% until 5% of the fatigue life of the material. From 5% to 40% of the fatigue life, the measurements were done every 2%. From 40% to 70%, at every 5%, and finally from 70% to rupture, at every 10%. Thus, sufficient data were obtained to plot a behavioral curve of the material throughout its fatigue life, with greater accuracy, greater amount of data at the beginning of fatigue life. For testing the first sample, fatigue life percentages for X-Ray measurements were determined based at N_f values from the indentation tests as stated before. And for each new X-Ray sample, the value of N_f was

updated.

A total of 8 as-machined samples were tested up to failure, in which 2 were fatigue cycled under the stress amplitude of 272 MPa, and 6 under the stress amplitude of 358 MPa. Annealed samples were also tested, and the results are shown further in this chapter. Table VI-11 resumes the samples submitted to X-Ray diffraction analysis.

Table VI-11: Samples submitted to X-Ray diffraction analysis.

Applied stress amplitude = 272 MPa	**Applied stress amplitude = 358 MPa**	
As-machined	**As-machined**	**Annealed**
T2EF55	T2EF45	T2EF48R
T2EF61	T2EF53	T2EF56R
	T2EF59	T2EF57R
	T2EF60	T2EF58R
	T2EF62	
	T2EF63	

In Figure VI-32 to Figure VI-39 variations in FWHM of X-Ray diffraction peaks measured during fatigue tests at different stress amplitudes are presented. The FWHM change measured at a given number of cycles is defined as the difference between FWHM values at this point and at N=0, i.e., $FWHM-FWHM_0$

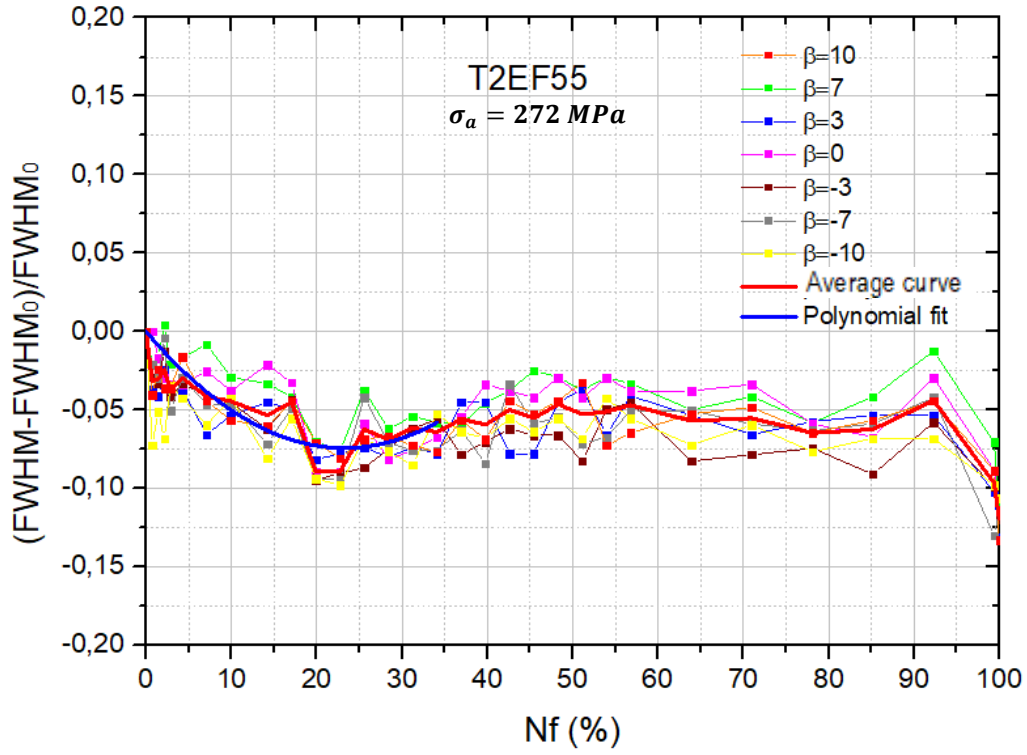

Figure VI-32: Evolution of FWHM with fatigue cycling at σ_a= 272 MPa (R=-1) for the sample T2EF55.

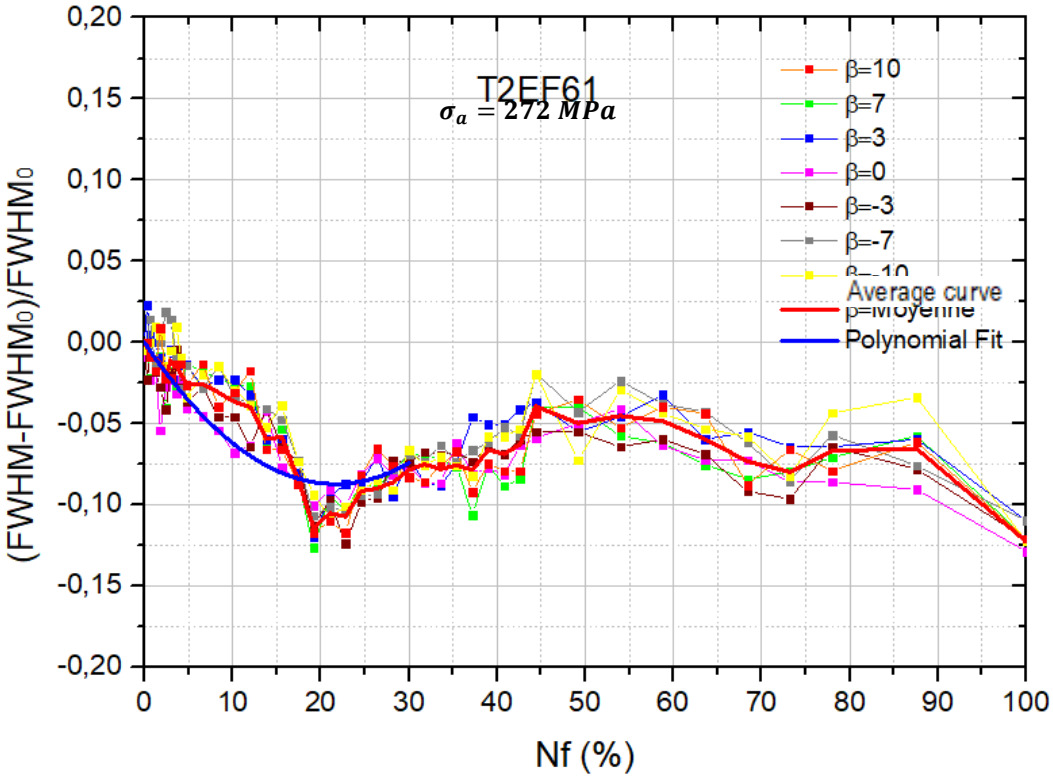

Figure VI-33: Evolution of FWHM with fatigue cycling at σ_a= 272 MPa (R=-1) for the sample T2EF61.

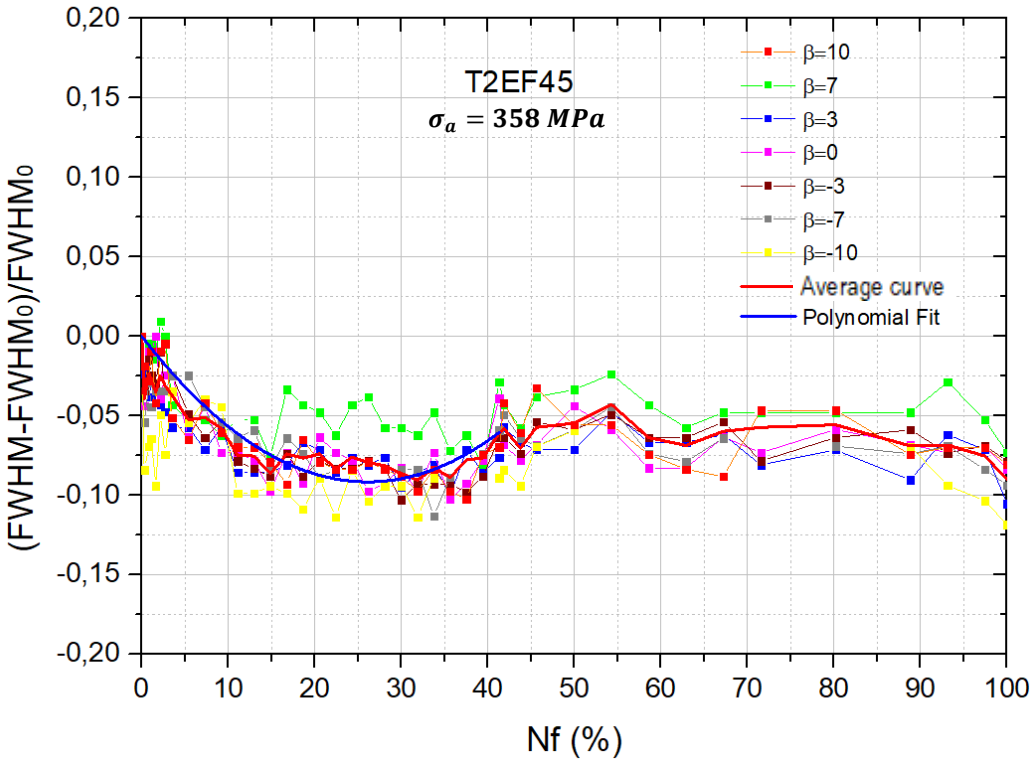

Figure VI-34: Evolution of FWHM with fatigue cycling at σ_a= 358 MPa (R=-1) for the sample T2EF45.

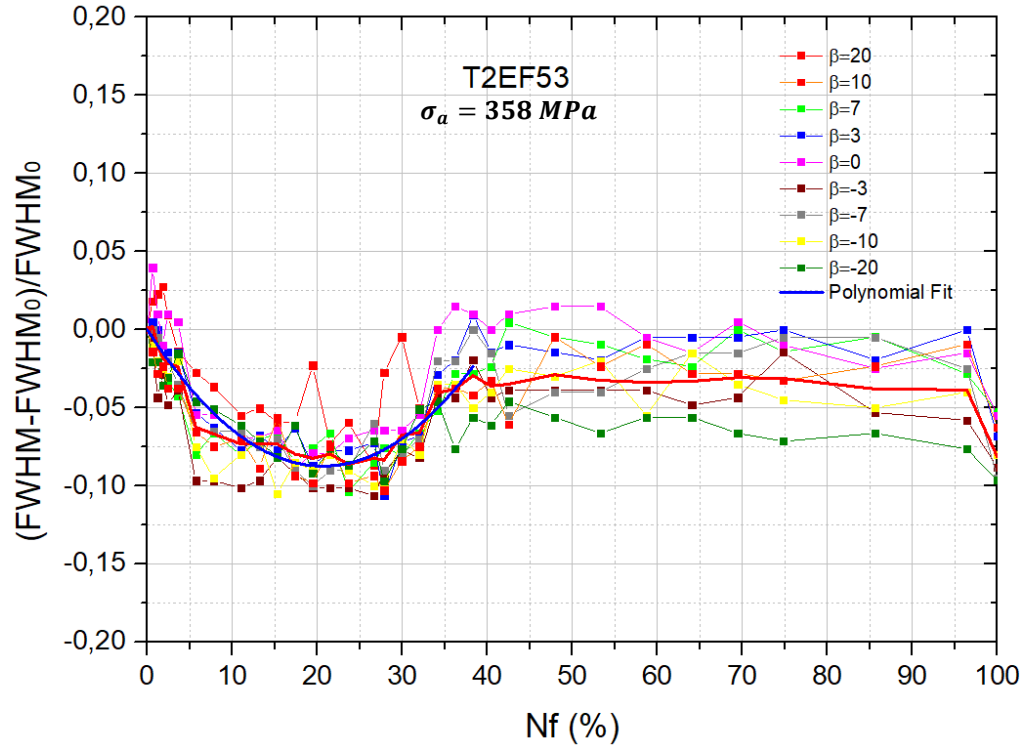

Figure VI-35: Evolution of FWHM with fatigue cycling at σ_a= 358 MPa (R=-1) for the sample T2EF53.

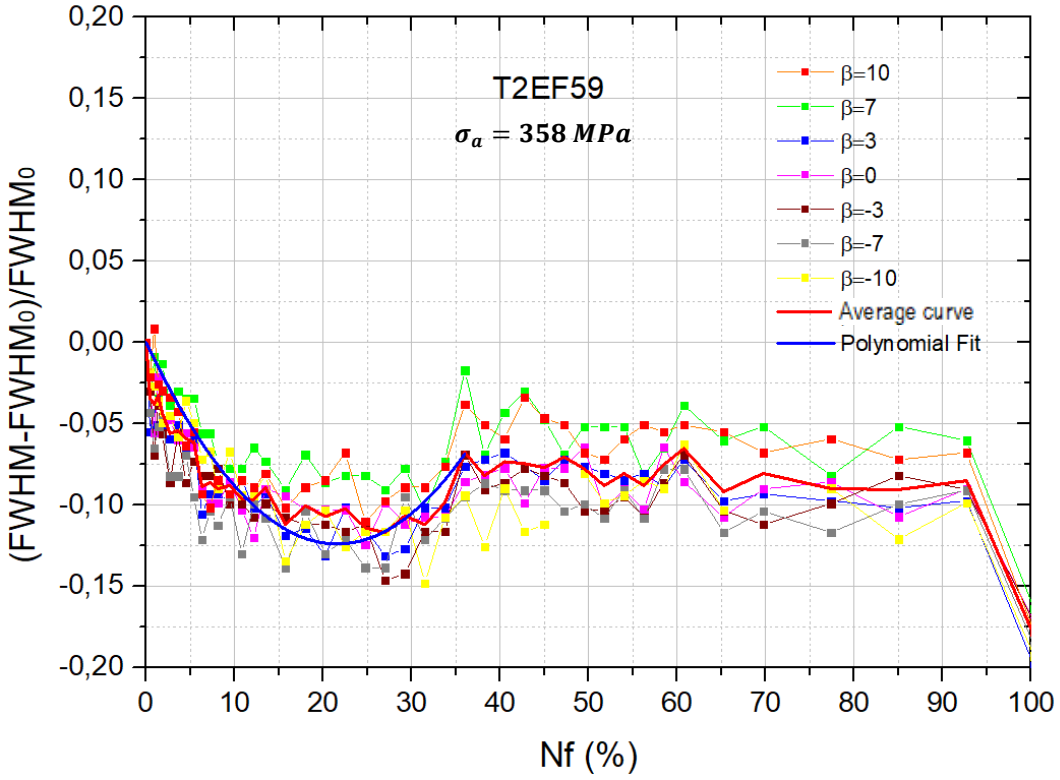

Figure VI-36: Evolution of FWHM with fatigue cycling at σ_a= 358 MPa (R=-1) for the sample T2EF59.

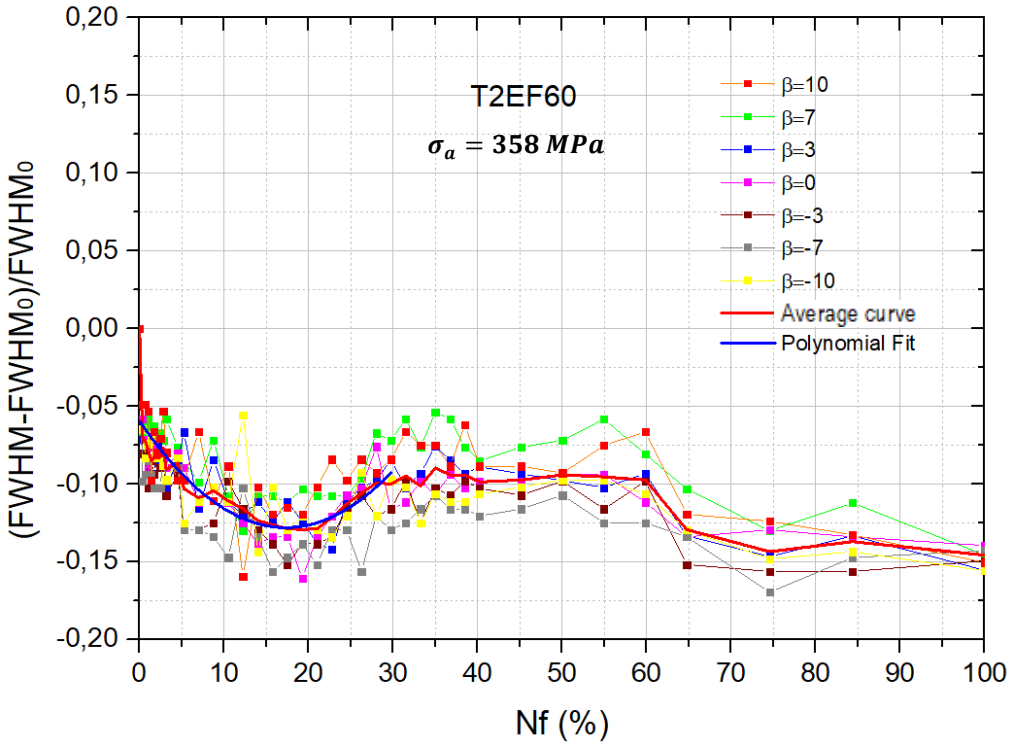

Figure VI-37: Evolution of FWHM with fatigue cycling at σ_a= 358 MPa (R=-1) for the sample T2EF60.

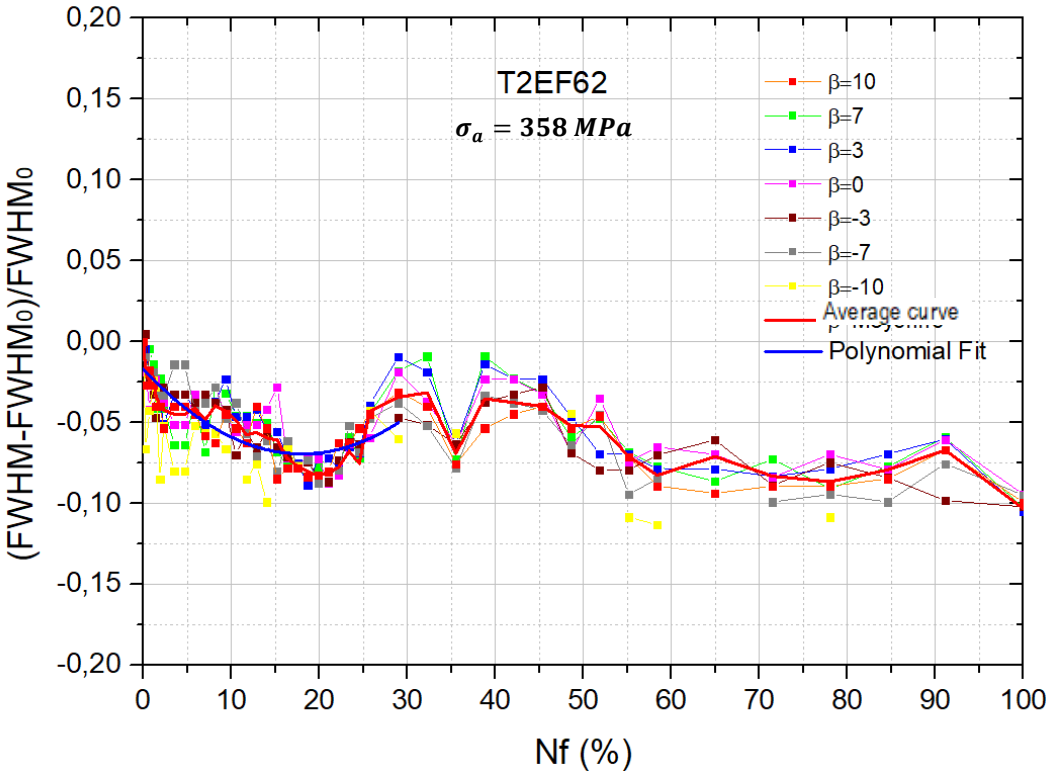

Figure VI-38: Evolution of FWHM with fatigue cycling at $\sigma_{a=}$ 358 MPa (R=-1) for the sample T2EF62.

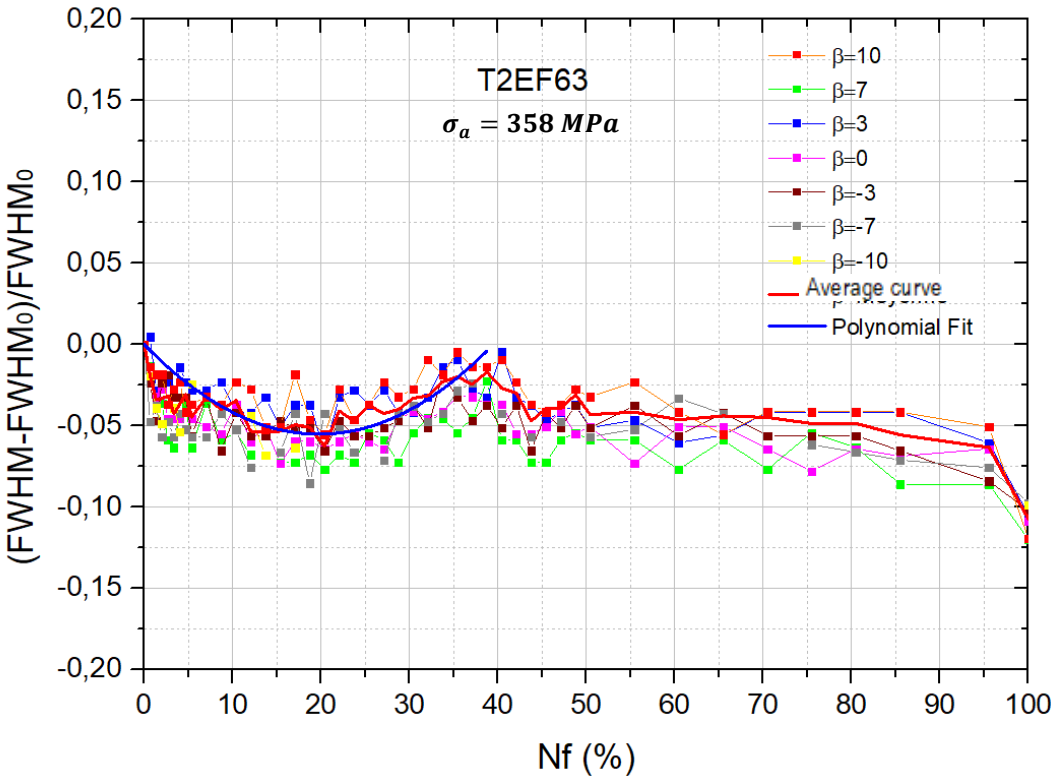

Figure VI-39: Evolution of FWHM with fatigue cycling at $\sigma_{a=}$ 358 MPa (R=-1) for the sample T2EF63.

As done before for the indentation results, for each sample, a second order polynomial in the form of $y=ax^2+bx+c$ was fitted, as shown by the solid blue curves in Figure VI-32 to Figure VI-39. In order to determine the fatigue life ratio in which the most important changes in the FWHM values occur, the inflection point of the curve (minimum or maximum x value) was determined by equalizing the first derivative of the polynomial to zero. Table VI-12 summarizes the inflection points obtained for the samples. Finally, an average value of 21% of the fatigue life was obtained, with standard deviation of 2.89%.

Table VI-12: : Inflection points obtained for the X-Ray samples.

Stress amplitude (σ in MPa)	Sample	Percentage of fatigue life
272	T2EF55	21.75
	T2EF61	21.85
358	T2EF45	26.68
	T2EF53	20.67
	T2EF59	21.95
	T2EF60	17.32
	T2EF62	19.80
	T2EF63	17.99

For all the samples, at both stress amplitudes (Figure VI-32 to Figure VI-39), it can be noted the same behavior for FWHM values during fatigue cycling. In the early cycles, a fast decrease in the FWHM takes place, followed by an increase until about half of the fatigue life, a plateau and an abrupt decrease at failure.

To determine the number of cycles in which the most important changes in FWHM occur, the results for variation of FWHM *vs* number of cycles (N) were plotted and a second order polynomial in the form of $y=ax^2+bx+c$ was fitted. Polynomials resulted of this procedure for each sample for stress levels of 272 and 358 MPa are shown in Figure VI-40 to Figure VI-47. The inflection point of the curve was determined as done by the percentage of N_f by equalizing the first derivative of the polynomial to zero. Table VI-13 summarizes the inflection points obtained for X-Ray samples.

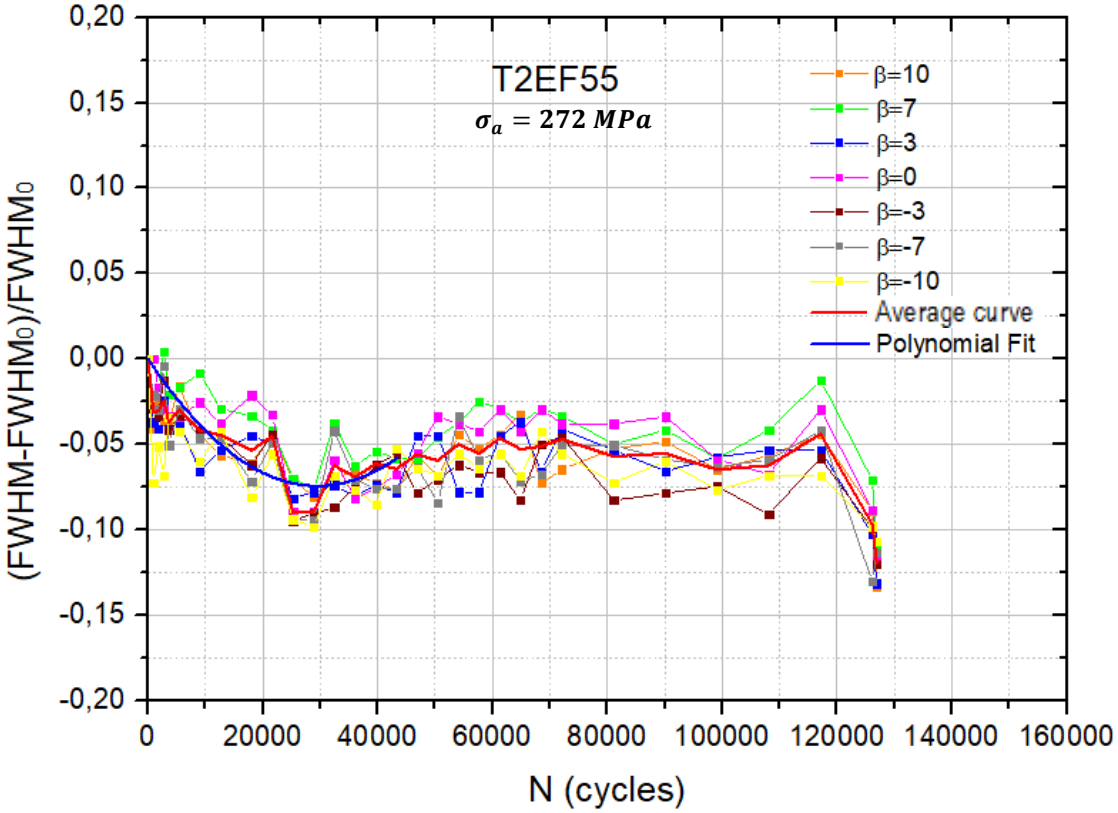

Figure VI-40: Evolution of FWHM vs number of cycles at $\sigma_{a=}$ 272 MPa (R=-1) for the sample T2EF55.

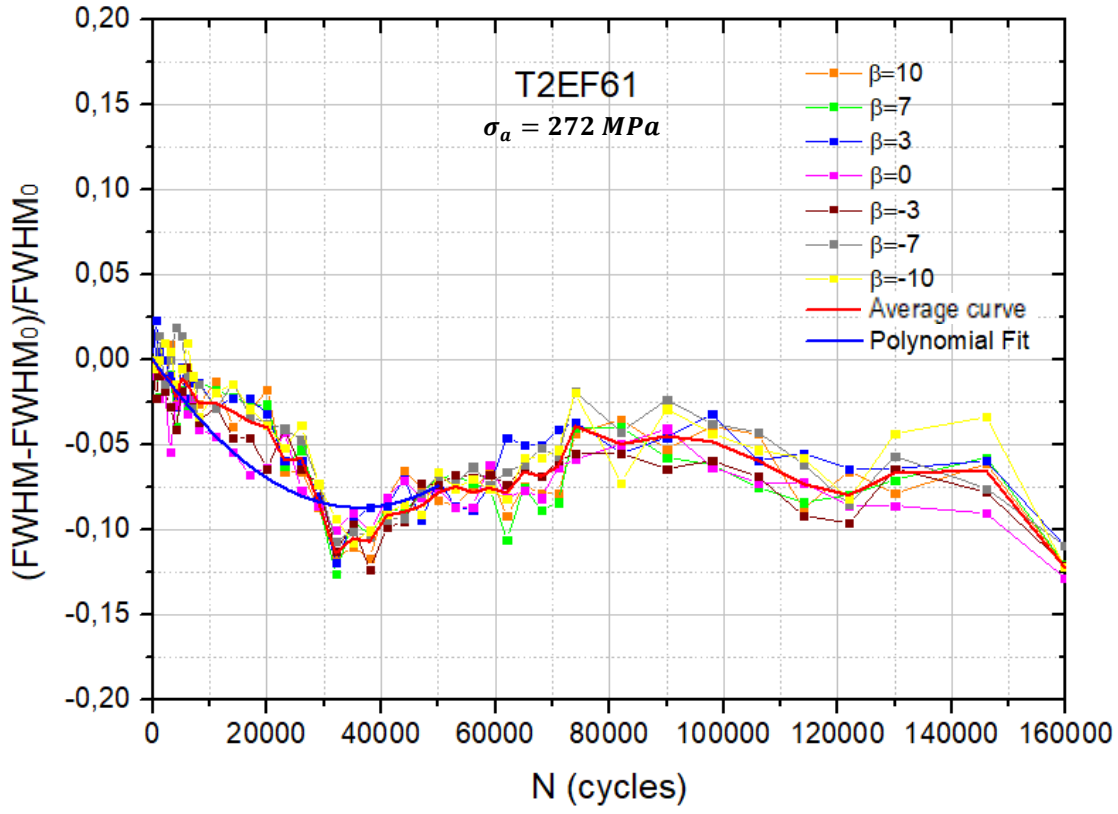

Figure VI-41: Evolution of FWHM vs number of cycles at $\sigma_{a=}$ 272 MPa (R=-1) for the sample T2EF61.

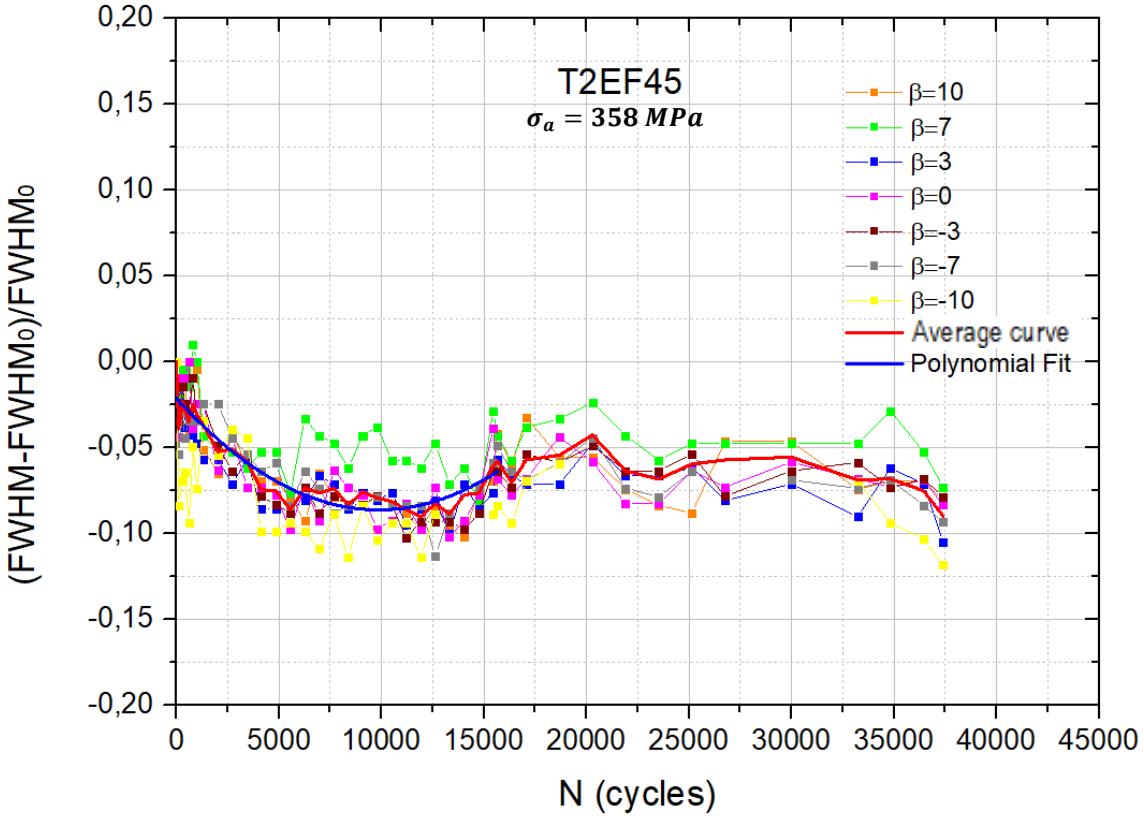

Figure VI-42: Evolution of FWHM vs number of cycles at $\sigma_{a=}$ 358 MPa (R=-1) for the sample T2EF45.

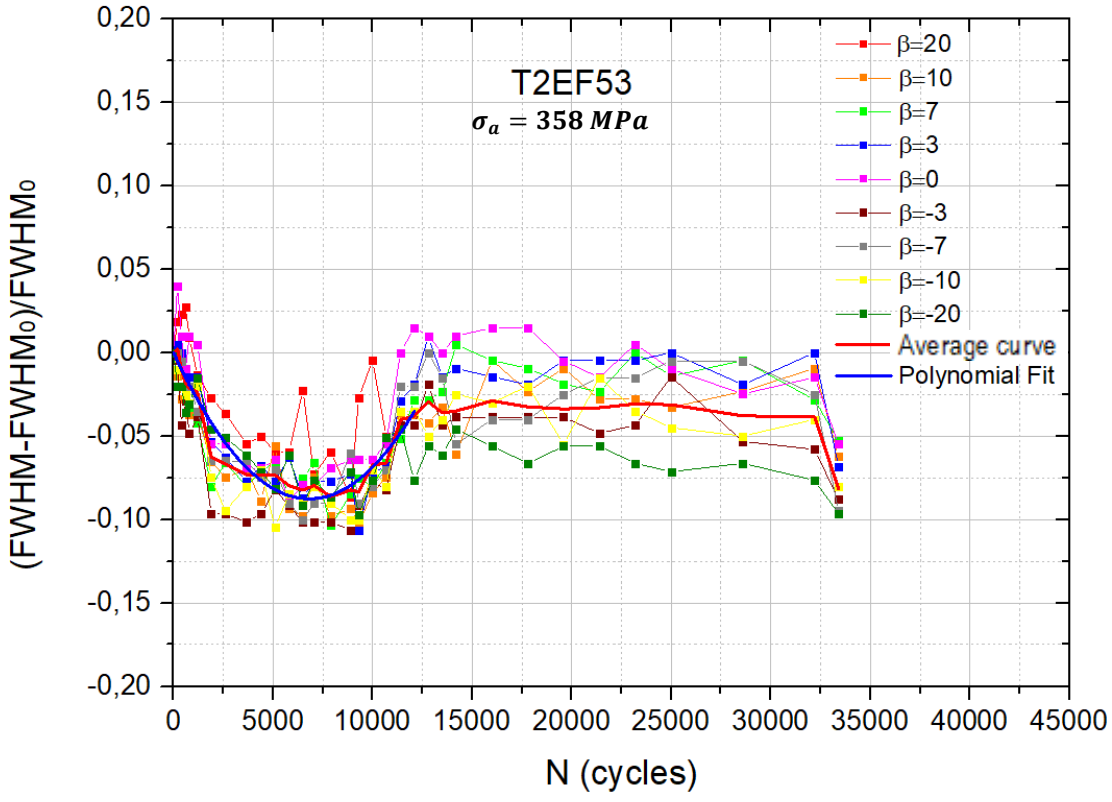

Figure VI-43: Evolution of FWHM vs number of cycles at $\sigma_{a=}$ 358 MPa (R=-1) for the sample T2EF53.

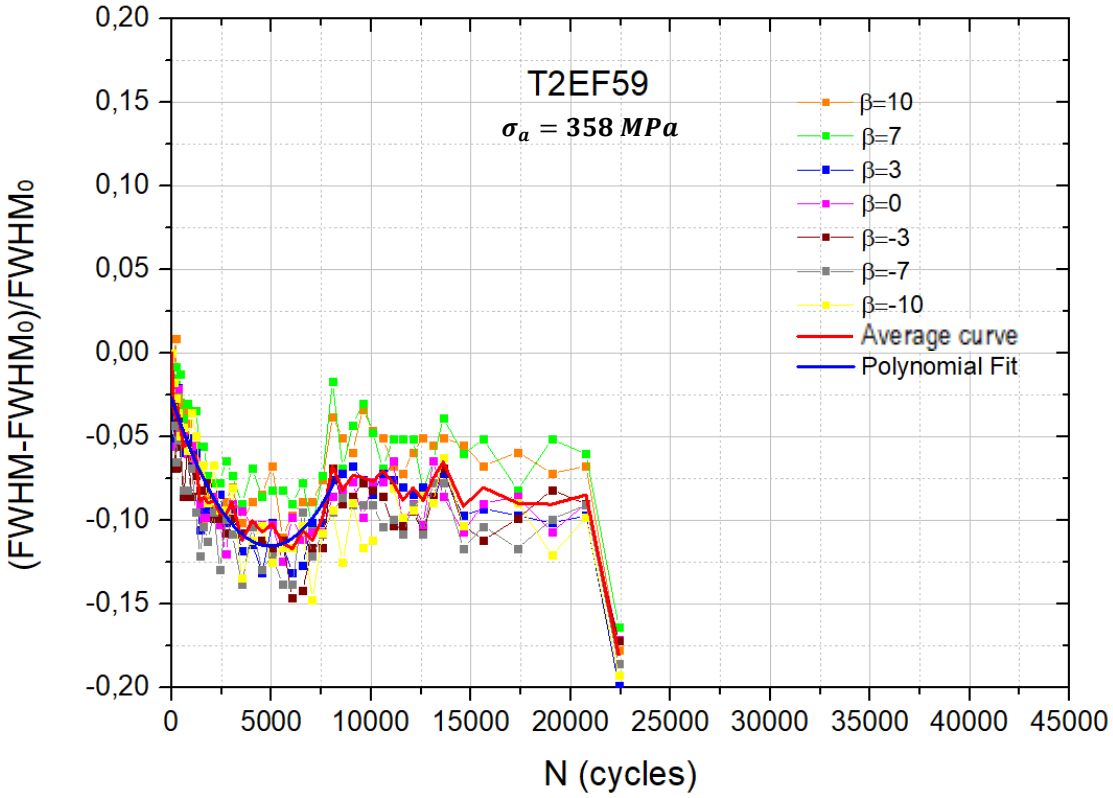

Figure VI-44: Evolution of FWHM vs number of cycles at $\sigma_{a=}$ 358 MPa (R=-1) for the sample T2EF59.

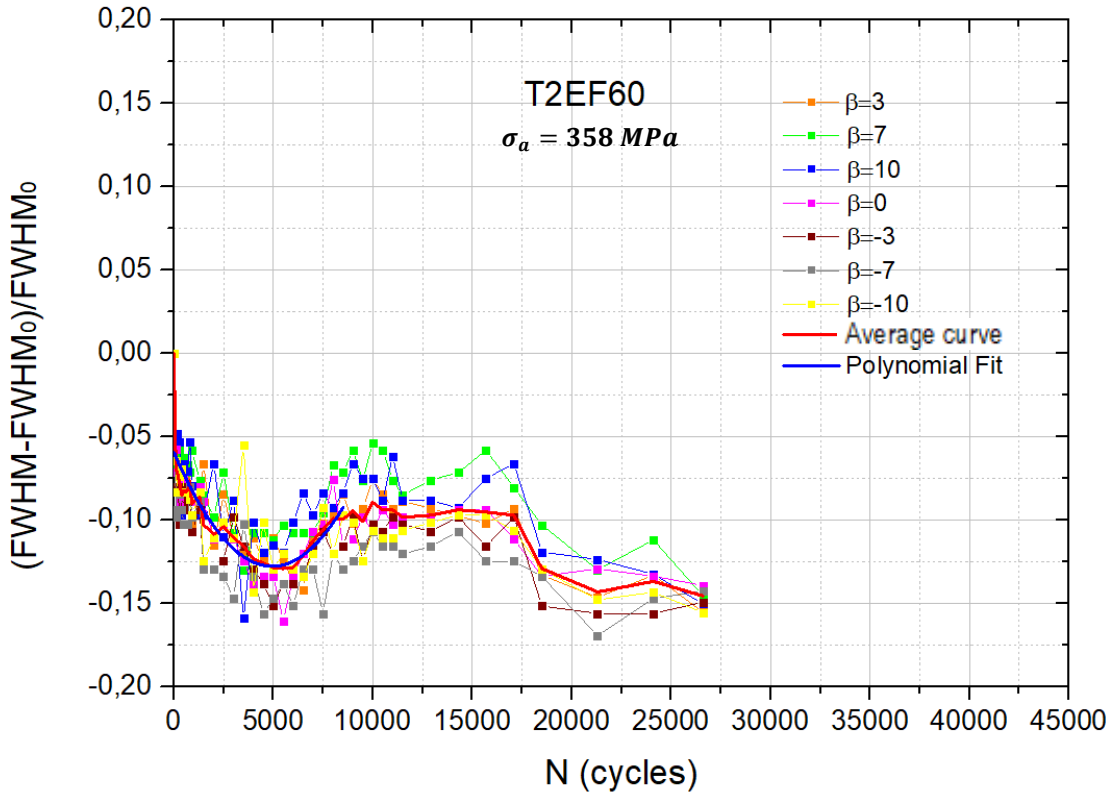

Figure VI-45: Evolution of FWHM vs number of cycles at $\sigma_{a=}$ 358 MPa (R=-1) for the sample T2EF60.

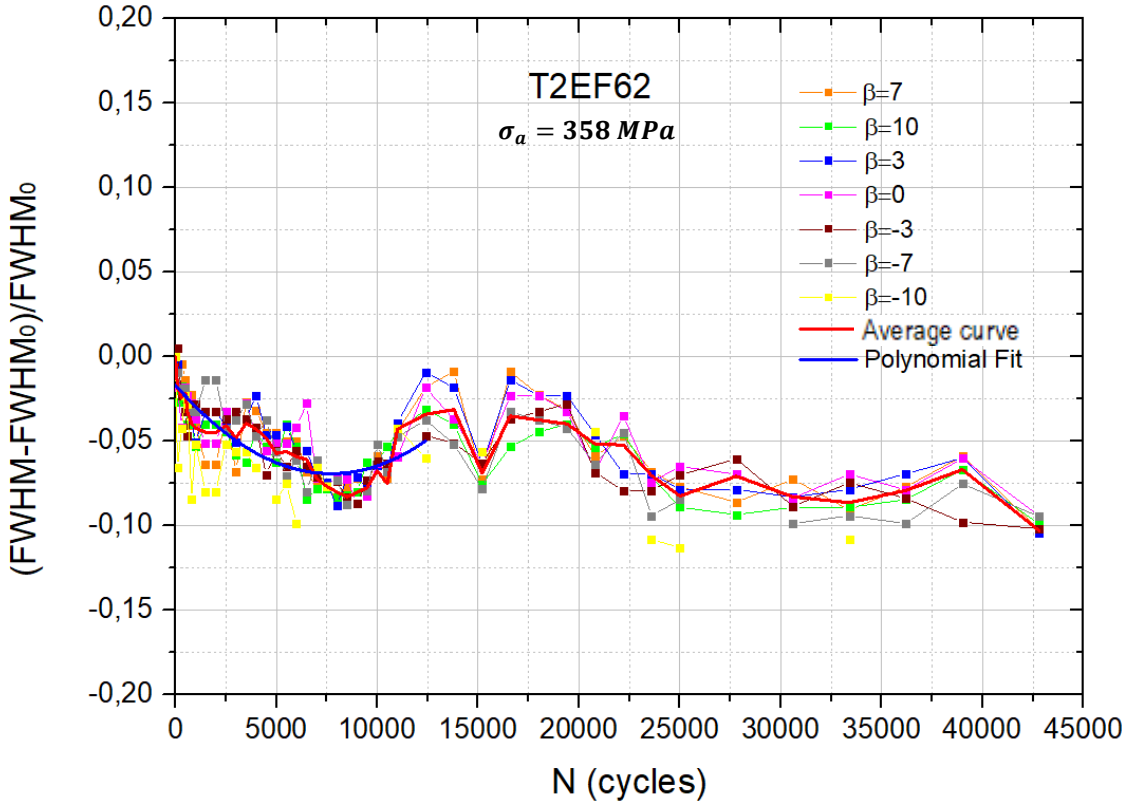

Figure VI-46: Evolution of FWHM vs number of cycles at σ_a= 358 MPa (R=-1) for the sample T2EF62.

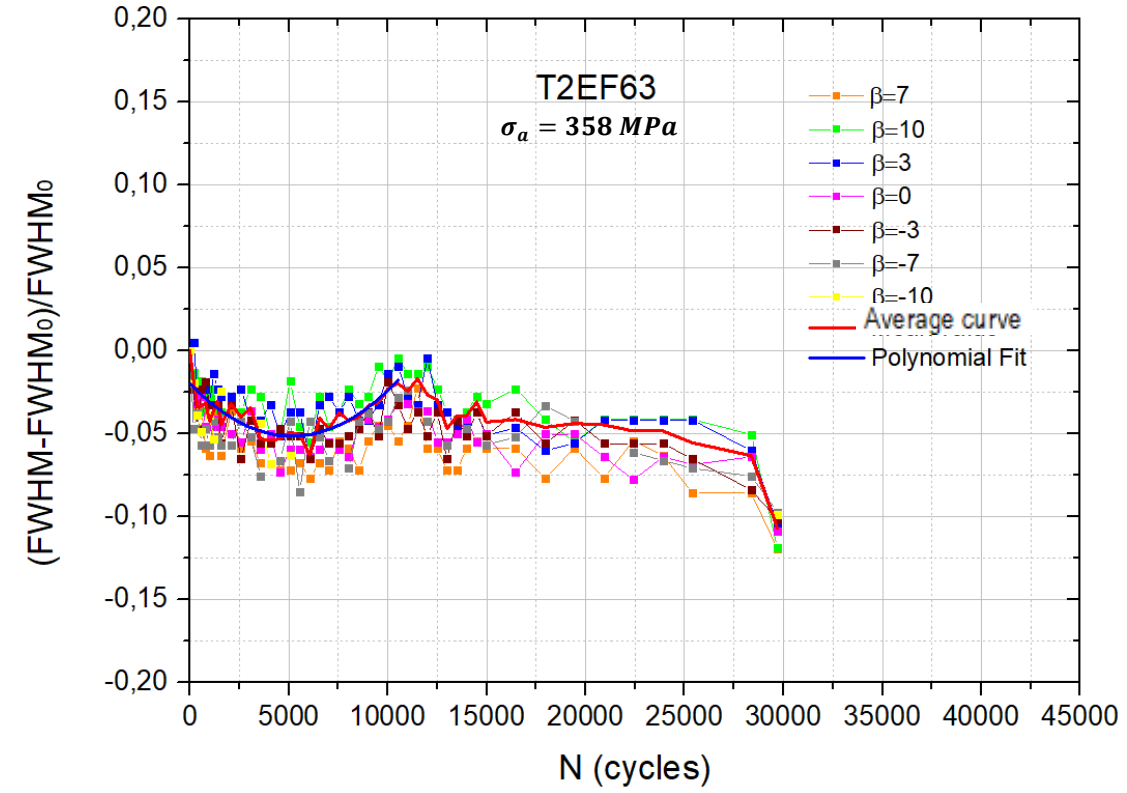

Figure VI-47: Evolution of FWHM vs number of cycles at σ_a= 358 MPa (R=-1) for the sample T2EF63.

Table VI-13: Inflection points obtained for the X-Ray samples (number of cycles).

Stress amplitude (σ in MPa)	Test sample	N (number of cycles)
272	T2EF55	27526
272	T2EF61	36336
358	T2EF45	9871
358	T2EF53	6824
358	T2EF59	4919
358	T2EF60	4946
358	T2EF62	7714
358	T2EF63	5177

Each value of number of cycles (N) obtained for each specimen was equated to the average percentage of the fatigue life (%N_f) showed in Table VI-12, i.e. 21%, in order to determine the total life in fatigue of the material. For example, for the sample T2EF55, the value of the inflection point shown in Table VI-13 is 27526, so if 21% of fatigue life corresponds to 27526 cycles, this means that the material fails after 131077 cycles (complete fatigue life). According to this procedure, by means of polynomial fitting, the number of cycles up to fatigue failure (*Nf*) of the samples can be determined.

As previously stated, the X-Ray diffraction analysis were real timing testing and all the samples were tested up to rupture. Therefore, the experimental N_f values (number of cycles up to failure) are compared to the values obtained by the adjustment of polynomials in Table VI-14 and shown graphically in Figure VI-48.

Table VI-14: Comparison between the values of experimental N_f and the values obtained by the method of adjustment of polynomials.

Stress amplitude (MPa)	N_f (cycles)	Samples					
		T2EF55	**T2EF61**				
272	**Experimental**	126900	159800				
	Polynomial fitting	131076	173031				
		T2EF45	**T2EF53**	**T2EF59**	**T2EF60**	**T2EF62**	**T2EF63**
358	**Experimental**	37400	33400	22400	26600	42800	29700
	Polynomial fitting	47008	32496	23428	23554	36736	24653

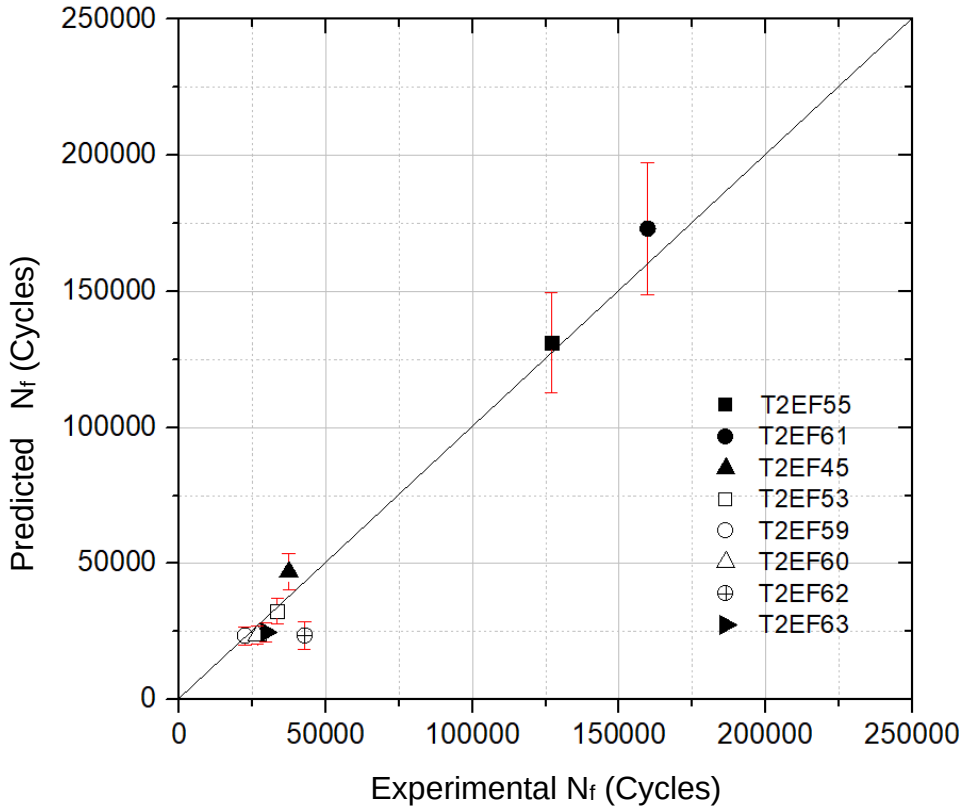

Figure VI-48: Graphic comparison between the values of experimental N_f and the values obtained by the method of adjustment of polynomials.

ANNEALED SAMPLES

X-Ray diffraction analysis were carried out at the stress amplitude of 358 MPa for 4 annealed samples, as previously showed in Table VI-11 The annealing treatment was done for 1 hour, at 850ºC, with cooling inside the oven. As done before for the as-machined samples, full-width-at-half-maximum (FWHM) analysis were done by means of the variation of the FWHM at each stage of the fatigue life in relation to the FWHM for the non-cycled specimen ($FWHM_0$). Figure VI-49 to Figure VI-52 show the results.

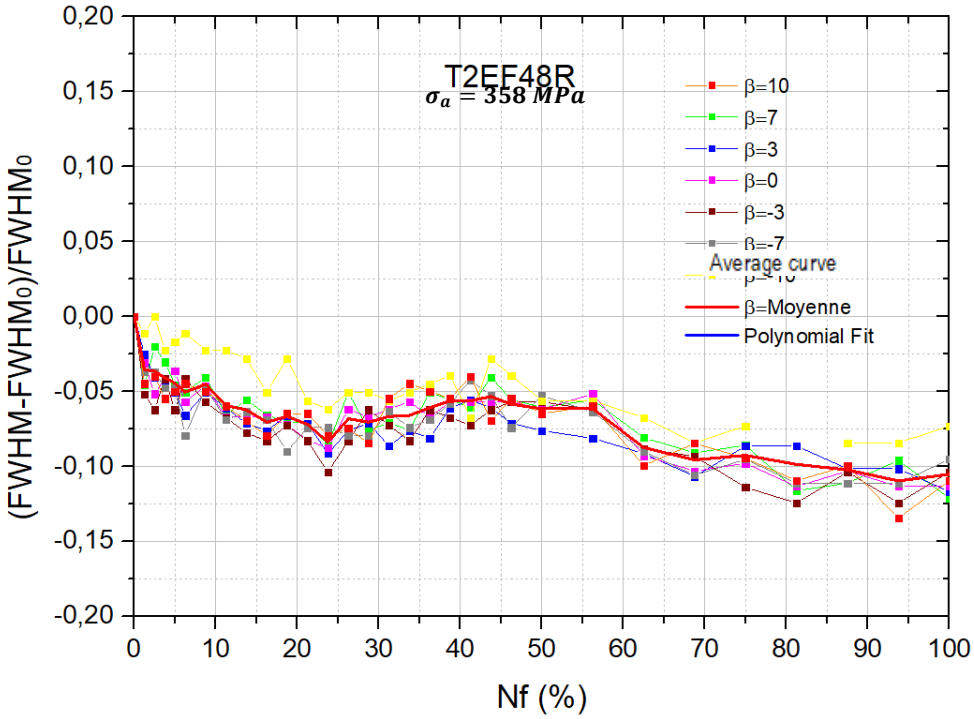

Figure VI-49: Evolution of FWHM vs *Nf* at σ_a= 358 MPa (R=-1) for the annealed sample T2EF48R.

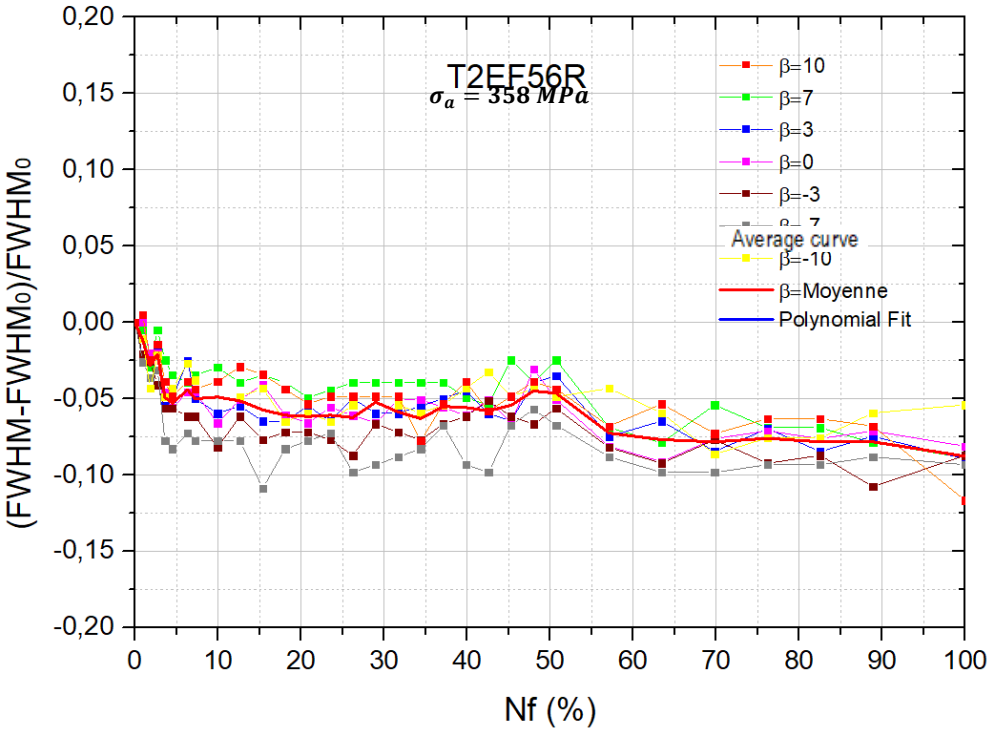

Figure VI-50: Evolution of FWHM vs *Nf* at σ_a= 358 MPa (R=-1) for the annealed sample T2EF56R.

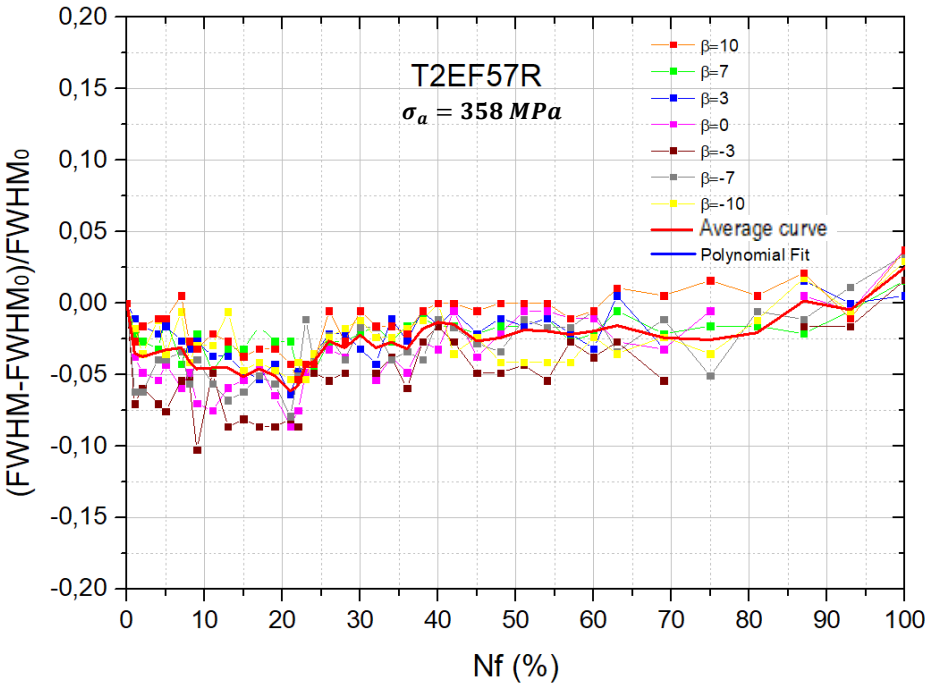

Figure VI-51: Evolution of FWHM vs *Nf* at σ_a= 358 MPa (R=-1) for the annealed sample T2EF57R.

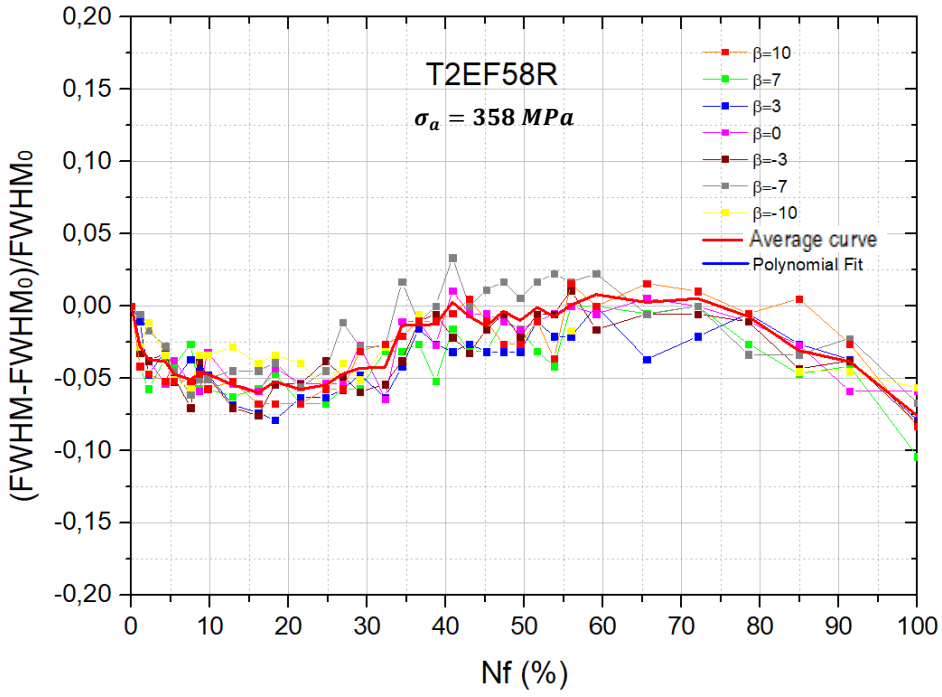

Figure VI-52: Evolution of FWHM vs *Nf* at σ_a= 358 MPa (R=-1) for the annealed sample T2EF58R.

Analysing Figure VI-49to Figure VI-52 it can be noted that annealed samples presented decrease of FWHM values at the early stages of fatigue, followed by increase in FWHM until half of the fatigue life of the material. After that, the samples do not have a standard behavior, presenting decrease, increase or even a plateau depending on the sample.

It was expected that after annealing, with lower strength properties and lower hardness, due to the multiplication of dislocations early in the fatigue life, that the values of FWHM experience an increase. The behaviour of increase in FWHM was observed by Pinheiro et al. [109], who did X-Ray diffractometry during the fatigue life of API 5L X60 steel. As annealed samples did not present the expected behaviour, metallographic analysis was done to study the microstructure of the samples. The surface of the specimen was prepared by grinding with a sequence of SiC papers from 80 to 1200 grit numbers under water cooling, followed by wet grinding with diamond micro powders from 6 μm to 1 μm and etching with 5% Nital. The material microstructure was observed using optical microscope with magnification factors of 100, 200, 500 and 1000x. The results are shown in Figure VI-53.

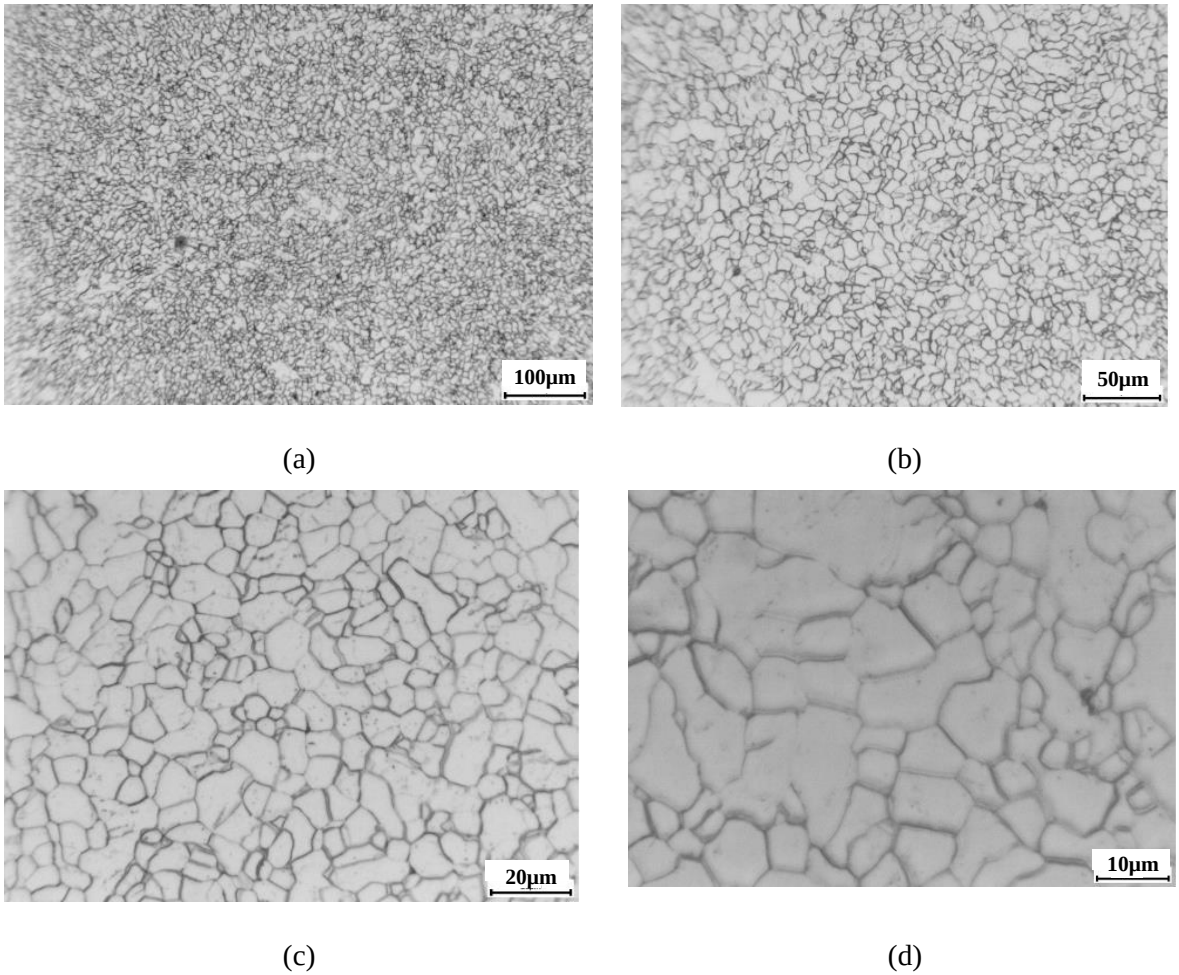

Figure VI-53: Microstructure of an annealed specimen observed through optical microscope, magnification factor of (a) 100x, (b) 200x, (c) 500x and (d) 1000x.

It is observed in Figure VI-53 a ferrite-pearlite structure, as for the as-machined and annealed samples used for the indentation analysis, as shown in Chapter IV, item IV-3. The

microstructure of well-defined grain boundaries is really similar to the annealed samples used for indentation tests. The annealing treatment with the indentation specimens was done at the Subsea Technology Laboratory (LTS), in Brazil, while the treatment of the X-Ray specimens was done in the *Institut Universitaire de Technologie*, IUT A of Lille, in France. It was decided to do a grain size analysis with the aid of the software Image J to better understand the differences between the microstructure of the samples treated in Brazil and in France. The results are shown in Figure VI-54.

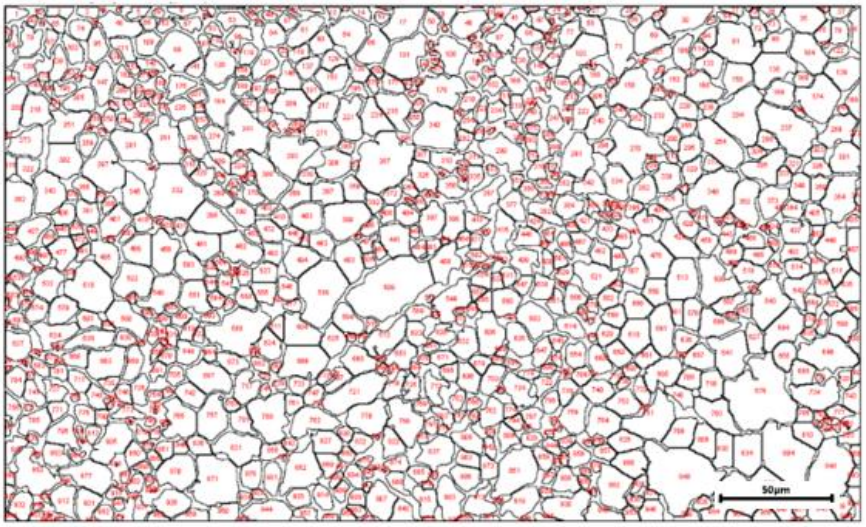

981 grains
78% of the total area
31µm in size

(a)

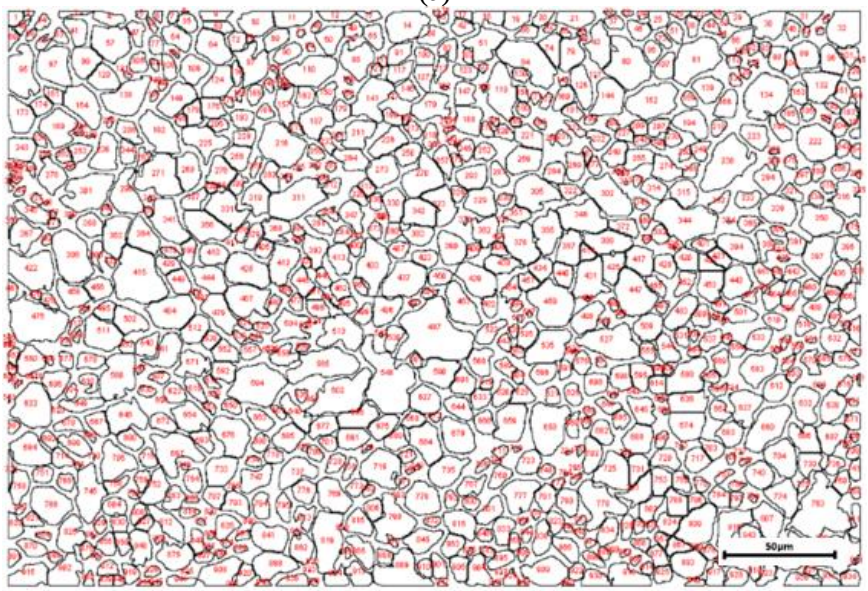

951 grains
69% of total area
20µm in size

(b)

Figure VI-54: Comparison between the microstructure of samples treated in (a) Brazil and (b) France.

For the specimen annealed in Brazil, Figure VI-54(a), 981 grains was analyzed, that fills 78% of the total area and the average of grain size is 31µm. For the sample annealed in France, Figure VI-54(b), 951 grains was analyzed, that fills 69% of the total area and the

average of grain size is 20µm. The difference in the grain size can explain the behavior of the sample. According to the theory of dislocations [117], grain boundaries act as obstacles to the dislocation slip, resulting in dislocation stacking in their sliding planes behind the contours. Thus, the larger the grain, the greater the number of dislocations stacked. The specimens annealed in Brazil, with grains considerably bigger (31µm), probably had more dislocations stacked in grain boundaries when compared with the specimens with smaller grains (20µm) annealed in France. Therefore, when cycling started, the samples annealed in Brazil, used for indentation tests, experienced a multiplication of these dislocations and microdeformations, leading to increase in hardness values (Figure VI-6), while the samples annealed in France experienced a first stage of rearrangement of the dislocation network, with decrease of the FWHM values, same behavior of the as-machined samples.

Both annealing treatments, although in different laboratories, were done under the same conditions (1 hour annealing at 850^{o}C with oven cooling). The differences in the microstructure of the samples may explain by the velocity of oven cooling, or other specification of each oven.

VI.3 COMPARISON OF THE INDENTATION AND X-RAY RESULTS

In the search of a new way to predict the fatigue life of metal structures under cyclic loads, two methods of studying the microstructural behavior of API 5L X65 grade steel samples were used: instrumented indentation tests and X-Ray diffraction analyses. Although the techniques used are different, the material tested was exactly the same, machined and the surface prepared under the same conditions, fatigue cycled at the same machine, under the same stress amplitudes for fully reversed loading (R=-1). Even though the depth of penetration of X-Ray diffraction for Cr-Kα radiation for this material is approximately 6µm [121], and the microindentation tests have been carried out at a penetration depth of 2µm from the surface, the area affected by indenter penetration, called plastic zone, is much larger than 2µm and can reach 10µm depending on the indenter model and the material [120]. Therefore, it is expected that the results of both analysis show the same trend.

Figure VI-55 and Figure VI-56 compare the results for microstructural changes obtained from indentation and X-Ray diffraction tests for stress amplitudes of 272 and 358 MPa, respectively.

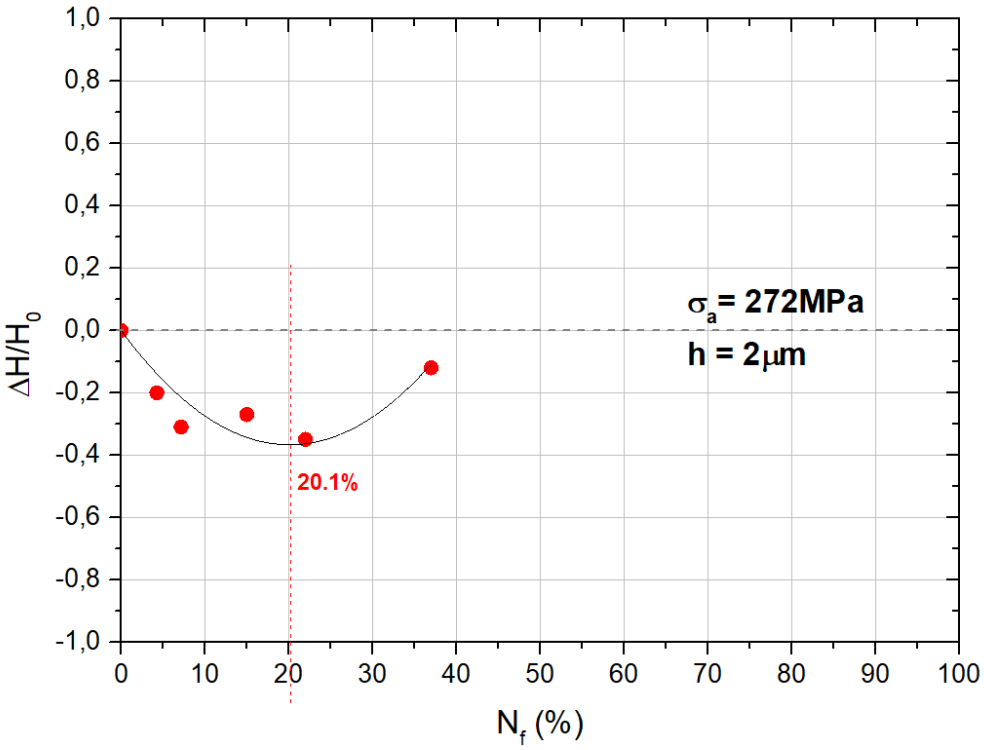

(a)

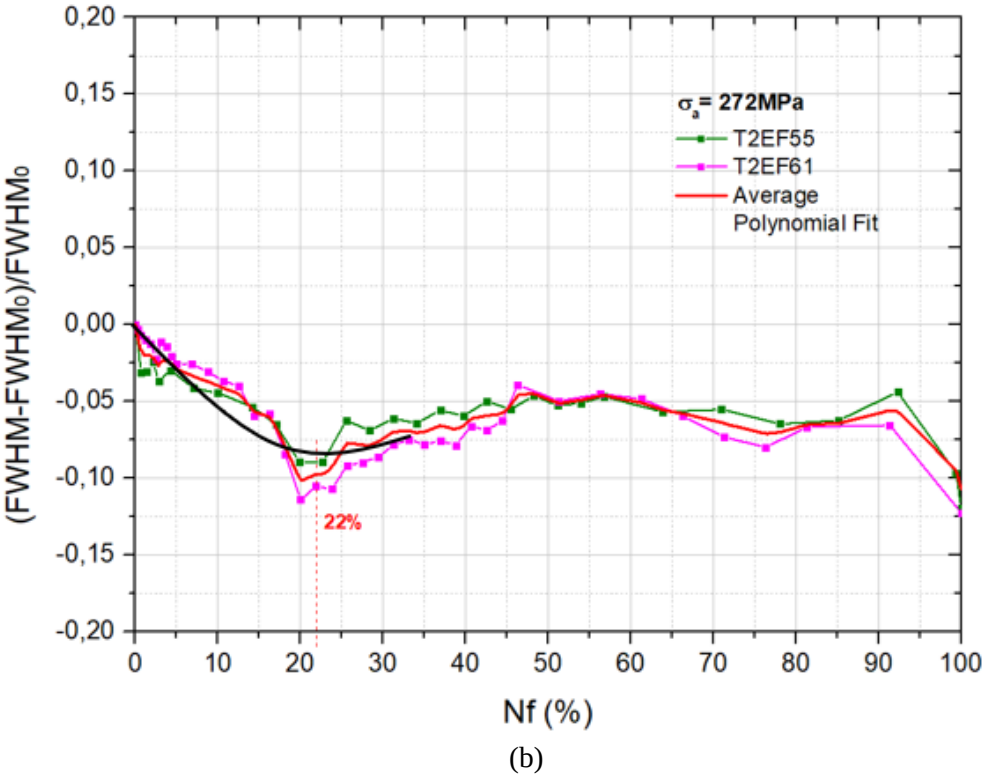

(b)

Figure VI-55: Comparison between (a) indentation and (b) X-Ray results for a stress amplitude of 272 MPa.

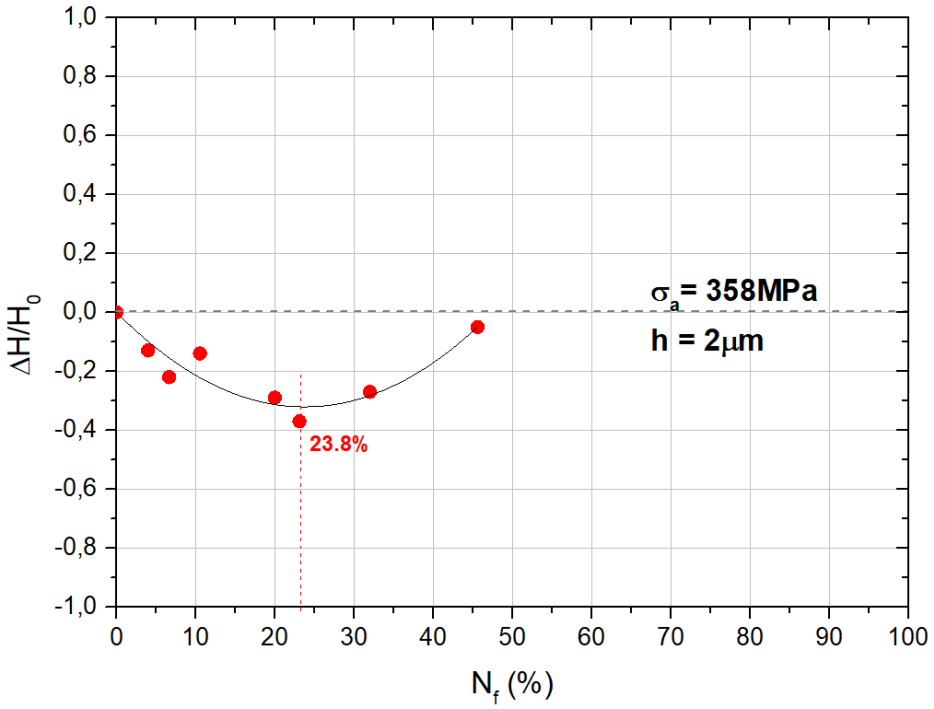

(a)

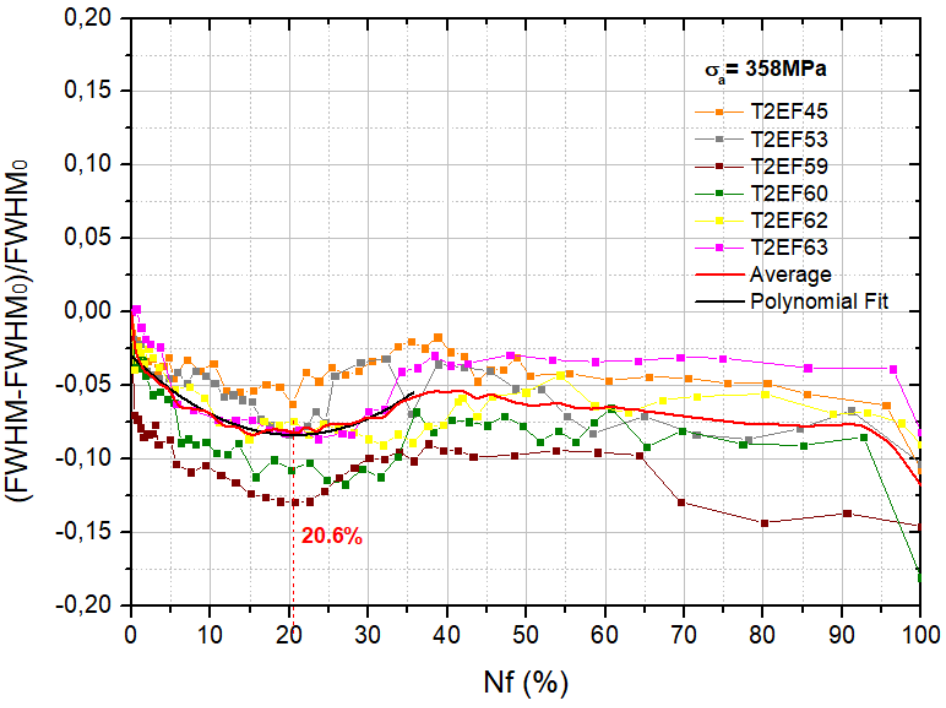

(b)

Figure VI-56: Comparison between (a) indentation and (b) X-Ray results for a stress amplitude of 358 MPa.

It can be noted from Figure VI-55 and Figure VI-56 that for as-machined samples, the same behavior is observed for the two analysis methods employed, which gives greater reliability to the results. The samples presented a decrease in both hardness and FWHM values at the beginning of the fatigue life, with major changes at around 20%, making a

point of change in the material behaviour at this percentage. The annealed results were not shown in this comparative study because, as explained before, the behaviour of treated samples used in X-Ray tests was not as expected due to differences in the microstructure of annealed samples used for indentation and for FWHM analysis. Figure VI-57 compares N_f values obtained by both methods of analysis, X-ray diffraction and instrumented indentation tests, showing a good correspondence between them.

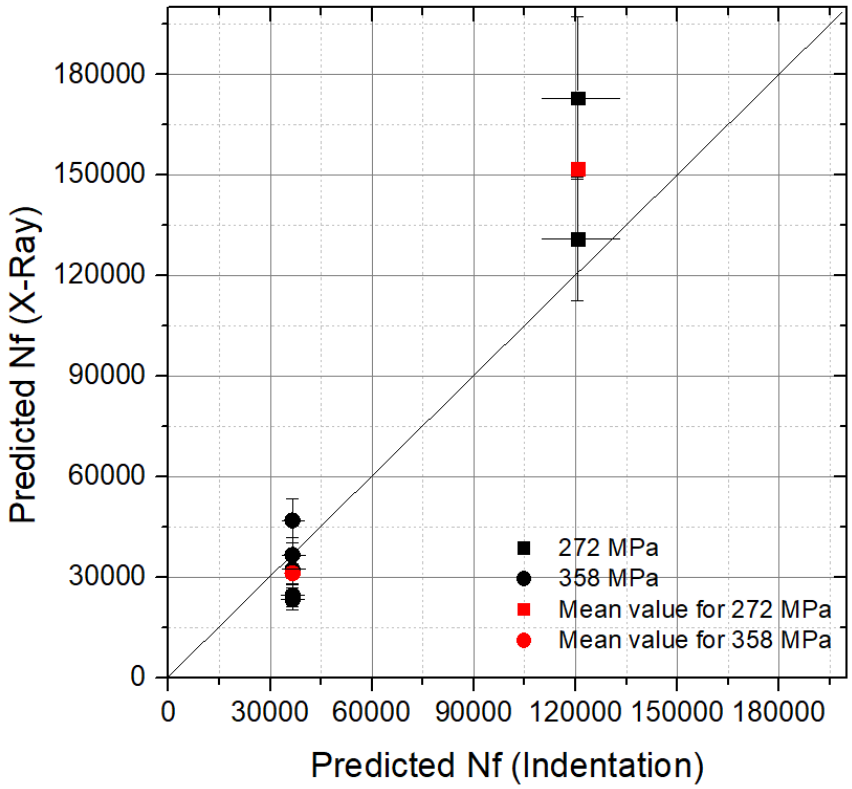

Figure VI-57: Graphic comparison between the values of predicted N_f for X-ray and indentation analysis.

High cycle fatigue phenomenon can be generally described by three distinct stages, namely initiation and propagation of microcracks (Stage I), macrocrack propagation (Stage II) and final failure (Stage III) [4]. In Stage I, strain localization leads to the formation of persistent slip bands (PSBs), extrusions and intrusions, which act as initiation sites for microcracks. Microcrack propagates along PSBs or slip planes of the crystalline structure with high shear stress. The rate of microcrack propagation is very low (on the order of nm/cycle), and microcracks are frequently interrupted at grain boundaries that they cannot easily overcome, when adjacent grains are not favorably oriented. In Stage II, macrocrack propagation (on the order of μm/cycle) occurs in a direction normal to the maximum tensile

stress applied until failure (Stage III). Considering that the microstructural changes measured in terms of variations in microhardness and FWHM present well-defined stages, it can be supposed that a connection could exist between them and the three stages of fatigue damage mechanisms previously described.

In Stage I of fatigue damage phenomenon, the decrease in microhardness and in FWHM can be associated with the movement and multiplication of dislocations and rearrangement of the initial dislocation network. A part of the initial dislocation network is produced during the pipe manufacturing process by cold working. Another part may come from the sample preparation (machining, grinding, and polishing), which is also likely to induce some level of residual stresses [15,107]. A decrease in microhardness values and in FWHM is related to a reduction in microdeformations, while an increase in these values is generally associated with an increase in microdeformations [124,125]. In that way, the level of microdeformations can be estimated using both methods, microindentation and X-Ray diffraction tests.

After decrease in microhardness and in FWHM values, it can be noted an inflexion point at approximately 21% of the fatigue life of the material, followed by an increase of the results (Figure VI-55 and Figure VI-56). It is supposed that at this critical point, the microstructure of the material begins responding in a different way the cyclic load applied. At this point of the fatigue life (nearly 21% of N_f), the network is more “organized”, and the cyclic loading will most likely increase lattice distortion, which entails an increase in dislocation density and microdeformations and finally, an increase in microhardness and in FWHM values. The existence of this critical point, this inflection in the curve, represents a very interesting perspective, since after the end of the initiation stage (Stage I) it would be possible to calculate the duration of the fatigue life of the material, until the beginning of macrocrack propagation.

Following the trend of the results in Figure VI-55 and Figure VI-56, after reduction, inflection point and increase of FWHM values, there is a plateau trend. This plateau represents almost 60% of the fatigue life of the material, and probably corresponds to the process of microcracks initiation and propagation. This process, which entails the creation of new free surfaces, can be considered as the propagation of a virtual crack, assuming that this crack would be the sum of individual microcracks propagating at a very low rate (on the order of nm/cycle) [15]. This plateau represents the final of Stage I, and could also be

associated with cyclic saturation of the material.

Stage II occurs in the last cycles with a rapid decrease in FWHM until complete fracture (Stage III). This behavior can be attributed to relaxation of microstresses due to macroscopic crack initiation and propagation (on the order of μm/cycle), preceding final failure. From Figure VI-55 and Figure VI-56 it can also be observed that Stage I takes much longer, almost the entire life of the material. When Stage II begins with macrocrack propagation, the operator has little time to act and avoid failure (Stage III).

CONCLUSIONS AND PERSPECTIVES

CONCLUSIONS AND PERSPECTIVES

The aim of this work is to study the microstructural behavior of an API 5L X65 grade steel pipeline during the fatigue damage phenomenon by means of microhardness and X-ray diffraction tests. A total of 53 samples were submitted to strain-controlled alternating bending fatigue tests at room temperature. Microdeformations were evaluated from measurements of the microhardness in 41 samples, in which 19 were submitted to annealing treatment. Microdeformations were also evaluated from measurements of the full width at half maximum (FWHM) of X-Ray diffraction peaks in 12 samples, in which 4 were annealed. The results of the two techniques were compared and show good agreement.

Optical microscope analysis was very efficient to compare grain size in as-machined and annealed samples. The images treated by the software Image J showed bigger grains and with more defined boundaries for annealed samples, what aided to explain the lower strength properties obtained in uniaxial tensile tests and lower hardness values obtained by instrumented indentation tests for the annealed specimens.

From microindentation results it could be clearly noticed that the most meaningful difference between the behaviors of an as-machined and an annealed specimen occurs at the beginning of the fatigue life, where the as-machined samples experimented a decrease in hardness values, while the annealed samples experimented an increase in the hardness values. Microindentation results also confirmed that fatigue is a surface phenomenon, once the studies of microhardness showed more pronounced variations at 2 μm in depth when compared to 4 and 6 μm of penetration depth.

From the FWHM of X-Ray diffraction peaks results it was possible to graphically characterize the three stages of fatigue damage. Stage I, nucleation and microcracking, is the longest stage, occupying most of the fatigue life of the material. The clear understanding of this stage is important because when moving on to the next stage of macrocraking, the material is already structurally compromised and is driven to failure abruptly, leaving the operator with little time to act. The results of X-Ray diffraction showed decay of the values of FWHM up to 20% of the fatigue life, with a subsequent increase of them up to 40%, followed by a long plateau. This behavior, characterized here as Stage I of the phenomenon of fatigue damage, is interpreted as initial movement and multiplication of dislocations and rearrangement of the initial dislocation network, resulting in decrease of hardness values.

With cycling, is observed increase in hardness due to increase in dislocation density and microdeformations, followed by the plateau of microcracks propagation. It is important to highlight that indentation tests showed the same behavior explained above for the initial stage of the fatigue life of the material, however, as the amount of data obtained in X-Ray diffraction was much bigger than in indentation tests, X-Ray tests was able to better characterize fatigue damage stages.

From both microindentation and X-ray results it was possible to conclude that the major changes in the microhardness values occurred around 20% of the fatigue life of the material for the as-machined condition. Knowing that, the authors calculated the number of cycles that correspond with this critical percentage for the six stress levels tested in this work (171, 225, 255, 272, 335 and 358MPa). Extrapolating the results for 100% of the fatigue life it was possible to calculate the number of cycles in which the material would fail. Using this methodology of analysis, it is expected to estimate the *Nf* value (number of cycles up to failure) of the material at each stress condition, without the necessity to cycle the material up to failure.

The results obtained show that the microindentation analysis and X-ray technique, even if it cannot completely elucidate the whole nature of fatigue damage phenomenon, can be used as tools to evaluate damage and to predict the fatigue life of metallic structures under service conditions before macroscopic cracking. A very new approach is suggested here in terms of the estimation of the duration of the fatigue life of steels. The portability and fastness of the X-Ray diffractometer equipment offer interesting perspectives for future works in the objective of quantifying changes in microdeformations in steels. Other techniques, like microindentation (as done in this work), dynamic indentation, nanoindentation, transmission electron microscopy (TEM) or finite element models can help to increase the reliability of the X-Ray diffraction peaks analysis.

FUTURE WORKS

The aspects of the research carried out in this thesis have some open issues that deserve further research. In relation to the fatigue analysis, a study of the mean stress effects in the fatigue damage phenomenon could be done, with fatigue bending tests with stress ratios different from -1. When minimum and maximum load are not identical in magnitude then it contains some amount of residual stress which is called mean stress. It is well known

that mean stress in tension has bad effect on the component fatigue life, which get reduced as mean stress get increased. But if mean stress is in compression then it increases the life of the material [126]. In operational condition, the equipment is generally submitted to different levels of maximum and minimum stresses and a mean stress is presented, and the effects of it in relation to the fatigue life of the material should be investigated. Still in relation to the fatigue tests, here, uniaxial fatigue tests were done. For future works it is recommended a study of biaxial or multiaxial fatigue analysis trying to get closer to operational conditions.

Transmission electron microscopy (TEM) is a microscopy technique in which a beam of electrons is transmitted through a specimen to form an image, and it could be used to follow the evolution of microstructural during the propagation of a microcrack. TEM analysis could be done in different percentages of the fatigue life to follow the behavior of dislocations and compare the results with the indentation and X-ray analysis performed in this work. TEM analysis were done by Pinheiro et al. [15] with samples of X-60 steel during the fatigue life of the material with good results.

The stress distribution in the fatigue sample during cycling could be better studied with a finite element analysis. Future studies could consider a model in a finite element software, like Abaqus, for better characterization of stress concentration regions in the sample. For example between the two holes, where the hardness reference values were measured (Figure VI-4) to confirm that it is a zero stress area, or in the width of the sample to confirm the stress values for lines 3 and 4, calculated here as 171 and 255MPa, respectively, for a stress amplitude of 272 MPa, and 225 and 335MPa, respectively, for a stress amplitude of 358MPa.

In relation to indentation tests, here instrumented cycling microindentation tests were performed, with 20 cycled of indentation and load increment of 100mN/min from 0.2 to 2N. The analyses were done at a penetration depth of 2μm from the surface of the sample. This penetration depth was chosen because it is the smallest value of depth that this technique can measure in this kind of material (Figure VI-58). Since fatigue in Stage I of the fatigue life is a surface phenomenon, dynamic indentation analysis could be done to calculate hardness values in penetration depths smaller than 2μm. To do dynamic indentation analysis, no more indentation tests are needed. It could be used the data obtained in this work with the

software of the machine CSM 2-107 and calculate the values of hardness for *hi* penetration depths for *hi*<2µm as the following equations.

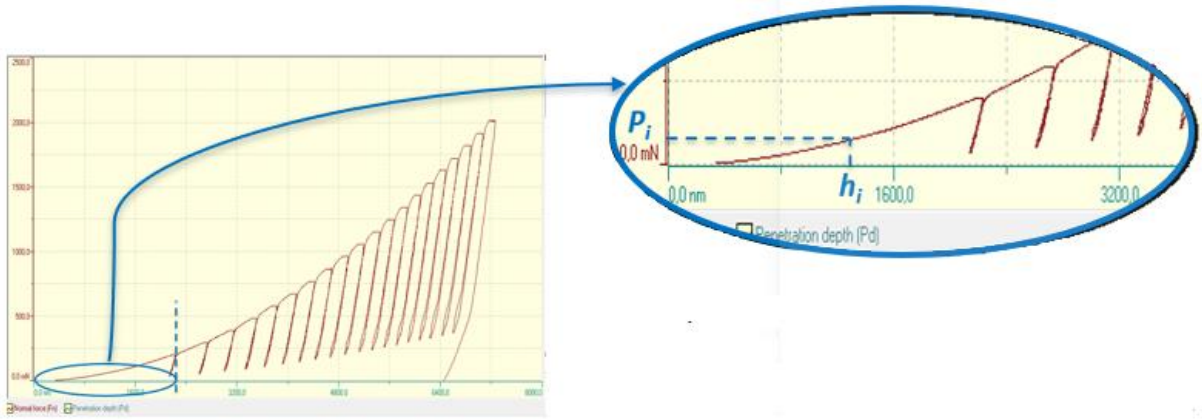

Figure VI-58: Load versus penetration depth curve for 20 cycles of indentation for a instrumented indentation test with zoom in the area with *hi*<2µm, where dynamic indentation analysis could be done.

$$H_i = \frac{P_i}{A_i}$$

Equation VI-7

where H_i is hardness and P_i is load values for penetration dephts *hi*<2µm. P_i values are given by the software, and A_i can be calculated by Equation VI-8.

$$A_i = 24.43\left[h_i + \left(h_b\left(1 - exp\left(-2\frac{h_i}{h_b}\right)\right)^{3/2}\right)\right]^2$$

Equation VI-8

where h_b is the truncation value related to the tip defect, for a Berkovich indenter, h_b =50 nm.

It is important to note that contact area calculation is different here because dynamic indentation analyses should be done with the real contact area (martens hardness calculation for example), and not with the project contact are calculated for instrumented hardness (H_{IT}).

For the X-Ray diffraction analysis, future works could consider other peak broadening analyses methods like Warren and Averbach [71,72], Williamson and Hall [73] or the variance method [74]. These are quantitative methods, with a big mathematical content, and the results should be compared with the qualitative method used in this work, the full width at half maximum (FWHM). Still in the theme of X-Ray diffraction analysis, measurements could be done in different diffraction planes. Here, just [211] plane was considered.

Future works can also consider the validation of the method developed in this work for other pipeline steels, like API X-52, X-60, X-70, or for other materials. Fatigue bending tests with other levels of stress amplitudes and an analysis of the influence of the roughness of the surface in the fatigue tests and in the indentation and X-ray results are also suggestions for future studies.

REFERENCES

REFERENCES

[1] de Souza Canelas, A. L. (2007). Evolução da importância econômica da indústria de petróleo e gás natural no Brasil: contribuição a variáveis macroeconômicas (*Doctoral dissertation, UNIVERSIDADE FEDERAL DO RIO DE JANEIRO*).

[2] FORBES. The Global 2000. The World's Largest Public Companies. USA: Forbes, 2019. Available in https://www.forbes.com/global2000/#342137c7335d, accessed in July 17, 2019.

[3] Drumond, G. P., Pasqualino, I. P., Pinheiro, B. C., & Estefen, S. F. (2018). Pipelines, risers and umbilicals failures: A literature review. *Ocean Engineering*, *148*, 412-425.

[4] Malitckii, E., Remes, H., Lehto, P., Yagodzinskyy, Y., Bossuyt, S., & Hänninen, H. (2018). Strain accumulation during microstructurally small fatigue crack propagation in bcc Fe-Cr ferritic stainless steel. *Acta Materialia*, *144*, 51-59.

[5] Tomkins, B., & Biggs, W. D. (1969). Low endurance fatigue in metals and polymers. *Journal of Materials Science*, *4*(6), 544-553.

[6] Peralta, P., & Laird, C. (1998). Fatigue fracture at bicrystal interfaces: experiment and theory. *Acta materialia*, *46*(6), 2001-2020.

[7] Vehoff, H., & Neumann, P. (1979). In situ SEM experiments concerning the mechanism of ductile crack growth. *Acta Metallurgica*, *27*(5), 915-920.

[8] Neumann, P. (1974). The geometry of slip processes at a propagating fatigue crack—II. *Acta Metallurgica*, *22*(9), 1167-1178.

[9] Paris, P., & Erdogan, F. (1963). A critical analysis of crack propagation laws. Journal of basic engineering, 85(4), 528-533.

[10] Bjerkén, C., & Melin, S. (2008). Influence of low-angle boundaries on short fatigue cracks studied by a discrete dislocation method. In *17th European Conference on Fracture* (pp. 257-264).

[11] Bjerkén, C., & Melin, S. (2009). Growth of a short fatigue crack–A long term simulation using a dislocation technique. *International Journal of Solids and Structures*, *46*(5), 1196-1204.

[12] Andersson, H., & Persson, C. (2004). In-situ SEM study of fatigue crack growth behavior in IN718. *International Journal of Fatigue*, *26*(3), 211-219.

[13] Jono, M., Sugeta, A., & Uematsu, Y. (2001). Atomic force microscopy and the

mechanism of fatigue crack growth. *Fatigue & Fracture of Engineering Materials & Structures*, *24*(12), 831-842.

[14] Ye, D., & Wang, Z. (2001). An approach to investigate pre-nucleation fatigue damage of cyclically loaded metals using Vickers microhardness tests. *International journal of fatigue*, 23(1), 85-91.

[15] Pinheiro, B.C. (2011). Étude par Diffraction des Rayons X des Modifications Microstructurales em Cours de Fatigue, *Thèse de Doctorat, Université Lille 1 - Sciences et Technologies*, Lille, France.

[16] Almarnaess, A. (1985). Fatigue handbook: offshore steel structures.

[17] Cui, W. (2002). A state-of-the-art review on fatigue life prediction methods for metal structures. *Journal of marine science and technology, 7(1), 43-56.*

[18] Wöhler, A. (1860). Versuche über die Festigkeit der Eisenbahnwagenachsen. *Zeitschrift für Bauwesen*, 10, 160-161.

[19] Budynas, R., & Nisbett, J. K. (2008). *Fatigue failure resulting from variable loading.*

[20] Shigley, J. E., & Mischke, C. R. (2008). Fatigue Failure Resulting from Variable Loading. *Mechanical Engineering Design, 370-73*.

[21] Meyers, M. A., & Chawla, K. K. (2008). *Mechanical behavior of materials*. Cambridge university press.

[22] Bozdana, A. T. (2019). ME215 – Engineering Materials I, Chapter 6 – Fatigue Properties. *Class notes of the Mechanical Engineering course of the University of Gaziantep, Turkey.* Disponible online at https://www.coursehero.com/file/7390458/ME215-6/. Accessed in July 29, 2019.

[23] Budynas, R.G. and Nisbett, J.K. (2015). *Shigley's Mechanical Engineering Design, Tenth Edition*. Chapter 6, pp. 273 – 294.

[24] Cunha, S. B., Pasqualino, I. P., & Pinheiro, B. C. (2009). Stress-life fatigue assessment of pipelines with plain dents. *Fatigue & Fracture of Engineering Materials & Structures*, 32(12), 961-974.

[25] Cui, W. (2002). A state-of-the-art review on fatigue life prediction methods for metal structures. *Journal of marine science and technology*, 7(1), 43-56.

[26] Malitckii, E., Remes, H., Lehto, P., Yagodzinskyy, Y., Bossuyt, S., & Hänninen, H. (2018). Strain accumulation during microstructurally small fatigue crack propagation in bcc Fe-Cr ferritic stainless steel. *Acta Materialia*, *144*, 51-59.

[27] Tomkins, B., & Biggs, W. D. (1969). Low endurance fatigue in metals and polymers. *Journal of Materials Science*, *4*(6), 544-553.

[28] Peralta, P., & Laird, C. (1998). Fatigue fracture at bicrystal interfaces: experiment and theory. *Acta materialia*, *46*(6), 2001-2020.

[29] Vehoff, H., & Neumann, P. (1979). In situ SEM experiments concerning the mechanism of ductile crack growth. *Acta Metallurgica*, *27*(5), 915-920.

[30] Neumann, P. (1974). The geometry of slip processes at a propagating fatigue crack—II. *Acta Metallurgica*, *22*(9), 1167-1178.

[31] Paris, P., & Erdogan, F. (1963). A critical analysis of crack propagation laws. *Journal of basic engineering*, 85(4), 528-533.

[32] Mughrabi, H. (1981). Cyclic plasticity of matrix and persistent slip bands in fatigued metals. *Continuum Models of Discrete Systems*, 4(0), 24l-257.

[33] Cottrell, A. H., & Hull, D. (1957). Extrusion and intrusion by cyclic slip in copper. *Proceedings of the Royal Society of London. Series A. Mathematical and Physical Sciences*, *242*(1229), 211-213.

[34] Wood, W. A. (1955). Fine Slip in Fatigue. *JOURNAL OF THE INSTITUTE OF METALS*, *84*(1), 5-6.

[35] Broitman, E. (2017). Indentation hardness measurements at macro-, micro-, and nanoscale: a critical overview. *Tribology Letters*, *65*(1), 23.

[36] Brinell, J. A. (1900). Way of determining the hardness of bodies and some applications of the same. *Teknisk Tidskrift*, *5*, 69.

[37] Rockwell, H. M., & Rockwell, S. P. (1919). U.S. Patent No. 1,294,171. Washington, DC: U.S. Patent and Trademark Office.

[38] Lips, E., Sack, J.: A hardness tester for microscopical objects. Nature 138, 328–329 (1936)

[39] ASTM E384 - 16: Standard Test Method for Microindentation Hardness of Materials. ASTM International, West Conshohocken (2016)

[40] ISO 6507-1-2005: Metallic Materials—Vickers Hardness Test— Part 1: Test Method. International Organization for Standardization, Geneva (2005)

[41] Oliver, W. C., & Pharr, G. M. (1992). An improved technique for determining hardness and elastic modulus using load and displacement sensing indentation experiments. *Journal of materials research*, *7*(6), 1564-1583.

[42] Chicot, D., Roudet, F., Zaoui, A., Louis, G., & Lepingle, V. (2010). Influence of visco-elasto-plastic properties of magnetite on the elastic modulus: multicyclic indentation and theoretical studies. *Materials chemistry and physics*, *119*(1-2), 75-81.

[43] King, R. B. (1987). Elastic analysis of some punch problems for a layered medium. *International Journal of Solids and Structures*, *23*(12), 1657-1664.

[44] Fischer-Cripps, A. C. (2006). Critical review of analysis and interpretation of nanoindentation test data. *Surface and coatings technology*, *200*(14-15), 4153-4165.

[45] Loubet J.L., Bauer M., Tonck A., Bec S., Gauthier B. (1993). Manuel, Mechanical properties and deformation behavior of materials having ultra-fine microstructures. NATO ASI, 233, 429-447.

[46] N'jock M.Y., Chicot D., Ndjaka J.M., Lesage J., Decoopman X., Roudet F., Mejias A. (2015). A criterion to identify sinking-in and piling-up in indentation of materials. International Journal of Mechanical Sciences, 90, 145-150.

[47] Chicot, D., N'Jock, M. Y., Puchi-Cabrera, E. S., Iost, A., Staia, M. H., Louis, G. & Aumaitre, R. (2014). A contact area function for Berkovich nanoindentation: Application to hardness determination of a TiHfCN thin film. Thin Solid Films, 558, 259-266.

[48] Ye, D. Y., Wang, D. J., & An, P. (1996). *Characteristics of the change in the surface microhardness during high cycle fatigue damage.* Materials chemistry and physics, 44(2),179-181.

[49] Ye, D., & Wang, Z. (2001). An approach to investigate pre-nucleation fatigue damage of cyclically loaded metals using Vickers microhardness tests. International journal of fatigue, 23(1), 85-91.

[50] Ye, D., Tong, X., Yao, L., & Yin, X. (1998). *Fatigue hardening/softening behaviour investigated through Vickers microhardness measurement during high- cycle fatigue*. Materials chemistry and physics, 56(3), 199-204.

[51] Casagrande, A., Cammarota, G. P., & Micele, L. (2011). Relationship between fatigue limit and Vickers hardness in steels. Materials Science and Engineering: A, 528(9), 3468-3473.

[52] Vuherer, T., Milović, L., & Gliha, V. (2011). Behaviour of small cracks during their propagation from Vickers indentations in coarse-grain steel: An experimental investigation. International Journal of Fatigue, 33(12), 1505-1513.

[53] Hirano, A., Sakane, M., & Hamada, N. (2005). Relationship Between Vickers Hardness and Fatigue Strength.

[54] Paduano, Q. S., Weyburne, D. W., & Drehman, A. J. (2011). An X-ray diffraction technique for analyzing structural defects including microstrain in nitride materials. Journal of Crystal Growth, 318(1), 418-422.

[55] Hirsch, P. B., & Kellar, J. N. (1952). A study of cold-worked aluminum by an X-ray microbeam technique. I. Measurement of particle volume and misorientations. Acta Crystallographica, 5(2), 162-167.

[56] Taira, S., & Honda, K. (1961). X-ray Investigation on the Fatigue Damage of Metals. Bulletin of JSME, 4(14), 230-237.

[57] Taira, S., Tanaka, K., & Tanabe, T. (1970). Study of tensile deformation of low-carbon steel by X-ray microbeam technique. Proc. 13th Jap. Congr. Mater. Res, 14-9.

[58] Shuji, T., & Keisuke, T. (1972). Study of fatigue crack propagation by X-ray diffraction approach. Engineering Fracture Mechanics, 4(4), 925-938.

[59] Moram, M. A., & Vickers, M. E. (2009). X-ray diffraction of III-nitrides. Reports on progress in physics, 72(3), 036502.

[60] Cullity, B. D. (1956). Elements of X-ray diffraction Reading. Published by Addison-Wesley Publishing Company, Inc., United States of America.

[61] Hammond, C., & Hammond, C. (2001). The Basics of Crystallography and Diffraction (Vol. 214). Oxford.

[62] Prevéy, P. S. (1992). Problems with Non-Destructive surface X-Ray diffraction residual stress measurement. Shot Peener, The, 5(4), 5-11.

[63] Djaziri, S., Thiaudière, D., Geandier, G., Renault, P. O., Le Bourhis, E., Goudeau, P., ... & Faurie, D. (2010). Controlled biaxial deformation of nanostructured W/Cu thin films studied by X-ray diffraction. Surface and Coatings Technology, 205(5), 1420-1425.

[64] Hecker, M. (2006, February). Stresses in Laterally Structured Copper Layer Systems Studied by X-ray Diffraction. In AIP Conference Proceedings (Vol. 817, No. 1, pp. 296-302). AIP.

[65] Manns, T., Gibmeier, J., & Scholtes, B. (2006). Determination of Real Space Residual Stress Distributions σij (z) of Surface Treated Materials with Diffraction Methods Part I: Angle-Dispersive Approach. In Materials science forum (Vol. 524, pp. 31-36). Trans Tech Publications.

[66] Genzel, C. (2001). X-ray stress analysis in presence of gradients and texture. Advances in X-ray Analysis, 44, 247.

[67] Luo, Q., & Jones, A. H. (2010). High-precision determination of residual stress of polycrystalline coatings using optimized XRD-sin2ψ technique. Surface and Coatings Technology, 205(5), 1403-1408.

[68] Janssen, G. C. A. M. (2007). Stress and strain in polycrystalline thin films. Thin solid films, 515(17), 6654-6664.

[69] Scardi, P., Polonioli, P., & Ferrari, S. (1994). Residual stress in stabilized zirconia thin films prepared by rf magnetron sputtering. Thin Solid Films, 253(1-2), 349-355.

[70] Teixeira, V., Andritschky, M., Fischer, W., Buchkremer, H. P., & Stöver, D. (1999). Effects of deposition temperature and thermal cycling on residual stress state in zirconia-based thermal barrier coatings. Surface and Coatings Technology, 120, 103-111.

[71] Warren, B. E., & Averbach, B. L. (1952). The separation of cold-work distortion and particle size broadening in X-ray patterns. Journal of applied physics, 23(4), 497-497.

[72] Warren, B. E., & Averbach, B. L. (1952). The Separation of Stacking Fault Broadening in Cold-Worked Metals. Journal of Applied Physics, 23(9), 1059-1059.

[73] Williamson, G. K., & Hall, W. H. (1953). X-ray line broadening from filed aluminum and wolfram. Acta metallurgica, 1(1), 22-31.

[74] Groma, I. (1998). X-ray line broadening due to an inhomogeneous dislocation distribution. Physical Review B, 57(13), 7535.

[75] Sarkar, A., Mukherjee, P., & Barat, P. (2008). X-ray diffraction studies on asymmetrically broadened peaks of heavily deformed zirconium-based alloys. Materials Science and Engineering: A, 485(1-2), 176-181.

[76] Wilkens, M. (1970). The determination of density and distribution of dislocations in deformed single crystals from broadened X-ray diffraction profiles. *Physica status solidi (a)*, *2*(2), 359-370.

[77] Wilkens, M. (1987). X-ray line broadening and mean square strains of straight dislocations in elastically anisotropic crystals of cubic symmetry. physica status solidi (a), 104(1), K1-K6.

[78] Ichikawa, R. U. (2013). Aplicações do método Warren-Averbach de análise de perfis de difração (Doctoral dissertation, Universidade de São Paulo).

[79] Kerber, M. B., Schafler, E., & Zehetbauer, M. (2005). Processing and evaluation of X-ray line profiles measured from nanostructured materials produced by severe plastic deformation. Rev. Adv. Mater. Sci, 10, 427-433.

[80] Krivoglaz, M. A. (1969). THEORY OF X-RAY AND THERMAL-NEUTRON SCATTERING BY REAL CRYSTALS.

[81] Krivoglaz, M. A. (1996). X-Ray and Neutron Scattering in Nonideal Crystals.

[82] Ungár, T. (2001). Dislocation densities, arrangements and character from X-ray diffraction experiments. Materials Science and Engineering: A, 309, 14-22.

[83] Tian, H. H., & Atzmon, M. (1999). Comparison of X-ray analysis methods used to determine the grain size and strain in nanocrystalline materials. Philosophical magazine A, 79(8), 1769-1786.

[84] Marinkovic, B., Avillez, R. R. D., Saavedra, A., & Assunção, F. C. R. (2001). A comparison between the Warren-Averbach method and alternate methods for X-ray diffraction microstructure analysis of polycrystalline specimens. Materials Research, 4(2), 71-76.

[85] Van Berkum, J. G. M., Vermeulen, A. C., Delhez, R., de Keijser, T. H., & Mittemeijer, E. J. (1994). Applicabilities of the Warren–Averbach analysis and an alternative analysis for separation of size and strain broadening. Journal of applied crystallography, 27(3), 345-357.

[86] Bourniquel, B., Sprauel, J. M., Feron, J., & Lebrun, J. L. (1989). Warren-Averbach Analysis of X-ray Line Profile (even truncated) Assuming a Voigt-like Profile. In International Conference on Residual Stresses (pp. 184-189). Springer, Dordrecht.

[87] Ichikawa, R. U., Martinez, L. G., Imakuma, K., & Turrillas, X. (2014). Development of a methodology for the application of the Warren-Averbach method. Anais do V Encontro Científico de Física Aplicada. Blucher Physics Proceedings, (1), 107-110.

[88] Bakshi, S. D., Sinha, D., & Chowdhury, S. G. (2018). Anisotropic broadening of XRD peaks of α′-Fe: Williamson-Hall and Warren-Averbach analysis using full width at half maximum (FWHM) and integral breadth (IB). Materials Characterization, 142, 144-153.

[89] Prabhu, Y. T., Rao, K. V., Kumar, V. S. S., & Kumari, B. S. (2014). X-ray analysis by Williamson-Hall and size-strain plot methods of ZnO nanoparticles with fuel variation. World Journal of Nano Science and Engineering, 4(01), 21.

[90] Azaroff, L.V. (1968). Elements of X-ray Crystallography, Mc Graw-Hill, New York, pp. 549-558.

[91] Warren, B.E. (1990). X-ray diffraction, Dover Publications, New York, pp. 251-252.

[92] Maeder, G., Lebrun, J. L., & Sprauel, J. M. (1981). Present possibilities for the X-ray diffraction method of stress measurement. NdT International, 14(5), 235-247.

[93] Dorn, S., Hirsch, T., & Mayr, P. (1994). Structural alterations of local damage in ball bearings subjected to rolling contact fatigue. Materials Science and Engineering: A, 189(1-2), 181-189.

[94] Prevéy, P. S. (1996). Current applications of X-ray diffraction residual stress measurement. Developments in Materials Characterization Technologies, 103-110.

[95] Prevéy, P. S. (1992). Problems with Non-Destructive surface X-Ray diffraction residual stress measurement. Shot Peener, The, 5(4), 5-11.

[96] Goto, T. (1991). Material strength evaluation and damage detection by X-ray diffraction. Advances in X-ray Analysis, 35(A), 489-501.

[97] Akiniwa, Y., Machiya, S., & Tanaka, K. (2006). Fatigue damage evaluation in SiCp/2024 by X-ray diffraction method. International journal of fatigue, 28(10), 1406-1412.

[98] Akiniwa, Y., Machiya, S., Kimura, H., Tanaka, K., Minakawa, N., Morii, Y., & Kamiyama, T. (2006). Evaluation of material properties of SiC particle reinforced aluminum alloy composite using neutron and X-ray diffraction. Materials Science and Engineering: A, 437(1), 93-99.

[99] Fourspring, P. M., & Pangborn, R. N. (1997). An X-Ray Diffraction Study of Microstructural Deformation Induced by Cyclic Loading of Steels. In Fatigue and Fracture Mechanics: 28th Volume. ASTM International.

[100] Olchini, A., Stamm, H., & Marques, F. D. S. (1998). Fatigue damage monitoring of laser surface treated steel by X-ray diffraction methods. Surface engineering, 14(5), 386-390.

[101] Pangborn, R. N., Weissmann, S., & Kramer, I. R. (1979). Prediction of fatigue life by X-ray diffraction methods. Fatigue & Fracture of Engineering Materials & Structures, 1(3), 363-369.

[102] Vijayan, K., Mani, A., Balasingh, C., & Singh, A. K. (1988). X-ray analysis of polycrystalline aluminum subjected to fatigue cycling. Bulletin of Materials Science, 10(3), 205-216.

[103] Kuo, H. K., & Cohen, J. B. (1983). Changes in residual stress, domain size and microstrain during the fatigue of AISI 1008 steel. Materials Science and Engineering, 61(2), 127-136.

[104] Pangborn, R. N., Weissmann, S., & Kramer, I. R. (1981). Dislocation distribution and prediction of fatigue damage. Metallurgical Transactions A, 12(1), 109-120.

[105] Winholtz, R. A., & Cohen, J. B. (1992). Changes in the macrostresses and microstresses in steel with fatigue. Materials Science and Engineering: A, 154(2), 155-163.

[106] Tanaka, K. (1975). Recent x-ray diffraction studies of metal fatigue in Japan. Journal of Strain Analysis, 10(1), 32-41.

[107] Lesage, J., Chicot, D., Perez, P., & Chatelet, J. M. (1994). X-ray diffraction study of microstructural modifications during fatigue. Euromat 94., 2, 616-620.

[108] Pinheiro, B., Lesage, J., Pasqualino, I., Benseddiq, N., & Bemporad, E. (2012). X-ray diffraction study of microstructural changes during fatigue damage initiation in steel pipes. Materials Science and Engineering: A, 532, 158-166.

[109] Pinheiro, B., Lesage, J., Pasqualino, I., Bemporad, E., & Benseddiq, N. (2013). X-ray diffraction study of microstructural changes during fatigue damage initiation in pipe steels: Role of the initial dislocation structure. Materials Science and Engineering: A, 580, 1-12.

[110] Pinheiro, B., Lesage, J., Pasqualino, I., Benseddiq, N., & Bemporad, E. (2015, May). Toward a Fatigue Life Assessment of Steel Pipes Based on X-Ray Diffraction Measurements. In ASME 2015 34th International Conference on Ocean, Offshore and Arctic Engineering (pp. V05BT04A027-V05BT04A027). American Society of Mechanical Engineers.

[111] American Association of State Highway and Transportation Officials, & American Society for Testing and Materials. (2004). E8M-04 Standard Test Methods for Tension Testing of Metallic Materials (Metric) 1. ASTM International.

[112] ASTM, E. (2014). E 415-2014. Standard test method for Analysis of carbon and low alloy steel by spark atomic emission spectrometry. ASTM annual book of standards.

[113] Spec, A. P. I. (2012). 5L: Specification for Line Pipe. American Petroleum Institute: Washington, DC, USA.

[114] Shackelford, J. F., & Muralidhara, M. K. (2005). Introduction to materials science for engineers.

[115] Callister, JR, W. D. *Ciência e Engenharia de Materiais-Uma Introdução. Rio de Janeiro: Livros Técnicos e Científicos* Editora, 2007 (p. 239). ISBN 978-85-216-1595-8.

[116] Shewmon, P. G (1969). Transformations in Metals. MacGraw-Hill. USA. 394 p.

[117] De Oliveira, B. F. (2014). *Efeito dos tratamentos térmicos sobre a microestrutura e as propriedades de um aço ARBL microligado com estrutura bruta de solidificação*. MSc

Dissertation, Universidade Estadual do Norte Fluminense Darcy, Rio de Janeiro, Brazil.

[118] Higgins, R. A. (1993). Applied Physical Metallurgy. 6ª ed. London, England. Arnold – Hodder Headline Group. 576 p.

[119] C. Schenck, Wechselbiegemaschine PWON, Maschinenfabrik GmbH, Darmstadt, Germany, 1971

[120] Chicot, D., Tilkin, K., Jankowski, K., & Wymysłowski, A. (2013). Reliability analysis of solder joints due to creep and fatigue in microelectronic packaging using microindentation technique. Microelectronics Reliability, 53(5), 761-766.

[121] AFNOR (1999). *Association Française de Normalisation, Essais non destructifs – Méthodes d'essais pour l'analyse des contraintes résiduelles par diffraction des rayons X*, XP A 09-285, Paris.

[122] Van Vliet, K. J., Prchlik, L., & Smith, J. F. (2004). Direct measurement of indentation frame compliance. Journal of materials research, 19(1), 325-331.

[123] Bandyopadhyay, P. P., Chicot, D., Kumar, C. S., Decoopman, X., & Lesage, J. (2013). Influence of sinking-in and piling-up on the mechanical properties determination by indentation: A case study on rolled and DMLS stainless steel. Materials Science and Engineering: A, 576, 126-133.

[124] Ning, J. I., & Lebrun, J. L. (1990). Microstructural study of static and dynamic deformed polycrystalline copper by X-ray diffraction profile analysis. Scripta Metallurgica et Materialia, 24(8), 1547-1552.

[125] Dalaei, K., Karlsson, B., & Svensson, L. E. (2010). Stability of residual stresses created by shot peening of pearlitic steel and their influence on fatigue behaviour. Procedia Engineering, 2(1), 613-622.

[126] Kumbhar, S. V., & Tayade, R. M. (2014). A case study on effect of mean stress on fatigue life. International Journal of Engineering Development and Research, 2(1), 304-308.